**Modelling the response of Arctic and Subarctic marine systems to climate warming**

by

Laura Castro de la Guardia

A thesis submitted in partial fulfillment of the requirements for the degree of

Doctor of Philosophy

Department of Earth and Atmospheric Sciences

University of Alberta

# Abstract

The Arctic and the North Atlantic Oceans are experiencing multiple stresses such as loss of sea ice, changing atmospheric patterns, increasing wind energy at the ocean surface and larger freshwater discharge to coastal regions. To address how the marine system may respond to these stresses I designed and analysed a suite of simulations using a state of the art ocean circulation- sea ice - biogeochemical coupled model. By combining physical oceanography, biogeochemistry and general ecology, this thesis attempts to give an interdisciplinary perspective on the simulated regional changes. The approach was to use sensitivity experiments to isolate the stimuli and the response, and to study the underlying mechanisms leading to the response. I was able to address the impacts of three stresses: large scale atmospheric forcing, stormy wind events, and increasing freshwater discharge. (1) In regard to the sensitivity of deep ocean ventilation to changes in large scale atmospheric patterns like the North Atlantic Oscillation (NAO), I find that ventilation within the deep Labrador Sea is sensitive to the NAO, but unlike previously suggested, the lateral oxygen fluxes dominate the ventilation process over air-sea oxygen fluxes. (2) Windy conditions, which are predicted to increase in the Arctic Ocean, are indeed responsible for a large part of the primary production and biogenic carbon export in the Arctic and Subarctic. The importance of stormy winds is highest in seasonal and ice free regions and lowest in light limited perennial ice regions. (3) The hosing experiments performed to measure the effect of increasing meltwater run-off from the Greenland Ice Sheet revealed that a positive feedback may develop within Baffin Bay with the potential to accelerate melting by bringing warm waters closer to marine terminating glaciers.

# Preface

Chapter 5 has been published as:

I was responsible for the data analysis and writing of the manuscript. X.Hu ran the simulation and assisted with the data analysis and writing. P.Myers provided advice and manuscript edits.

# Dedication

**This thesis is dedicated to my grandmothers, Abuela Emma and Abuela Lourdes,**

**as they have been essential pillars in my life**.

Abuela Emma quit her job to care for me and my sister and helped us go through school. Even today, at the age of 90, she still likes to cook the lunch for me so that I have more time to study. She is the foundation of my strength. Abuela Lourdes played an essential role in developing my English when I was a child, and still today, she insists on speaking English when I visit her in Cuba. She is the foundation of my perseverance.

**Esta tesis esta dedicada a mis abuelas, Abuela Emma y Abuela Lourdes,**

**ya que han sido pilares esenciales en mi vida**.

Abuela Emma renuncio a su trabajo para cuidarnos a mi hermana y a mi y ayudarnos en nuestro despeño en la escuela. Incluso hoy, a la edad de 90 año, le gusta cocinarme el almuerzo para que yo tenga más tiempo de estudiar. Ella es el pilar de mi fuerza. Abuela Lourdes jugó un papel esencial en mi aprendizaje del idioma Inglés cuando yo era una niña, incluso hoy, insiste en conversar conmigo en Inglés cuando yo la visito en Cuba. Ella es el pilar de mi perseverancia.

# Acknowledgements

I am grateful to my supervisor, Prof. Paul G. Myers, and co-supervisor Prof. Eric D. Galbraith for their guidance and support during all these years. I have come to admire Prof. Myers for placing the student's professional and personal growth first. I am very fortunate that Prof. Galbraith accepted to co-supervise me, he has been of great to consult about BLING and biochemistry in general.

I thank Dr. Xianmin Hu and Dr. Mariona Claret for their diligent work in the coupling of BLING and NEMO, which was made in a record time! It is this break-through that allowed me to present the first NEMO-BLING couple model results. The work presented in this thesis would not have been possible without the technical work they did, and their continuous support throughout.

Big THANK goes to all my colleagues outside and inside the numerical and fluid dynamic lab at the University of Alberta and the ArcTrain program and students. They have been an amazing support. Special thanks to Yarisbel Garcia, Nathan Grivault, Natasha Ridenour and Inge Deschepper who helped me to proofread and clarify the chapters in this thesis at the expense of taking time off their busy schedule (e.g. conversing loudly in the lab, computer gaming and chatting with friends abroad, ohh, just kidding), to Alain Gervais for his help on the technical formatting of this thesis, and most specially to Yarisbel Garcia and Daniel Ferrer for being friends during good moods, bad moods, stress moods, etc.

My family has also been a crucial component during these times. My most recent family member, my husband-Konstantin Stoletov tried to teach me how to balance studying and outdoor activities. From climbing and running with him, I realized that the most challenging summits give the most satisfaction upon reaching the top. This thesis became my most challenging summit ever. This way the writing process became a fun outdoor project which I often used as an excuse to stop Konstantin from dragging me to go outside.

My whole family (siblings, parents, aunts & uncles, cousins and grandmothers) has been amazing in providing moral support and encouragement. I should highlight my incredible parents who did not let me suffer alone the hardships of graduate school, literally! My father did his M.Sc. at the same time as me, and my mother did her Ph.D., also at the same time as me. They were not only devoted parents but also great colleagues to laugh about graduate school.

# Contents

# List of Figures

# List of Tables

# Chapter 1

# Introduction

Since the end of the pre-industrial revolution in the 1850s, atmospheric concentration of greenhouse gases have been rising. Most remarkably, atmospheric carbon dioxide ($CO_2$) concentrations have increased nearly 30% since 1958, with 2017 concentration estimated at $406\,ppm$, and continuing to increase at $2.13\,ppm\,yr^{-1}$ (data from NOAA ESRL-Station Mauna Loa: $http://www.esrl.noaa.gov$). In response, the global mean temperature has risen by $0.85°C$ with the majority of the warming occurring after the 1970s and at higher latitudes (Hartmann et al., 2013).

In the Northern Hemisphere, temperature increases have already exceeded $1.5°C$ relative to the 1951-1980 climatology (data from $https://data.giss.nasa.gov/gistemp/$). This warming amplification at northern latitudes is linked to processes driven by positive albedo feedbacks resulting from the loss of snow and ice in both land and the ocean (Serreze and Francis, 2006; Screen and Simmonds, 2010; Screen et al., 2012). Observations show that snow cover extent and depth on land areas (Kunkel et al., 2016) have decreased at a slower rate than sea ice and snow cover over the Arctic Ocean (Comiso and Nishio, 2008; Tivy et al., 2011). This is because the ocean is playing an increasingly important role in accelerating sea ice basal melt (Ramudu et al., 2018) and delaying sea ice formation in autumn (Polyakov et al., 2017). The loss of sea ice exposes larger areas of the Arctic Ocean to incoming solar radiation and atmospheric warming, causing it to absorb more heat which is then used to prevent sea ice formation in autumn and melt more ice in summer. Indeed, the amount of solar energy absorbed by the ocean during summer has increased by an amount equivalent to melting of an additional 0.97 to 1.3 m of ice during the summer (Stroeve et al., 2011). More heat in the Arctic Ocean, however, does not only a result from more heat trapped within the surface Arctic water during summer, heat is also advected from the tropics into the Northern Oceans by major ocean currents that form part of the Meridional Overturning Circulation (MOC).

## 1.1 Northern Ocean's general circulation

The MOC is an oceanic circulation system with a key role in the redistribution of mass and heat around the world's oceans (Kuhlbrodt et al., 2007). The MOC brings heat and salt to the polar regions and transports cold and fresh waters towards the equator. In the Northern Oceans (including North Atlantic and Arctic Oceans), the cold and fresh Pacific Water mixes with the warm and salty Atlantic Water. The Northern Oceans are a key region where water masses are formed as a result of this exchange of heat and salt. Pacific Water enters the Arctic Ocean at the surface (above $50\,m$) through Bering Strait in the Anadyr and the Alaskan Coastal currents (Figure 1.1). This current system carries very little heat, and it is most important through its effect in reducing the salinity of the surface Arctic Water, contributing to stronger stratification (Rudels et al., 1991) and thus leading to more heat trapped within the Arctic Ocean surface during summer. The Atlantic Water enters the Northern Oceans in the North Atlantic Current (NAC), one of the major currents of the MOC. The NAC branches within the Subpolar Gyre (Figure 1.1). One branch takes waters into the Labrador Sea and the other continues into the Nordic Seas. Waters that follow the Labrador Sea pathway reach Baffin Bay in the West Greenland Current (WGC), and from Baffin Bay it may reach some of the deepest channels within the Canadian Arctic Archipelago (CAA) (Steffen, 1985). Waters that follow the Nordic Seas pathway reach well into the Arctic Basin (Figure 1.1).

Although Atlantic Water is warm, this inflow does not directly contribute to melting sea ice within the Arctic Ocean. As the NAC flows into high latitudes, it undergoes significant transformation (e.g. cooling and freshening) within the Labrador, Irminger and the Nordic Seas resulting in the Atlantic Water sinking below the surface, before reaching the sea ice covered regions: Baffin Bay, the CAA and the Arctic Ocean (e.g. Smedsrud et al., 2013). However, the large heat losses of the Atlantic Water within the Labrador Sea, the Irminger Sea and the Nordic Seas is one reason for these areas to be presently ice-free. Most recently the warmer NAC and its penetration further north have been associated with declines in sea ice within the Barents Sea (Årthun et al., 2012; Onarheim and Årthun, 2017; Li et al., 2017).

The Atlantic Water transformation within the Northern Ocean leads to the formation of the warm Atlantic Water layer found at intermediate depth within the Arctic Ocean (Ramudu et al., 2018), and to the formation of deep waters in the North Atlantic which drive the MOC (Kuhlbrodt et al., 2007). Harsh winter conditions over the ice-free regions of the Northern Oceans drive large heat losses from the ocean to the atmosphere. The different rate at which the surface ocean loses heat in the Labrador Sea, the Irminger Sea and the Nordic Seas determines the extent of vertical mixing and the main deep water formation process. For example, it determines the predominance of deep convection in the central Labrador Sea (Sathiyamoorthy and Moore, 2002; Holdsworth and Myers, 2015; Rhein et al., 2017) and in the Irminger Sea (Våge et al., 2011), cascading

in Davis Strait region (Marson et al., 2017) and gradual water transformation within the Nordic Seas (Isachsen et al., 2007; Eldevik et al., 2009). The type of transformation and where it occurs results in different water masses that will sink to different depths within the ocean.
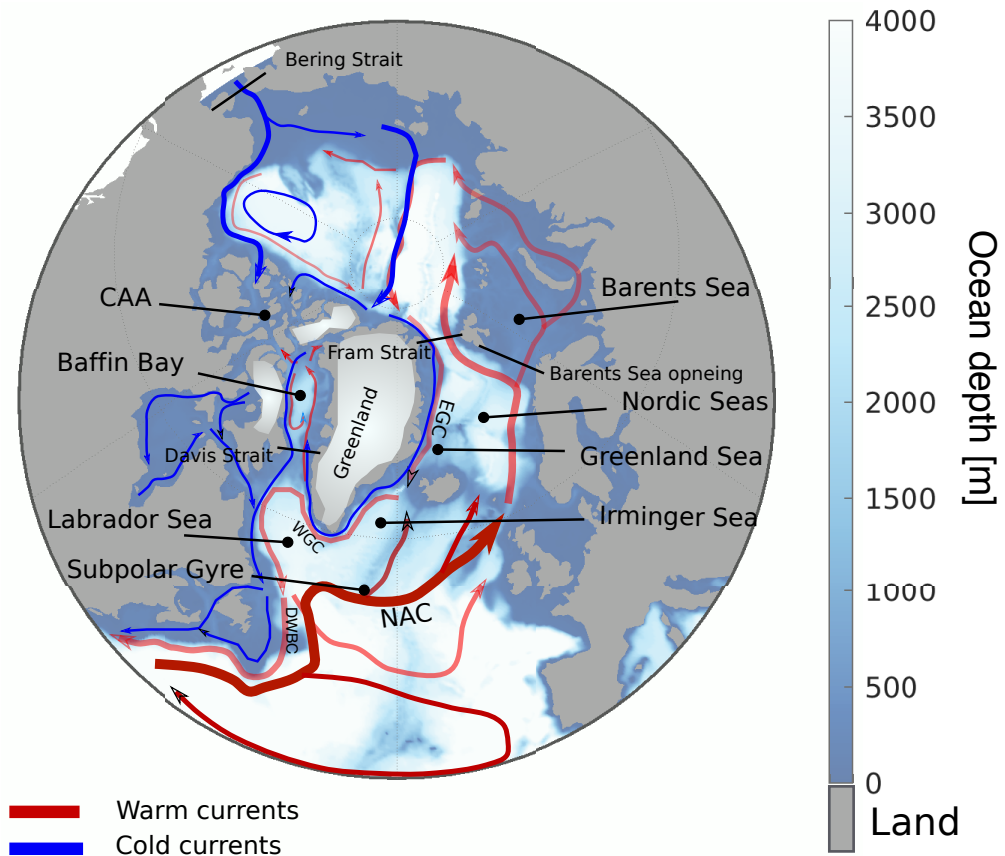


**Figure 1.1.** Schematic of circulation within the broad study region of the Northern Oceans (north of $40°N$). The warm North Atlantic Current flows into the Northern Oceans through two main pathways: the Nordic Seas branch and the Irminger Sea branch. Currents are represented by solid red and blue lines. The red or blue colours indicate waters within the current are warm and cold, respectively, while the transparency of the colour indicates the current travels below the surface. Abbreviations are: Canadian Arctic Archipelago (CAA), Deep Western Boundary Current (DWBC), East Greenland Curren (EGC), North Atlantic Current (NAC) and West Greenland Curren (WGC).

## 1.2   Ventilation of deep waters

These dense water formation regions are vital regulators of the world's climate and marine ecosystem, as they act as conduits facilitating the transport of oxygen ($O_2$) and $CO_2$ (along with other gases) from the surface to the deep ocean. Cool surface waters have higher affinity for gas uptake. Therefore, as the ocean surface waters are cooled they take in more gas and, as they sink, the dissolved gases are brought down to the deeper

ocean. At depth, the gases are effectively isolated from the atmosphere over times scales of 100 to 1000 years, equivalent to the idealized timescale of the MOC (Kuhlbrodt et al., 2007). From a climatic perspective, this water formation is a mechanism that pumps atmospheric $CO_2$ into the deep ocean, the solubility pump. From a biological perspective, the water formation acts to oxygenate (ventilate) the deep basins (e.g. process called ventilation). Higher $O_2$ concentration at depth contribute to maintaining a healthy ecosystem by sustaining the $O_2$-dependant life forms in the deep ocean and by promoting nitrification (e.g. production of nitrate) rather than denitrification (e.g. consumption of nitrate).

The newly ventilated waters are transported south in the density-driven Deep Western Boundary Current (DWBC), or are recirculated within the North Atlantic in the cyclonic circulation of the Subpolar Gyre (van Aken et al., 2011; Rhein et al., 2015, 2017). Therefore, benefits of ventilation are not limited to the ecosystem within the formation regions, but have a much larger impact area. Observed inter-annual changes in deep convection in the Labrador Sea suggest that this process is strongly regulated by the magnitude of winter heat fluxes (Dickson et al., 1996; Sathiyamoorthy and Moore, 2002; Yashayaev and Loder, 2017) and the salinity of surface waters (Dickson et al., 1988; Belkin et al., 1998). This suggests that under the warming predicted by the *business as usual* climate change scenario, transformation processes, and thus the ventilation of the deep ocean, may be threatened by changing atmospheric circulation patterns and increasing freshwater exports as a result of the decreasing sea ice cover (Saenko et al., 2015).

Indeed, the loss of Arctic sea ice is already causing a weakening in the Icelandic low in the Nordic Seas (Screen et al., 2018). This has consequences on atmospheric patterns such as the North Atlantic Oscillation (NAO) which is defined by the pressure difference between the Icelandic Low and the Azores High (Hurrell and Deser, 2009). The NAO index is an important determinant of the strength of the westerly winds and heat loss in the Northern Oceans. The link between the weakening of the Icelandic Low and the loss of sea ice suggest that in the future there will be more frequent years with a negative NAO, which is associated with weaker westerly winds. Screen et al. (2018) suggest that we are already experiencing a weakening in the strength of the westerly winds and a southward shift of the jet stream in winter, and Wang et al. (2017) suggest that as a result of the warming in the high Arctic the North Atlantic Storm Track is being displaced northward. In autumn - winter, the mean pathway of storms in the North Atlantic is from the Labrador Sea through the Nordic Seas and into the Arctic Ocean and the Barents Sea (Wang et al., 2017). The reduction of stormy weather conditions during the autumn-winter season would significantly reduce the regional ocean heat loss (Holdsworth and Myers, 2015), which in the North Atlantic, and particularly within the Labrador Sea, would result in shallow convection and a reduction in deep water formation (Dickson et al., 1996; Sathiyamoorthy and Moore, 2002; van Aken et al., 2011; Holdsworth and Myers, 2015; Yashayaev and Loder, 2017), thus resulting in a reduction in ventilation (Rhein et al., 2017).

4

Although there are still no direct links between the NAO index and ventilation, it is suggested that in the Labrador Sea, the higher $O_2$ content during NAO+ years are a result of higher air-sea $O_2$ fluxes caused by the characteristically stronger winds that accompany the NAO+ years (Koelling et al., 2017). This hypothesis, however, does not consider the lateral import of $O_2$ to the Labrador Sea from neighbouring regions, such as the Irminger Sea, where winter deep convection also occurs (Bacon et al., 2003; de Jong et al., 2012; Fröb et al., 2016; de Jong and de Steur, 2016). Ventilated waters in the Irminger Sea can be advected into the Labrador Sea in the East/West Greenland Current system (Bacon et al., 2003). Additionally, as the ice retreats from the Greenland Sea and the high Arctic, waters in these regions may become more important to the oxygenation of the deep ocean. For instance, climate warming-induced sea ice loss from the Greenland Sea increases the surface ocean area exposed to atmospheric cooling in winter which is expected to drive larger ocean heat losses and thus deeper convective mixing (Saenko et al., 2015). Therefore, the Greenland Sea has the potential to become a source of ventilated waters to the Labrador Sea via the East Greenland current. Similarly, the loss of sea ice in the Arctic Ocean may increase the $O_2$ content in Arctic waters because of their low salinity and cold temperature which gives them a characteristically high $O_2$ solubility. The Arctic Water can enter the Labrador Sea through Davis Strait, Hudson Strait and in the East/West Greenland Current system.

To date, however, estimates of the lateral $O_2$ fluxes into the Labrador Sea are limited and with low temporal representation (e.g. Howatt et al., 2018). Meanwhile lateral advection of $O_2$ is suggested to be a significant contributor of dissolved $O_2$ to the $O_2$ minimum zones within the Tropical Pacific Ocean (Stramma et al., 2010). These data gaps in the study of lateral $O_2$ fluxes are in part because only recently (at the end of the $20^{st}$ century), biogeochemical sensors have been incorporated into moorings to measure *in situ* dissolved $O_2$ concentration (Mowlem et al., 2008). Therefore, numerical simulations are still among the best available tools to learn about how lateral $O_2$ fluxes have influenced ventilation in the past. Numerical modelling also allows for the study of the impact of large atmospheric patterns (e.g. NAO) on the $O_2$ fluxes. These are particularly important questions to address given their sensitivity to sea ice loss and the current climate trends.

## 1.3   Phytoplankton productivity

At the same time, increasing open water regions throughout the Arctic also increases the amount of light reaching the ocean surface, which benefits the growth of photosynthetic organisms, such as phytoplankton (Perovich et al., 1997). These primary producers are ubiquitous in the Arctic with their growth being strongly limited by light (**?**). Phytoplankton are important in taking-in dissolved $CO_2$ and releasing $O_2$. Therefore, stimulating their growth increases the amount of $O_2$ in surface waters. In nearly all sectors of the Arctic and Subarctic, sea ice loss has resulted in a lengthening of the open water season (Markus et al., 2009; Stroeve et al., 2014), which has

5

been positively correlated to a larger magnitude and extent of phytoplankton blooms (Arrigo et al., 2008; Pabi et al., 2008).

A phytoplankton bloom refers to the explosive (rapid) growth behaviour exhibited by the phytoplankton community once or twice per year. The Arctic Ocean is characterized by one phytoplankton bloom per year, the spring bloom. In the Arctic, a combination of light limitation prior to spring and a small resupply of nutrients in the summer-autumn period, causes phytoplankton to be strongly limited by either light or nutrients (e.g. Harrison and Cota, 1991; Popova et al., 2010; Ardyna et al., 2014; Janout et al., 2016). A strong positive correlation between the break-up of sea ice in the springs of 2014 and 2015 and the timing of the spring phytoplankton blooms on the eastern Arctic shelf helped confirm that light is the limiting factor in spring (Janout et al., 2016). However, while losing the sea ice increases the extent and magnitude of the phytoplankton bloom (Arrigo et al., 2008; Pabi et al., 2008), the loss of sea ice alone is unlikely to lead to a longer lasting or a secondary bloom in autumn, because once phytoplankton blooms during spring it consumes all the available nutrients in surface waters, and its growth becomes progressively limited by nutrient. Therefore, for the phytoplankton bloom to last longer, the loss of sea ice should be accompanied by an increase in the generation of physical processes that resupply the surface waters with nutrients. Three of these physical processes are: surface turbulence created by winds, and the input of nutrients by the general ocean circulation and river discharge. In this thesis I focus on the impact of surface ocean turbulence.

### 1.3.1 Nutrient replenishment by wind turbulence

Wind driven turbulent mixing may be becoming an important source of nutrients. Ardyna et al. (2014) found a spatial correlation between areas where stormy winds (exceeding $10\,ms^{-1}$) blew over open water, and increasing chlorophyll-a concentrations over these areas in autumn. This is one of the first studies to identify a phytoplankton bloom in autumn, and they suggest that it is becoming a more common feature in time and space, due to late sea ice formation and increasingly windy conditions in the Arctic. Although Ardyna et al. (2014) do not elaborate on the physical mechanisms behind the correlation because of limitation to their data, studies in ice-free regions have shown that stormy conditions can generate vertical shears that result in a short pulse of nutrients to surface waters (Rumyantseva et al., 2015; Pan et al., 2017; Wu et al., 2007). In a similar study in the Arctic Ocean, but focusing on vertical heat fluxes, Ramudu et al. (2018) also demonstrated that the presence of a cyclone in winter can enhance the upward turbulent heat fluxes by 70%.

Collectively, these studies suggest that the energy input to the ocean by stormy winds enhance the upwelling flux of either nutrients and/or heat, to the surface. In correspondence with the northward shift of the North Atlantic Storm Track (Wang et al., 2017), stormy wind conditions are increasing in the Arctic (Ardyna

et al., 2014). This suggests that stormy weather systems may already be playing a significant role resupplying nutrients to surface waters throughout the Arctic and Subarctic, and thus, loss of sea ice alone may not be the only explanation for the observed trends in phytoplankton productivity. Estimating the relative role of wind-induced turbulence on phytoplankton growth over the entire Arctic could help predict the future response of phytoplankton. By using numerical experiments one could isolate the role of the stormy winds from that of the sea ice loss, and help to identify the dominant mechanisms taking place in recent years.

## 1.4 Freshwater inputs

The accelerated retreat of glaciers and rapid thawing of snow packs and permafrost as a result of Arctic warming have been steadily increasing river fluxes into the Arctic Ocean (Peterson et al., 2002); and as the Arctic continues to warm, so are the river fluxes predicted to continue increasing (Nummelin et al., 2015, 2016). An effect of increasing river and glacier discharge is the reduction of salinity in coastal regions and consequent increase in the sea surface height (SSH) (Brunnabend et al., 2012). Such changes can potentially modify the structure and/or the speed of the coastal currents.

The largest source of land ice in the Northern Hemisphere is the Greenland Ice Sheet, which is located east of Baffin Bay and the Labrador Sea. Melting of the Greenland Ice Sheet is a direct consequence of regional atmospheric warming but has also been linked to ocean warming (Holland et al., 2008b; Motyka et al., 2011; Straneo and Heimbach, 2013). Model estimates of Greenland Ice Sheet freshwater discharged into Baffin Bay (located to the west of Greenland) between 1958-2010, suggest that Baffin Bay received $250 \, km^3 \, yr^{-1}$ of freshwater between 1958-1990, and between 2005-2010 this freshwater input increased by 40% (Bamber et al., 2012). This acceleration is attributed to the increasing rate of melting of tide-water glaciers, which have their grounding base submerged in the ocean and are exposed to local ocean warming (Holland et al., 2008b; Motyka et al., 2011; Straneo and Heimbach, 2013). An explanation as to why the local ocean temperatures are higher is that transport of Atlantic Water into the Northern Oceans in the NAC is stronger and warmer (Holland et al., 2008b; Motyka et al., 2011; Walczowski et al., 2012; Straneo and Heimbach, 2013), but it has also been shown that larger freshwater discharge may change the local circulation which may lead to warming of the subsurface ocean layers (Brunnabend et al., 2012; Nummelin et al., 2016). Numerical models estimate that the Northern Hemisphere will warm an additional $2 - 2.5°C$ by 2050 (Kirtman et al., 2013). This will correspond with increasingly larger freshwater discharge into the ocean (Nummelin et al., 2015). Therefore, one could hypothesize that an increasing SSH on the western coast of Greenland could result in an acceleration of the coastal current which can result in increasing transport of the Atlantic Water within the West Greenland Current and thus may positively feedback to accelerate Greenland Ice Sheet melting.

## 1.5 Motivation and goals

The uncertainty surrounding the response of the Northern Hemisphere marine system to global climate change was the motivation for the research conducted during this thesis. The goal of the research is to increase the understanding of how the Northern Oceans respond to global change. The principal methodology consists of setting up, running, and analysing the output of a suite of experiments with a state of the art ocean sea ice and biogeochemical model. I answer three specific questions: (Q1) What is the significance of lateral $O_2$ transport into the Labrador Sea in the process of ventilation and how is this process influenced by the NAO? (Q2) What is the role of wind induced turbulence on the Arctic primary production? (Q3) Is there a feedback between glacier melt and regional ocean circulation? These questions are answered as independent contributions (i.e. stand alone chapters) containing introductory background, specific methodology, evaluation of the numerical simulation, and a discussion of the results pertaining to the particular question.

This thesis is divided into six chapters (considering the present chapter as Chapter 1). In Chapter 2, I describe the modelling framework of NEMO and BLING. This includes a description of the three models coupled to simulate the general ocean circulation, the sea ice dynamics and thermodynamics, and the marine biogeochemistry. In addition, Chapter 2 also lists the simulations and describe the model configurations used. The Chapters that follow, Chapter 3, Chapter 4 and Chapter 5, are written as independent papers that answer Q1, Q2 and Q3, respectively. Finally, in Chapter 6, I provide a concluding statement that summarizes the thesis main findings and their scientific contributions.

# Bibliography

Ardyna, M., Babin, M., Gosselin, M., Devred, E., Rainville, L., and Tremblay, J.-E. (2014). Recent Arctic Ocean sea ice loss triggers novel fall phytoplankton blooms. *Geophysical Research Letters*, 41(17):6207–6212.

Arrigo, K. R., van Dijken, G., and Pabi, S. (2008). Impact of a shrinking Arctic ice cover on marine primary production. *Geophysical Research Letters*, 35(19). L19603.

Bacon, S., Gould, W. J., and Jia, Y. (2003). Open-ocean convection in the Irminger Sea. *Geophysical Research Letters*, 30(5). 1246.

Bamber, J., den Broeke, M., Ettema, J., Lenaerts, J., and Rignot, E. (2012). Recent large increases in freshwater fluxes from Greenland into the North Atlantic. *Geophysical Research Letters*, 39(19).

Belkin, I. M., Levitus, S., Antonov, J., and Malmberg, S. (1998). "Great Salinity Anomalies" in the North Atlantic. *Progress in Oceanography*, 41(1):1–68.

Brunnabend, S.-E., Schröter, J., Timmermann, R., Rietbroek, R., and Kusche, J. (2012). Modeled steric and mass-driven sea level change caused by Greenland Ice Sheet melting. *Journal of Geodynamics*, 59-60:219 – 225.

Comiso, J. C. and Nishio, F. (2008). Trends in the sea ice cover using enhanced and compatible AMSR-E, SSM/I, and SMMR data. *Journal of Geophysical Research*, 113(C2):C02S07.

de Jong, M. F. and de Steur, L. (2016). Strong winter cooling over the Irminger Sea in winter 2014–2015, exceptional deep convection, and the emergence of anomalously low SST. *Geophysical Research Letters*, 43(13):7106–7113.

de Jong, M. F., van Aken, H. M., Våge, K., and Pickart, R. S. (2012). Convective mixing in the central Irminger Sea: 2002–2010. *Deep Sea Research Part I: Oceanographic Research Papers*, 63:36 – 51.

Dickson, R., Lazier, J., Meincke, J., Rhines, P., and Swift, J. (1996). Long-term coordinated changes in the convective activity of the North Atlantic. *Progress in Oceanography*, 38(3):241 – 295.

Dickson, R. R., Meincke, J., Malmberg, S., and Lee, A. J. (1988). The "great salinity anomaly" in the Northern North Atlantic 1968-1982. *Progress in Oceanography*, 20(2):103–151.

Eldevik, T., Nilsen, J. E. Ø., Iovino, D., Anders Olsson, K., Sandø, A. B., and Drange, H. (2009). Observed sources and variability of Nordic seas overflow. *Nature Geoscience*, 2:406.

Fröb, F., Olsen, A., Våge, K., Moore, G. W. K., Yashayaev, I., Jeansson, E., and Rajasakaren, B. (2016). Irminger Sea deep convection injects oxygen and anthropogenic carbon to the ocean interior. *Nature Communications*, 7:13244.

Harrison, W. G. and Cota, G. F. (1991). Primary production in polar waters: relation to nutrient availability. *Polar Research*, 10(1):87–104.

Hartmann, D., Klein Tank, A., Rusticucci, M., Alexander, L., Bronnimann, S., Charabi, Y., Dentener, F., Dlugokencky, E., Easterling, D., Kaplan, A., Soden, B., Thorne, P., Wild, M., and Zhai, P. (2013). Observations: Atmosphere and Surface. In Stocker, T., Qin, D., Plattner, G.-K., Tignor, M., Allen, S., Boschung, J., Nauels, A., Xia, Y., Bex, V., and Midgley, P., editors, *Climate Change 2013: The Physical Science Basis. Contribution of Working Group I to the Fifth Assessment Report of the Intergovernmental Panel on Climate Change*, book section 2, pages 159–254. Cambridge University Press, Cambridge, United Kingdom and New York, NY, USA.

Holdsworth, A. M. and Myers, P. G. (2015). The influence of high-frequency atmospheric forcing on the circulation and deep convection of the Labrador Sea. *Journal of Climate*, 28(12):4980–4996.

Holland, D. M., Thomas, R. H., de Young, B., Ribergaard, M. H., Lyberth, B., Holland, M. M., Finnis, J., Barrett, A. P., and Serreze, M. C. (2008). Acceleration of Jakobshavn Isbrae triggered by warm subsurface ocean waters. *Nature Geoscience*, 1:659–664.

Holmes, R. M., McClelland, J. W., Peterson, B. J., Tank, S. E., Bulygina, E., Eglinton, T. I., Gordeev, V. V., Gurtovaya, T. Y., Raymond, P. A., Repeta, D. J., Staples, R., Striegl, R. G., Zhulidov, A. V., and Zimov, S. A. (2012). Seasonal and annual fluxes of nutrients and organic matter from large rivers to the Arctic Ocean and surrounding seas. *Estuaries and Coasts*, 35(2):369–382.

Howatt, T., Palter, J., Matthews, J. B. R., deYoung, B., Bachmayer, R., and Claus, B. (2018). Ekman and eddy exchange of freshwater and oxygen across the labrador shelf-break. *Journal of Physical Oceanography*, 0(0):in press.

Hurrell, J. W. and Deser, C. (2009). North Atlantic climate variability: the role of the North Atlantic Oscillation. *Journal of Marine Systems*, 78(1):28–41.

Isachsen, P. E., Mauritzen, C., and Svendsen, H. (2007). Dense water formation in the nordic seas diagnosed from sea surface buoyancy fluxes. *Deep Sea Research Part I: Oceanographic Research Papers*, 54(1):22 – 41.

Izett, J. G. and Fennel, K. (2018). Estimating the cross-chelf export of riverine materials: Part 2. Estimates of global freshwater and nutrient export. *Global Biogeochemical Cycles*, 32(2):176–186. 2017GB005668.

Janout, M. A., Hlemann, J., Waite, A. M., Krumpen, T., Appen, W., and Martynov, F. (2016). Sea–ice retreat controls timing of summer plankton blooms in the Eastern Arctic Ocean. *Geophysical Research Letters*, 43(24):12,493–12,501.

Kirtman, B., Power, S., Adedoyin, J., Boer, G., Bojariu, R., Camilloni, I., Doblas-Reyes, F., Fiore, A., Kimoto, M., Meehl, G., Prather, M., Sarr, A., Schar, C., Sutton, R., van Oldenborgh, G., Vecchi, G., and Wang, H. (2013). Near-term Climate Change: Projections and Predictability. In Stocker, T., Qin, D., Plattner, G.-K., Tignor, M., Allen, S., Boschung, J., Nauels, A., Xia, Y., Bex, V., and Midgley, P., editors, *Climate Change 2013: The Physical Science Basis. Contribution of Working Group I to the Fifth Assessment Report of the Intergovernmental Panel on Climate Change*, book section 11, pages 953–1028. Cambridge University Press, Cambridge, United Kingdom and New York, NY, USA.

Koelling, J., Wallace, D. W. R., Send, U., and Karstensen, J. (2017). Intense oceanic uptake of oxygen during 2014–2015 winter convection in the Labrador Sea. *Geophysical Research Letters*, 44(15):7855–7864. 2017GL073933.

Kuhlbrodt, T., Griesel, A., Montoya, M., Levermann, A., Hofmann, M., and Rahmstorf, S. (2007). On the driving processes of the Atlantic meridional overturning circulation. *Reviews of Geophysics*, 45(2). RG2001.

Kunkel, K., Robinson, D., Champion, S. Yin, X., Estilow, T., and Frankson, R. M. (2016). Trends and extremes in Northern Hemisphere snow characteristics. *Current Climate Change Reports*, 2(65).

Le Fouest, V., Babin, M., and Tremblay, J.-É. (2013). The fate of riverine nutrients on Arctic shelves. *Biogeosciences Discussions*, 10(6):3661 – 3677.

Li, D., Zhang, R., and Knutson, T. R. (2017). On the discrepancy between observed and CMIP5 multi-model simulated Barents Sea winter sea ice decline. *Nature Communications*, 8:14991.

Markus, T., Stroeve, J. C., and Miller, J. (2009). Recent changes in Arctic sea ice melt onset, freezeup, and melt season length. *Journal of Geophysical Research*, 114(C12):C12024.

Marson, J. M., Myers, P. G., Hu, X., Petrie, B., Azetsu-Scott, K., and Lee, C. M. (2017). Cascading off the West Greenland Shelf: A numerical perspective. *Journal of Geophysical Research: Oceans*, 122(7):5316–5328.

Motyka, R. J., Truffer, M., Fahnestock, M., Mortensen, J., Rysgaard, S., and Howat, I. (2011). Submarine melting of the 1985 Jakobshavn Isbræfloating tongue and the triggering of the current retreat. *Journal of Geophysical Research: Earth Surface*, 116(F1).

Mowlem, M., Hartman, S., Harrison, S., and Larkin, K. (2008). Intercomparison of biogeochemical sensors at ocean observatories. EurOceans Research & Consultancy Report. 44. pp 45, http://www.whoi.edu/cms/files/EUR-OCEANS˙SensorIntercomparisonReport˙39645.pdf.

Nummelin, A., Ilicak, M., Li, C., and Smedsrud, L. H. (2016). Consequences of future increased Arctic runoff on Arctic Ocean stratification, circulation, and sea ice cover. *Journal of Geophysical Research: Oceans*, 121(1):617–637.

Nummelin, A., Li, C., and Smedsrud, L. H. (2015). Response of Arctic Ocean stratification to changing river runoff in a column model. *Journal of Geophysical Research: Oceans*, 120(4):2655–2675.

Onarheim, I. H. and Årthun, M. (2017). Toward an ice-free Barents Sea. *Geophysical Research Letters*, 44(16):8387–8395.

Pabi, S., van Dijken, G. L., and Arrigo, K. R. (2008). Primary production in the Arctic Ocean, 1998–2006. *Journal of Geophysical Research: Oceans*, 113(C8).

Pan, S., Shi, J., Gao, H., Guo, X., Yao, X., and Gong, X. (2017). Contributions of physical and biogeochemical processes to phytoplankton biomass enhancement in the surface and subsurface layers during the passage of Typhoon Damrey. *Journal of Geophysical Research: Biogeosciences*, 122(1):212–229.

Perovich, D. K., Elder, B. C., and Richter-Menge, J. A. (1997). Observations of the annual cycle of sea ice temperature and mass balance. *Geophysical Research Letters*, 24(5):555–558.

Peterson, B. J., Holmes, R. M., McClelland, J. W., Vorosmarty, C. J., Lammers, R. B., Shiklomanov, A. I., Shiklomanov, I. A., and Rahmstorf, S. (2002). Increasing river discharge to the Arctic Ocean. *Science*, 298(5601):2171–2173.

Polyakov, I. V., Pnyushkov, A. V., Alkire, M. B., Ashik, I. M., Baumann, T. M., Carmack, E. C., Goszczko, I., Guthrie, J., Ivanov, V. V., Kanzow, T., Krishfield, R., Kwok, R., Sundfjord, A., Morison, J., Rember, R., and

Yulin, A. (2017). Greater role for Atlantic inflows on sea–ice loss in the Eurasian Basin of the Arctic Ocean. *Science*, 356(6335):285–291.

Popova, E. E., Yool, A., Aksenov, Y., and Coward, A. C. (2013). Role of advection in arctic ocean lower trophic dynamics: A modeling perspective. *Journal of Geophysical Research: Oceans*, 118(3):1571–1586.

Popova, E. E., Yool, A., Coward, A. C., Aksenov, Y. K., Alderson, S. G., de Cuevas, B. A., and Anderson, T. R. (2010). Control of primary production in the arctic by nutrients and light: insights from a high resolution ocean general circulation model. *Biogeosciences*, 7(11):3569–3591.

Ramudu, E., Gelderloos, R., Yang, D., Meneveau, C., and Gnanadesikan, A. (2018). Large Eddy Simulation of Heat Entrainment Under Arctic Sea Ice. *Journal of Geophysical Research: Oceans*, 123(1):287–304.

Årthun, M., Eldevik, T., Smedsrud, L. H., Skagseth, O., and Ingvaldsen, R. B. (2012). Quantifying the influence of Atlantic heat on Barents Sea ice variability and retreat. *Journal of Climate*, 25(13):4736–4743.

Rhein, M., Kieke, D., and Steinfeldt, R. (2015). Advection of North Atlantic Deep Water from the Labrador Sea to the southern hemisphere. *Journal of Geophysical Research: Oceans*, 120(4):2471–2487.

Rhein, M., Steinfeldt, R., Kieke, D., Stendardo, I., and Yashayaev, I. (2017). Ventilation variability of Labrador Sea Water and its impact on oxygen and anthropogenic carbon: a review. *Philosophical Transactions of the Royal Society of London A: Mathematical, Physical and Engineering Sciences*, 375(2102).

Rudels, B., Larsson, a.-M., and Sehlstedt, P.-I. (1991). Stratification and water mass formation in the Arctic Ocean: some implications for the nutrient distribution. *Polar Research*, 10(1):19–32.

Rumyantseva, A., Lucas, N., Rippeth, T., Martin, A., Painter, S. C., Boyd, T. J., and Henson, S. (2015). Ocean nutrient pathways associated with the passage of a storm. *Global Biogeochemical Cycles*, 29(8):1179–1189.

Saenko, O. A., Yang, D., Gregory, J. M., Spence, P., and Myers, P. G. (2015). Separating the influence of projected changes in air temperature and wind on patterns of sea level change and ocean heat content. *Journal of Geophysical Research: Oceans*, 120(8):5749–5765.

Sathiyamoorthy, S. and Moore, G. W. K. (2002). Buoyancy flux at ocean weather station Bravo. *Journal of Physical Oceanography*, 32(2):458–474.

Screen, J. A., Deser, C., and Simmonds, I. (2012). Local and remote controls on observed Arctic warming. *Geophysical Research Letters*, 39(10):L10709.

Screen, J. A., Deser, C., Smith, D. M., Zhang, X., Blackport, R., Kushner, P. J., Oudar, T., McCusker, K. E., and Sun, L. (2018). Consistency and discrepancy in the atmospheric response to Arctic sea-ice loss across climate models. *Nature Geoscience*, 11(3):155–163.

Screen, J. A. and Simmonds, I. (2010). The central role of diminishing sea ice in recent arctic temperature amplification. *Nature*, 464(1334).

Serreze, M. C. and Francis, J. A. (2006). The Arctic amplification debate. *Climatic Change*, 76(3-4):241–264.

Smedsrud, L. H., Esau, I., Ingvaldsen, R. B., Eldevik, T., Haugan, P. M., Li, C., Lien, V. S., Olsen, A., Omar, A. M., Otterå, O. H., Risebrobakken, B., Sandø, A. B., Semenov, V. A., and Sorokina, S. A. (2013). The role of Barents Sea in the Arctic climate system. *Reviews of Geophysics*, 51(3):415–449.

Steffen, K. (1985). Warm water cells in the North Water, Northern Baffin Bay during winter. *Journal of Geophysical Research: Oceans*, 90(C5):9129–9136.

Stramma, L., Johnson, G. C., Firing, E., and Schmidtko, S. (2010). Eastern pacific oxygen minimum zones: Supply paths and multidecadal changes. *Journal of Geophysical Research: Oceans*, 115(C9).

Straneo, F. and Heimbach, P. (2013). North Atlantic warming and the retreat of Greenland's outlet glaciers. *Nature*, 504(7478):36–43.

Stroeve, J. C., Markus, T., Boisvert, L., Miller, J., and Barrett, A. (2014). Changes in arctic melt season and implications for sea ice loss. *Geophysical Research Letters*, 41(4):1216–1225.

Stroeve, J. C., Maslanik, J., Serreze, M. C., Rigor, I., Meier, W., and Fowler, C. (2011). Sea ice response to an extreme negative phase of the Arctic Oscillation during winter 2009/2010. *Geophysical Research Letters*, 38(2):L02502.

Tivy, A., Howell, S. E. L., Alt, B., McCourt, S., Chagnon, R., Crocker, G., Carrieres, T., and Yackel, J. J. (2011). Trends and variability in summer sea ice cover in the Canadian Arctic based on the Canadian Ice Service Digital Archive, 19602008 and 19682008. *Journal of Geophysical Research: Oceans*, 116(C3). C03007.

van Aken, H. M., de Jong, M. F., and Yashayaev, I. (2011). Decadal and multi-decadal variability of Labrador Sea Water in the north-western North Atlantic Ocean derived from tracer distributions: Heat budget, ventilation, and advection. *Deep Sea Research Part I: Oceanographic Research Papers*, 58(5):505 – 523.

Våge, K., Pickart, R. S., Sarafanov, A., Knutsen, Ø., Mercier, H., Lherminier, P., van Aken, H. M., Meincke, J., Quadfasel, D., and Bacon, S. (2011). The Irminger Gyre: Circulation, convection, and interannual variability. *Deep Sea Research Part I: Oceanographic Research Papers*, 58(5):590 – 614.

Walczowski, W., Piechura, J., Goszczko, I., and Wieczorek, P. (2012). Changes in atlantic water properties: an important factor in the european arctic marine climate. *ICES Journal of Marine Science*, 69(5):864–869.

Wang, J., Kim, H.-M., and E.K.M., C. (2017). Changes in Northern Hemisphere winter storm tracks under the background of Arctic amplification. *Journal of Climate*, 30:3705–3724.

Wu, Y., Platt, T., Tang, C. C. L., and Sathyendranath, S. (2007). Short-term changes in chlorophyll distribution in response to a moving storm: a modelling study. *Marine Ecology Progress Series*, 335:57–68.

Yashayaev, I. and Loder, J. W. (2017). Further intensification of deep convection in the Labrador Sea in 2016. *Geophysical Research Letters*, 44(3):1429–1438. 2016GL071668.

# Chapter 2

# Modelling framework NEMO3.4 (OPA-LIM2-BLINGv0) to simulate Arctic Ocean biogeochemistry

## 2.1 Introduction

Models are an important tool for exploring how the marine ecosystem responds to climate-change related stresses, such as warming and increasing freshwater fluxes to the ocean. Although observational ocean studies using satellites and moorings offer the advantage of monitoring the response of the marine system to climate stresses, isolating cause-effect is particularly difficult because multiple stresses are often acting all at once (e.g. changing atmospheric circulation, warming, sea ice melting, larger river runoff). In these cases, a regional modelling experiment at high resolution (as performed in this thesis) can offer insight and can serve to bridge the understanding between the observed ocean response and the leading forcing causing the observed response. Modelling experiments are not a perfect substitute of reality, but they are useful tools that help researchers learn more about the processes that control the marine system

In this thesis I use the ocean engine NEMO 3.4 (**N**ucleus for **E**uropean **M**odelling of the **O**cean version 3.4), which is a primitive equation model that can be used at regional or global scale (Madec and the NEMO team, 2008). The physical ocean component of NEMO is derived from ocean model OPA v8.2 (**O**céan **PA**rallélisé version 8.2). After its incorporation within NEMO in the 1990s (Madec et al., 1998), the ocean module OPA was improved within NEMO under the leadership of the NEMO consortium.

NEMO offers its users the flexibility to include a sea ice module and/or a biogeochemical module (Figure

2.1). In this thesis OPA has been coupled with sea ice model LIM2 (**L**ouvian-la-neuve **I**ce **M**odel version 2) and biogeochemical model BLINGv0 (**B**iogeochemistry with **L**ight **I**ron **N**utrient and **G**asses version 0). The latter was embedded in the NEMO framework using TOP (Tracer in the Ocean Paradigm) during the course of this Ph.D. Embedding BLING in NEMO is an important step especially when considering that the ocean's response to climate is known to be tightly controlled not only by the physical, but also by the biogeochemical state of the marine system.
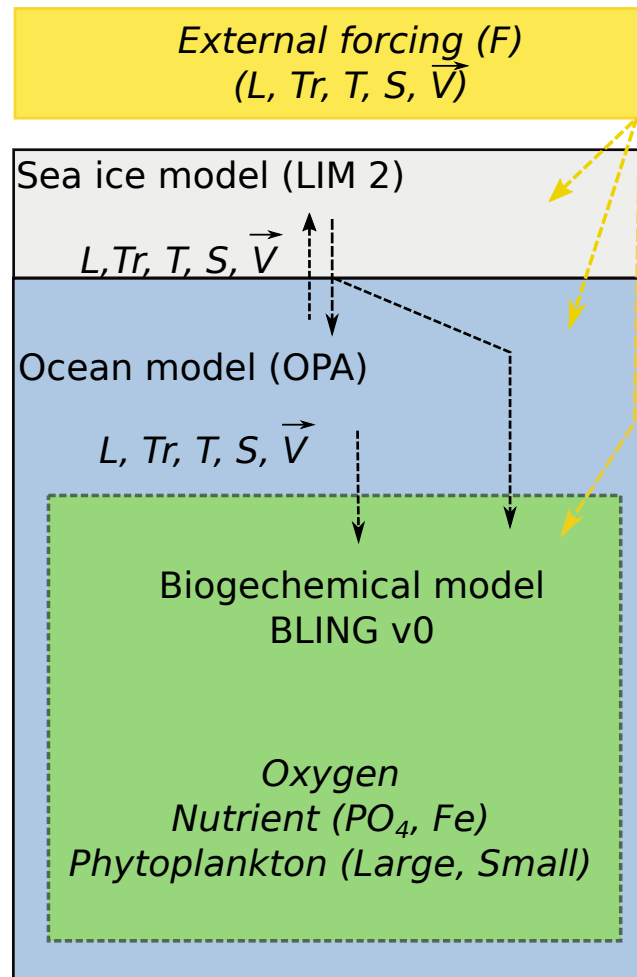


**Figure 2.1.** Schematic of the NEMO framework using OPA-LIM-BLING coupling. External forcing (yellow) inputs the field of light, (L), biological tracers (Tr) (e.g. iron (Fe) in dust particles), heat (T), salinity (S) and momentum (V) to all three components. The same fields are modified and exchanged between model compartments. For example in ice covered waters the amount of light that reaches the ocean surface is modulated by the presence of sea ice, meanwhile the intensity of mixing modulates the light available reaching the biogeochemical module. LIM and OPA communicate with each-other back and forth whereas BLING only receives information from OPA and LIM and does not communicate back. The arrows point at the direction of the communication between modules and forcing fields.

## 2.2 Ocean Model: OPA

The ocean module represents the dynamics and thermodynamics of the ocean. OPA has 6 core assumptions: spherical earth approximations, thin-shell approximation, incompressibility approximation, hydrostatic approximation and turbulent closure scheme. The core assumptions are key to solving the primitive equations (see next section). In addition to the core assumptions, 3 optional approximations are used to run the simulations in this thesis. These optional assumptions define the user's choice of some physical processes. The list of the assumptions is found below starting with the 6 core assumptions.

### 2.2.1 Assumptions

- **Spherical Earth approximation**: the Earth is best described as an ellipsoid with a surface defined by the geoid. The geoid is the height of an equipotential surface of the Earth's gravity field. The geoid is not smooth, rather, it has lumps due to the differences in density of the Earth interior that causes differences in the strength of the gravity fields at different locations. This approximation maps the ellipsoidal geoid Earth on to a spherical equipotential surface and gravity is assumed constant ($g$; Table 2.1). The assumption also states that the vertical gravity vector is always directed towards the centre of the solid Earth.

- **Thin-shell approximation**: this approximation is based on the much larger radius of the solid Earth ($\approx 6400\,km$) relative to the depth of the ocean (mean: $\approx 4\,km$, range: 0 - $10\,km$). Thus, OPA assumes that the distance from the center of the Earth to any given location within the ocean is equal to the Earth's radius.

- **Boussinesq approximation**: states that the ocean density varies very little from a reference density ($\rho_w$, $= 1035\,kg\,m^{-3}$), and thus this reference density can be assumed constant throughout the water column. Therefore the density in the momentum equation is replaced by a constant value $\rho_0 = \rho_w$, except where the density is multiplying the buoyancy forces (e.g. gravity $g$), in which cases the buoyancy term (e.g. $\frac{gH}{\mathbf{U}^2}$) is assumed to be close to unity (e.g. $\mathbf{U} \approx \sqrt{gH}$). With this exception, the approximation preserves convection and internal wave processes in the ocean. This simplifies the momentum equation by eliminating density-induced non-linearities from the inertial terms.

- **Hydrostatic approximation**: states that the pressure at any point in a fluid at rest (e.g. hydrostatic) is only due to the weight (e.g. the buoyancy) of the overlying fluid. The hydrostatic approximation assumes that the vertical acceleration of the velocity is much smaller than the vertical pressure gradient, therefore it can be ignored and the vertical momentum equation is in hydrostatic balance (Eq. 2.2). This adds a

simplification to the equation of motion governing the vertical component of the velocity, but means that convective processes must now be parameterized.

- **Incompressibility approximation**: incompressibility assumes that densities will remain constant and that the volume of the fluid will not change if a compressive stress is applied. The incompressibility assumption simplifies the mass continuity equation into the volume continuity equation which leads to the divergence of the velocity equalling zero everywhere in the model domain (Eq. 2.3).

- **Turbulent closure scheme**: this scheme is used to parameterize the small-scale processes (e.g. sub-gridscale processes) and their effect on the mean flow. The need for a closure scheme derives from the decomposition of the flow field into a mean and a fluctuating component (e.g. the Reynolds decomposition). This decomposition results in infinite non-linear terms, thus OPA decouples the mean flow and the fluctuating component (e.g. small-scale processes), to avoid solving an infinite number of equations.

- **Closure assumption for the turbulent length scale (optional):** this assumption is used to ensure the magnitude of the length scales are bounded to the strongly stratified portion of the water column. The magnitude's range is limited by the distance to the surface or to the bottom (which ever is shortest). Additionally, the range is constrained to be equal to or smaller than the variations of model vertical grid thickness, $e3$.

- **Linear free surface approximation (optional):** a free surface means the surface of the ocean is allowed to change with time. The variable for the free-surface is the sea surface height, $\eta$. The linear approximation means that despite the changes in sea surface height, the thickness of the first vertical level is kept constant through time, such that the volume of the first grid cell does not change in time. As a result changes in sea surface height will modify the salinity of the surface water, resulting in a salinity content that is not exactly conserved. However, these sea surface height-induced salinity changes are considered negligible relative to other processes, like precipitation and evaporation, which have a much stronger control on surface salinity.

- **Clear sky assumption for solar radiation (optional):** my simulations does not consider cloud-cover in the calculations of light at the surface of the ocean. Reason why forcing field that accounts for cloud cover must be used to properly estimate the solar radiation reaching the surface of the sea ice and ocean.

### 2.2.2 Primitive equations

OPA has six basic equations, each representing a physical principle. The equations describe the changes in the amount of salt, temperature, momentum and internal energy within a volume of ocean. However, because the
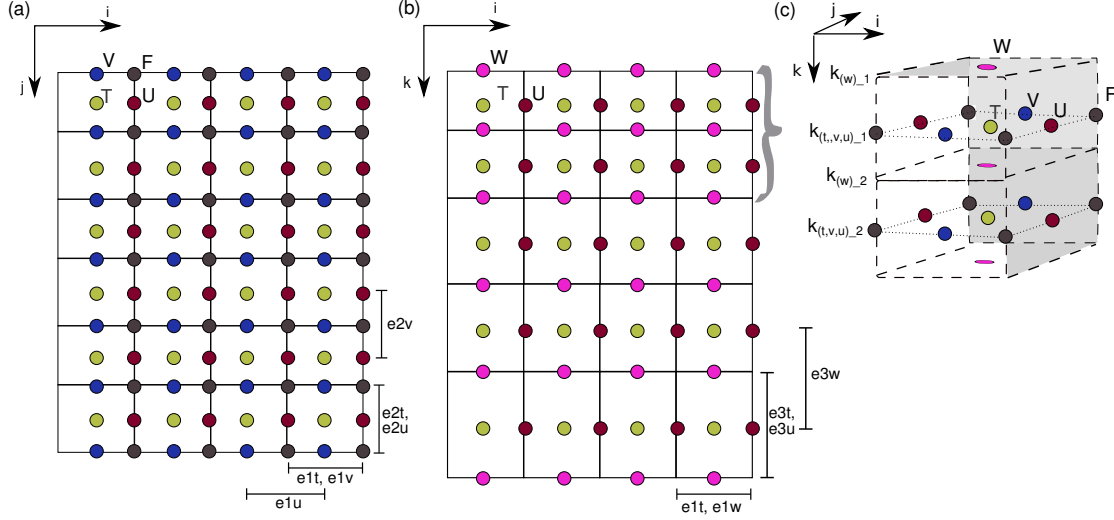
**Figure 2.2.** Schematic of the Arakawa C-grid used in OPA. Showing the locations of tracers (T), zonal velocity (U), meridional velocity (V), vertical velocity (W), and vorticity/Coriolis (F) within (a) the 2D ij plane, (b) ik plane and (c) the 3D cubic volume. The thickness of cube in the i (or x) direction is *e1*, in the j (or y) direction is *e2* and in the k (or z) direction is *e3*. The thickness is relative to where the variable is located within the grid, always with the midpoint of the thickness indicating the location of the variable. In each panel the labelled grid points are at location $i = 1$; $j = 1$; $k = 1$.

internal energy cannot be directly measured, OPA uses the changes in heat and pressure to derive the changes in the internal energy.

OPA solves the three dimensional primitive equations in spherical coordinates with the equations discretized on a staggered Arakawa C-grid with orthogonal set of unit vectors: **i**, **j** and **k** (Figure 2.2). The vertical discretization uses a linear free surface approximation with partial step z-coordinate at the bottom. Advective terms are solved using the leap-frog scheme while diffusive terms use a forward scheme for time-stepping.

The six equations represent the horizontal momentum balance, the vertical momentum equation assuming hydrostatic equilibrium, the continuity equation using the incompressibility assumption, the heat conservation equation, the salt conservation equations and an equations of state to solve for density. The equations are bounded by the assumptions listed in the previous section.

- Horizontal momentum: Navier-Stokes equation

$$\frac{\partial \mathbf{U}_h}{\partial t} = -(U_h \cdot \nabla)U_h - fk \times \mathbf{U}_h - \frac{1}{\rho_0}\nabla_h P + D^u + F^u \tag{2.1}$$

where the first term on the RHS is the inertial term calculated using the **U** as the 3D velocity field ($\mathbf{U} = \mathbf{U}_h + w\mathbf{k}$) defined as the sum of the horizontal velocity ($\mathbf{U}_h$) along the horizontal planes **i** and **j** (subscript *h*) and the vertical velocity ($w$) along the **k** plane. The second term on the RHS is the role of the Coriolis force $f = 2\omega \sin\delta$ (where $\omega$ is the angular velocity of the rotating planet Earth and $\delta$ is the latitude). The

20

third term on the RHS is the horizontal pressure gradient $\nabla_h P$ using the reference density $\rho_0$ (Table 2.1). The fourth and fifth terms on the RHS are the small-scale momentum processes parametrization, $D^u$, and surface forcing, $F^u$, respectively.

- Vertical momentum equation in hydrostatic equilibrium

$$\frac{\partial P}{\partial z} = -\rho g \eta \tag{2.2}$$

This formulation accounts for a linear free surface boundary conditions which is represented by including the dependence of the pressure ($P$) at a given z-level on the sea surface height ($\eta$), in addition to the density ($\rho$) and gravity ($g$).

- Continuity equation assuming incompressibility

$$\nabla \cdot \mathbf{U} = 0 \tag{2.3}$$

the divergence of the velocity field ($\nabla \cdot \mathbf{U}$) is zero everywhere. The equation describes the conservation of linear momentum over the model domain whereby the flux coming into the domain must equal the flux going out (e.g. $A_{in}V_{in} = A_{out}V_{out}$). It is used to solve for vertical velocity ($w$) using a diagnostic relation with $\mathbf{U}_h$: $\frac{\partial u}{\partial i} + \frac{\partial v}{\partial j} + \frac{\partial w}{\partial k} = 0$.

- Heat conservation equation: to solve for potential temperature, T

$$\frac{\partial T}{\partial t} = -\nabla \cdot (T\mathbf{U}) + D^T + F^T \tag{2.4}$$

where $t$ is time, $D^T$ parametrizes the temperature changes due to small-scale physics, and $F^T$ due to surface forcing.

- Salt conservation equation: to solve for salinity, S

$$\frac{\partial S}{\partial t} = -\nabla \cdot (S\mathbf{U}) + D^S + F^S \tag{2.5}$$

where $D^S$ represent the parametrization of salinity changes due to small-scale physics, and $F^S$ is the surface forcing.

- Density equation of state: to solve for *in situ* density, $\rho$, as a function of temperature ($T$), salinity ($S$), and

pressure ($P$)

$$\rho = \rho(T, S, P) \tag{2.6}$$

OPA's prognostic variables are a 2D linear sea surface height ($\eta$) and the 3D velocity ($U$), potential temperature ($T$), salinity ($S$) and density fields ($\rho$). Potential temperature and salinity are the only two active tracers. The time evolution of the active tracers depends on the interaction of processes. For example, the value on the next step (NXT) depends on the value of the current state (NOW) and the change caused by advection (ADV), lateral diffusion (LDF), vertical diffusion (ZDF), the bottom boundary layer parametrizations (BBL), and the contribution from external forcing: surface boundary conditions (SBC), penetrative solar radiation (QSR), and bottom boundary conditions (BBC). In Eq. 2.7 these processes are summarized using $NXT$ on the LHS of the equation to represent the next time step.

$$NXT = NOW + ADV + LDF + ZDF + BBL + SBC + QSR + BBC \tag{2.7}$$

### 2.2.3 Boundary conditions

The boundary conditions describe the interaction of the ocean with coastlines, bottom topography, and air-sea or ice-sea interfaces (arrows in Figure 2.3). OPA prescribes boundary conditions to the primitive equations at each of these boundaries, whereby the ocean may exchange heat, salt and/or momentum fluxes. The boundaries are described using the depth of the ocean ($H$), $z = -H(\mathbf{i}, \mathbf{j})$, and the sea surface height, $\eta$, $z = \eta(\mathbf{i}, \mathbf{j}, \mathbf{k}, \mathbf{t})$ .
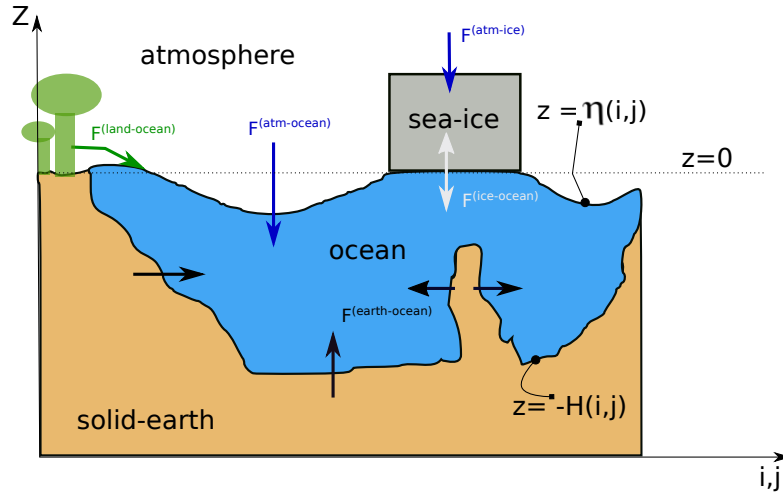


**Figure 2.3.** Schematic of model boundaries and fluxes (arrows) associated with each boundary. The arrow head points in the direction of the flux, with double headed arrows (e.g. sea ice- ocean flux) indicating a feedback between boundaries. Hypothetical ocean section depicting the and ocean bottom, $H$, with a sea floor mount, and a free surface represented by $\eta$ (which is estimated relative to the reference surface $z = 0$). $\eta$ describes the shape of the air-sea interface, but fluxes at this interface exchange across the $z = 0$.

- **Land-ocean interface**: the simulations are set-up to have an input flux of freshwater from the continental margin to the ocean (green arrow in Figure 2.3). The user chooses the dataset of freshwater input. In this thesis I used river runoff from (Dai et al., 2009) updated to include modelled Greenland runoff and ice-sheet melt fluxes (Bamber et al., 2012). The flux is prescribed as an idealized salt flux at the air-sea interface in the vicinity of the river mouths with an enhanced mixing parametrization to represent the turbulence created by the flowing stream. This allows a re-distribution of the freshwater flux over a certain depth. In this thesis mixing is enhanced over the top $10m$.

- **Solid earth-ocean interface**: the simulations are set-up assuming heat and salt fluxes from the solid Earth to the ocean were negligible. This is generally true except at very specific regions in the world oceans (e.g. hydrovents in the Arctic). In the simulations used in this thesis, only momentum is exchanged at the solid earth-ocean boundary (black arrows in Figure 2.3). For the momentum exchanges a kinematic boundary condition is used (Eq. 2.8). This is calculated as the divergence of the horizontal velocity, $\mathbf{U}_h$, due to the ocean-floor gradient,$\nabla_h(H)$.

$$w = -\mathbf{U}_h \cdot \nabla_h(H) \tag{2.8}$$

This condition also specified zero ocean velocity perpendicular to any solid boundaries (e.g. coastlines are streamlines), such that, only velocities parallel to the boundary are allowed to exist. Therefore the ocean momentum exchange is limited to frictional processes. Frictional processes are solved using a non-linear bottom friction scheme (Eq. 2.9). This assumes that bottom friction is a quadratic function of the vertical eddy coefficient. The vertical eddy coefficient at the bottom is computed at every time-step considering the square of the meridional ($v$) and zonal ($u$) components of the velocity in the bottom level (e.g. $\sqrt{u_b^2 + v_b^2 + e_b}$) and using a constant turbulent kinetic background, $e_b$ (Table 2.1). In equation Eq.2.9, $C_D$ is the default bottom drag coefficient (Table 2.1) and $\mathbf{U}_h^b$ is the horizontal velocity field at the bottom.

$$F_h = C_D \mathbf{U}_h^b \sqrt{u_b^2 + v_b^2 + e_b} \tag{2.9}$$

- **Atmosphere-ocean and atmosphere-ice interface**: heat, salt and horizontal momentum are exchanged at this interface (blue arrows in Figure 2.3). This boundary is assumed to be a linear free-surface, meaning that although the sea surface height ($\eta$) changes with time, the thickness of the first vertical level ($\mathbf{k} = 1$) is fixed in time. Note in Figure 2.3 that the vertical boundary conditions are applied at $z = 0$, rather than at the moving surface $z = \eta$.

Heat, salt and horizontal momentum exchanges are solved using the kinematic surface conditions represented by the time varying sea surface height, $\eta$, and the divergence of the horizontal velocity, $\mathbf{U}_h$, due to the $\eta$ gradient (Eq.2.10). With the additional consideration of atmospheric fluxes of freshwater at the surface including the runoff plus precipitation minus evaporation term $PME$.

$$w = \frac{\partial \eta}{\partial t} + \mathbf{U}_h|_{z=0} \cdot \nabla_h(\eta) + PME \tag{2.10}$$

The evolution of $\eta$ is a function of atmospheric and land freshwater fluxes ($PME$) and the divergence of the velocity due to the net height of the water column ($\eta + H$) (Eq.2.11).

$$\frac{\partial \eta}{\partial t} = -\nabla \cdot [(H + \eta)\mathbf{U}_h] + PME \tag{2.11}$$

The linear free-surface approximation states that as the sea surface height changes, the volume of the surface cell stays fixed. This causes salinity to change as the sea surface height evolves. For example, when the sea surface height increases the salinity of the first grid cell decreases. Therefore the total salt content in the simulations using a linear free-surface is not exactly conserved, however changes in salinity due to the changes in the sea surface height are negligible compared to variations due to PME.

The CORE bulk formulation (Large and Yeager, 2004) is used to compute the turbulent transfer of momentum, heat and salt fluxes over sea ice and open ocean using an inertial dissipative method. This formulation estimates the turbulent fluxes using the atmospheric data input: wind speed, air temperature and specific humidity (at 10 or $2\,m$ height). In particular, the horizontal momentum input includes the wind stress formulation (Eq. 2.12) as a linear function of the air density, $\rho_a$, the air drag coefficient, $C_A$ (Table 2.1), and the square of the wind velocity, $u_a$.

$$\tau_a = \rho_a C_A |u_a| u_a \tag{2.12}$$

The $C_A$ and $\rho_a$ are calculated using the CORE formulation (Large and Yeager, 2004). The air-drag coefficient is a function of height, atmospheric stability and wind speed, and the air density is a function of height, humidity and temperature.

- **Sea ice-ocean interface**: there is an exchange of momentum, heat and salt (white arrow in Figure 2.3). The sea surface temperature is constrained to the freezing point of the sea surface water. The sea ice salinity is assumed constant at 4 *psu*. The fluxes at this interface vary with season, during freezing there is positive salt flux (salinity at the sea surface increases) while during melting season there is a negative

salt flux (salinity at the sea surface decreases). More detail about the tracer exchanges at this interface will be discussed within the sea ice model section. Momentum fluxes are dominated by friction (e.g the drag coefficient) when sea ice is *land-locked*, and by stress when sea ice is mobile.

**Table 2.1.** Ocean model parameters

| Parameter | Value | Units | Description |
|---|---|---|---|
| $g$ | 9.8 | $m\,s^{-2}$ | Constant gravitational acceleration |
| $e_b$ | $2.5*10^{-3}$ | $m^2\,s^{-2}$ | Turbulent kinetic energy background |
| $\rho_0$ | 1020 | $kg\,m^3$ | Reference ocean density |
| $\rho_a$ | CORE formulation | $kg\,m^{-3}$ | Air density |
| $C_A$ | CORE formulation | [no unit] | Air drag coefficient |
| $C_D$ | $10^{-3}$ | [no unit] | Default ocean-bottom drag coefficient |
| $C_p$ | $4*10^3$ | $J\,Kg^{-1}\,{}^\circ K$ | Specific heat capacity (when constant) |

### 2.2.4 Tracer fluxes at air-sea and solid Earth boundaries

At the ocean floor the vertical diffusion of heat and salinity are set to zero, implying that these experiments do not consider geothermal energy. The bottom fluxes for biochemical tracers are described in the biogeochemical model section.

At the surface, the forcing on any ocean tracer, $F^C$, is composed of an external flux, $F_{ext}$, which is independent of water exchanges (e.g. iron flux through dust deposition), and two additional fluxes ($F_{wf}^i$ and $F_{wf}^d$) which are linked to the water exchange with the atmosphere (e.g evaporation, precipitation) or land run-off (Eq. 2.13). These last two fluxes represent a direct ($F_{wf}^d$) and an indirect ($F_{wf}^i$) effect of the surface flux on the tracer concentration at the sea surface. A direct effect is when the water exchanged carries a concentration of the tracer (e.g. precipitation carrying salinity of zero). An indirect effect occurs when the flux tends to dilute or concentrate the tracer at the ocean surface (e.g. ice melting flux).

$$F^C = F_{ext} + F_{wf}^d + F_{wf}^i \tag{2.13}$$

The salinity flux, $F^S$, at the sea surface is a function of the direct and indirect additional fluxes on the surface salinity, $S|_{k=1}$ (Eq. 2.14). The direct fluxes are precipitation and river runoff which carry a salinity ($S = 0$) and the indirect fluxes depend on the sea ice melting or freezing. The two fluxes are combined in the freshwater budget, $EMP_S$. Assuming a linear free surface, $EMP_S$ is defined as the total surface freshwater budget: evaporation minus precipitation minus river run-off plus the rate of change of sea ice thickness. This causes the salt content to be not exactly conserved.

$$F^S = EMP_S\,S|_{k=1} \tag{2.14}$$

Precipitation and run-off are assumed to have no effect on the temperature of the surface water such that $F_{wf}^i = F_{wf}^d = 0$. Therefore, the temperature flux at the surface, $F^T$, is only a function of the external flux, $F_{ext}$, which is the non-penetrative part of the net surface heat flux, $Q_n s$ (Eq. 2.15).

$$F^T = \frac{Q_n s}{\rho_0 C_p} \tag{2.15}$$

where $\rho_0$ is the reference density and $C_p$ is the specific heat capacity(Table 2.1).

$C_p$ is actually a function of ocean temperature, salinity, and pressure and in OPA it follows the formulation in Fofonoff (1983). However because $C_p$ is only used to convert surface heat flux into temperature, the dependence on pressure is neglected, which together with the weak relationship between $C_p$ and temperature and salinity, leads to OPA using $C_p$ as a constant (Table 2.1).

## 2.2.5 Tracer advection

Tracer advection uses the Total Variance Dissipation (TVD) scheme. The TVD scheme derives the equations in space using a mix of upstream and centered derivatives and in time using a leap-frog scheme. TVD scheme is used in both the horizontal and vertical tracer advection. Through using this scheme OPA guarantees the absence of spurious oscillations (eg.g. dispersive overshoots) in regions of strong curvature in the advected quantity by locally lowering the order of accuracy to the level of first-order upstream advection (Shchepetkin and McWilliams, 1998).

This advection scheme uses the principle of monotonicity in which the concentration of a scalar being advected must either be conserved or diffused (Shchepetkin and McWilliams, 1998). Therefore the method prevents negative values, but also prevents advection from amplifying existing extrema or steep gradients (e.g. sharp fronts, thermoclines or strong advective currents). In order to insure monotonicity (positive values) the TVD method has a flux limiter to limit the antidiffussion flux. On the other hand, the TVD method may cause an excess of vertical diffusion of the thermocline. James (1996) described how the excess vertical diffusion caused a development of a vertical flow on z-coordinate model. Nonetheless, an early sensitivity study of the OPA tracer advective scheme concluded that TVD scheme was one of the best choices for studying biogeochemical tracer advection on a z-coordinate configuration (Lévy et al., 2001).

## 2.2.6 Subgrid-scale physics

The role of subgrid-scale physics is to dissipate the energy and maintain the stability of the model with minimal interference within the resolved portion of the flow. They represent the effect of small scale motions that result from the expansion of the advective terms (e.g. the Reynold's averaging). My simulations use the Turbulent

Kinetic Energy (TKE) closure scheme to calculate an approximate magnitude for the small-scale fluxes and parameterizes them back into the momentum equation. This formulation is, perhaps, the weakest part of the model, while at the same time it is also one of the most essential components in long-term simulations. These small scale process are a delicate balance between the surface input of kinetic energy and heat and the ocean motion.

In the primitive equations listed in Eq. 2.1 to 2.6, the subgrid-scale physics was represented by $\mathbf{D}^u$, $\mathbf{D}^S$, $\mathbf{D}^T$. These have a vertical ($\mathbf{D}^{vu}$, $\mathbf{D}^{vS}$, $\mathbf{D}^{vT}$) and a lateral ($\mathbf{D}^{lu}$, $\mathbf{D}^{lS}$, $\mathbf{D}^{lT}$) component because of differences in the effect of gravity on the horizontal and vertical dimensions of the flow. The vertical and lateral components must be solved independently. However, both are driven by the large-scale quantities along neutral surfaces.

The vertical momentum and tracer diffusion are solved using a second order derivative (Eq. 2.16). The scale of processes that are a major source of vertical turbulence (e.g. shear instabilities) are always smaller than the vertical model resolution, therefore vertical turbulent motions must always be parametrized. Vertical turbulence is assumed to be a linear function of large scale quantities, in other words, this process is represented in a way analogous to molecular diffusion. Consequently, one can expect to underestimate the role of turbulent diffusion and dissipation.

$$\mathbf{D}^{vu} = \frac{\partial}{\partial z}(A^{vm}\frac{\partial \mathbf{U}_h}{\partial z})$$
$$\mathbf{D}^{vS} = \frac{\partial}{\partial z}(A^{vT}\frac{\partial S}{\partial z}) \tag{2.16}$$
$$\mathbf{D}^{vT} = \frac{\partial}{\partial z}(A^{vT}\frac{\partial T}{\partial z})$$

where $A^{vT}$ and $A^{vm}$ are coefficients of molecular diffusivity and viscosity, respectively. The lateral diffusive and dissipative terms for tracers are built as 3D isoneutral second order derivatives with tracer mixing as a result of large-scale quantity of gradients using a rotated bilaplacian operator. Meanwhile for momentum, it is assumed that mixing occurs along the horizontal geopotential surfaces, and the diffusive and dissipative terms are solved using bi-laplacian operators (full equations in Madec and the NEMO team (2008) p 96).

Lateral turbulence on the other hand, can be divided into mesoscale (e.g. eddies) and sub-mesoscale processes (e.g. diffusion). The mesoscale processes can be explicitly solved if the configuration has sufficient resolution, for examples in regions where the mesoscale is above the grid-spacing. Sub-mesoscale processes, however must always be parametrized. In configurations where the lateral grid-spacing is not sufficient to resolve mesoscale process (i.e. non-eddy permitting configurations), these need to be parametrized too. In OPA, the parametrization scheme use to solve the horizontal mesoscale process is similar to the closure scheme use to parametrized the vertical subgrid-scale physics.

**Vertical subgrid-scale physics**

The vertical subgrid-scale physics is used to compute the vertical eddy (molecular) viscosity ($A_u^{vm}$, $A_v^{vm}$) and diffusivity ($A_T^{vT}$, $A_S^{vT}$) coefficients. The eddy viscosity and diffusivity are initialized with a background value of $A^{vm0} = 10^{-4} m^2 s^{-1}$ and $A^{vT0} = 10^{-5} m^2 s^{-1}$, respectively. These background values are also used as the minimum values for $A^{vm}$ and $A^{vT}$ to avoid numerical instabilities caused by too weak vertical diffusion.

This thesis uses the turbulent eddy kinetic (TKE) dependant vertical diffusion parametrization to compute vertical physics. The TKE model computes $A^{vm}$ (Eq. 2.17) and $A^{vT}$ (Eq. 2.18) from the TKE turbulent closure model. In other words, they are derived from a prognostic equation for mean turbulent kinetic energy, $\bar{e}\,[m^2 s^{-2}]$ (Eq. 2.19), and a closure assumption for the turbulent length scale.

$$A^{vm} = C_k l_k \sqrt{(\bar{e})} \tag{2.17}$$

$$A^{vT} = \frac{A^{vm}}{P_{rt}} \tag{2.18}$$

$$\frac{\partial \bar{e}}{\partial t} = \frac{A^{vm}}{e_3}[(\frac{\partial u}{\partial k})^2 + (\frac{\partial v}{\partial k})^2] - A^{vT} N^2 + \frac{1}{e_3}\frac{\partial}{\partial k}[\frac{Avm}{e_3}\frac{\partial \bar{e}}{\partial k}] - c_\in \frac{\bar{e}^{-3/2}}{l_\in} + F^e \tag{2.19}$$

where $N$ is the Brunt-Vaisälä or Buoyancy frequency, $l_\in$ and $l_k$ are the dissipation mixing length scales, $P_{rt}$ is the Prandtl number, and the vertical mixing constants: Kolmogorov dissipation, $C_k = 0.7$, and the vertical eddy coefficient $C_\in = 0.1$. The value of $P_{rt}$ depends on the value of the Richardson Number, $Ri$, when $Ri \leq 0.2$, $P_{rt} = 1$, if $Ri \geq 2$, $Prt = 10$, and when $0.2 \leq Ri \geq 2$, $Prt = 5Ri$. $k$ represents the vertical levels and $F^e$ is a prescribed surface and bottom input of turbulent kinetic energy.

The time evolution of $\bar{e}$ depends on the production of turbulent kinetic energy by (1) vertical shear, and its destruction by (2) stratification, (3) vertical diffusion, and (4) vertical dissipation (RHS terms of Eq. 2.19 listed in order). This formulation does not ensure positivity, for which $\bar{e}$, is forced to have a minimum value of $10^{-6} m^2 s^{-2}$. In addition, the fifth term, is either the surface input ($F^e$) of turbulent kinetic energy prescribed from the wind stress $\bar{e} = ebb|\tau|$, where $ebb = 60$ unless the ocean is covered by sea ice in which case $ebb = 3.75$. To avoid very small values, $\bar{e}$ has a set minimum input at the surface of $10^{-4} m^2 s^{-2}$. For the bottom input ($F^e$) which equals the value of $\bar{e}$ of the layer above. During convection $N^2$ becomes negative and stratification (term 2 on the RHS) becomes the principal source term in the equation. The TKE turbulent closure scheme is also used to smooth out statistically unstable density profiles during convection (see next sub-section).

A closure assumption is needed to limit the magnitude range of the mixing length scale. Here the range is limited by the distance to the surface or to the bottom (which ever is shortest). This is done by deriving the magnitude of the dissipation mixing length scales from a first order approximation, $l_\in = l_k = \sqrt{2\bar{e}}/N$. The vertical range of the length scale, is additionally, constrained to be equal to or smaller than the variations of the

model vertical grid thickness, $e3$, by forcing $\frac{\partial l}{\partial k} \leq e3$ (where $l = l_k = l_\in$). This ensures the magnitude of the length scales are bounded to the strongly stratified portion of the water column.

**Convection scheme**

A consequence of the hydrostatic approximation is that vertical acceleration is ignored because it is much smaller than the pressure gradient differences. This makes it impossible to solve directly for convective processes and thus convection must be parametrized. The objective of the convection scheme is to restore the static stability of the water column. In this thesis, the convective scheme combines an enhanced vertical diffusion scheme with the turbulent closure scheme to effectively and rapidly restore the static stability of the water column. The convective scheme is activated wherever and whenever there is an instability (e.g. denser water over lighter water). OPA defines instabilities based on the buoyancy frequency, $N^2$, whereby a cell is defined as unstable if $N^2 < 10^{-12}$.

An instability activates the enhanced vertical diffusion scheme for tracers and momentum, by increasing the magnitude of the vertical eddy viscosity, $A^{vm}$, and eddy diffusivity, $A^{vT}$ to $10\,m^2s^{-1}$ (several orders of magnitude larger than the background values of $A^{vm0}$ and $A^{vT0}$). The magnitude is increased not only at the T-point of the cell where the instability was detected, but also at the T-point of its four closest neighbouring cells.

## 2.3 Sea ice model: LIM 2

The sea ice is an important boundary between the atmosphere and the ocean. This thesis uses the Louvian-la-Nueve sea-ice model version 2 (LIM2). The role of the sea ice module is to solve for the sea ice dynamics and thermodynamics. LIM2 accounts for the effect of brine pockets, and of small-scale changes in sea ice thickness on salt and heat fluxes.

The LIM2 thermodynamic component follows Fichefet and Maqueda (1997) and the dynamic component incorporates an elastic-vicous-plastic (EVP) rheology (Hunke and Dukowicz, 1997). LIM2 solves the equations on a finite difference curvilinear coordinates with the equations discretized on a staggered Arakawa C-grid (Figure 2.2). LIM2 conserves momentum (e.g. sea ice is an elastic-viscous plastic continuum), energy and salt (e.g. halo-thermodynamics), and explicitly represents subgrid differences in ice-thickness. In this section I only focus on the main characteristics of the sea ice model dynamics and thermodynamics and focus on the light parametrization and tracer fluxes which affect the biogeochemical module. The central sources used to developed this section are Fichefet and Maqueda (1997) and Hunke and Dukowicz (1997).

### 2.3.1 Sea ice dynamics

The EVP rheology derives from the viscous-plastic (VP) rheology of Hibler (1979) which proposes that the ice pack will diverge with little or no stress, but that it will resist compression and shear under convergence. This results in the viscosity of sea ice, increasing with pressure (a measure of the ice strength) and decreasing with larger strain rates. But as the strain approaches zero the solution becomes unstable, which is the main reason for adding an elastic formulation to the viscous plastic. The elastic formulation gives a more rigid behaviour to the sea ice when strain decreases (Hunke and Dukowicz, 1997). This regulation is needed for numerical stability rather than to represent a physical process.

The EVP rheology sees the sea ice as a two dimensional elastic-viscous plastic continuum, LIM uses two ice categories to represent the sea ice: lead or thin ice, $h$, and consolidated or thick ice, $H$. The fractional area of the cell covered by thick ice is given by the ice concentration, $(1 - P_{frld})$, and the fraction of open water is given by the open lead fraction, $P_{frld}$. If $(1 - P_{frld}) = 0$ then $P_{frld} = 100\%$, which means that there is no thick ice ($H = 0$), however, there may be thin ice ($h > 0$) or open water ($h = 0$). LIM2 treats the two categories as a two-dimensional fluid that resist deformation because of their internal strength. This strength is called internal stress tensor and it increases with the sea ice thickness and concentration. The thin ice, $h$, has no internal strength.

The motion of sea ice depends on the mass, $m$, of sea ice and snow available within each grid cell (Eq.2.20). The mass is estimated by differentiating between thick and thin ice using a constant value for ice density ($\rho_i$) and snow ($\rho_s$) (Table 2.2). The snow thickness over thin ice is $h_s$ and over thick ice is $H_s$. The snow thickness results from the accumulation of precipitation or melting due to surface atmospheric temperatures, meanwhile the ice thickness ($H$ and $h$) depends on the growth and melt of sea ice which are determined by the internal heat budget.

$$m = \rho_i \left[ (1 - P_{frld}) H + P_{frld} h \right] + \rho_s \left[ (1 - P_{frld}) H_s + P_{frld} h_s \right] \tag{2.20}$$

Ice motion and deformation is influenced by the winds and the ocean. The evolution of the sea ice dynamic is described by the conservation of linear momentum (Eq. 2.21). The first term of the RHS of Eq. 2.21 captures the role of stress forces on the sea ice surfaces, $(1 - P_{frld})$. LIM2 considers two stresses: the wind stress on the ocean surface ($\tau_a$) and the ocean stress on the bottom of sea ice ($\tau_w$). The second term in the RHS considers the force of gravity, $g$, on the mass of sea ice and snow, $m$, driving the ice-motion as a result of the tilt of the ocean surface caused by sea surface height differences, $\nabla \eta$, between adjacent cells. The third term on the RHS describes the influences of the Earth's rotation on the sea ice motion by including Coriolis force, $f = 2\omega \sin\delta$, and the fourth term explains the sea ice deformation as a function of the sea ice internal stress, $\sigma$.

$$m\frac{\partial \mathbf{U}_h}{\partial t} = (1 - Pfrld)(\tau_a + \tau_w) - mg\nabla\eta - mf\mathbf{k} \times \mathbf{U} + \nabla \cdot \sigma \tag{2.21}$$

where $\mathbf{U}_h$ is the horizontal velocity of sea ice, $t$ is time, $\mathbf{k}$ is the unit vector.

At the land-ocean boundary, the no-slip condition is applied on the sea ice too. This means that the ice in contact with coastal regions has zero along-coast velocity. This is an attempt to represent land-fast conditions, however, LIM2 does not include a proper representation of land-fast ice which would include, in addition, some form of basal stress parametrization (e.g. Lemieux et al., 2015). Not having the basal parametrization of land-fast ice was shown to result in higher than observed ice-fluxes around the Arctic (Lemieux et al., 2015).

## 2.3.2 Ice thermodynamics

The thermodynamics (e.g. the sea ice growth and melt rates) are described by the snow-ice-energy budget which manages the flow of heat through the sea ice and snow. To derive the thermodynamic changes, LIM2 uses a three layer approach: one snow layer, and two sea ice layers of equal thickness. The sea ice thermodynamics depends on temperature and salinity of the sea ice which is computed taking into consideration the heat capacity of the snow-ice system, the effect of the sub-grid-scale snow and ice thickness distribution, and the latent heat stored within the brine pockets of the two ice layers.

Sea ice formation can occur three ways: (1) the creation of new thin ice in open water when seawater temperature is at freezing point and the surface ocean keeps loosing heat, (2) the congelation of thick ice at its basal interface with the ocean when sea water, already at freezing point, continues to loose heat, and (3) the conversion of snow into ice due to excessive snow loading and consequent sinking of the sea ice below the ocean surface layer. Sea ice melt may occur at the ice-ocean basal interface and the ice-atmosphere surface interface if the temperature of the ocean or atmosphere, respectively, is above the freezing point.

At the surface, growth and melt of snow and ice is given by Eq.2.22 where the changes in thickness, $H$, are determined from the ratio between the surface energy balance, $F^{net}$, and the volumetric latent heat of fusion, $L_x$. The subscript $x$ is used to represent that the changes in thickness, $H$, and can be for either snow ($s$) or ice ($i$).

$$\frac{dH_x}{dt} = -\frac{F^{net}(T)}{L_x} \tag{2.22}$$

where the volumetric latent heat of fusion of snow ($L_s$) and ice ($L_i$) is a measure of the energy of melting.

The surface energy balance is calculated as the balance between processes that act to enlarge $F^{net}$ (e.g. shortwave downwelling radiation reaching the ice surface and penetrating within the ice after accounted for albedo, the downwelling longwave radiation flux and the conductive flux from the sea ice/snow interior towards

the ice surface) and processes that act to decrease $F^{net}$ (e.g. the emissivity-temperature relation at the ice surface, and the turbulent and sensible latent heat). Under positive values of $F^{net}$ the temperature, $T$, of the sea ice or snow surface is fixed at the melting point and ablation (melt) occurs.

At the base of the sea ice, ice growth and melt is given by the imbalance between the ocean heat flux at the ice-ocean interface ($F_w$) and the conductive heat flux from the ice towards the ice-interior ($F_c$). Ice growth occurs when $F_c > F_w$ (Eq. 2.23).

$$\frac{dH_i}{dt} = -\frac{F_w - F_c}{L_i}$$ (2.23)

The horizontal growth of sea ice is determined by changes in sea ice concentration. Lateral growth can only occur where there is open water. Whereas sea ice only forms if the heat budget, $B_l$, of these open water areas is negative. The thickness of the newly formed sea ice is a constant, $h_o$ (Table 2.2). Melting of sea ice within a fully ice cover region will result in a creation of a lead or polynya.

**Table 2.2.** Sea ice model parameters

| Parameter | Value | Units | Description |
|---|---|---|---|
| $L_i$ | 300.330 | $MJm^{-3}$ | Volumetric latent heat of fusion for ice |
| $L_s$ | 110.121 | $MJm^{-3}$ | Volumetric latent heat of fusion for snow |
| $h_o$ | 0.05 | $m$ | Thickness of new sea ice |

### 2.3.3   Ice induced tracer flux: T and S

During sea ice formation the ocean gains heat and salt while during sea ice melting the ocean cools and dilutes. In other words, melting is associated with a cooling flux, $Q_M < 0$, and positive freshwater flux, $F_M > 0$, while freezing is associated with a warming flux, $Q_F > 0$, and negative freshwater flux, $F_F < 0$. Where there is thin sea ice, the solar radiation can penetrate and become an ocean heat surface flux, $Q_{PS}$. The surface ocean heat at the base of sea ice, $Q_B$, is generally 0. At the base of sea ice there is also generally a negative freshwater flux, $F_B$, due to the production of sea ice caused by the cold surface temperatures. At the ice-ocean interface, the heat flux is calculated with equation Eq. 2.24 and the freshwater flux with equation Eq. 2.25.

Formation of sea ice in the open ocean occurs if atmospheric cooling drives the surface ocean temperature below the freezing point, $T_f$. This is an unstable condition, thus, the sea surface temperature needs to be warmed to $T_f$. This is achieved by freezing sea water (e.g. increasing the magnitude of $Q_F$). The change of state process releases heat (e.g. surface ocean gains heat or $Q_F > 0$).

$$Q_{io} = Q_M + Q_F + Q_{PS} + Q_B$$ (2.24)

$$F_{io} = F_M + F_F + F_B \qquad (2.25)$$

### 2.3.4 Light parametrizations: Qsr and ZQsr

The focus of this section is on how LIM2 treats the shortwave solar radiation (input in the atmospheric forcing) as it hits the surface of the sea ice and penetrates through the sea ice. The resulting of these processes are then used by BLING to convert into photosynthetically available radiation which is then influences phytoplankton growth.

The solar flux reaching the surface of the ocean, $Q_{sr}$, is the fraction of the total incident light, $Q_I$, that was not reflected back into space by the surface albedo, $\alpha$ (Eq. 2.26). Light calculations in LIM2 assume clear-skies, which means that they do not directly consider cloud-cover, however the incident light, $Q_I$, is an atmospheric forcing variable. My choice of atmospheric forcing field derives the incident light considering latitude and cloud cover. In LIM2 the ocean $\alpha$ is a constant value but the sea ice and snow $\alpha$ depends on the atmospheric surface temperature (Table 2.3).

$$Q_{sr} = Q_I(1 - \alpha) \qquad (2.26)$$

The sea ice cover modulates the amount light reaching the surface ocean. Light is attenuated as it passes through the ice downwards into the ocean. The attenuation coefficient of light within the sea ice is $k = 1\,m^{-1}$, based on observations of melting and dry ice (e.g. non-melting ice) in the Beaufort Sea (Light et al., 2008). Therefore, light reaching the ocean surface across the domain, is not only dependant on latitude, cloud cover and surface albedo but also on the sea ice thickness.

A more complete representation of the light reaching the ocean surface is presented by Eq. 2.27, where the total light at the surface ocean on any model grid cell, $ZQ_{sr}$, is given by the light over the non-ice covered portion of the grid cell (first term RHS) and the light over the ice-covered portion of the grid cell (second term RHS). In the ice-covered regions, the amount of light that can be transmitted through the sea ice depends on the mean thickness of the snow - ice cover system. The fraction of solar flux transmitted through the snow-ice system, $fstric$, is estimated using the CORE bulk formulation.

$$ZQ_{sr} = Q_{sr}P_{frld} + [(1 - P_{frld})fstric] \qquad (2.27)$$

where $P_{frld}$ is the open water fraction of the grid cell, and $(1 - P_{frld})$ is the ice covered fraction of the grid cell.

**Table 2.3.** Sea ice model parameters for albedo following Shine and HendersonSellers (1985). Values are presented in percentage of light reflected.

| Parameter | Value | Description |
|-----------|-------|-------------|
| $\alpha_{dsnw}$ | 0.8 | Albedo of dry snow |
| $\alpha_{msnw}$ | 0.65 | Albedo of melting snow |
| $\alpha_{fice}$ | 0.72 | Albedo of frozen bare ice |
| $\alpha_{mice}$ | 0.53 | Albedo of melting ice |
| $\alpha_{oce}$ | 0.066 | Albedo of open ocean under clear sky |

## 2.4   Biogeochemical model

During the course of this Ph.D. BLING was embedded in the ANHA4 domain of NEMO. BLINGv0 has four prognostic tracers: dissolved inorganic iron (Fe), dissolved inorganic phosphate (P), dissolved oxygen ($O_2$) and dissolved organic phosphate (DOP). The diagnostic variables are phytoplankton growth, net primary production, export production, biomass and chlorophyll-a concentration. These diagnostic variables are key to evaluating the performance of the phytoplankton compartment of the model simulation.

Compared to other more complex biogeochemical models embedded in NEMO, BLINGv0 is relatively simple in having only 4 compartments, compared the 24 biogeochemical compartments in the Pelagic Interaction Scheme for Carbon and Ecosystem Studies (PISCES), the principal ocean biogeochemical model of NEMO (Aumont and Bopp, 2006; Aumont et al., 2015). Using BLING as the choice for biogeochemical modelling has the benefit of lower computational demands, the advantage for running long simulations on high resolution grids like ANHA4. Potential uses of this computationally-light biogeochemical module include running multiple simulations to study how the model responds to induced physical environmental changes and climate experiments.

**Light parametrization: PAR**

From the light that reaches the ocean surface, $ZQ_{sr}$ (Eq. 2.27), only 43% is photosynthetically available to phytoplankton. This is commonly known as the photosynthetically active radiation (*PAR*). At the surface ocean, the PAR is simply a linear function of how much light has arrived (Eq. 2.28).

$$PAR = ZQ_{sr}\,0.43 \tag{2.28}$$

Below the surface level ($k > 1$), *PAR* declines due to absorption of light by the water and chlorophyll concentration (Eq. 2.29). This absorption is resolved as an exponential function of water and chlorophyll optical properties of the water above (subscript $k - 1$). In this thesis, the *PAR* parametrization considers the absorption of red light by water, $zk_{r0}$, and by chl-a, $xk_{rp}$ (Table 2.3). Initial sensitivity testing proved no significant im-
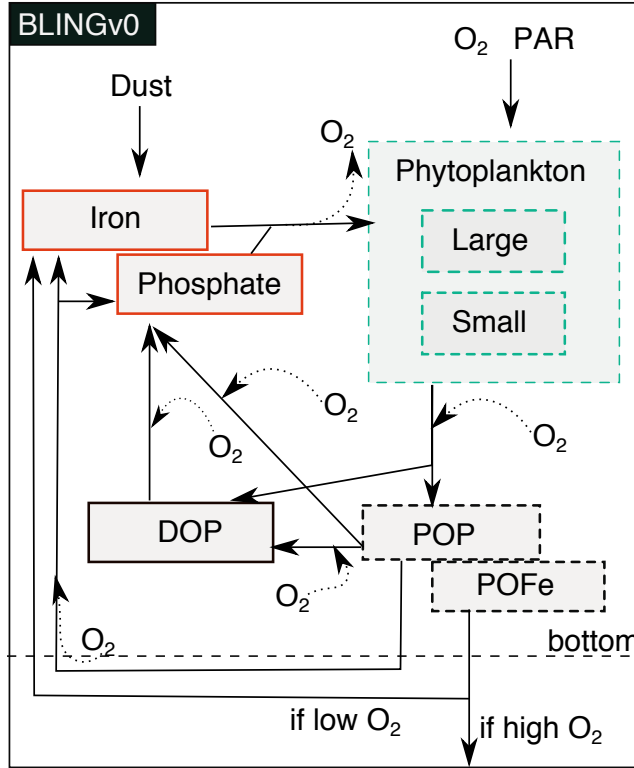
**Figure 2.4.** Schematic of BLING (version 0) biogeochemical model and the interaction between the its compartments. BLINGv0 also considers the oxygen ($O_2$) changes as a result of these interactions. There are three major pools: (red) inorganic nutrient, (green) living phytoplankton, (black) dissolved and particulate organic matter pools. The dissolved organic matter is represented by dissolved organic phosphate (DOP), and the particulate organics are represented by particulate organic phosphate (POP) and particulate organic iron (POFe). Solid-edge box encircles the four prognostic tracers while dashed-edge boxes encircle the selected diagnostic tracers. Surface boundary conditions include the external flux of iron in dust and the photosynthetically active radiation (PAR).

provement if blue and green light absorption coefficients were also included. The concentration of chlorophyll-a in the depth level above ($chl_{k-1}$) is used to quantify the red absorption by living phytoplankton (second term in RHS of Eq. 2.30).

$$PAR = PAR\,e^{(-zkr_{k-1})} \tag{2.29}$$

$$zkr_{k-1} = xk_{r0} + xk_{rp}\,chla_{k-1} \tag{2.30}$$

**Table 2.4.** Biogeochemical parameters for light absorption. All parameters are dimensionless.

| Parameter | Value | Description |
|---|---|---|
| $xk_{r0}$ | 0.067 | Red absorption coefficient |
| $xk_{rp}$ | $1.258 * 10^{-4}$ | Red absorption coefficient of chlorophyll |

Although *PAR* is calculated for each vertical level, within the mixing layer BLING assumes that light is distributed equally and thus *PAR* is averaged over the mixing layer, yielding $I_{mix}$ in Eq. 2.39. This is done to represent the vertical movement that phytoplankton undergo within a mixing layer. This parameterization assumes that the number of species able to mildly adjust their buoyancy is small compared to those who do not have this capability.

In the simulations used during this thesis the mixing layer depth is defined as the depth of the *actively mixing layer* (variable turbocline in OPA) which is not to be confused with the depth of the *mixed layer*. OPA derives the mixed layer depth using a density criterion (threshold $\rho = 0.01$), whereas it derives the turbocline using a turbulent mixing criterion relying only on the vertical physics and a threshold for the vertical eddy diffusivity coefficient ($A^{vT} > 5e^{-4} m^2 s^{-1}$). Because the turbocline represents the active mixing it is more accurate to use it as the dependant variable for mixing of biological tracers. Both metrics (turbocline and mixed layer depth), however, tend to yield similar values with the turbocline being slightly deeper in regions with strong mixing such as the central Labrador Sea (Figure 2.5).
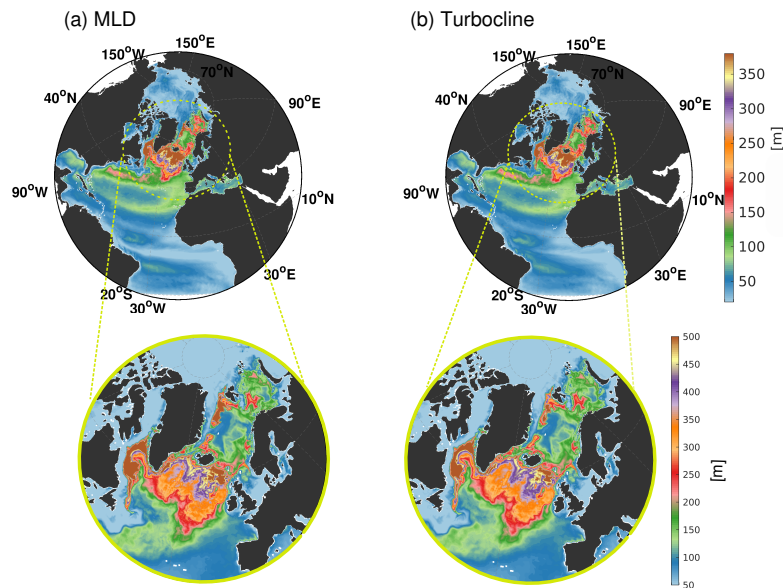


**Figure 2.5.** Simulated annual (a) mixed layer and (b) turbocline depth climatology from 2002-2008. The mixed layer depth is derived using a density criterion (a density threshold) while the turbocline is derived using a mixing criterion (a threshold on the vertical eddy diffusivity coefficient).

**Prognostic equations**

The four prognostic equations of BLINGv0 (Eq. 2.31 to 2.34) described the time evolution of each tracer due to changes in their sources (positive) and sinks (negative).

- Dissolved organic phosphate (DOP) as the organic matter

$$\frac{dDOP}{dt} = (1 - frac_{POP})\phi_{DOP}jP_{uptake} + \phi_{DOP}jP_{reminP} - \gamma_{DOP}DOP + jDOP_{river} + jDOP_{ice} \quad (2.31)$$

- Dissolved inorganic phosphate (P) as the macro-nutrients

$$\frac{dP}{dt} = jP_{recycle} + (1 - \phi_{DOP})jP_{reminP} + \gamma_{DOP}DOP - jP_{uptake} + jP_{river} + jP_{ice} \quad (2.32)$$

- Dissolved inorganic iron (Fe) as the micro-nutrients

$$\frac{dFe}{dt} = jFe_{recycle} + jFe_{reminP} - jFe_{uptake} - jFe_{adsorg} - jFe_{adsinorg} + jFe_{river} + jFe_{ice} + jFe_{atm} \quad (2.33)$$

- Dissolved oxygen ($O_2$)

$$\frac{dO_2}{dt} = -(O_2 : P)\,jP + jO_{2atm} + jO_{2ice} \quad (2.34)$$

In the prognostic equations, the fluxes are represented with the letter $j$ in the front. Fluxes followed by the subscripts *river* or *ice* are associated with river runoff or sea ice freeze and melt cycles, respectively. These river nutrient fluxes where added during the course of this Ph.D., and its activation was made flexible to the user. The *river* fluxes are added at the surface as a function of runoff. The *ice* tracer fluxes are a built-in feature of the OPA-LIM2 interactive processes, which translates to all of BLING's tracers because this interaction is handled through TOP. In this way, BLING tracers are treated in a similar way as the salinity fluxes (Section 2.3.3, Eq. 2.25). A positive tracer flux occurs when sea ice freezes, causing an increase in the tracer concentration within the surface water, and a negative flux occurs when sea ice melts, causing tracer concentration to decrease within surface waters. The surface water is defined as the first model level $k = 1$ with depth $0 - 1\,m$.

In Eq.2.31, the first term is a source of *DOP* due to phytoplankton cell lysis measured as a fraction of the non-particulate uptake (describe in more detail in section 2.4.4). The second term is a source of *DOP* due to remineralization of particulate organic phosphate (*POP*) into *DOP*. The third term is the sink of DOP due to the remineralization of *DOP* into inorganic phosphate, *P*. The fourth term is the river source of *DOP* (if activated) and the fifth term is the ice fluxes of *DOP* in ice cover waters, and can be either a sink or source term depending on the season. In Eq 2.31 and 2.32, the constants, $\gamma_{DOP}$ and $\phi_{DOP}$, are the decay time-scale of DOP and the fraction of primary production that did not become particulate and that is converted to DOP, respectively (Table 2.5).

In Eq.2.32 and 2.33 the fluxes $jP_{reminP}$ and $jFe_{reminP}$ are source terms representing the slow remineralization of *POP* into inorganic phosphate and iron, respectively. The fluxes $jP_{recycle}$ and $jFe_{recycle}$ represent the

fast recycling of *DOP* by heterotrophic bacteria which convert *DOP* into inorganic phosphate and iron, respectively. The fluxes $jP_{uptake}$ and $jFe_{uptake}$ are the sinks of inorganic phosphate and iron, respectively, due to phytoplankton uptake. The $jP_{uptake}$ is derived from the product of phytoplankton biomass ($B_{inst}$; Eq. 2.42) and net phytoplankton growth rate ($\mu$; Eq. 2.39). Meanwhile the $jFe_{uptake}$, formulation is more complicated as iron is not only required for growth but is also needed during light harvesting by phytoplankton (Galbraith et al., 2010).

In Eq. 2.33 the terms $jFe_{adsorg}$ and $jFe_{adsinorg}$ represent the loss of inorganic iron from the water column due to its adsorption to organic and inorganic particles within the water column, respectively. To parametrize these fluxes the formulation uses an ad-hoc ligand to iron concentration relationship because of scarce research in the area of iron ligands (Galbraith et al., 2010).

In Eq. 2.34, the first term shows that BLING derives the oxygen fluxes (Eq. 2.34) from the phosphate fluxes ($jP$) using a stoichiometric ratio of oxygen to phosphate ($O_2 : P$) as in Gruber et al. (2001). The negative sign in front of the ($O_2 : P$) ratio indicates that there is an opposite relation between phosphate and oxygen fluxes. When phosphate is *created* oxygen is *respired* and when phosphate is *respired* oxygen is *created*.

In Eq. 2.33 and 2.34 the fluxes, $jFe_{atm}$ and $jO_{2atm}$, are the atmospheric input of iron and oxygen, respectively. The atmospheric flux of iron is derived from the dust depositions following a relationship between dust particle size and iron concentrations (Galbraith et al., 2010). A monthly dust deposition climatology was taken from the Global Ozone Chemistry Aerosol Radiation and Transport (GOCART) model (Ginoux et al., 2001). Most of the atmospheric flux of iron inputed into the Atlantic and Arctic Oceans derive from the Sahara dust storms and thus deposits in the North Atlantic (Figure 2.6). In terms of the $jO_{2atm}$ it is a function of the atmospheric wind field and the ocean oxygen saturation (see section 2.4.1).

**Table 2.5.** Biogeochemical model productivity parameters

| Parameter | Value | Units | Description |
|---|---|---|---|
| $P_c^o$ | $10^{-5}$ | $s^{-1}$ | Maximum carbon specific growth rate at $0°C$ |
| $\kappa_{eppley}$ | 0.063 | $(°C)^{-1}$ | Temperature dependence of growth |
| $K_{PO_4}$ | $10^{-4}$ | $molP\,m^{-3}$ | Phosphate uptake half saturation constant |
| $R_{respiration}$ | 0 | [no units] | Fraction of gross production respired |
| $P^*$ | $1.7436 * 10^{-5}$ | $molP\,m^{-3}$ | Pivotal phytoplankton biomass |
| $\gamma_{biomass}$ | 0.5 | $day^{-1}$ | Biomass adjustment time constant |
| $\gamma_{DOP}$ | 0.25 | $yr^{-1}$ | Decay timescale of dissolved organic matter |
| $\phi_{DOP}$ | 0.1 | [no units] | Fraction of non-particulate uptake converted to DOP |
| $O_2 : P$ | 150 | $molO_2\,(molP)^{-1}$ | Oxygen to phosphate ratio |
| $C : P$ | 106 | $molC\,(molP)^{-1}$ | Carbon to phosphate Redfield ratio |
| $e$ | 2.718281828 | [no units] | Universal constant |
| $Mc$ | 12.011 | $mol\,g^{-1}$ | Molar mass of Carbon |
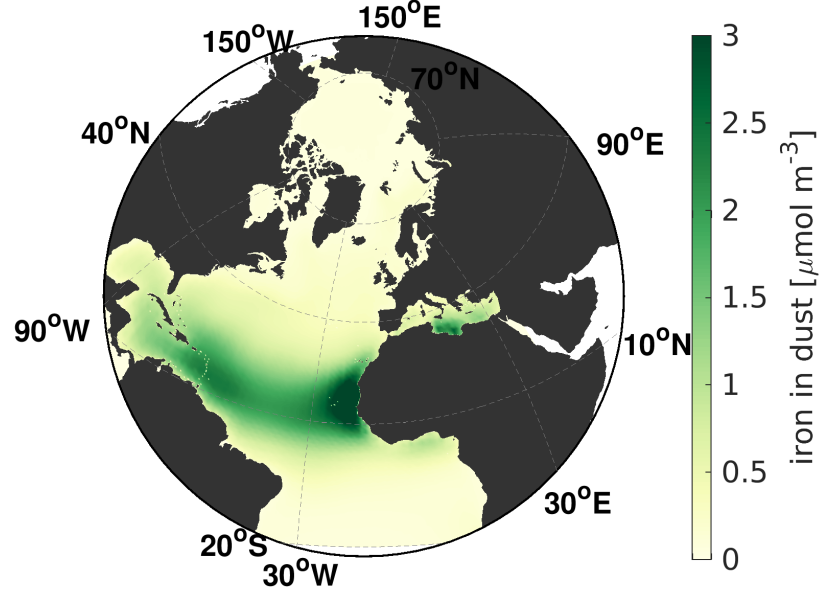
**Figure 2.6.** Climatological surface flux of Iron in BLINGv0 derived from estimates of dust particle size following Galbraith et al. (2010).

### 2.4.1 Air-sea gas exchange: $O_2$

The air-sea oxygen fluxes ($jO_{2atm}$) are a function of the air-sea gas transfer velocity and the surface ocean oxygen solubility (Eq. 3.5). It is assumed that the atmosphere is always super-saturated with oxygen, such that there is a positive pressure from the atmosphere into the ocean. The air-sea oxygen fluxes depend on Schmidt number ($Sch_{no}$), gas transfer coefficient ($k_w$), and the oxygen-saturation levels ($[O_2]_{sat}$) at the sea-surface (Keeling et al., 1998). The $k_w$ is a quadratic function of the wind speed. The $Sch_{no}$ has a linear dependency on the surface temperature (Eq. 2.37) and the $[O_2]_{sat}$ has an exponential dependence on surface water temperature (Eq. 2.38). Both are calculated using the coefficients listed in Table 2.6. The surface water oxygen saturation influences the diffusive air-sea gas flux, which determines how much of the gas can enter the surface water. The diffusive air-sea gas flux is calculated based on the difference between the surface ocean oxygen equilibrium concentration, $[O_2]_{sat}$, and the actual surface ocean oxygen concentration, $[O_2]_{surf}$.

$$jO_{2atm} = k_w \left([O_2]_{sat} - [O_2]_{surf}\right) \tag{2.35}$$

The $[O_2]_{surf}$ and concentration of oxygen below the surface are estimated from the phosphate fluxes using Eq. 2.34.

$$k_w = 0.39 P_{frl} (wndm)^2 \sqrt[2]{\frac{660}{Sch_{no}}} \tag{2.36}$$

**Table 2.6.** Oxygen fluxes calculation constants. Coefficients for oxygen saturation and Schmidt number.

| Coefficients | Value | Calculation |
|---|---|---|
| $a1o$ | $1929.7e0$ | for Schmidt number |
| $a2o$ | $117.46e0$ | for Schmidt number |
| $a3o$ | $3.116e0$ | for Schmidt number |
| $a4o$ | $0.0306e0$ | for Schmidt number |
| $a0$ | $2.00907e0$ | for oxygen saturation |
| $a1$ | $3.22014e0$ | for oxygen saturation |
| $a2$ | $4.05010e0$ | for oxygen saturation |
| $a3$ | $4.94457e0$ | for oxygen saturation |
| $a4$ | $-2.56847e-01$ | for oxygen saturation |
| $a5$ | $3.88767e0$ | for oxygen saturation |
| $b0$ | $-6.24523e-03$ | for oxygen saturation |
| $b1$ | $-7.37614e-03$ | for oxygen saturation |
| $b2$ | $-1.03410e-02$ | for oxygen saturation |
| $b3$ | $-8.17083e-03$ | for oxygen saturation |
| $c0$ | $-4.88682e-07$ | for oxygen saturation |
| $S_e$ | $298.15$ | entropy for oxygen saturation |

where $P_{frl}$ is the ice-free area, *wndm* is the wind velocity which is input in the atmospheric forcing. The $Sch_{no}$ is normalized to the $Sch_{no}$ of carbon dioxide at $20°C$ ($Sch_{no} = 660$).

$$Sch_{no} = a1o - a2o\,T^2 + a3o\,T^3 - a4o\,T^4 \tag{2.37}$$

$$
\begin{aligned}
O_{2_{sat}} &= e^{A+B+C} \\
A &= a0 + a1\,T_s + a2o\,T_s^2 + a3\,T_s^3 - a4\,T_s^4 + a5\,T_s^5 \\
B &= b\,S + b1\,S\,T_s + b2\,S\,T_s^2 + b3\,S\,T_s^3 \\
C &= c\,S^2
\end{aligned}
\tag{2.38}
$$

In Eq. 2.38, $T_s$ measures the entropy of the surface waters ($T_s = ln(\frac{S_e - T}{273.15 + T})$) where $T$ is the temperature in degree Celsius, $S$ is the salinity, and all other variables are coefficients listed in Table 2.6.

## 2.4.2 Phytoplankton Productivity (PP)

The carbon specific growth rate or productivity ($\mu$) equals carbon specific photosynthesis rate ($P^c$) minus the respiration rate ($R_{respiration}$). However, following previous biogeochemical models, BLING assumes that $R_{respiration}$ is a fixed fraction of $\mu$ which leads to $\mu$ equalling $P^c$ (Eq. 2.39).

$$\mu = P^c - R_{respiration} \tag{2.39}$$

$$\mu = P^c = P_m^c (1 - e^{-\frac{I_{mix}}{I_k}}) \tag{2.40}$$

The Eq. 2.40 indicates the dependence of the carbon specific photosynthetic rate on temperature, nutrient concentration and light. In equation 2.40, $P_m^c$ $[s^{-1}]$ is the light saturated, macro-nutrient and temperature limited primary production that multiplies the light limitation term. The latter is represented as an exponential function of the ratio between the total amount of light available to phytoplankton within the mixed layer, $I_{mix}$, and the scaling term, $I_k$, determining the degree of light limitation. This formulation causes photosynthesis to always be light limited because for any value of $I_{mix}$ and $I_k$ the term $(1 - e^{-\frac{I_{mix}}{I_k}}) < 1$ (where $e$ is a universal constant listed in Table 2.5).

$P_m^c$ can be estimated using Eq. 2.41 whereby the temperature limitation is represented as an exponential function (first term in RHS) and the nutrient limitation is calculated using the Liebig's law of the minimum (second term). To estimate the temperature limitation BLING uses the grid-cell averaged ocean temperature, $T$, the temperature dependant growth coefficient $\kappa_{epply}$ and a constant maximum carbon specific growth rate, $P_0^c$ (Table 2.5). The nutrient limitation is a function of the dissolved iron and phosphate concentrations. Phosphate acts as a general macronutrient (e.g. represent the mean of the sum of phosphate plus nitrogen). The phosphate limitation is calculated using the Monod relationship ($\frac{PO_4}{K_{PO_4}+PO_4}$), while the formulation for iron limitation, $Def_{Fe}$ is more complex (see Galbraith et al. (2010)). In the Monod relationship, $K_{PO_4}$, is the constant for phosphate half saturation (Table 2.5).

$$P_m^c = [P_0^c e^{\kappa_{epply}T}] [min(Def_{Fe}, \frac{PO_4}{K_{PO_4}+PO_4})] \tag{2.41}$$

In BLING, both $P_m^c$ (Eq. 2.41) and the light limitation (Eq. 2.40) have a dependency on iron. This is aimed at representing that phytoplankton require iron not only as a nutrient but also to harvest light. The lack of iron limits the harvesting efficiency of photons within photosystem I and II, and the synthesis of chlorophyll.

### 2.4.3 Biomass and chl-a

The instantaneous biomass, $B_{inst}$, is estimated from the phytoplankton productivity ($\mu$), and the chlorophyll-a concentration (chl) is estimated from biomass. These three tracers are non-conservative, meaning that quantities are computed within each model grid cell independently from its neighbouring grid cells. Neither productivity, biomass or chlorophyll are advected, therefore, these variables can be seen as a potential maximum for the *in*

*situ* production within an area.

BLING uses two phytoplankton classes: small and large. Each class contributes a different percentage to the biomass (Eq. 2.42): the instantaneous biomass, $B_{inst}$, is the sum of the biomass of small and large phytoplankton multiplied by the scale factor, $P*$, the pivotal phytoplankton biomass (Table 2.5). The biomass of each class is derived from the ratio between productivity, $P_m^c$, and mortality, $\lambda$, whereby mortality is a function of temperature (Eq. 2.45). In BLING, the biomass of large phytoplankton (first term in Eq. 2.42) has a cubic relation with $B_{inst}$ to represent that this class is less affected by zooplankton grazing. To derive the change in biomass, $B$, the instantaneous biomass is adjusted to the previous timestep using the adjustment time constant $\gamma_{biomass}$ (Table 2.5).

$$B_{inst} = (\frac{P_m^c}{\lambda})^3 P^* + \frac{P_m^c}{\lambda} P^* \tag{2.42}$$

$$\frac{dB}{dt} = (B_{inst} - B)\gamma_{biomass} \tag{2.43}$$

Chlorophyll-a (*chl*) is estimated from the biomass, using the constant molar mass of carbon ($M_c$), and the Redfield ratio for the carbon to phosphate ratio ($C:P$; Table 2.5). This formulation is modulated by the ambient iron concentrations through its dependence on the chlorophyll to carbon ratio ($\Theta$). The formulation for $\Theta$ is made to accounts for photoadaptation and is detailed in Galbraith et al. (2010).

$$chl = B M_c (C:P) \Theta \tag{2.44}$$

### 2.4.4   Export rates and mortality

The food web assumes that large (micro) and small (pico and nano) phytoplankton are grazed by large (meso) and small (micro) zooplankton. A product of grazing and mortality of alga and zooplankton in surface water is the sinking of particulate organics, either as aggregates, cell bodies or fecal derivatives. Observations and modelling of high sinking algal fluxes (e.g. alga cells or alga aggregates) are typically associated with blooms of large phytoplankton (Boyd and Stevens, 2002) while elevated levels of fecal export fluxes are associated with elevated zooplankton activity (Aksnes and Wassmann, 1993). BLING takes these two into consideration and models the total sinking flux as a combination of the flux of sinking algal cells and aggregates (as a result of mortality) and the flux of fecal matter from zooplankton.

BLING diagnoses mortality, $\lambda$, of the two phytoplankton classes due to grazing as an exponential function of temperature (Eq. 2.45) and the detritus or particulate organic loss rate, $fPOP$, is modelled based on the formulation of Evans and Parslow (1985) (Eq. 2.46).

$$\lambda = \lambda_0 e^{\kappa_{epply} T} \tag{2.45}$$

where $\lambda_0$ is the non-grazed phytoplankton specific mortality ($\lambda_0$; Table 2.5)

$$\frac{\partial fPOP}{\partial z} = (frac_{P0P} BP_m^c) - Z_{remin} POP \tag{2.46}$$

In Eq. 2.46, $POP$ is the particulate organic phosphate, and the prefix $f$ in front of $POP$ indicates that is the downward flux of POP. In the equation $fPOP$ is the balance between a fix fraction ($frac_{POP}$) of the phytoplankton production ($BP_m^c$) that becomes particulate (first term on RHS), and the loss of $POP$ to remineralization (second term on RHS). The magnitude of the export flux is strongly influenced by the nutrient supply to the surface layer which controls the biomass and productivity and the oxygen concentrations (as remineralization needs oxic conditions).

In Eq. 2.46, $frac_{POP}$ is the fraction of $POP$ remaining after phytoplankton growth ($\frac{P_m^c}{\lambda}$). The formulation of $frac_{POP}$ (Eq. 2.47) has an exponential dependence on temperature ($e^{k_{remin} T}$) and a quadratic dependence on growth rate ($\frac{P_m^c}{\lambda}$). This formulation captures 61% of field observations globally confirming the dependence of export production on temperature and growth rate (Dunne et al., 2005).

$$frac_{POP} = \frac{0.18 + 0.82 (\frac{P_m^c}{\lambda})^2}{1 + (\frac{P_m^c}{\lambda})^2} e^{k_{remin} T} \tag{2.47}$$

where $\lambda$ is the carbon specific-temperature dependant phytoplankton mortality rate (Eq. 2.45), $T$ is the prognostic ocean temperature and $k_{remin}$ is the constant temperature dependence on detritus production (Table 2.5).

The formulation for the particulate organic export is also dependant on depth since the remineralization, $Z_{remin}$, of particulate organic carbon (Eq.2.48), is a function of the sinking speed, $w_{sink}$ (Eq. 2.49). The remineralization at a given depth of the ocean will decrease if the sinking speed ($w_{sink}$) of the organic particles increases (denumerator of Eq.2.48). Additionally, the remineralization of particulate organic phosphate is oxygen-dependent (numerator of Eq.2.48), whereby remineralization reaches a minimum when oxygen concentrations are close to the lowest levels.

$$Z_{remin} = \gamma_{POP} * \frac{\frac{O_2}{kO_2 + O_2} (1 - remin_{min}) + remin_{min}}{w_{sink}} \tag{2.48}$$

where $\gamma_{POP}$ is the remineralization rate parameter, $kO_2$ is the half saturation constant for oxygen consumption during remineralization, and $remin_{min}$ is the minimum yield of remineralization at minimum oxygen concentrations. These three variables are constant which values are in Table 2.7. $O_2$ is the specific oxygen concentration estimated using Eq. 2.34.

The sinking speed is constant ($w_{sink_0}$) above the depth $z_{wsink}$. Below $z_{wsink}$ the sinking speed accelerates following equation Eq. 2.49, where $z$ is the depth in meters and $w_{acc}$ is the constant acceleration of the sinking speed. Constants, $z_{wsink}$, $w_{acc}$, and $w_{sink_0}$ are listed in Table 2.7. This acceleration represents the fact that particulate organic mater increases in weight as it sink due to the agglomeration of new particles.

$$w_{sink} = w_{acc} * (z - z_{wsink}) + w_{sink_0} \tag{2.49}$$

**Table 2.7.** Biogeochemical model parameters for remineraliztion, export and mortality

| Parameter | Value | Units | Description |
|---|---|---|---|
| $z_{wsink}$ | 80 | $m$ | Critical sinking depth |
| $w_{sink_0}$ | 16 | $m\,day^{-1}$ | Sinking rate above critical sinking depth |
| $w_{acc}$ | 0.05 | $day^{-1}$ | Acceleration of sinking rate below critical sinking depth |
| $\gamma_{POP}$ | 0.12 | $days^{-1}$ | Re-mineralization rate of sinking POP |
| $remin_{min}$ | 0.3 | [no units] | Minimum anaerobic respiration rate at oxygen depletion |
| $kO_2$ | 20 | $mmol O_2\,m^{-3}$ | Half saturation constant for aerobic respiration |
| $O_{2(min)}$ | 1 | $mmol\,m^{-3}$ | Minimum oxygen concentration for aerobic respiration |
| $Fe:P_{sed}$ | 10.6 | $mmol Fe (mmol P)^{-1}$ | Sedimentary iron to phosphate ratio |
| $k_{remin}$ | −0.032 | $(°C)^{-1}$ | Temperature dependence on detritus production |
| $\lambda_0$ | 0.19 | $day^{-1}$ | Carbon specific phytoplankton mortality rate |

## 2.4.5   Ocean floor fluxes: $P, Fe, O_2$

Sinking particulate organic phosphate that reaches the ocean floor is instantaneously remineralized and returned back to the ocean as inorganic phosphate (Eq. 2.50). This process consumes oxygen, and thus the oxygen concentration at the ocean floor will decrease as a function of falling particulate organic phosphate (Eq. 2.51). Sinking particulate organic iron that reaches the ocean floor is either lost from the ocean (e.g. it gets buried in the sediment) if anoxic conditions prevail (e.g. oxygen concentration are below a minimum threshold, $O_{2(min)}$; Eq. 2.52)) or it is instantaneously returned to the bottom ocean layer (Eq. 2.53) if the oxygen concentration at the ocean floor is above the $O_{2(min)}$ threshold.

$$bP = -fPOP \tag{2.50}$$

$$bO_2 = O_2 : fPOP \tag{2.51}$$

$$bFe = -Fe : P_{sed}\,fPOP - fPOFe \qquad\qquad if(O_2 \leq O_{2(min)}) \tag{2.52}$$

$$bFe = -Fe : P_{sed}\,fPOP \qquad\qquad if(O_2 > O_{2(min)}) \tag{2.53}$$

$$\tag{2.54}$$

where $Fe : P_{sed}$ is the sedimentary iron source and $O_{2(min)}$ is the minimum oxygen concentration for aerobic respiration (Table 2.7). The negative sign in these equations indicates the flux direction is into the water column (e.g. ocean gains), and a positive sign is a flux from the ocean towards the sediment (e.g. tracer is loss from the ocean).

This bottom condition causes high phosphate and iron concentrations in the deep ocean ($k = bottom$) when oxygen concentrations are high (Figure 2.7b,d,f). But also may cause an enrichment of surface waters if the region is shallow and well mixed (e.g. Hudson Bay and the Labrador Sea in Figure 2.7a,c,e). In particular, in Hudson Bay the high rate of remineralization causes the lowest oxygen concentrations near the sea floor within the our domain (Figure 2.7f).
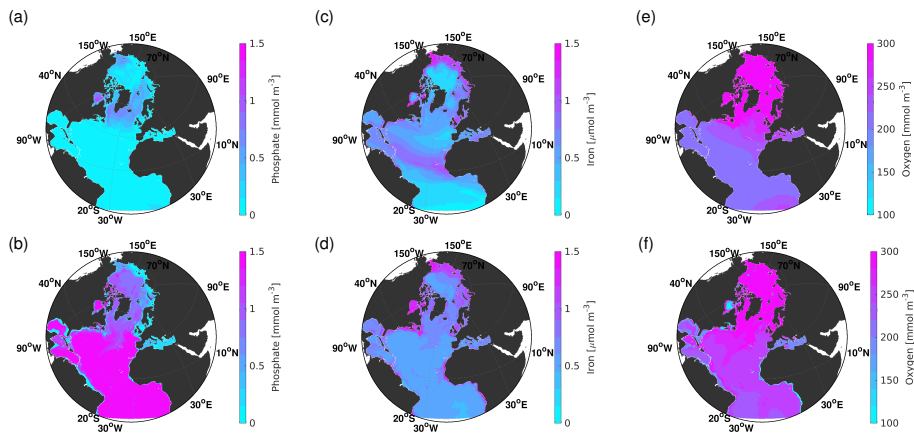


**Figure 2.7.** Simulated climatology (2002-2008) surface (model level $k = 1$) and bottom (model level $k = bottom$) of phosphate (a,b), iron (c,d) and oxygen (e,f). Surface concentrations are plotted on the first row and bottom concentrations on the second row.

## 2.5   Model configurations

The NEMO model can be used in a global or regional configuration. I chose to use NEMO in a regional configuration because it is more computationally feasible to run multiple experiments relative to running a global configuration. With a regional configuration, experiments can also be run at much higher resolution which allows for a more effective identification of regional patterns.

The two regional configurations used in this thesis are the North Atlantic and Arctic (NAA) and the Arctic and North Hemisphere Atlantic at 1/4 degree resolution (ANHA4). To avoid the north pole singularity over the ocean, these configurations move the grid-pole onto land. The NAA configuration placed the grid-pole over Canada meanwhile the ANHA4 configuration has one grid-pole over Canada and another over Russia. The grid resolution increases in proximity to the grid-pole, this causes the marked increase in horizontal resolution in

the western Arctic relative to the eastern Arctic Ocean in both configurations. Both configurations use Earth Topography (ETOPO1), for the solid earth and land boundaries. ETOPO1 is a smooth version of a global relief model of the Earth's surface. It integrates land topography and ocean bathymetry and was built by combining regional data sets (Amante and Eakins, 2009).

The spatial domain of NAA is smaller but has higher spatial resolution in some regions of the western Arctic (e.g. Baffin Bay) than that of the ANHA4 configuration (Figure 2.8a). The NAA configuration has three open boundaries: North Atlantic at $45°N$, North Pacific at $60°N$, and at the exchange region with Hudson Bay. The NAA configuration has a horizontal resolution ranging from less than $8\,km$ in the western side of the domain to $15\,km$ in the eastern side. The ANHA4 configuration has a much larger domain. It encircles the Arctic Ocean (including Hudson Bay) and the North Atlantic north of $20°S$ (map inset in Figure 2.8b). ANHA4 configuration has only two open boundaries: one at Bering Straits and the other at $20°S$ in the North Atlantic Ocean. The spatial resolution is over $20\,km$ at the Equator, $14\,km$ in the Labrador Sea and less than $8\,km$ within the western Arctic (Figure 2.8b)).

In the vertical domain, NAA has 46 levels while ANHA4 has 50 levels. The resolution of each vertical level is not a linear function of depth, resulting in the NAA configuration having coarser vertical resolution at the surface but finer at depth (compare Figure 2.8c and d, but note the colour bar differences). For example, in ANHA4, the upper 27 vertical levels describe the first $240\,m$ of the ocean surface meanwhile in the NAA configuration, 24 levels resolve $1000\,m$.

The NAA configuration was used to study Baffin Bay circulation response to a melting Greenland ice-sheet. Baffin Bay was an ideal basin to study with this configuration because of its high spatial resolution ($12\,km$), its proximity to Greenland, and its distance from all the open boundaries. On the other hand, BLING was coupled to the ANHA4 configuration to have a larger area in which to evaluate BLING diagnostic variables without having the spurious influence of boundary conditions. The ANHA4 configuration, having boundaries far from the Labrador Sea, also allowed me to study Labrador Sea oxygen fluxes and its contribution to the subpolar gyre as part of the NSERC program VITALS that my Ph.D. project was part of. Additionally, the much higher surface resolution (e.g. ANHA4, 27 vertical levels describe the upper $240\,m$ of the ocean) is an advantage for simulating phytoplankton growth, most of which occurs in the upper ocean.

## 2.6 Model experiments

Table 2.8, lists the configuration, the atmospheric forcing, the parameter tested and the chapter in which more details of the experiments are given.

The ANHA4 configuration was used to run a hindcast simulation along with multiple sensitivity experiments
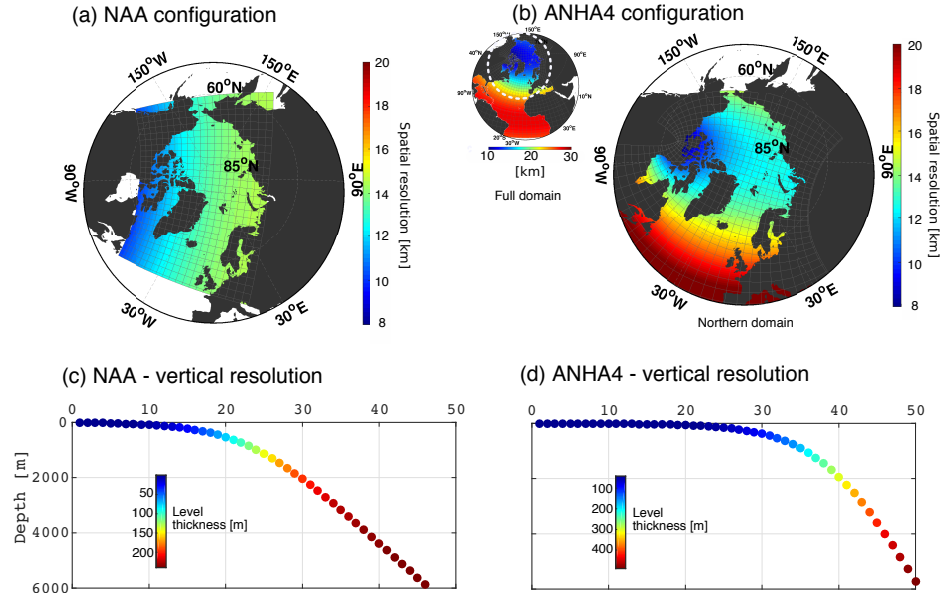
**Figure 2.8.** Model configurations used in this thesis. Spatial domain and resolution of (a) NAA and (b) ANHA4. Vertical levels and resolution in (c) NAA and (d) ANHA4. Note the differences in the vertical color scale between the two simulations. Map inset in (b) shows the full domain of ANHA4, but note that the colour scale is different.

**Table 2.8.** List of simulations used in this thesis

| Exp.name (code) | Config. | Atm. forcing | Parameter changed | Chapter |
|---|---|---|---|---|
| CONTROL - Long hindcast (ENG3) | ANHA4 | COREv2 | none | 3 & 4 |
| CONTROL - Present day (ENG4) | ANHA4 | CMC-GDPS | none | 3 & 4 |
| NAO-+ (ELC001) | ANHA4 | COREv2 | NAO forcing | 3 |
| NAO+- (ELC002) | ANHA4 | COREv2 | NAO forcing | 3 |
| CALM (ELC004) | ANHA4 | CMC-GDPS -filtered | high frequency winds | 4 |
| Greenland Ice Sheet melt (x10) | NAA | COREv2 | Ice Sheet liquid runoff | 5 |

with BLING. The ANHA4-BLING control and experiments simulation help test the performance of BLING in NEMO and to identify the limitations (Table 2.8).

The ten experiments run with the NAA configuration were done by Dr. Xianmin Hu (X.Hu) and are described in detail in his Ph.D. dissertation (Xianmin, 2012). He used the NAA experiments to understand the influence of Greenland Ice Sheet melt on the Arctic freshwater fluxes to the Atlantic Ocean through the Canadian Arctic Archipelago and Fram Strait. I used his experiments during my thesis with the goal of understanding how a melting Greenland Ice Sheet affected the hydrographic properties and circulation within Baffin Bay. To strengthen the implications of my results, I collaborated with X.Hu to include part of his work on the CAA and Fram Strait freshwater fluxes. The results of this collaboration is included within Chapter 5.

# Bibliography

Aksnes, D. L. and Wassmann, P. (1993). Modeling the significance of zooplankton grazing for export production. *Limnology and Oceanography*, 38(5):978–985.

Amante, C. and Eakins, B. W. (2009). ETOPO1 1 Arc-minute global relief model: procedures, data sources and analysis. *NOAA Technical Memorandum NESDIS NGDC-24*, 19.

Aumont, O. and Bopp, L. (2006). Globalizing results from ocean in situ iron fertilization studies. *Global Biogeochemical Cycles*, 20(2).

Aumont, O., Ethé, C., Tagliabue, A., Bopp, L., and Gehlen, M. (2015). PISCES-v2: an ocean biogeochemical model for carbon and ecosystem studies. *Geoscientific Model Development*, 8(8):2465–2513.

Bamber, J., den Broeke, M., Ettema, J., Lenaerts, J., and Rignot, E. (2012). Recent large increases in freshwater fluxes from Greenland into the North Atlantic. *Geophysical Research Letters*, 39(19).

Boyd, P. and Stevens, C. (2002). Modelling particle transformations and the downward organic carbon flux in the NE Atlantic Ocean. *Progress in Oceanography*, 52(1):1–29.

Dai, A., Qian, T., T., T. K., and D., M. J. (2009). Changes in continental freshwater discharge from 1948-2004. *Journal of Climate*, 22:2773–2791.

Dunne, J. P., Armstrong, R. A., Gnanadesikan, A., and Sarmiento, J. L. (2005). Empirical and mechanistic models for the particle export ratio. *Global Biogeochemical Cycles*, 19(4).

Evans, G. T. and Parslow, J. S. (1985). A Model of Annual Plankton Cycles. *Biological Oceanography*, 3(3):327–347.

Fichefet, T. and Maqueda, M. A. M. (1997). Sensitivity of a global sea ice model to the treatment of ice thermodynamics and dynamics. *Journal of Geophysical Research*, 102(C6):12609–12646.

Fofonoff, N.P. Millard, R. (1983). Algorithms for computation of fundamental properties of seawater. In *UNESCO technical papers in marine science*, volume 44, page 53. UNESCO, PARIS.

Galbraith, E. D., Gnanadesikan, A., Dunne, J. P., and Hiscock, M. R. (2010). Regional impacts of iron-light colimitation in a global biogeochemical model. *Biogeosciences*, 7(3):1043–1064.

Ginoux, P., Chin, M., Tegen, I., Prospero, J. M., Holben, B., Dubovik, O., and Lin, S.-J. (2001). Sources and distributions of dust aerosols simulated with the GOCART model. *Journal of Geophysical Research: Atmospheres*, 106(D17):20255–20273.

Gruber, N., Gloor, M., Fan, S.-M., and Sarmiento, J. L. (2001). Air-sea flux of oxygen estimated from bulk data: Implications For the marine and atmospheric oxygen cycles. *Global Biogeochemical Cycles*, 15(4):783–803.

Hibler, W. D. (1979). A dynamic thermodynamic sea ice model. *Journal of Physical Oceanography*, 9:815–846.

Hunke, E. C. and Dukowicz, J. K. (1997). An elastic-viscous-plastic model for sea ice dynamics. *Journal of Physical Oceanography*, 27(9):1849–1867.

James, I. (1996). Advection schemes for shelf sea models. *Journal of Marine Systems*, 8(3):237 – 254. Joint Numerical Sea Modelling.

Keeling, R. F., Stephens, B. B., Najjar, R. G., Doney, S. C., Archer, D., and Heimann, M. (1998). Seasonal variations in the atmospheric $O_2/N_2$ ratio in relation to the kinetics of air-sea gas exchange. *Global Biogeochemical Cycles*, 12(1):141–163.

Large, W. G. and Yeager, S. G. (2004). Diurnal to decadal global forcing for ocean and sea-ice models: the datasets and flux climatologies. NCAR Technical Note TN–460+ STR. *National Center for Atmospheric Research*.

Lemieux, J.-F., Tremblay, L. B., Dupont, F., Plante, M., Smith, G. C., and Dumont, D. (2015). A basal stress parameterization for modeling landfast ice. *Journal of Geophysical Research: Oceans*, 120(4):3157–3173.

Lévy, M., Estublier, A., and Madec, G. (2001). Choice of an advection scheme for biogeochemical models. *Geophysical Research Letters*, 28(19):3725–3728.

Light, B., Grenfell, T. C., and Perovich, D. K. (2008). Transmission and absorption of solar radiation by arctic sea ice during the melt season. *Journal of Geophysical Research: Oceans*, 113(C3).

Madec, G., Delecluse, P., Imbard, M., and Lévy, C. (1998). *OPA 8.1 ocean general circulation model reference manual*. Note du Pôle de modélisation, Institut Pierre-Simon Laplace (IPSL), France, No 11, 91pp.

Madec, G. and the NEMO team (2008). *NEMO ocean engine*. Note du Pôle de modélisation, Institut Pierre-Simon Laplace (IPSL), France, No 27, ISSN No 1288-1619.

Shchepetkin, A. F. and McWilliams, J. C. (1998). Quasi-monotone advection schemes based on explicit locally adaptive dissipation. *Monthly Weather Review*, 126(6):1541–1580.

Shine, K. P. and HendersonSellers, A. (1985). The sensitivity of a thermodynamic sea ice model to changes in surface albedo parameterization. *Journal of Geophysical Research: Atmospheres*, 90(D1):2243–2250.

Xianmin, H. (2012). *Simulation of Freshwater Associated with the Canadian Arcitc Archipelago*. PhD thesis, University of Alberta, Canada.

# Chapter 3

# Labrador Sea oxygen budget: a new perspective on the role of advective $O_2$ fluxes and the North Atlantic Oscillation using the NEMO-BLING model

Laura Castro de la Guardia, Mariona Claret, Xianmin Hu, Kumiko Azetsu-Scott, E. D. Galbraith, P. G. Myers

## 3.1 Abstract

Winter deep ocean ventilation in the Labrador Sea maintains the high oxygen levels at depth throughout the North Atlantic. This favours aerobic respiration and nitrification, essential processes in a healthy ocean. The Labrador Sea ventilation, however, is vulnerable to climate change accompanied by changing atmospheric conditions such as the North Atlantic Oscillation (NAO). During NAO+, the cold and windy conditions, which are positively correlated to stronger air-sea oxygen fluxes, has been linked to higher oxygen content in the Labrador Sea, while the opposite is true during NAO-. While air-sea oxygen fluxes are thought to be the principal source of oxygen into the Labrador Sea, little research has been conducted to quantify lateral sources from neighbouring regions, such as the Irminger Sea or Arctic Ocean. In this study we question the relative

role of air-sea and lateral advective oxygen fluxes to the Labrador Sea oxygen inventory and export using an ocean - sea ice - biogeochemical model hindcast (1958 - 2016). We also carry out NAO sensitivity experiments. We find that while deeper convection, favoured during NAO+ years, is critical to the ventilation of Labrador Sea, the air-sea fluxes do not dominate the ventilation process. Our simulations suggest that lateral fluxes play a significant role in oxygenating the surface waters of the Labrador Sea and that during deep convection this oxygen is transferred from the surface to greater depth. This shallow to mid-depth (above $1556\,m$) lateral advection contributes 75% of the deep Labrador Sea oxygen export, while air-sea fluxes contribute only 25%. These results highlight the importance of colder Arctic waters export to the North Atlantic and convection in the Irminger Sea as potential sources of oxygen to the Labrador Sea.

## 3.2  Introduction

The Labrador Sea is one of the most important regions in the World's Oceans where strong winter cooling and wind forcing causes open-ocean deep convection, a vertical mixing process that can produce a mixed layer depth (MLD) exceeding $1000\,m$. The vigorous mixing during convection brings surface waters in contact with deep waters causing an overall cooling and de-salinification within the Labrador Sea that increases the solubility of oxygen (*Keeling and Garcia*, 2002; Yashayaev, 2007; van Aken et al., 2011). Subsurface waters are also typically oxygen under-saturated, due to accumulated net respiration, which further pre-conditions the waters for high gas uptake. The winter convective process in the Labrador Sea, thus, combines oxygen under-saturated waters with higher solubility and strong wind forcing, to drive characteristically high winter air-sea oxygen uptake that is thought to ventilate the subsurface waters in the Labrador Sea (*Körtzinger et al.*, 2008; Rhein et al., 2017; Koelling et al., 2017).

After winter convection, the summer stratification traps the highly oxygenated waters below the surface. These waters are then advected at depth to the eastern Subpolar Gyre and the subtropical North Atlantic in the Labrador Current and the Deep Western Boundary Current (van Aken et al., 2011; Rhein et al., 2015, 2017). The ventilation of deep waters is an important mechanism that regulates biological processes such as aerobic respiration. The North Atlantic Deep Water is the most important oxygen source to the global deep ocean. Thus the variability and intensity of ventilation in the Labrador Sea is of relevance to the well-being of marine ecosystems throughout the world's ocean.

The North Atlantic Oscillation (NAO) index represents two modes of variability in the atmospheric circulation over the North Atlantic: NAO+ and NAO-. This index is a measure of the magnitude and phase of the NAO oscillation. During NAO+ there are higher sensible heat fluxes (e.g. stronger cooling) and stronger winds over the Labrador Sea (Sathiyamoorthy and Moore, 2002; van Aken et al., 2011). Therefore, under NAO+

conditions the Labrador Sea tends to experience large heat losses that lead to deeper convection (Dickson et al., 1996; Sathiyamoorthy and Moore, 2002; van Aken et al., 2011; Yashayaev and Loder, 2017). The direct links between the NAO+ and high oxygen uptake are still unknown, however it has been proposed that the primary cause of the observed high oxygen content during NAO+ years is the higher air-sea oxygen fluxes caused by the intense mixing and strong winds (Koelling et al., 2017).

Convection depth is dictated by the freshwater content of the surface ocean (above $1000\,m$) and the local atmospheric forcing, namely winter cooling and strong winds, whose intensity is influenced by the NAO (e.g. Dickson et al., 1988; Belkin et al., 1998; Dickson et al., 1996; Sathiyamoorthy and Moore, 2002; Yashayaev and Loder, 2017). For example, when large inputs of relatively fresh Arctic Water arrive to the Labrador Sea during the Great Salinity Anomaly events deep convection is halted (Dickson et al., 1988; Belkin et al., 1998). Historical records have shown that years with strong winter cooling have more intense deep convection relative to years with weak winter cooling (Yashayaev, 2007; *Lozier et al.*, 2010; Rhein et al., 2017). This variability in the depth of convection has been identified as the primary driver of regional oxygen concentration at intermediate depth ($500 - 2000\,m$) in the Labrador Sea (van Aken et al., 2011). Previous research describes how years with strong convection result in high oxygen concentrations in the Labrador Sea while years with weak convection are marked by gradual de-oxygenation of the Labrador Sea subsurface waters (van Aken et al., 2011; Rhein et al., 2017).

While local air-sea oxygen fluxes are typically assumed to be the dominant flux of oxygen into the Labrador Sea subsurface water, lateral advective oxygen fluxes from neighbouring regions, such as the Irminger sea and/or the Arctic Ocean (Fig. 3.1), could also be important. In the Irminger Sea, ventilation may also occur through deep convection, although deep convection is commonly shallower than $1000\,m$ (de Jong et al., 2012; Fröb et al., 2016; de Jong and de Steur, 2016). These ventilated waters could potentially be advected into the Labrador Sea in the East/West Greenland Current system (Bacon et al., 2003). The Arctic Ocean, although covered by sea ice, could also be a potential oxygen source to the Labrador Sea because of the characteristically high oxygen solubility of Arctic Waters due to their low salinity and cold temperature. Arctic waters enter the Labrador Sea through Davis Strait in the Baffin Island - Labrador Current system, through Hudson Strait in the Hudson Strait outflow-Labrador Current system and through the southern Labrador Sea in the West-East Greenland Current system (Fig. 3.1). To date, however, there are no estimates/measurements of the lateral oxygen fluxes into the Labrador Sea, except for eddy flux estimations in (Howatt et al., 2018).

This study aims to present one of the first estimates of the lateral advective transport and its relative importance to the Labrador Sea oxygen content and export variability. We use a state of the art ocean- sea ice-biogeochemical model over the historical time period (1958 - 2016) to address the relative importance of advective versus local air-sea fluxes. We use two sensitivity experiments to determine how the NAO index influences

the oxygen fluxes.
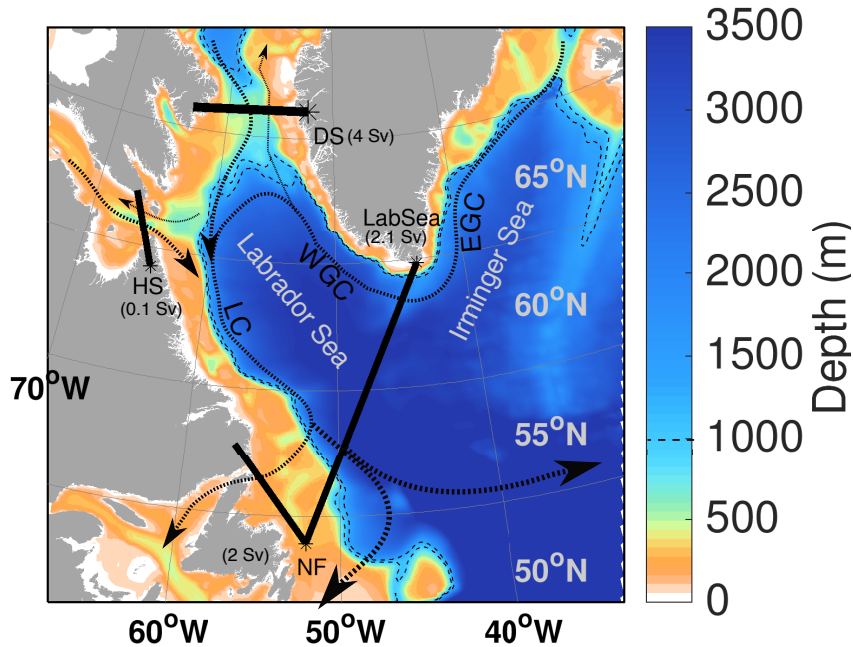


**Figure 3.1.** Western Subpolar Gyre bathymetry (background colour) and mean circulation in the Labrador Sea (dashed-lines with arrow). The Labrador Sea is defined as the region within the four sections (thick-solid lines): Davis Strait (DS), south Labrador Sea (LabSea), Hudson Strait (HS), Newfoundland (NF). The simulated mean volume transport across each section is included in brackets (1980-2009). The mean cyclonic circulation is dominated by the West Greenland Current (WCG) along Greenland and the Labrador Current (LC) along the Labrador coast, Canada. The WGC is a continuation of the East Greenland Current (EGC) coming from the Irminger Sea. The 1000 and 1565 $m$ isobath are delineated with thin dashed lines. The 1000 $m$ isobath separates the shelf and interior regions as discussed in Figure 3.4, and the surface of the 1565 $m$ isobath is used for calculating the deep oxygen inventory of Fig. 3.5, 3.6b, 3.12 and 3.13cd.

## 3.3 Method

### 3.3.1 Simulation details

Our simulations run using the marine biogeochemical model, Biogeochemistry with Light Iron and Nutrient limitation and Gases (BLING) version 0 (Galbraith et al., 2010) coupled to the ocean module Nucleus for European Modelling of the Ocean (NEMO) version 3.4 (Madec and the NEMO team, 2008) and the sea-ice model, Louvain la-neauve Ice Model (LIM) version 2 (*Vancoppenolle et al.*, 2009) with the elastic-viscous plastic (EVP) rheology (Fichefet and Maqueda, 1997). NEMO and LIM are coupled using a two-way communication, meanwhile BLING is coupled using one-way communication. This means that biologeochemical tracers are affected by sea ice and ocean processes, but they do not affect the physical state of the ocean or sea ice.

BLING has two phytoplankton classes, small and large, and four prognostic tracers: dissolved inorganic phosphate, dissolved oxygen, dissolved organic phosphate and dissolved iron. Oxygen is produced during photosynthesis and it is consumed during re-mineralization and recycling. Each phytoplankton class contributes different percentages to primary production, recycling and re-mineralization. BLING has a tendency for high production and carbon export in the North Atlantic but represents the observed spatial and seasonal patterns (Galbraith et al., 2010). This will cause higher oxygen at the surface and lower at subsurface depth where most of the re-mineralization occurs. A more complete description and evaluation of BLING can be found in Galbraith et al. (2010).

We chose BLING over more complex biogeochemical models coupled with the NEMO-LIM framework because of its low computational cost given the small number of prognostic tracers. In principle, this would permit us to run experiments over centuries and in future climate simulations using high spatial resolution at a relatively low additional computational cost. The present study, focusing on a relatively short simulation of five-ds and measuring the sensitivity of NEMO-BLING to atmospheric forcing, provides an opportunity to evaluate the NEMO-BLING model.

We ran four simulations: an extend hindcast simulation (1958-2009), a shorter present-day simulation (2002-2016) and two sensitivity experiments each $20yr$ in length. A summary of our simulations is given in Fig. 3.2. All the simulations ran on a regional configuration of the Arctic and the Northern Hemisphere Atlantic with horizontal resolution of $0.25°$ (ANHA4). This configuration has one open boundary near Bering Strait in the Pacific Ocean and a second one at $20°$S in the Atlantic Ocean. At the open boundaries there is an exchange of heat, momentum and tracers.
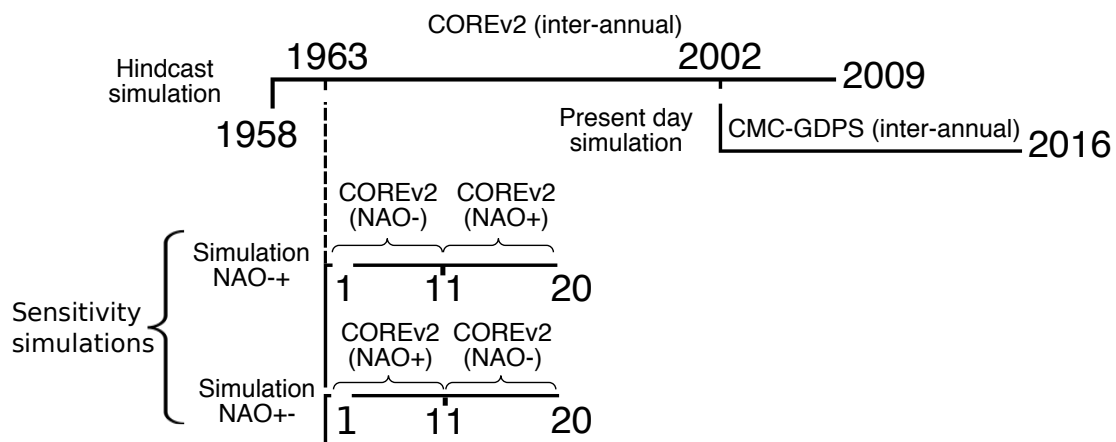


**Figure 3.2.** BLINGv0-NEMO3.4-LIM2 simulations used in this study. Showing start to end year. The abbreviation over each simulation indicated the atmospheric forcing used to run that part of the simulation period.

The hindcast simulation was initialized using climatological ocean temperature and salinity from the Polar

55

Science Center Hydrographic Climatology (PHC 3.0) (Steele et al., 2001), zero ocean velocities and a constant sea ice cover of $3\,m$ thickness in all grid-cells where the ocean temperature was colder than the freezing point of seawater: $-1.8°C$. The biological fields were initialized with a combination of observed climatologies and model fields. Initial fields of dissolved oxygen and phosphate concentration were derived from the World Ocean Atlas 2013 (WOA13) version 2 (*Garcia et al.*, 2014a,b). Initial fields for dissolved iron and organic phosphate were built by averaging the last 20-years of a 100-year global simulation using Geophysical Fluid Dynamics Laboratory-Earth System Model version 2 (GFDL-ESM2) coupled with BLING version 0 (*Galbraith et al.*, 2015). We forced the simulation with atmospheric data from Coordinated Ocean Research Experiment version 2 (COREv2) (Large and Yeager, 2009). COREv2 is a gridded re-analysis product with spatial resolution of $2.5°$. It includes monthly precipitation, daily short-wave and long-wave radiation, and four-hourly air temperature, humidity, and wind velocity at $10\,m$. Open boundary conditions for ocean temperature, salinity and velocities were derived from a global simulation of NEMO at $0.25°$ resolution ran by GEOMAR, Helmholtz Center for Ocean Research Kiel (simulation id: ORCA025-K3415; $http : //www.geomar.de/$).

The present day simulation was initialized using the fields from the hindcast simulation on the $31^{st}$ of December 2001 (Fig. 3.2). This simulation was forced with atmospheric data from the Canadian Meteorological Centers Global Deterministic Prediction System (CMC-GDPS) on a stereographic grid (*Smith et al.*, 2014). CMC-GDPS is derived from a reanalysis of a numerical weather prediction model and has a grid resolution of $30\,km$ at $60°N$. The data include hourly short-wave and long-wave radiation flux, precipitation, $10m$ wind speed and $2m$ air temperature and humidity (*Smith et al.*, 2014). Open boundary conditions were derived from the Global Ocean Reanalysis and Simulations version 3 (GLORYS2v3) (Masina et al., 2015). Open boundary conditions of monthly climatology for biological tracers: dissolved oxygen, dissolved phosphate, dissolved iron and dissolved organic phosphate were derived from the same GFDL-ESM2 simulation used to build the initial conditions.

Dust deposition is an external source of iron to the surface ocean which is implemented following a relationship between dust particle size and iron concentrations (Galbraith et al., 2010). A monthly dust deposition climatology was taken from the Global Ozone Chemistry Aerosol Radiation and Transport (GOCART) model (*Ginoux et al.*, 2001).

Inter-annual freshwater sources from land (i.g. river, glacier melt and land runoff) were added to the ocean surface layers near discharge areas as a salinity flux with temperature equal to the ambient seawater and using an enhanced mixing scheme to disperse the freshwater-signal over the top $10m$ of the water column. We use world river discharge and runoff data from Dai et al. (2009) and we updated Greenland's freshwater sources with glacier melt-water and tundra runoff from Bamber et al. (2012). The freshwater sources were carefully remapped onto ANHA4 grid to avoid losing part of this freshwater flux. Land sources of organic or inorganic

constituents were not added to the freshwater sources. All boundary and atmospheric forcing data were inter-polated on the fly to the model time step of 1080 seconds. After initializing, the simulations evolve without restoring.

**NAO sensitivity simulations**

We created two perpetual year forcing sets using the observed NAO winter index (December - March) from the normalized sea level pressure between Lisbon, Portugal and Stykkisholmur, Iceland. We defined a strong index as being above or below 1.5 standard deviations of the mean NAO index (1958-2009). Strong NAO+ index years were: 1989, 1990, 1992 and 1994. Strong NAO- index years were: 1958, 1960, 1963, 1965, 1968 and 1969. We created the perpetual year NAO+ forcing (NAO- forcing) for our sensitivity simulations by averaging COREv2 atmospheric forcing, runoff and boundary conditions of the above-mentioned strong NAO+ years (NAO- years). The resulting perpetual year forcing (Fig. 3.3) has the expected atmospheric conditions typical to an NAO+ or NAO- persisting from winter (DJF: December, January, February) to summer (JJA: June, July, August). The NAO+ atmospheric forcing captures the anomalously low atmospheric pressure, stronger westerly winds and cooler atmospheric temperatures in the Labrador Sea region relative to climatological conditions (left column in Fig. 3.3). Likewise, the NAO- atmospheric forcing captures the anomalously high atmospheric pressure, weaker westerly winds and warmer atmospheric temperatures in the Labrador Sea region relative to climatological conditions (right column in Fig. 3.3)

The two sensitivity simulations were run for 20 years. The first simulation, *NAO-+*, was forced for the first 10 years with NAO- forcing (e.g. year 1 to 10), and for the last 10 years the forcing was switched to NAO+ (e.g. year 11 to 20). The second simulation, *NAO+-*, was forced for the first 10 years with NAO+ forcing and for the last 10 years the forcing was switched to NAO-. With these two simulations we were able to isolate the role of the NAO index on the Labrador Sea oxygen budget and oxygen fluxes. Both simulations were initialized using ocean, sea ice and biogeochemical fields from the hindcast simulation on the $31^{st}$ of December 1962 (Fig. 3.2). We chose the end of 1962 as the starting conditions because deep oxygen concentrations in the Labrador Sea in the long hindcast simulation seemed to have stabilized by this year (e.g. see solid blue line in Fig. 3.5).

### 3.3.2 Simulated mixed layer depth

In this study, we use the simulated *actively mixing layer* depth (defined as the turbocline in NEMO) rather than the more commonly used simulated *mixed layer* depth. The turbocline is similar to the mixed layer depth, however NEMO derives the mixed layer depth using a density criterion (threshold $\Delta \rho = 0.001 \, kgm^{-3}$), whereas to derive the turbocline NEMO uses a turbulent mixing criterion that relies on the vertical physics alone (e.g.
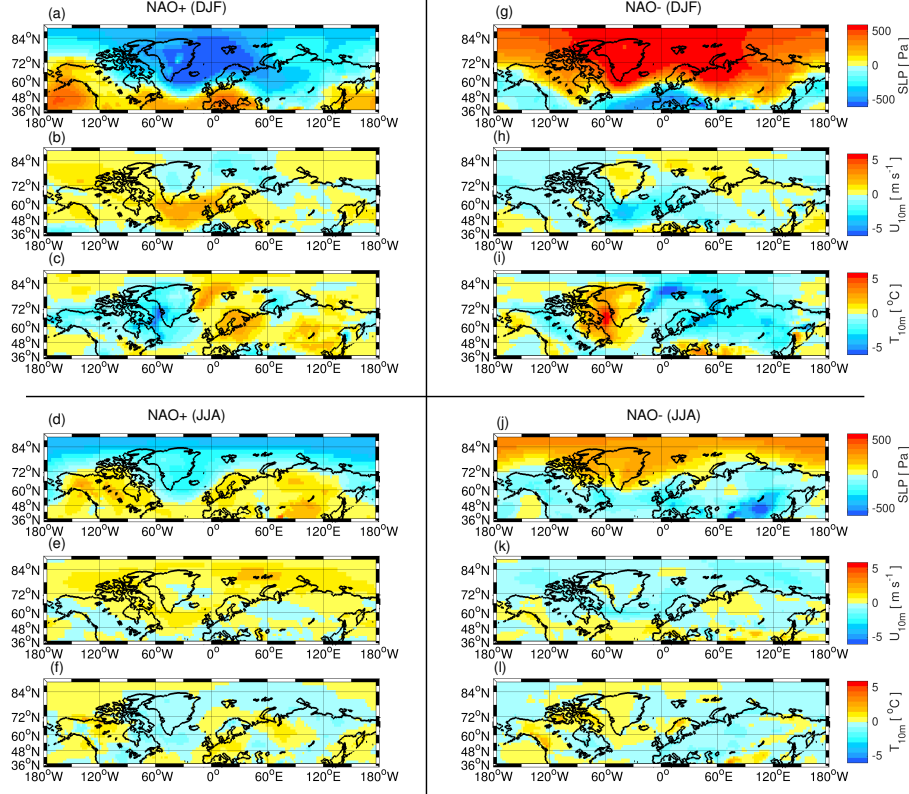
**Figure 3.3.** Anomaly of the winter (DJF) and summer (JJA) atmospheric conditions of our perpetual year NAO + forcing (left) and NAO - forcing (right) relative to the mean conditions between 1958 to 2009: sea level pressure (SLP), zonal wind at 10 meters ($U$10) and temperature at 10 meters ($T$10). A negative sign represents values that are lower in the perpetual year forcing relative to the mean.

using a threshold for the vertical eddy diffusivity coefficient of $> 5e^{-4} m^2 s^{-1}$). The present study uses the turbocline as the simulated MLD because the biogeochemical model, BLING is coupled with NEMO using turbocline, thus the variations of oxygen concentrations are ultimately linked to the variations in the depth of the turbocline.

### 3.3.3 Simulated oxygen budget

The inter-annual oxygen content in the Labrador Sea was calculated by spatially integrating the oxygen concentration ($[O_2]$; units $moles\,m^{-3}$) within the Labrador Sea region (defined in Fig. 3.1) between Davis Strait, Hudson Strait, and two arbitrary sections: the southern Labrador Sea and the Newfoundland sections. In eq. 3.1 the oxygen concentration is integrated over the regional volume, $V$, and averaged over one year ($y_i$; 01 Jan. - 31 Dec.) to obtain the mean oxygen content per year. The change in oxygen content (eq. 3.2; units $moles\,yr^{-1}$) is estimated by taking the time derivative of the oxygen content using a forward finite difference.

$$O_2^{y_i} content = \int_V [O_2]\, dV \tag{3.1}$$

$$\frac{dO_2 content}{dt} = \frac{O_2^{y_{i+1}} content - O_2^{y_i} content}{y_{i+1} - y_i} \tag{3.2}$$

The temporal changes in the oxygen content are defined by the temporal changes in oxygen sources and sinks. We consider three oxygen fluxes: biologically derived-fluxes ($F_{O_2}^{bio}$), air-sea fluxes ($F_{O_2}^{air-sea}$), and advective fluxes which include lateral ($F_{O_2}^{hori.adv}$) and vertical ($F_{O_2}^{vert.adv}$) fluxes. The effects of solubility due to changes in temperature and salinity (*Gruber et al.*, 2001) are considered at every model time-step and are thus included in the oxygen fluxes presented here. All fluxes are in *moles yr*$^{-1}$. Fluxes such as $F_{O_2}^{bio}$ and $F_{O_2}^{air-sea}$ are model outputs while advective fluxes are computed from the 5-day model output of velocity and oxygen concentrations.

The biological fluxes are calculated as in *Gruber et al.* (2001), by combining the processes taking place within the water column (first term on the RHS of eq. 3.3) and within the sediments (second term on the RHS of eq. 3.3). BLING derives the oxygen fluxes within the water column from the flux of phosphate, $F_{PO_4}$, using a stoichiometric ratio of oxygen to phosphate ($r_{O_2:PO_4}$) as in *Gruber et al.* (2001). However, we chose a value of $r_{O_2:PO_4} = -150$, based on revised estimates of mean alga elemental composition (*Anderson*, 1995). The negative sign of the $r_{O_2:PO_4}$ ratio indicates that there is an opposite relation between phosphate and oxygen fluxes. The flux of phosphate, $F_{PO_4}$, is represented in BLING by the *creation* of phosphate due to recycling and re-mineralization, and its *utilization* by phytoplankton. These fluxes were integrated over the Labrador Sea volume, $V$.

The oxygen sediment flux ($F_{O_2}^{sed}$) is derived from the re-mineralization of sinking particulate organic phosphate ($Remin_{POP}$) that reaches the sediment (eq.3.4). BLING assumes that all particulate organic phosphate reaching the ocean floor is instantaneously returned to the water column as inorganic phosphate, $PO_4$. We estimate the total contribution of this flux within the Labrador Sea by integrating over the sea-floor area, $A$.

$$F_{O_2}^{bio} = r_{O_2:PO_4} * \int_V F_{PO_4}\, dV + F_{O_2}^{sed} \tag{3.3}$$

$$F_{O_2}^{sed} = r_{O_2:PO_4} * \int_A Remin_{POP}\, dA \tag{3.4}$$

The air-sea oxygen fluxes ($F_{O_2}^{air-sea}$) are derived from the air-sea gas transfer velocity and the diffusive air-sea gas flux (eq. 3.5). We assumed that the atmosphere has a constant partial pressure of oxygen. Additionally gas transfer coefficient ($k_w$) is a quadratic function of the wind speed and has dependency on the Schmidt number,

which in turns, depend on ocean temperature (Keeling et al., 1998). To determine the total air-sea oxygen fluxes over the Labrador Sea we then integrated over the regional area, $A$.

$$F_{O_2}^{air-sea} = \int_A k_w * ([O_2]_{sat} - [O_2]_{surf}) \, dA \tag{3.5}$$

The horizontal advective oxygen fluxes ($F_{O_2}^{hori.adv}$) were calculated as the oxygen flowing across each of the four sections at the boundaries of our Labrador Sea region (Fig. 3.1). The flux was calculated at each section by multiplying the concentration of oxygen, $[O_2]$, by the velocities, $\mathbf{U}$, perpendicular to the section and integrating across the section area, $A$ (Eq.3.6).

$$F_{O_2}^{hori.adv} = \int_A \mathbf{U} * [O_2] \, dA \tag{3.6}$$

The vertical advective fluxes ($F_{O_2}^{vert.adv}$) were calculated by integrating the product of the oxygen concentration, $[O_2]$, and the vertical velocities, $\mathbf{W}$, across the surface area, $A$, of the $1565\,m$ isobath (Eq.3.7). This surface is convenient because it is a model level. This flux replaces $F_{O_2}^{air-sea}$ when considering the oxygen budget for the deep Labrador Sea.

$$F_{O_2}^{vert.adv} = \int_A \mathbf{W} * [O_2] \, dA \tag{3.7}$$

Note that because of practical limitations we did not save the diffusive coefficient at every model time-step ($1080s$). Therefore we cannot directly estimate diffusive fluxes ($F_{O_2}^{diff}$). The magnitude of these fluxes depend on the density instabilities that develop during each model time-step and which define the magnitude of the diffusive coefficient. Thus, estimating the diffusive flux from the saved diffusive coefficient (5-day-mean output or the mean of 480 model-time-steps) makes the calculations inaccurate. However, one can estimate the importance of diffusive fluxes from our budget calculations as the residual between the derivative of oxygen content and the sum of the fluxes ($F_{O_2}^{diff} = \frac{dO_2 content}{dt} - \sum F_{O_2}$). Our results suggest that diffusive fluxes play a very small role in the Labrador Sea since $\frac{dO_2 content}{dt} - \sum F_{O_2} \approx 0$ (e.g. difference between blue and orange lines in Fig. 3.5a,b). This suggests that the biological, air-sea and advective fluxes are sufficient to explain the time evolution of the annual mean oxygen content within the Labrador Sea in our simulation (Eq. 3.8).

$$\frac{dO_2 content}{dt} = \sum F_{O_2} = F_{O_2}^{bio} + F_{O_2}^{air-sea} + F_{O_2}^{hori.adv} + F_{O_2}^{vert.adv} \tag{3.8}$$

### 3.3.4   Definition of deep Labrador Sea

We define the deep Labrador Sea as the water body below $1500\,m$. This depth was chosen because only during years with strong ventilation (e.g. 1987-94, 2000, 2008 and 2015-16) does the formation of Labrador Sea Water exceed $1500\,m$, while in typical years the lower boundary of the Labrador Sea Water, an indication of ventilation, is usually above that depth (*Yashayaev and Loder*, 2009, 2016; Yashayaev and Loder, 2017). This makes our ventilation analysis of the deep Labrador Sea more convenient to identify only the most significant ventilation events during our hindcast. We adjusted this depth to below $1565\,m$ to line it up with our model vertical grid. This small modification facilitates the calculations of the vertical fluxes and increases their accuracy by avoiding averaging of the vertical velocities. Considering all water below $1565\,m$ means that in our budget calculations we include the oxygen brought into the Labrador Sea in the overflow waters (typically below $2500\,m$). However, the overflow waters flow in and out of the Labrador Sea through our southern Labrador Sea section (*Xu et al.*, 2015) and thus their influence is minor when considering the net advection of oxygen across this section.

### 3.3.5   Observed data

**Bottle data: temperature, salinity, oxygen**

*In situ* bottle data for temperature, salinity, and oxygen was collected on cruises led by the Ocean Science Division of the Bedford Institute of Ocean Sciences (BIO) from 1958 to 2009. This data can be obtained by submitting a request to BIO. Most stations were sampled only once per year between April and August, and many stations were not re-visited yearly. By combining all data we can estimate the mean temperature, salinity and oxygen conditions in the Labrador Sea between 1958 to 2009. We used the combined data to compare with a model climatology from April to August over the same period. We used the inter-annual bottle data over the deep Labrador Sea (converted to a 5-day means timeseries) to compare with the model inter-annual variability and timing of ventilation events.

**Mixed layer depth**

Observed daily MLD data from an Array of Real-time Geostrophic Oceanography (ARGO) were obtained from the Scripps Institution of Oceanography and the University of California, San Diego (*http* : //*mixedlayer.ucsd.edu*/). The MLD data was derived using the salinity and temperature profiles of the ARGO floats (*Holte et al.*, 2017). We spatially averaged the daily MLD profiles within the Labrador Sea considering only days with at least 5 floats within the region. We then built five-day temporal mean for the ARGO MLD to match the simulated MLD. The five-day temporal mean of ARGO MLD excluded outliers (daily values that were one standard deviation away from the five-day mean).

## 3.4 Results

### 3.4.1 Evaluation of simulated deep oxygen concentrations and MLD

Our hindcast simulation captured the basin-wide vertical structure of temperature, salinity and oxygen climatology in the Labrador Sea from observations (Fig. 3.4a-c). We additionally evaluated the model by subdividing the Labrador Sea into shelves and interior regions based on the $1000\,m$ isobath (map inset in Fig. 3.4a). We found that on the shelves (shallower than $1000\,m$) the simulation was slightly colder ($1^{\circ}C$), fresher (0.2) and more oxygenated ($39\,mmol\,m^{-3}$), and in the interior (below $1000\,m$), the simulations was warmer ($1.2^{\circ}C$), saltier (0.2) and also more oxygenated ($29\,mmol\,m^{-3}$), but these differences were not significant (Fig. 3.4d-f). Fresher, colder and highly oxygenated shelf waters could result from higher Arctic Water influx through Davis Strait. Indeed, our simulation's net volume transport at Davis Strait ($3.3 \pm 1.2Sv$) is 30% greater than the mooring estimates ($2.3 \pm 0.7Sv$), although it falls within the margin of model and mooring variability (*Curry et al.*, 2011). The positive sign of the transport indicates that the net flow enters the Labrador Sea.
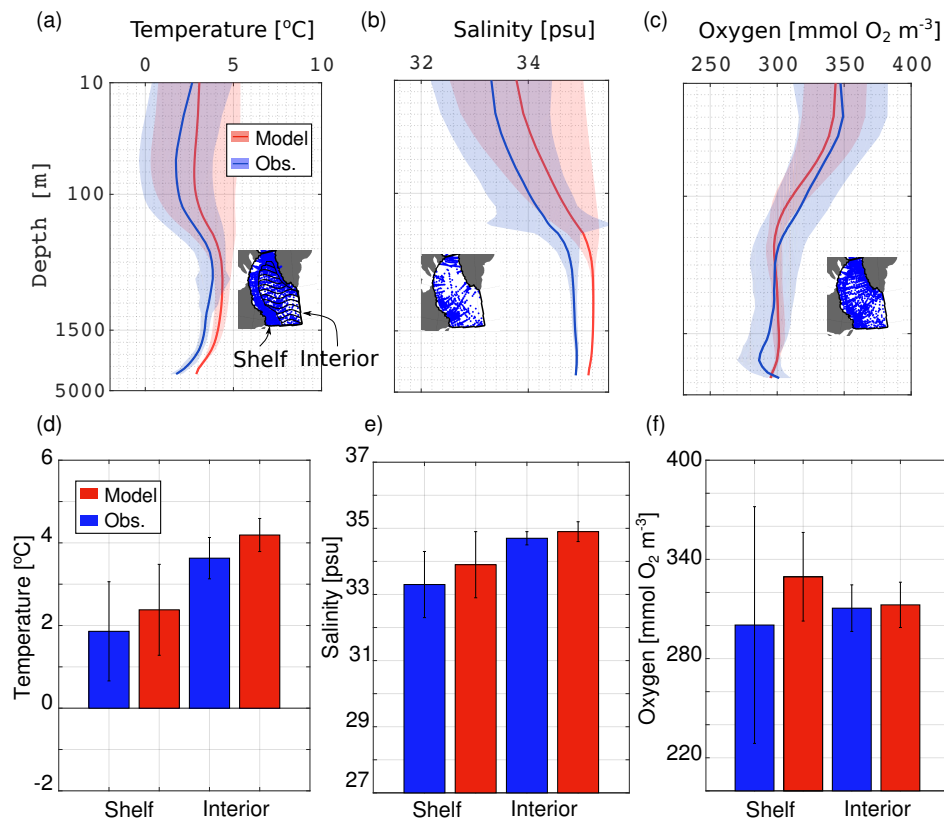


**Figure 3.4.** Evaluation of model fields (red) with observations (blue) of climatological values from April to May 1958 - 2009. Profile of (a) temperature, (b) salinity and (c) oxygen within the Labrador Sea (area with outlined in map inset). Mean shelf and interior (d) temperature, (e) salinity, and (f) oxygen. Map inserted show the location of the available bottle data (blue dots) for each variable. Hashed area of map inset of panel (a) delineates the shelves and interior regions. Bottle data in the Labrador Sea was provided by BIO, Canada.
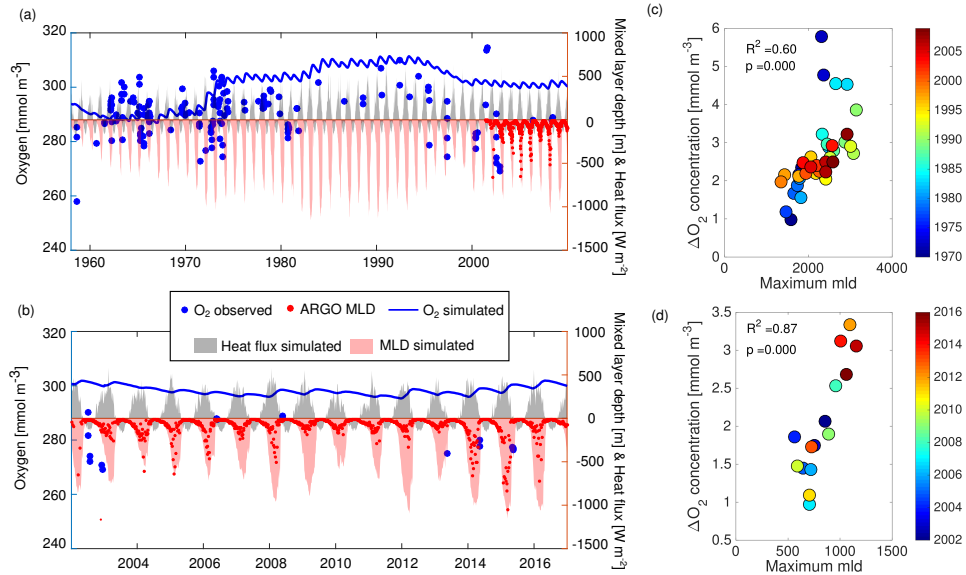
**Figure 3.5.** Drivers of deep oxygen concentration in the Labrador Sea. (a-b) Simulated evolution of deep oxygen concentration (blue solid line), mixed layer depth (MLD; red shade) and heat fluxes (grey shade) along with bottle oxygen data (blue dots) and ARGO mixed layer depth (red dots) over (a) historical simulation, and (b) present day simulation. (c-d) Correlations between the maximum change in deep oxygen concentration and mixed layer depth. Maximum change is measured as the difference between minimum before deep convection and maximum after deep convection. Deep oxygen concentration is calculated for all profiles below $1565\,m$.

In terms of temporal variability, the hindcast simulation reproduces the observed variability of the deep oxygen concentration between 1958 and 2009, with the best fit to the observed data between 1960-1970 (Fig. 3.5a). The 1960s was a period of minimum oxygen in the deep Labrador Sea. The end of this period coincides with the Great Salinity Anomaly (between 1968-1970) where large amounts of freshwater enter the Nordic Seas, Irminger Sea and the Labrador Sea halting open water deep convection, in all three basins (Dickson et al., 1988) and likely also halting the ventilation in these basins. The low oxygen regime ended with a ventilation event between 1972 and 1975 (blue line in Fig. 3.5a starts increasing), which in our simulation was marked by high surface ocean heat losses (grey shade in Fig. 3.5a) and deeper MLD (pink shade in Fig. 3.5a) in relation to previous years. Observed temperature profiles within the central Labrador Sea also indicate that this period could have experienced a ventilation event based on colder temperatures extending from the surface to $2000\,m$ deep which suggest that there was strong mixing at some point between 1973-1977 (*Yashayaev and Loder*, 2009). After 1975, our simulated oxygen concentration is about 10% (10 to $20\,mmol\,m^{-3}$) higher than the observations. This suggests that our simulation may have overestimated the intensity of the ventilation event or that our simulation could be underestimating re-mineralization and recycling which act as oxygen sinks.

Throughout the 1980s two additional strong ventilation events can be identified in the observed data. Suggested by the few data points, the first event may have occurred in 1983 and the second around 1989. These two ventilation events can be identified in Fig. 3.5 as a steep increase in the deep oxygen concentration between

1982 - 1984 and between 1985 - 1994. Our simulation captures these ventilation events with similar timing, although the magnitude increase of the second event is much less pronounced in the simulation. In our simulation these two events coincide with years of relatively deep winter MLD and larger winter heat losses. In the literature, this second ventilation event was also associated with convective mixing that reached the record depth of 2000$m$ (confirmed using temperature and salinity profiles) which led to the formation of a distinct class of Labrador Sea Water (*Yashayaev and Loder*, 2009).

From 1995 to early 2000, the deep Labrador Sea loses oxygen. This de-oxygenation event is easily identified in both the data and the simulation as a negative trend in the oxygen concentration (Fig. 3.5a,b). In the simulation the event coincides with years of unusually shallow convection (pink shade in Fig. 3.5a). Recent study shows a progressive warming of the waters above 1600$m$ in the central Labrador Sea since 1995 (*Yashayaev and Loder*, 2016). This suggests that the de-oxygenation event may be linked to a reduction of winter mixing.

In the more recent period 2002-2016, oxygen concentration increases slightly, following response to the deep convection events of 2008, 2014, 2015 and 2016 (Fig. 3.5b). Although we did not have access to sufficient oxygen bottle data to compare the simulated oxygen trend during this most recent d, data presented in the literature does suggest these deep convection years were accompanied by increasing oxygen concentration in the Labrador Sea (Rhein et al., 2017; *Yashayaev and Loder*, 2016; Yashayaev and Loder, 2017). The authors suggested that these ventilation events were associated with cooler atmospheric conditions in the Labrador Sea which induced stronger winter convection.

Comparing the simulated mean MLD in the Labrador Sea (red shade in Fig. 3.5a,b) with the ARGO-derived MLD between 2002 - 2016 (red dots in Fig. 3.5a,b) showed that the simulation captured the observed inter-annual changes and that it estimated reasonably well the mean MLD over the Labrador Sea region. In some years (e.g. 2009, 2013) the simulation appears largely to overestimate the depth of convection, however one should consider that ARGO-derived MLD could underestimate when ARGO floats distribution is biased towards the shelves and/or outside of the convection region, as is the case for 2009 and 2013.

In our simulation, the maximum MLD explains up to 60% ($p < 0.01$) of the inter-annual variability in deep oxygen concentration between 1970- 2009 (Fig. 3.5c) and up to 87% ($p < 0.01$) if we only consider the recent past 2002-2016. The strong positive relation between the MLD and oxygen concentrations in the Labrador Sea was also noted using biogeochemical ARGO floats (*K. et al.*). The weaker correlation over the historical time-period is associated with years 1973, 1974, 1983, 1984. These years coincide with strong ventilation events, which suggests that during these years processes not directly related to deep convection (e.g. lateral advection) contributed to the oxygenation of the deep Labrador Sea. An interesting coincidence is that these four years follow the 1972 and 1983 Labrador Sea maxima in the Great Salinity Anomaly of 1970s and 1980s, respectively (Dickson et al., 1988; Belkin et al., 1998). We thus suggest that one possibility is that intrusion of large amounts

of Arctic Water, with potentially high oxygen concentration due to its cold temperatures, may have contributed to the higher oxygenation of the Labrador Sea in the following years when convection was re-established.

### 3.4.2    Simulated oxygen inventory

**Oxygen fluxes**

We consider the evolution of the oxygen content over the full Labrador Sea basin (Fig. 3.6a) as well as the deep Labrador Sea alone (Fig. 3.6b). The temporal-mean basin-integrated oxygen content (black solid line with open circles in Fig. 3.6a,b) helps highlight the different Labrador Sea oxygen regimes and the relative importance of each flux transitioning from one oxygen regime to the next.

The year to year changes in the oxygen content (blue solid line in Fig. 3.6a) over the full basin are almost completely explained by the sum of the oxygen fluxes (orange solid line in Fig. 3.6a), air-sea exchanges (yellow dotted line in Fig. 3.6a), horizontal advective transport (green dotted line in Fig. 3.6a,b), and biological activity (purple dotted line in Fig. 3.6a,b). This similarity in the variability of the sum of all fluxes and the change in oxygen content indicates that these oxygen fluxes capture most of the variability in the oxygen content within the Labrador Sea.

However, considering only the deeper basin, the change in the oxygen content is not fully explained by the sum of the fluxes (e.g. gap between the orange and blue line between 1980-2000). This difference could be the result of not including the diffusive fluxes in our calculations, especially considering that the period where the gaps are larger coincide with periods of strong ventilation (e.g. 1973, 1980-1994). For the deep Labrador Sea, the sum of fluxes considers the vertical advection across $1565\,m$ depth (yellow dotted line in Fig. 3.6b), and the horizontal advection and biological fluxes below $1565\,m$.

There is an initial positive trend (1958-1963) in the simulated air-sea and lateral advective oxygen fluxes in the Labrador Sea which we assumed are related to the model adjustment from the initial conditions. In the deep Labrador Sea (below $1565\,m$; Fig. 3.6b), the trend in the vertical and advective fluxes lasts longer (from 1958 to 1980). It is possible that this deep trend is a combination of the model adjustment from the initial conditions and/or the deep ocean responding to the NAO index changing from negative to positive (grey shade in Fig. 3.6c). To avoid including noise from the spin-up period and this early change in the NAO forcing, we focus our discussion below on the oxygen budget between period 1980 - 2009 when all fluxes are relatively stable.

The inter-annual variability of the oxygen budget in the Labrador Sea ($10 \pm 2.7\,T\,mol\,O_2\,yr^{-1}$ ) is primarily driven by the changes in the air-sea and horizontal advective oxygen fluxes (yellow and green dashed lines, respectively, in Fig. 3.6a). The biological fluxes (purple dotted line in Fig. 3.6a) are small ($-0.5 \pm 0.2\,T\,mol\,O_2\,yr^{-1}$), and thus have a minor contribution to the total change in oxygen content. The negative sign
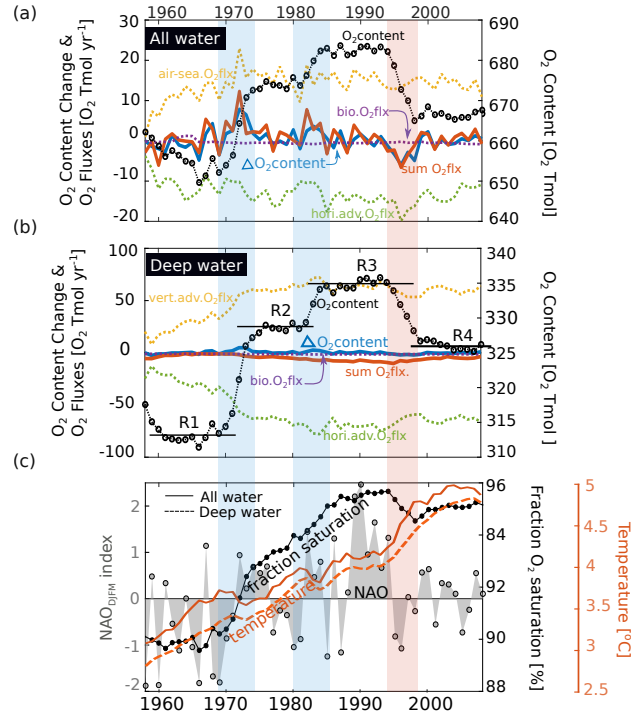
**Figure 3.6.** Labrador Sea oxygen budget from 1958 to 2009 considering (a) all water in the Labrador Sea and (b) only the deep Labrador Sea, volume below 1565 $m$. In (b) four periods of relatively stable oxygen content in all water and deep water are marked using R1, R2, R3, R4 segments. (c) Mean temperature (orange) and salinity (blue) changes considering all water (solid lines) and below 1565 $m$ (dashed lines) along with the NAO winter index (grey shade). Plotted on the right y-axis of *a* and *b* is the oxygen content (black dotted line with circles). Plotted on the left y-axis of *a* and *b* are the derivative of the oxygen content (thick blue line), the sum of fluxes (thick orange line), horizontal advective lateral flux (green dotted line), biological flux (purple dotted line), air-sea flux (yellow dotted line only in *a*) and vertical advective flux at 1565 $m$ (dotted blue line only in *b*.

of the biological fluxes indicates that annual re-mineralization is greater than annual production.

Between 1980 - 2009, the mean air-sea flux ($14.6 \pm 2.1\,Tmol\,O_2\,yr^{-1}$) balanced the net lateral advective flux ($-13.7 \pm 2.4\,Tmol\,O_2\,yr^{-1}$) considering all water. These estimates of the mean air-sea fluxes and net lateral advective oxygen flux are within $5\,Tmol$ of the North Atlantic climatology presented in *Gruber et al.* (2001). The negative sign in the advective fluxes in our simulation indicates that oxygen is exported out of the Labrador Sea.

The net advective flux is the sum of the oxygen advected across the four sections in Fig. 3.1. Oxygen enters the Labrador Sea through Hudson Strait ($1.0 \pm 0.1\,Tmol\,O_2\,yr^{-1}$) and Davis Strait ($38.3 \pm 2.5\,Tmol\,O_2\,yr^{-1}$). These two fluxes are restricted to the upper water column by a sill depth shallower than $1000\,m$. Oxygen is exported through the south Labrador Sea section ($-31.8 \pm 2.8 Tmol\,O_2\,yr^{-1}$) and the Newfoundland section ($-21.3 \pm 2.1 Tmol\,O_2\,yr^{-1}$). The shelf depth for the Newfoundland section is shallow (e.g. less than $500\,m$), while in the south Labrador Sea section the exchange can reach depths greater than $3000\,m$. Although the south Labrador Sea is the primary export route, oxygen also enters the Labrador Sea through this section at

depths shallower than $1565\,m$ (Fig. 3.7). The net surface to mid-depth transport (e.g. surface to $1565\,m$), is $35.5 \pm 3.8\,T\,mol\,O_2\,yr^{-1}$. Here, most of the oxygen influx occurs along the northern part of the section in the East-West Greenland Current system (Fig. 3.7). This current carries waters from the Irminger Sea and further north from the Nordic Seas and the Arctic Ocean, as the West Greenland Current is a continuation of the East Greenland Current with roots in Fram Strait.
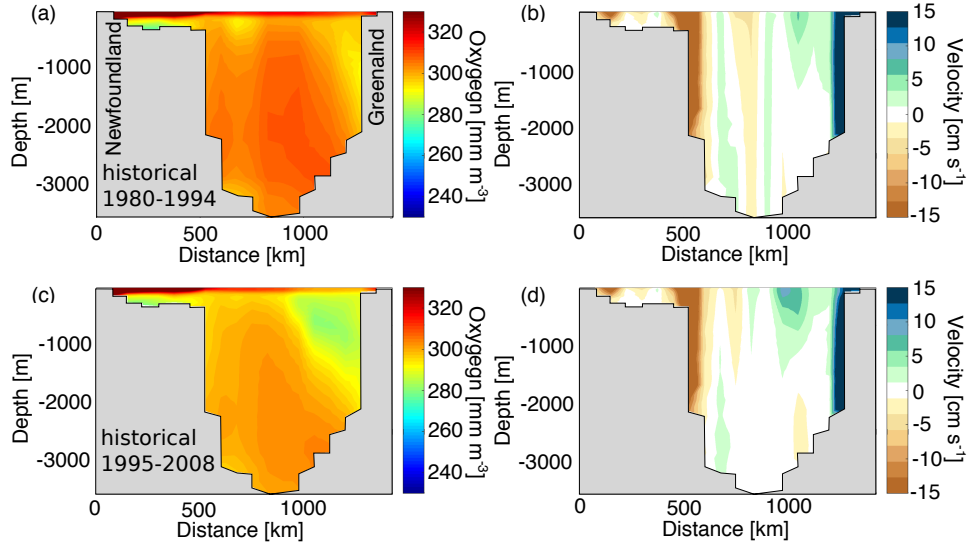


**Figure 3.7.** Oxygen concentration and velocities at the south Labrador Sea section (in Fig. 3.1 labelled as LabSea) during (a,b) the ventilation event of 1980-1994 and (c,d) the de-oxygenation event of 1995-2008. Changes from ventilation to de-oxygenation event manifest as reduction in the oxygen concentration entering the Labrador Sea on the West Greenland Current (a vs. c) corresponding with northward (positive) flow (in b an d).

When considering the deep Labrador Sea oxygen inventory the inter-annual variability in oxygen content is small ($0.2 \pm 1.5\,T\,mol\,O_2\,yr^{-1}$) (Fig. 3.6b). The major oxygen input is the vertically advected oxygen across the $1565\,m$ isobath surface ($62.0 \pm 4.8\,T\,mol\,O_2\,yr^{-1}$). This flux is balanced by the advective export through the deep parts of the south Labrador Sea section ($67.3 \pm 5.1\,T\,mol\,O_2\,yr^{-1}$). Biological fluxes are again a minor sink of oxygen ($-1.4 \pm 0.07\,T\,mol\,O_2\,yr^{-1}$). There is a high co-variability between the net vertical and advective fluxes of the same year ($r^2 = -0.99$; $p < 0.01$) indicating the role of the Labrador Sea as a source of oxygen to the deep Atlantic Ocean and Subpolar Gyre on a year to year basis.

**Oxygen regimes and transitions**

The mean oxygen content within the Labrador Sea from 1958 to 2009 was $669 \pm 10\,T\,mol\,O_2$, with approximately half ($325 \pm 8\,T\,mol\,O_2$) found in the deep Labrador Sea (black line with open circles Fig. 3.6a,b). During this period, the Labrador Sea had four stable oxygen regimes, two periods of relatively high oxygen content (R2 and R3 in Fig. 3.6b) and two periods of low oxygen content (R1 and R5 in Fig. 3.6a,b) that were separated by

sharp changes in the oxygen content. Most notably, there are two sharp ventilation events (blue shades in Fig. 3.6) and one de-oxygenation event (pink shade in Fig. 3.6). A change in the NAO from negative to positive led the ventilation events and a change in the NAO from positive to negative led the de-oxygenation event (grey area with filled circles in Fig. 3.6c). The NAO index explained 48% ($r = 0.69$; $p < 0.01$) of the variability in oxygen content of both, *the full* and *the deep* Labrador Sea.

The NAO index had a mild effect on the temperature of all Labrador Sea water (orange solid line in Fig. 3.6c) and the deep Labrador Sea water (orange dashed line in Fig. 3.6c). Although our simulation gains heat from 1960-2009, which suggest it had not fully adjusted, when the NAO shifts to positive the waters cooled (or the warming rate decreased) and when the NAO shifts to negative the waters warmed steeply. These NAO+ induced cooling events increased the deep Labrador Sea seawater oxygen solubility which allows more of the oxygen entering the Labrador Sea to be dissolved within Labrador Sea during NAO+ years. In response to increasing dissolved oxygen concentration, the fraction of oxygen saturation rises closer to its maximum value of 100% (black line with filled circles in Fig. 3.6c). The oxygen regimes, thus, are a balance between oxygen influx, sinks and the changes in solubility.

From 1960 to 1968, the Labrador Sea was in a period of minimum oxygen content ($649\,Tmol\,O_2$). The two ventilation events that followed, 1970 - 1973 and 1980- 1984 (blue shade in Fig. 3.6), were characterized by an increase in the oxygen content at rate of $4.1\,Tmol\,O_2\,yr^{-1}$. This transitioned the Labrador Sea towards its maximum oxygen content ($684\,Tmol\,O_2$). The ventilation events, not only coincided with a change in the NAO from predominantly negative to positive (grey shade in Fig. 3.6c) and ocean cooling (orange lines in Fig. 3.6c), but also with an increase in wind speed (linked to the NAO+ year) which augmented the air-sea fluxes (by $3.2\,Tmol,O_2\,yr^{-1}$) and a higher lateral influx of oxygen. The oxygen transport through Davis Strait increased by $2.6\,Tmol,O_2\,yr^{-1}$, and through the south Labrador Sea section above 1565 *m* it increased by $2.8\,Tmol\,O_2\,yr^{-1}$. This combination of larger oxygen influx and cool waters caused the Labrador Sea to take in more oxygen and the fraction of oxygen saturation to approach 100% (black solid line with filled circles in Fig. 3.6c).

Although our simulation captured the record mixing event between 1989 - 1994 (see the MLD in Fig. 3.5) when the NAO+ index was strongest (*Yashayaev and Loder*, 2009), the oxygen content did not increase as sharply as observed (van Aken et al., 2011). In our simulation, however, during this period the Labrador Sea did not cool down as much as during the previous ventilation events (orange lines in Fig. 3.6c), or as indicated by observational studies (*Yashayaev and Loder*, 2009; van Aken et al., 2011). The absence of a strong cooling event resulted in the minor increase oxygen concentration taken-in, as simulated Labrador Sea waters were already close to oxygen saturation (black solid line with filled circles in Fig. 3.6c). This emphasises the importance of solubility to oxygen inventory in the Labrador Sea (Koelling et al., 2017).

From 1995 to 1998 the NAO index shifted from positive to negative. This ended the high oxygen regime

and transitioned the Labrador Sea towards a new low oxygen regime (red shade in Fig. 3.6). This transition, a de-oxygenation event, was characterized by a sharp decrease in the atmospheric oxygen flux (yellow line in Fig 3.6a) and an increased rate of warming within the Labrador Sea (orange line in Fig. 3.6c). During this transition the oxygen content declined at a rate of $-3.2\,T\,mol\,O_2\,yr^{-1}$. The air-sea fluxes declined by $2.5\,T\,mol\,O_2\,yr^{-1}$, the lateral advected oxygen through Davis Strait declined by $5.4\,T\,mol\,O_2\,yr^{-1}$, and through the south Labrador Sea section above 1565 $m$ the flux declined by $5.8\,T\,mol\,O_2\,yr^{-1}$ (Figure 3.7). Observational studies suggest that this de-oxygenation event coincides with progressive warming within the central Labrador Sea caused by shallower MLD (van Aken et al., 2011; Rhein et al., 2017; *Yashayaev and Loder*, 2016). In our simulation the shoaling of deep convection (see the MLD in Fig. 3.5) causes a more pronounced rate of warming during this period (orange line in Fig. 3.6c).

The deep Labrador Sea experienced the same oxygen regime with similar timing in the oxygen content transitions as did the full basin (Fig. 3.6b). Dominant processes leading a positive (negative) transition of the deep Labrador Sea oxygen content were a cooling (warming) of the water (orange solid line in Fig. 3.6c) and an increase (decrease) in the vertical advected oxygen flux (yellow dotted line in Fig. 3.6b). The timing of the transitions also line up with the shifting of the NAO index, which suggests a strong connection between surface processes and deep ocean, in accordance with the dominant role of deep convection in the ventilation of deep Labrador Sea water, a relation that has been referred to as convective ventilation (van Aken et al., 2011).

**Lateral oxygen fluxes during ventilation and de-oxygenation**

During the high oxygen regimes (1980-1994), the Labrador Sea was a larger oxygen exporter across the south Labrador Sea section below 1565 $m$ (yellow bar in Fig. 3.8a). This was possible because of a larger vertical influx through the 1565 $m$ model surface (brown bar in Fig. 3.8a). Our simulation suggests that 75% of the change in the vertical oxygen fluxes is due to a larger advective inflow above 1565 $m$ through Davis Strait (blue bar in Fig. 3.8a) and the southern Labrador Sea sections (orange bar in Fig. 3.8a), and that only 25% is due to larger air-sea oxygen fluxes (green bar in Fig. 3.8a).

Comparing the lateral oxygen fluxes between high and low oxygen regimes reveal contrasting mechanisms contributing to the decrease in lateral advection through the southern Labrador Sea section and through the Davis Strait section. At the Labrador Sea section, the transport of oxygen in the upper 1565 of the water column decreases during the de-oxygenation period due to a decrease in the oxygen concentration transported in the West Greenland current (Fig. 3.7a,c) despite an increase of $5\,cm\,s^{-1}$ in the velocity of the West Greenland current (Fig. 3.7b,d). Meanwhile at Davis Strait, there is no apparent change in oxygen concentration between the ventilation and the de-oxygenation periods (Fig. 3.9a,c), but there is a decline in the net volume transport into the Labrador Sea due to a weakening of the Baffin Island Current core (at distance 100 $km$ in Fig. 3.9b,d)
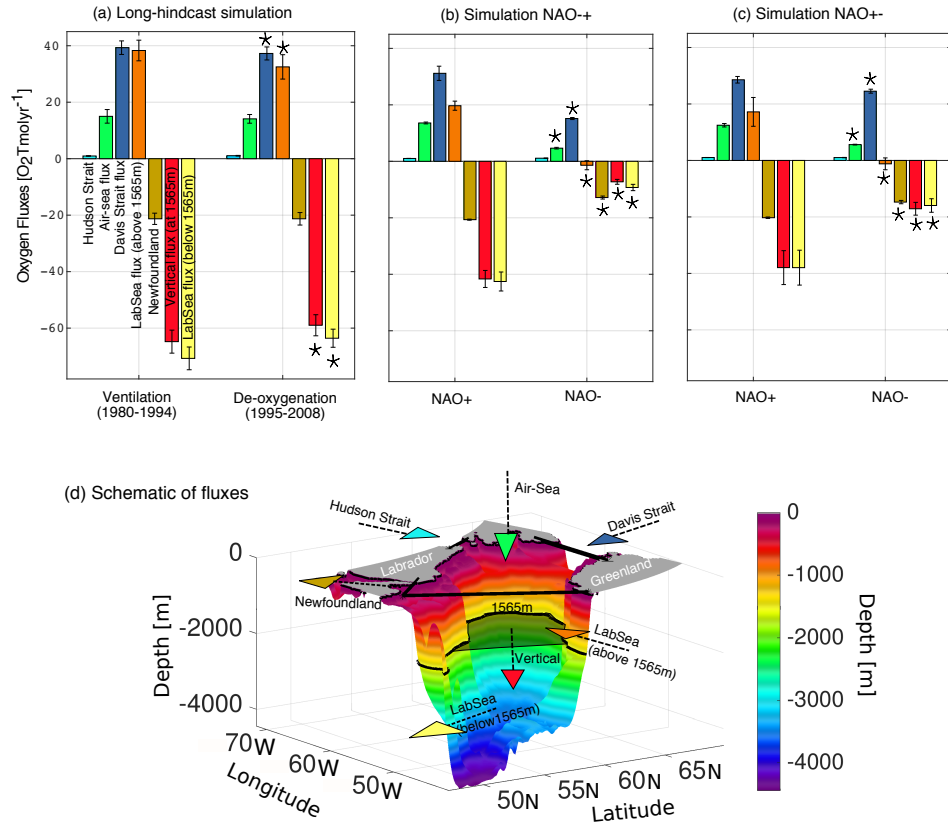
**Figure 3.8.** Comparing Labrador Sea oxygen fluxes in (a) the hindcast simulation during ventilation and de-oxygenation periods and in the (b) sensitivity simulation *NAO-+* and (c) simulation *NAO+-* during NAO+ and NAO- periods, and (d) 3D basin schematic with arrows head colours and direction matching barplot (a) colour and sing. Hudson Strait (bright blue), air-sea flux (green), Davis Strait flux (dark blue), south Labrador Sea section flux above $1565\,m$ (orange), Newfoundland (brown), vertical fluxes across the $1565\,m$ isobath (red), south Labrador Sea section flux below $1565\,m$ (yellow). Positive (negative) sign and indicates into (out) of the Labrador Sea with the exception of vertical flux, which negative indicates moving oxygen from surface to subsurface waters. Stars above bars indicate the fluxes that were significantly different ($p < 0.05$) between periods.

which brings the oxygen into the Labrador Sea. Mooring current velocities at Davis Strait between 2004-2005 show the two core structure as in Fig. 3.9d with the southward flowing core, the Baffin Island current, extending over most of the strait in the upper $100\,m$ of the water column with velocities $\geq -15\,cm$, and northward flowing core, the West Greenland Current, confined to the west Greenland shelf break (*Curry et al.*, 2011).

### 3.4.3 Sensitivity to the NAO phase

In the hindcast simulation a shift in the NAO index from strong negative to positive between $1968 - 1971$, led to a net gain in oxygen content within the Labrador Sea of $18\,Tmol\,O_2$, and when the NAO index shifted from strong positive to negative between $1994 - 1999$ there was a net oxygen content loss of $17\,Tmol\,O_2$. We isolated the role of the NAO pattern by re-creating these transitions using two idealized modelling experiments (Fig.
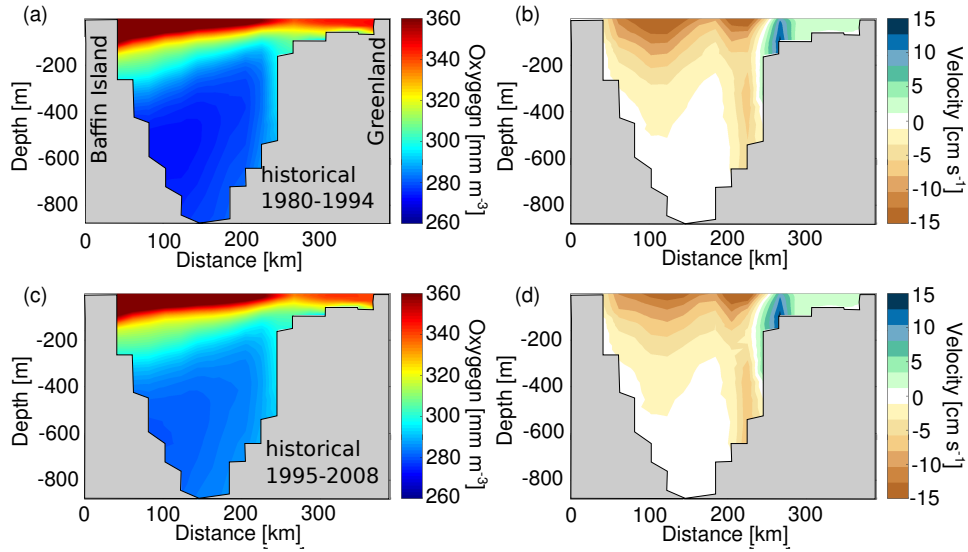
**Figure 3.9.** Oxygen concentration (a,c) and velocities (b,d at Davis Strait (in Fig. 3.1 labelled as DS) during the ventilation event of 1980-1994 (a,b) and the de-oxygenation event of 1995-2008 (c,d). Changes from ventilation to de-oxygenation event manifest as weakening in the flow entering the Labrador Sea (southward (negative) velocities in b and d). The simulated velocity fields (in b and d) and current cores matched well the mooring observations (*Curry et al.*, 2011)

3.2). The simulation *NAO-+* aimed at isolating the influence of the NAO on the ventilation of the Labrador Sea and the simulation *NAO+-* aimed at isolating the de-oxygenation of Labrador Sea.

**Lateral oxygen fluxes**

In both sensitivity simulations, and considering only the last five years of NAO+ and NAO- periods, the NAO+ period was characterized by 3 times the air-sea oxygen fluxes (green bar in Fig. 3.8b,c), 1.25 times the oxygen influx through Davis Strait (blue bar in Fig. 3.8b,c) and 12 times the oxygen influx through the southern Labrador Sea section above $1565\,m$ (orange bar in Fig. 3.8b,c) relative to the NAO- period. During NAO+ there is an influx of oxygen in the southern Labrador Sea section above $1565\,m$ ($14.5 \pm 3.0\,Tmol\,O_2\,yr^{-1}$). Meanwhile, during NAO- the same southern Labrador Sea section above $1565\,m$ becomes an export of oxygen ($-1.2 \pm 1.0\,Tmol\,O_2\,yr^{-1}$).

Interestingly, these oxygen sources are confined to the upper ocean, yet the export occurs at depth, suggesting that the surface oxygen signal is transferred to the deeper ocean within the Labrador Sea. Indeed, during NAO+ relative to NAO-, the export of oxygen through the south Labrador Sea section below $1565\,m$ is quadrupled (yellow bar in Fig. 3.8b,c), following the increase in vertical advective flux (brown bar in Fig. 3.8b,c).

Similar to the hindcast simulation, the oxygen influx through Davis Strait increases due to a stronger western boundary current rather than a change in the current's oxygen concentration (Fig. 3.10). Meanwhile the oxygen flux entering above $1565\,m$ through the southern Labrador Sea changes due to an increase in oxygen
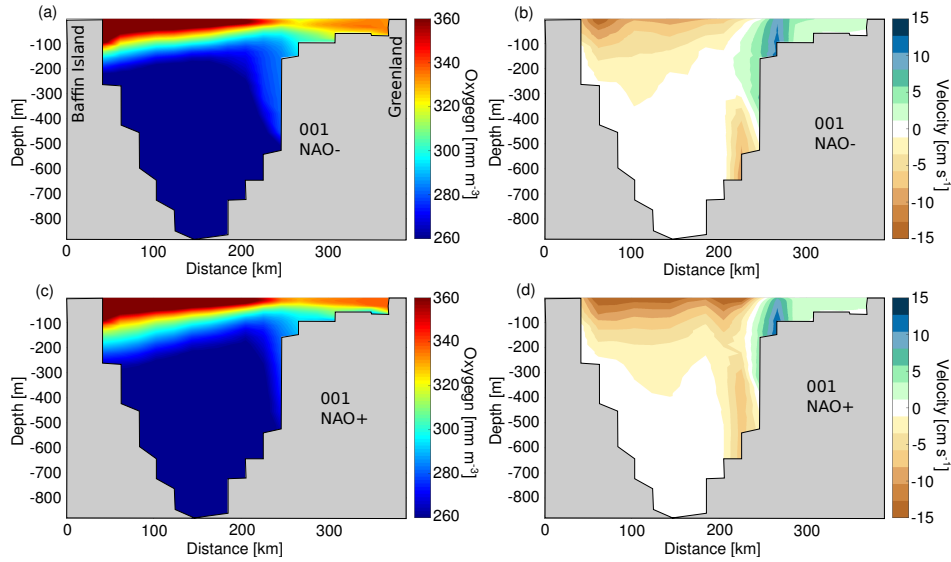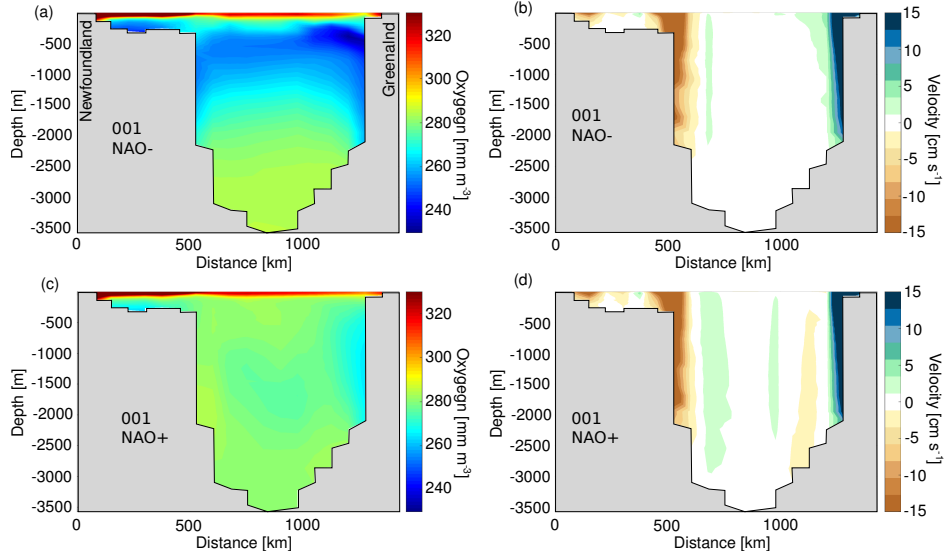
**Figure 3.10.** Mean oxygen concentration and velocities at Davis Strait section (in Fig. 3.1 labelled DS) during the NAO- and NAO+ years. Sections are made with the simulation *NAO-+*, but the same changes were present in simulation *NAO+-*.

concentration in the West Greenland Current. This suggests that convection in the Irminger Sea (or upstream in terms of sub-polar mode water formation) could be an important source of oxygen to the Labrador Sea during strong NAO+ years (Fig. 3.11). Previous studies have shown that during years of extreme cold winters during positive NAO (e.g. early 1990-1994, 2015-2016) deep convection in the Irminger Sea can ventilate the top $1400\,m$ of the water column (Våge et al., 2011; de Jong and de Steur, 2016). The observed convective events in the Irminger occurred relatively close to our south Labrador Sea section (east of the southern tip of Greenland) thus potentially transferring the oxygenated signal within the same year.

**Temperature, salinity and MLD**

In both sensitivity simulations the surface-ocean heat losses in winter were higher (grey shade in Fig. 3.12a,b) and the MLD was deeper (black shade in Fig. 3.12a,b) during the NAO+ than during NAO- period. These variables are responding to the atmospheric forcing. During the NAO+ the winter winds speed over the Labrador Sea was $8\,ms^{-1}$ greater than during NAO- (Figure 3.3b vs h) and the averaged winter temperature was at least $10°C$ colder than during NAO- (Figure 3.3c vs. i) .

In the two simulations during the NAO- the ocean loses less heat and the MLD is shallower than during the NAO+, clearly showing the dependence of deep convection and strong atmospheric forcing (Yashayaev, 2007; Rhein et al., 2017; *Lozier et al.*, 2010). Also interesting is the elapsed time by which the MLD responded to the changing atmospheric forcing. The response of the MLD when the forcing is switched to NAO- in the simulation *NAO+-* is almost immediate (e.g. within the first two years the MLD shoals). However, when the
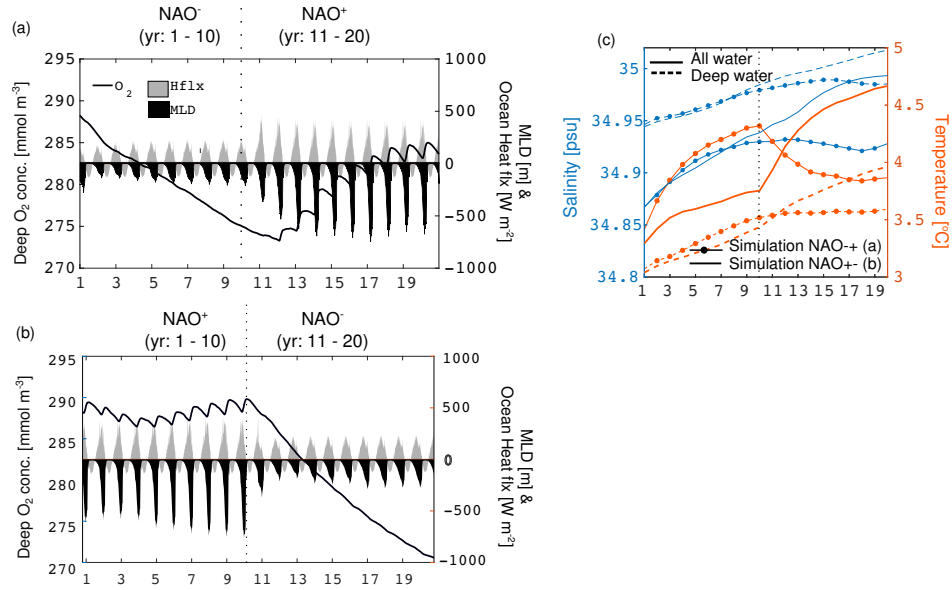
**Figure 3.11.** Mean oxygen concentration and velocities at the south Labrador Sea section (in Fig. 3.1 labelled LabSea) during the NAO- and NAO+ years. Sections are made with the simulation *NAO-+*, but the same changes were present in simulation *NAO+-*.

forcing is switched to NAO+, after 10 years of NAO- in simulation *NAO-+*, the MLD takes 4 years to reach values similar to those in the simulation *NAO+-* during NAO+. Yashayaev (2007) suggest that this lag is due to a convection memory of the waters to previous warm conditions causing a *thermal inertia*, and thus, several years of NAO+ forcing are required to finally erase the memory, as our simulation shows.

The deep ocean warming during NAO- ranged from $0.4°C d^{-1}$ in simulation *NAO-+* to $0.9°C d^{-1}$ in simulation *NAO+-* (orange dashed lines in Fig. 3.12c). The mean rate of de-oxygenation associated with the NAO-in both simulations was $1.5 mmol m^{-3} yr^{-1}$ (black line in Fig. 3.12a,b). When the forcing was NAO+, oxygen increased at $1.1 mmol m^{-3} yr^{-1}$ (black line in Fig. 3.12a) and the warming rate of deep waters was three times slower (Fig. 3.12c). In the simulation *NAO-+* the Labrador Sea deep waters also became saltier during the NAO- (blue lines with filled circles in Fig.3.12c), meanwhile in the simulation *NAO+-* there is a continuous salinity drift that becomes more pronounced on the second half of the simulation period when the forcing is switched to NAO - (blue lines without filled circles in Fig.3.12c).

At the end of the 20yr period, the final temperature and salinity of both simulations was much larger in simulation *NAO+-* than simulation *NAO-+* (blue and orange lines in Fig.3.12c). This contrasting response depended only in the order in which the NAO forcing was administered to each simulation and suggest that there is a numerical sensitivity to the initial atmospheric forcing conditions. Initiating the simulation with weak perpetual atmospheric forcing conditions, such as our perpetual year NAO-, helps alleviate the model drift within the Labrador Sea.

73

**Figure 3.12.** Sensitivity of the simulated Labrador Sea to the North Atlantic Oscillation (NAO). (a-b) Changes in ocean heat flux, mixed layer depth (MLD) and and deep ocean oxygen concentrations. (c) Changes in temperature and salinity for the full water column (solid lines) and deep ocean (datshed lines). Sensitivity simulation in (a) is forced from yr01 to yr10 with perpetual year negative NAO, and from yr10 to yr20 the forcing is switched to perpetual NAO+ year. Sensitivity simulation in (b) the forcing is inverted: from yr01 to yr10 we forced with perpetual NAO+ year, and from yr11 to yr20 we forced with perpetual NAO- year. The deep Labrador Sea is defined as waters below 1565 m. In this study, the MLD represents the mixing depth defined by the variable turbocline in NEMO.

## Oxygen content

Warmer waters during the NAO- reduced the solubility and thus the capacity of the Labrador Sea to hold oxygen. This combined with a decline in the oxygen sources entering the Labrador Sea (e.g. air-sea and advective oxygen fluxes) to cause a rapid de-oxygenation of the Labrador Sea over the *full* and *deep* Labrador Sea in both sensitivity simulations (Fig. 3.13).

The four panels of Fig.3.13 show the sharp difference between the two NAO phases (the left vs. right side of the vertical dotted line) in the oxygen content (black line with open circles), air-sea or vertical fluxes (yellow dashed line) and lateral fluxes (green dashed line). Meanwhile biological fluxes (purple line) are unaffected by the NAO phase in our simulations.

Considering the full water column in simulation *NAO-+*, the oxygen content and fluxes response follow immediately after the change in NAO forcing in year 11. For example, one can see the rapid increase in the oxygen content and air-sea fluxes from year 11 to year 12 (Fig. 3.13a). However for the deep Labrador Sea the two sensitivity simulations show different behaviour. When the change is from NAO- to NAO+ (Fig. 3.13b) the increase oxygen response of the oxygen content and fluxes lag one year behind the change in the NAO index (e.g. oxygen content and fluxes increase from year 11 to 12). When the change is from NAO+ to NAO- (Fig.
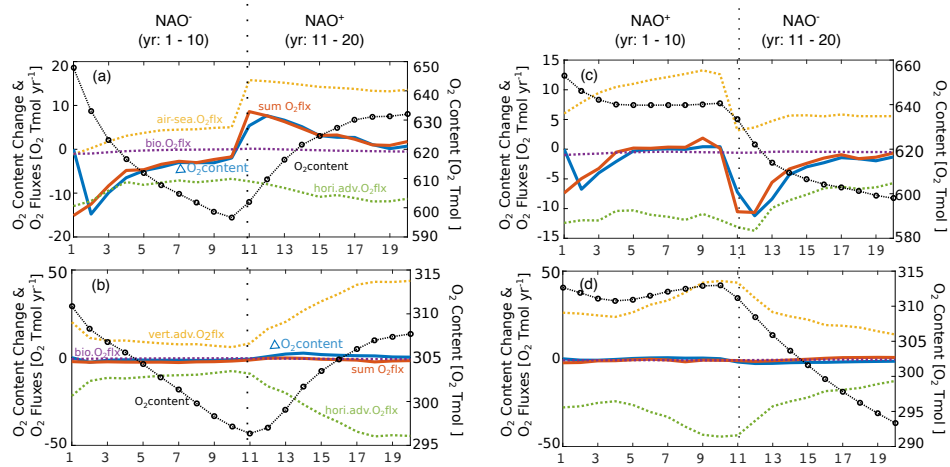
**Figure 3.13.** Simulated Labrador Sea oxygen content and fluxes in response to different phases of the North Atlantic Oscillation (NAO). In (a-b) the simulation starts with NAO negative forcing (yr01 to yr10), and ends with NAO positive forcing (from yr11 to yr20). In (c-d) the forcing is inverted: from yr01 to yr10 we forced with perpetual year NAO positive, and from yr11 to yr20 we forced with perpetual year NAO- negative. (a,c) Integrated (surface to bottom integrated) oxygen content and oxygen fluxes, (b,d) integrated oxygen content and fluxes considering only the deep Labrador Sea. The deep Labrador Sea is defined as waters below 1565 m. In panel (a) and (b) the MLD is the mixing layer depth defined as the turbocline in our simulation.

3.13d) the oxygen content decreases immediately, however the vertical input fluxes do not decline until after one year (yellow dotted line in Fig. 3.13d). The immediate decline in the oxygen content, even though the oxygen sources are still high, is caused by the change in solubility due to warming of deep waters induced by shallower mixed layer depth during the first year of NAO- (year 11 in Fig.3.12b). The declining vertical fluxes in the following year caused an acceleration in the de-oxygenation rate of deep waters in this simulation (Fig. 3.13d).

## 3.5 Discussion

Periodic winter ventilation of in the Labrador Sea is a process of significant importance to the deep ocean ecosystem through its role in the oxygenation of the deep layers of the North Atlantic (van Aken et al., 2011; Rhein et al., 2017, 2015). The strongest ventilation events recorded in the history of the Labrador Sea occurred during the winter 1990-1994 (*Yashayaev and Loder*, 2009; van Aken et al., 2011). This ventilation event was linked to high oxygen solubility and unusually deep MLD induced by cold surface temperatures and extreme heat loses attributed to the strong NAO+ index (Rhein et al., 2017; van Aken et al., 2011). In our modelling study, using hindcast and two NAO sensitivity simulation we were able to confirm the NAO+ is indeed linked to higher ventilation rates of the deep Labrador Sea and stronger deep convection whereas the NAO- is linked to de-oxygenation and shallower MLD.

However while most studies suggest that the principal oxygen source during the ventilation events is the larger air-sea flux and the water undersaturation (Koelling et al., 2017), our analysis suggest that a more significant source of oxygen are the lateral advective fluxes entering the Labrador Sea above $1565\,m$ from the west Greenland Current and the Baffin Island Current. We find that the lateral oxygen advected into the Labrador Sea constitute 75% of the net vertical flux entering the deep Labrador Sea (below $1565\,m$). Meanwhile air-sea fluxes constitute only 25% of the net vertical influx into the deep Labrador Sea waters. Thus lateral fluxes have a significant contribution to the oxygen exported out of the Labrador Sea below $1565\,m$. This quantification reveals for the first time that lateral advection of oxygen into the Labrador Sea may have a key role in the ventilation of the deep Labrador Sea and more importantly, in the oxygenation of the deep waters throughout the North Atlantic. A previous study alluded to the significance of other sources of oxygen co-existing with air-sea fluxes, when presenting climatological estimates of air-sea flux ($9.4\,TmolO_2$) in the North Atlantic that were half the net lateral export south of the Subpolar Gyre ($17.4\,TmolO_2$) (*Gruber et al.*, 2001).

Additionally, results from our NAO sensitivity simulation support the convection memory hypothesis which suggest that the Labrador Sea stratification builds-up during consecutive warm years due to a *thermal inertia* and thus it may take several cold winters to erode the built-up stratification (Yashayaev, 2007). We find that switching to the cold NAO+ forcing after 10 years of warm NAO- conditions requires two years of NAO+ forcing before convection deepened below $1000\,m$, and five years to erase the NAO- signal. Meanwhile when switching to NAO-, after 10 years of NAO+, the MLD shoals immediately, leading to warming and de-oxygenation of the deeper waters within the first year.

Our study agrees that the Labrador Sea as an important conduit for oxygen in surface waters to be brought down to great depth. Supporting previous findings our results suggest that this process is sensitive to NAO forcing, it is enhanced during NAO+ years and it is hampered during NAO- years. However, our simulations suggest that lateral oxygen advection into the Labrador Sea may be a more important oxygen source than air-sea fluxes. Therefore, to explain the net oxygen that ultimately sinks within the Labrador Sea and is then exported to the Subpolar Gyre at depth (below $1565\,m$), one must consider the lateral advected oxygen above $1565\,m$. This study brings attention to the importance of a monitoring line that can allow for a quantification of the oxygen fluxes entering the Labrador Sea above mid depth in the Baffin Island Current and the West Greenland Current in order to understand better the oxygen inventory in the Labrador Sea.

## 3.6  Acknowledgments

# Bibliography

Anderson, L. A. (1995), On the hydrogen and oxygen content of marine phytoplankton, *Deep Sea Research Part I: Oceanographic Research Papers*, *42*(9), 1675 – 1680, doi:https://doi.org/10.1016/0967-0637(95)00072-E.

Bacon, S., W. J. Gould, and Y. Jia (2003), Open-ocean convection in the Irminger Sea, *Geophysical Research Letters*, *30*(5), n/a–n/a, doi:10.1029/2002GL016271, 1246.

Bamber, J., M. den Broeke, J. Ettema, J. Lenaerts, and E. Rignot (2012), Recent large increases in freshwater fluxes from Greenland into the North Atlantic, *Geophysical Research Letters*, *39*(19), doi:10.1029/2012GL052552.

Belkin, I. M., S. Levitus, J. Antonov, and S. Malmberg (1998), "Great Salinity Anomalies" in the North Atlantic, *Progress in Oceanography*, *41*(1), 1–68, doi:10.1016/S0079.

Curry, B., C. M. Lee, and B. Petrie (2011), Volume, freshwater, and heat fluxes through Davis Strait, 2004–05, *Journal of Physical Oceanography*, *41*(3), 429–436, doi:10.1175/2010JPO4536.1.

Dai, A., T. Qian, T. K. T., and M. J. D. (2009), Changes in continental freshwater discharge from 1948-2004, *Journal of Climate*, *22*, 2773–2791.

de Jong, M. F., and L. de Steur (2016), Strong winter cooling over the Irminger Sea in winter 2014–2015, exceptional deep convection, and the emergence of anomalously low SST, *Geophysical Research Letters*, *43*(13), 7106–7113, doi:10.1002/2016GL069596.

de Jong, M. F., H. M. van Aken, K. Våge, and R. S. Pickart (2012), Convective mixing in the central Irminger Sea: 20022010, *Deep Sea Research Part I: Oceanographic Research Papers*, *63*, 36 – 51, doi:https://doi.org/10.1016/j.dsr.2012.01.003.

Dickson, R., J. Lazier, J. Meincke, P. Rhines, and J. Swift (1996), Long-term coordinated changes in the convective activity of the North Atlantic, *Progress in Oceanography*, *38*(3), 241 – 295, doi:https://doi.org/10.1016/S0079-6611(97)00002-5.

Dickson, R. R., J. Meincke, S. Malmberg, and A. J. Lee (1988), The "great salinity anomaly" in the Northern North Atlantic 1968-1982, *Progress in Oceanography*, *20*(2), 103–151, doi:10.1016/0079.

Fichefet, T., and M. A. M. Maqueda (1997), Sensitivity of a global sea ice model to the treatment of ice thermodynamics and dynamics, *Journal of Geophysical Research*, *102*(C6), 12,609–12,646, doi:10.1029/97JC00480.

Fröb, F., A. Olsen, K. Våge, G. W. K. Moore, I. Yashayaev, E. Jeansson, and B. Rajasakaren (2016), Irminger Sea deep convection injects oxygen and anthropogenic carbon to the ocean interior, *Nature Communications*, *7*, 13,244, doi:10.1038/ncomms13244.

Galbraith, E. D., A. Gnanadesikan, J. P. Dunne, and M. R. Hiscock (2010), Regional impacts of iron-light colimitation in a global biogeochemical model, *Biogeosciences*, *7*(3), 1043–1064, doi:10.5194/bg-7-1043-2010.

Galbraith, E. D., J. P. Dunne, A. Gnanadesikan, R. D. Slater, J. L. Sarmiento, C. O. Dufour, G. F. de Souza, D. Bianchi, M. Claret, K. B. Rodgers, and S. S. Marvasti (2015), Complex functionality with minimal computation: Promise and pitfalls of reduced-tracer ocean biogeochemistry models, *Journal of Advances in Modeling Earth Systems*, *7*(4), 2012–2028, doi:10.1002/2015MS000463.

Garcia, H. E., R. A. Locarnini, T. P. Boyer, J. I. Antonov, O. Baranova, M. Zweng, J. Reagan, and D. Johnson (2014a), World Ocean Atlas 2013: Dissolved Oxygen, Apparent Oxygen Utilization, and Oxygen Saturation, *S. Levitus, Ed., A. Mishonov Technical Ed., NOAA Atlas NESDIS*, *3*.

Garcia, H. E., R. A. Locarnini, T. P. Boyer, J. I. Antonov, O. Baranova, M. Zweng, J. Reagan, and D. Johnson (2014b), World Ocean Atlas 2013: Dissolved Inorganic Nutrients (phosphate, nitrate, silicate), *S. Levitus, Ed., A. Mishonov Technical Ed., NOAA Atlas NESDIS*, *4*.

Ginoux, P., M. Chin, I. Tegen, J. M. Prospero, B. Holben, O. Dubovik, and S.-J. Lin (2001), Sources and distributions of dust aerosols simulated with the GOCART model, *Journal of Geophysical Research: Atmospheres*, *106*(D17), 20,255–20,273, doi:10.1029/2000JD000053.

Gruber, N., M. Gloor, S.-M. Fan, and J. L. Sarmiento (2001), Air-sea flux of oxygen estimated from bulk data: Implications For the marine and atmospheric oxygen cycles, *Global Biogeochemical Cycles*, *15*(4), 783–803, doi:10.1029/2000GB001302.

Holte, J., L. D. Talley, J. Gilson, and D. Roemmich (2017), An Argo mixed layer climatology and database, *Geophysical Research Letters*, *44*(11), 5618–5626, doi:10.1002/2017GL073426, 2017GL073426.

Howatt, T., J. Palter, J. B. R. Matthews, B. deYoung, R. Bachmayer, and B. Claus (2018), Ekman and eddy exchange of freshwater and oxygen across the labrador shelf-break, *Journal of Physical Oceanography*, *0*(0), in press., doi:10.1175/JPO-D-17-0148.1.

Keeling, R. F., and H. E. Garcia (2002), The change in oceanic O2 inventory associated with recent global warming, *Proceedings of the National Academy of Sciences*, *99*(12), 7848–7853, doi:10.1073/pnas.122154899.

Keeling, R. F., B. B. Stephens, R. G. Najjar, S. C. Doney, D. Archer, and M. Heimann (1998), Seasonal variations in the atmospheric $O_2/N_2$ ratio in relation to the kinetics of air-sea gas exchange, *Global Biogeochemical Cycles*, *12*(1), 141–163, doi:10.1029/97GB02339.

Koelling, J., D. W. R. Wallace, U. Send, and J. Karstensen (2017), Intense oceanic uptake of oxygen during 2014–2015 winter convection in the Labrador Sea, *Geophysical Research Letters*, *44*(15), 7855–7864, doi: 10.1002/2017GL073933, 2017GL073933.

Körtzinger, A., U. Send, D. W. R. Wallace, J. Karstensen, and M. DeGrandpre (2008), Seasonal cycle of O2 and pCO2 in the central Labrador Sea: Atmospheric, biological, and physical implications, *Global Biogeochemical Cycles*, *22*(1), GB1014, doi:10.1029/2007GB003029.

Large, W. G., and S. G. Yeager (2009), The global climatology of an interannually varying air–sea flux data set, *Climate Dynamics*, *33*(2), 341–364, doi:10.1007/s00382-008-0441-3.

Lozier, M. S., V. Roussenov, M. C. Reed, and R. G. Williams (2010), Opposing decadal changes for the North Atlantic meridional overturning circulation, *Nature Geoscience*, *3*, 728, doi:10.1038/ngeo947.

Madec, G., and the NEMO team (2008), *NEMO ocean engine*, Note du Pôle de modélisation, Institut Pierre-Simon Laplace (IPSL), France, No 27, ISSN No 1288-1619.

Masina, S., A. Storto, N. Ferry, M. Valdivieso, K. Haines, M. Balmaseda, H. Zuo, M. Drevillon, and L. Parent (2015), An ensemble of eddy-permitting global ocean reanalyses from the MyOcean project, *Climate Dynamics*, pp. 1–29, doi:10.1007/s00382.

Rhein, M., D. Kieke, and R. Steinfeldt (2015), Advection of North Atlantic Deep Water from the Labrador Sea to the southern hemisphere, *Journal of Geophysical Research: Oceans*, *120*(4), 2471–2487, doi:10.1002/2014JC010605.

Rhein, M., R. Steinfeldt, D. Kieke, I. Stendardo, and I. Yashayaev (2017), Ventilation variability of Labrador Sea Water and its impact on oxygen and anthropogenic carbon: a review, *Philosophical Transactions of the Royal Society of London A: Mathematical, Physical and Engineering Sciences*, *375*(2102), doi:10.1098/rsta.2016.0321.

Sathiyamoorthy, S., and G. W. K. Moore (2002), Buoyancy Flux at Ocean Weather Station Bravo, *Journal of Physical Oceanography*, *32*(2), 458–474, doi:10.1175/1520-0485(2002)032⟨0458:BFAOWS⟩2.0.CO;2.

Smith, G. C., F. Roy, P. Mann, F. Dupont, B. Brasnett, J.-F. Lemieux, S. Laroche, and S. Bélair (2014), A new atmospheric dataset for forcing ice–ocean models: Evaluation of reforecasts using the Canadian global deterministic prediction system, *Quarterly Journal of the Royal Meteorological Society*, *140*(680), 881–894, doi:10.1002/qj.2194.

Steele, M., R. Morley, and W. Ermold (2001), PHC: A global ocean hydrography with a high-quality Arctic Ocean, *Journal of Climate*, *14*(9), 2079–2087.

van Aken, H. M., M. F. de Jong, and I. Yashayaev (2011), Decadal and multi-decadal variability of Labrador Sea Water in the north-western North Atlantic Ocean derived from tracer distributions: Heat budget, ventilation, and advection, *Deep Sea Research Part I: Oceanographic Research Papers*, *58*(5), 505 – 523, doi:https://doi.org/10.1016/j.dsr.2011.02.008.

Vancoppenolle, M., T. Fichefet, H. Goosse, S. Bouillon, G. Madec, and M. A. M. Maqueda (2009), Simulating the mass balance and salinity of Arctic and Antarctic sea ice. 1. Model description and validation, *Ocean Modelling*, *27*(1–2), 33–53, doi:10.1016/j.ocemod.2008.10.005.

Våge, K., R. S. Pickart, A. Sarafanov, Ø. Knutsen, H. Mercier, P. Lherminier, H. M. van Aken, J. Meincke, D. Quadfasel, and S. Bacon (2011), The Irminger Gyre: Circulation, convection, and interannual variability, *Deep Sea Research Part I: Oceanographic Research Papers*, *58*(5), 590 – 614, doi:https://doi.org/10.1016/j.dsr.2011.03.001.

K., W. M., H. R. C., G. Denis, Y. Igor, and T. Virginie (2018), Oxygen saturation surrounding deep water formation events in the labrador sea from argoo2 data, *Global Biogeochemical Cycles*, *32*(4), 635–653, doi:10.1002/2017GB005829.

Xu, X., P. B. Rhines, E. P. Chassignet, and W. J. Schmitz (2015), Spreading of Denmark Strait Overflow Water in the Western Subpolar North Atlantic: Insights from Eddy-Resolving Simulations with a Passive Tracer, *Journal of Physical Oceanography*, *45*(12), 2913–2932, doi:10.1175/JPO-D-14-0179.1.

Yashayaev, I. (2007), Hydrographic changes in the labrador Sea, 1960-2005, *Progress in Oceanography*, *73*, 242–276, doi:10.1016/j.pocean.2007.04.015.

Yashayaev, I., and J. W. Loder (2009), Enhanced production of labrador sea water in 2008, *Geophysical Research Letters*, *36*(1), n/a–n/a, doi:10.1029/2008GL036162, l01606.

Yashayaev, I., and J. W. Loder (2016), Recurrent replenishment of Labrador Sea Water and associated decadal-scale variability, *Journal of Geophysical Research: Oceans*, *121*(11), 8095–8114, doi:10.1002/2016JC012046.

Yashayaev, I., and J. W. Loder (2017), Further intensification of deep convection in the Labrador Sea in 2016, *Geophysical Research Letters*, *44*(3), 1429–1438, doi:10.1002/2016GL071668, 2016GL071668.

# Chapter 4

# Modelling the response of Arctic phytoplankton to high-frequency wind events and sea ice loss

L. Castro de la Guardia, Y. Garcia Quintana, M. Claret, X. Hu, E. D. Galbraith, P. G. Myers

## 4.1   Abstract

The recent increases in Arctic primary production have been attributed to increasing open water areas and frequency of stormy days over ice-free areas. In this paper, we quantify the relative contribution of sea ice loss and stormy winds to annual primary production and carbon export over six regions in the Arctic and Subarctic: Labrador Sea (LS), Barents Sea (BS), Hudson Bay (HB), Baffin Bay (BB), Beaufort Sea (BG) and the Canadian Arctic Archipelago (CAA). Our analysis is focused on two model simulations with identical state of the art sea ice-ocean-biogeochemical model but different atmospheric forcing: a present day simulation (CONTROL) and an idealized simulation forced with an atmospheric field without high frequency wind events (CALM). Contrasting differences between the CONTROL and CALM simulations revealed that the high frequency winds are responsible for 36% (range 13%- 46%) of the primary production and 27% (range 11% - 41%) of the carbon export over the six regions, with the largest impact in the LS and HB. High frequency wind generated early autumn-mixing causing an up-welling of nutrients by deepening the isopycnals before light conditions limited phytoplankton growth in autumn. The loss of sea ice in the CONTROL simulation enhanced primary production

in HB (11%) and in the CAA (19%), but in the CALM simulation it only enhanced primary production (24%) and carbon export (26%) in the CAA. This suggests a regional dependence on high frequency winds for the increasing ice-free seasons to enhanced primary production.

## 4.2 Introduction

Accelerated Arctic sea ice loss (e.g., Serreze et al., 2007; Comiso et al., 2008, 2017) is hypothesized to be the leading driver of increasing Arctic Ocean's primary production by phytoplankton through its effect on the amount of light available at the ocean surface (Arrigo et al., 2008; Pabi et al., 2008). In the high Arctic, where perenial sea ice conditions exist, the loss of sea ice increases the open water area which is correlated with larger annual phytoplankton growth (Arrigo et al., 2008; Pabi et al., 2008). In seasonally ice-cover regions, the loss of sea ice increases the length of the ice-free season which extends the phytoplankton growing season.

However, while phytoplankton growth at high latitudes is limited by light in winter and spring, the growth is limited by nutrients in summer and autumn when a strong stratification inhibits the upward mixing of nutrients (Harrison and Cota, 1991). Increasing freshwater input from sea ice melt strengthens the surface ocean stratification further limiting the vertical nutrient exchanges. Hence, higher productivity in a year with high sea ice loss should be accompanied by a source of energy that can help break the stratification and can resupply nutrients to the surface or a surface source of additional nutrient such as river runoff.

Winds are one of the primary sources of energy for ocean mixing near the surface (Huang and Qiao, 2009). The loss of sea ice also allows wind energy to be transferred more effectively into the ocean. Therefore, the increase in phytoplankton productivity in recent years may not only be the result of increasing light at the ocean surface due to a longer growing season and/or larger ice-free area, but may also be the result of increasing nutrient supply by more intense wind mixing. Indeed, an analysis of the Atlantic storm track pathway showed that the storms' path is displacing northward, bringing more wind energy into the Arctic Ocean in recent years (Wang et al., 2017).

As a result, the number of stormy winds events (i.e. wind speed $\geq 10\,ms^{-1}$) over Arctic open water areas are increasing, and are regionally correlated with the magnitude of the autumn chlorophyll-a concentration (a proxy for phytoplankton productivity) (Ardyna et al., 2014). Ardyna et al. (2014) hypothesized that these stormy winds are mixing the waters and increasing the nutrient availability stimulating phytoplankton production in autumn. This hypothesis is supported by a study in the Strait of Georgia that found that wind speeds of $6\,ms^{-1}$ caused substantial nutrient entrainment leading to an increase in surface phytoplankton growth (Yin et al., 1996). However, others suggest that a correlation between wind and chlorophyll-a is not always conclusive of higher productivity. For example, Carranza and Gille (2015) suggest that in the Southern Ocean increases in

chlorophyll-a concentration due to wind-mixing are caused by the up-welling of chlorophyll-a from the sub-chlorophyll maximum (chlorophyll-a below the mixed layer). At the same time, others have suggested that strong winds can negatively affect phytoplankton productivity by deepening the mixed layer below the photic zone (Weise et al., 2002).

Ardyna et al. (2014) were unable to explain the underlying physical mechanisms relating stormy winds and chlorophyll-a concentration in the Arctic because of limitations to their satellite data. However, *in situ* and modelling studies in the North Atlantic and North Pacific Oceans have shown that during the passage of a storm the surface ocean beneath it receives a significant amount of energy that is translated into vertical shears capable of eroding the surface stratification and supplying the surface water with nutrients which can then support phytoplankton growth (e.g. Wu et al., 2007; Rumyantseva et al., 2015; Pan et al., 2017). These studies are among the first to emphasize the importance of storms and the mechanisms in which storms can positively impact primary production. However they focused on the impact of a single storm over open water regions, which adds temporal and spatial limitations to their findings, and thus cannot be extrapolated to infer the annual importance of storms within ice-covered regions of the Arctic. In part, because within ice-covered regions the mixing processes may differ from ice-free regions, for instance the sea ice may absorb large amount of the energy in the wind.

Our study focuses on quantifying the contribution of stormy winds and sea ice loss to the annual primary production over six Arctic and Subarctic regions with varied ice regimes (Figure 4.1). We use an ocean circulation, sea ice and biogeochemical coupled model to run sensitivity experiments that allow us to isolate the role of stormy winds. We then compare years with high and low sea ice loss to isolate the regional impact of losing the sea ice cover. Using the simulated seasonal cycle of chlorophyll-a we identify the processes driving the productivity in each region. The goal is to increase the understanding of the role of high-frequency winds and sea ice loss throughout the Arctic and Subarctic, in light of recent findings suggesting that sea ice losses along with increasing heat and moisture fluxes may enhance storm genesis within the Arctic during summer (Deser et al., 2000; Simmonds and Rudeva, 2012; Day et al., 2017).

## 4.3 Methods

Arctic and Subarctic regions can be characterized as ice-free, seasonally ice-covered or perennial ice-covered region based on the seasonality of sea ice locally. We define ice-free regions as having less than 25% sea ice concentration year-round, perennial ice-covered regions as having sea ice concentration above 40% year-round, and seasonally ice-covered regions as having sea ice concentration less than 25% for a minimum of three months, but more than 40% the rest of the year. Based on this definition, we chose two ice-free regions
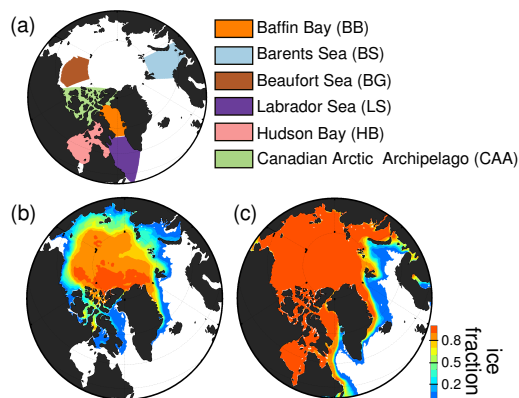
**Figure 4.1.** Selected Arctic regions for the analysis of storms and sea ice loss on primary production and carbon export. (a) Map identifying the selected regions in different colours. Regions were selected based on the simulated sea ice regime. (b) Sea ice fraction at minimum sea ice extent (i.e. model September averaged 2002-2015). (c) Sea ice fraction at maximum sea ice extent (i.e. model March averaged 2002-2015).

(Labrador Sea and Barents Sea), two seasonally ice-covered regions (Baffin Bay and Hudson Bay), and two perennial ice-covered regions (Beaufort Sea and the Canadian Arctic Archipelago) (Figure 4.1).

### 4.3.1 Numerical model

Our numerical simulations use the ocean model Nucleus for European Modelling of the Ocean (NEMO) version 3.4 (Madec and the NEMO team, 2008) coupled to the sea-ice model Louvain la-neauve Ice Model (LIM) version 2 (Vancoppenolle et al., 2009) and the marine biogeochemical model, Biogeochemistry with Light Iron and Nutrient limitation and Gases (BLING) version 0 (Galbraith et al., 2010).

BLING is a new addition to the NEMO modelling framework. It is an intermediate complexity biogeochemical model that has the capacity to estimate phytoplankton production and export. It includes a parametrization to represent iron limitation on the light harvesting capacity of phytoplankton, in addition to the more common limitations of light, temperature and nutrients on phytoplankton productivity (Galbraith et al., 2010). The advantage of using BLING over other more complex bioegeochemical modules already coupled to NEMO is that we can integrate the experiments over several decades at high spatial resolution and at a relatively low computational cost. This represents an advantage when there is an interest of repeating experiments to isolate the role of winds, for example.

We ran our simulation from Jan 1958 to Dec 2015 using the regional configuration Arctic and the Northern Hemisphere Atlantic with horizontal resolution of $0.25°$ (ANHA4). In ANHA4 the three dimensional primitive equations are discretized on a tri-polar-grid and a z-coordinate with fifty levels. This configuration has two open boundaries: one near to the Bering Strait in the Pacific Ocean and the other one at $20°S$ across the Atlantic Ocean. At the open boundaries there is an exchange of heat, momentum and tracers, but within the interior the

model evolves without restoring.

**Initial Conditions**

We initialized the model in Jan 1958 using climatological ocean temperature and salinity from the Polar Science Center Hydrographic Climatology (PHC 3.0) (Steele et al., 2001) ($http : //dss.ucar.edu/datasets/ds285.2/$), zero ocean velocities and a constant sea ice cover of $3m$ thickness in all grid-cells where the ocean temperature was colder than the freezing point of $-1.8°C$. The biological fields were initialized using a combination of observed climatologies and model results. For dissolved oxygen and phosphate concentration we used climatological fields of the World Ocean Atlas 2013 (WOA213) version 2 (Garcia et al., 2014) ($http : //www.nodc.noaa.gov/OC5/woa13/$), and for dissolved iron and organic phosphate we used climatological fields from a simulation using a global configuration at $1°$ resolution of the Generalized Finite Difference Methods-Earth System Model version 2 (GFDM-ESM2) coupled with BLING version 0 (Galbraith et al., 2015). This last simulation ran for 100 years and the climatologies were built from the last 20 years.

**Boundary conditions**

From Jan 1958 until Dec 2001 we used the data produced from a global simulation of NEMO at $0.25°$ resolution ran by GEOMAR, Helmholtz Center for Ocean Research Kiel (simulation id: ORCA025-K3415; $http : //www.geomar.de/$). From Jan 2002 to Dec 2015, we switched to the Global Ocean Reanalysis and Simulations (GLORYS2v3; (Masina et al., 2015)). Boundary conditions for biological tracers (dissolved oxygen, dissolved phosphate, dissolved iron and dissolved organic phosphate) were derived from climatologies built from an Earth System Model simulation (GFDL-ESM2; (Galbraith et al., 2015)). All boundary conditions were interpolated on the fly to the model time step of 1080 seconds.

A source of iron at the surface of the ocean was added following the relation between dust deposition and iron concentrations described in (Galbraith et al., 2010). The climatological dust deposition input at the surface of the ANHA4 domain was derived from the Global Ozone Chemistry Aerosol Radiation and Transport (GOCART) model (Ginoux et al., 2001).

To represent freshwater sources from land we used the monthly inter-annual river runoff from Dai et al. (2009) and Greenland melt-water runoff from (Bamber et al., 2012). Runoff sources were carefully remapped onto ANHA4 grid to give a more realistic freshwater input to the ocean. Runoff sources did not contain nutrients or dissolved organic products. Freshwater runoff was added as salt-fluxes with temperature equal to the temperature of the nearby surface ocean.

**Atmospheric forcing data**

From Jan 1958 to Dec 2001 we forced the model with Atmospheric data from Coordinated Ocean Research Experiment version 2 (COREv2; (Large and Yeager, 2009)). This data includes inter-annually varying monthly precipitation, daily shortwave and longwave radiation, and six-hourly air temperature, specific humidity, zonal and meridional wind velocities at $10m$-above ground.

From Jan 2002 to Dec 2015, we switch the atmospheric forcing data to the Canadian Meteorological Centers Global Deterministic Prediction System (CMC-GDPS; (Smith et al., 2014)). This data is derived from a reanalysis of a forecast model and it includes hourly shortwave and longwave radiation fluxes, precipitation, wind velocities at $10m$-above ground, and air temperature and specific humidity at $2m$-above ground. These forcing data are in good approximation of the weather conditions experienced between 2002 and 2015 (Smith et al., 2014).

### 4.3.2 Sensitivity experiment

We ran two twin simulations using identical numerical cores and modifying only the atmospheric forcing data. The two experiments start in Jan 2002, as a continuation of the simulation started in Jan 1958, and run until Dec 2015. Our analysis is focused on the recent period of Jan 2002 to Dec 2015 that uses the higher spatial and temporal resolution atmospheric forcing data of CMC-GDPS, which is more likely to represent better the high-frequency wind events in the North Atlantic and the Arctic. Additionally, having had 43 years for the ocean-sea ice-biogeochemical model to evolve prior to analysing the solutions make our results more independent from the initial conditions.

Our CONTROL simulation was forced with the CMC-GDPS re-forecast atmospheric data. The CONTROL simulation includes the present day high-frequency atmospheric wind events. Our sensitivity simulation, CALM, was forced with a filtered version of the CMC-GDPS atmospheric data. The CALM simulation does not includes high-frequency atmospheric wind events, because they were filtered out.

The filter version of the CMC-GDPS data were created using a $10\,day$ window length filter to the fields of temperature and wind (zonal and meridional components). The $10\,day$ window length was chosen based on a previous study which results show that this window length was effective at removing the high-frequency wind events in the North Atlantic (Holdsworth and Myers, 2015). This window length also captures the mean lifetimes of Arctic storms, which are commonly $3\,day$, but may range from 1 to $13\,day$ (Simmonds and Rudeva, 2012).

In our study regions (Figure 4.1), the wind speed of the CMC-GDPS-filtered was lower than in the unfiltered CMC-GDPS fields, however the winds within each region preserved their average direction (Figure 4.2).
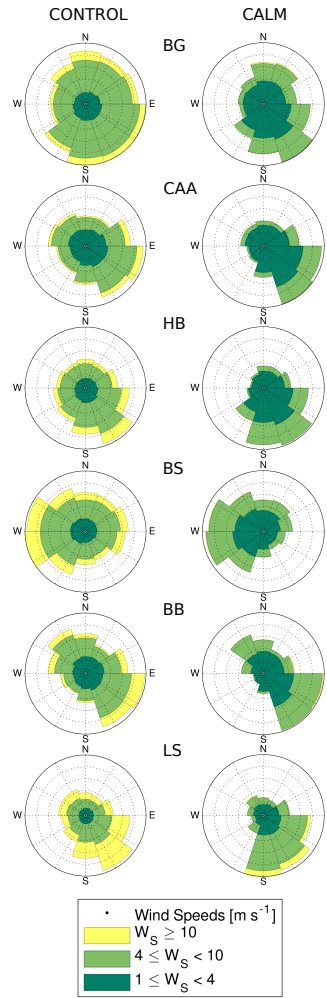
**Figure 4.2.** Regional wind patterns in CONTROL and CALM simulations during autumn (Oct-Dec). Comparing unfiltered CMC-GDPS fields of wind speed and direction (left) to filtered CMC-GDPS (right). Abbreviations: Beaufort Sea (BG), Canadian Arctic Archipelago (CAA), Hudson Bay (HB), Barents Sea (BS), Baffin Bay (BB) and Labrador Sea (LS).

Noticeably, most of the winds with wind speeds $\geq 10\,ms^{-1}$ were smoothed out by the filter. These are commonly associated with storm weather systems (Wang et al., 2017), and were those correlated with the autumn phytoplankton bloom by Ardyna et al. (2014).

An animation of the filtered and unfiltered atmospheric fields showed that our moving average removes storm-like events throughout the Arctic and Subarctic, but temperature and background wind fields remain almost unchanged (supplementary video; a snapshot of this animation is in Figure 4.3). The overall ocean response to the filtered and unfiltered atmospheric field is similar in terms of the depth integrated barotropic circulation (Figure 4.4). Largest differences include a weaker anticyclonic circulation within the Beaufort Sea and a weaker cyclonic circulation within the Labrador Sea in the CALM simulation relative to the CONTROL simulation (Figure 4.4c).
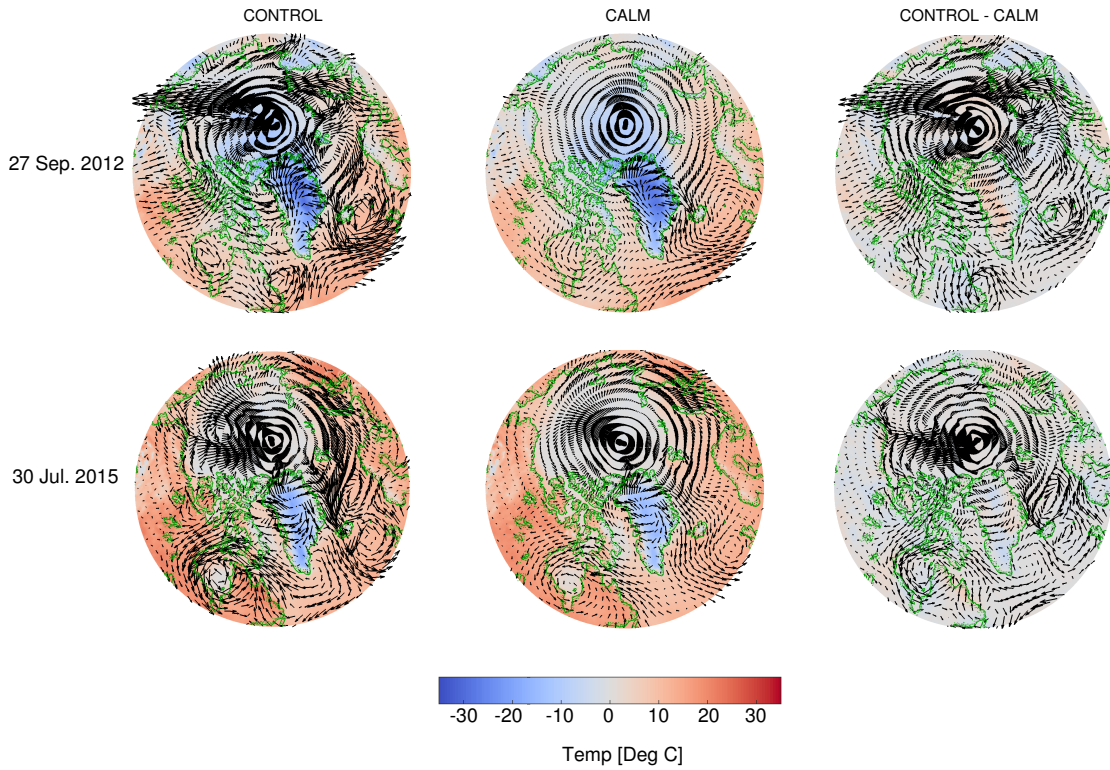
**Figure 4.3.** Snap shot of the wind and temperature fields use to force the CONTROL (left) and CALM (middle) simulations and their difference (right). Background color is mean temperature for the day. Size of the arrows show the wind speed, and the arrow heads point in the direction where the wind is going to.
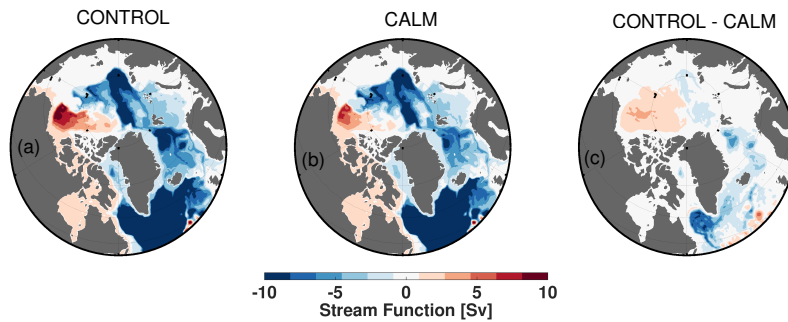


**Figure 4.4.** Depth integrated barotropic circulation in the (a) CONTROL and (b) CALM simulations. (c) Difference between the two simulations (CONTROL minus CALM) shows that the absence of high-frequency winds in the CALM simulation weakens the strength of the circulation but does not affect the large scale circulation patterns.

There were small differences in the nutrient concentration at the ocean surface between the CONTROL and CALM simulations. The annual mean concentrations differences was $< 0.03 mmol P m^{-3}$ in the upper $50 m$. The vertical distribution of phosphate in upper $300 m$ (Figure 4.5) shows that in both, the CONTROL and the CALM simulations, the nutricline depth is similar, between 30 and $100 m$ (depending on the basin) and with

approximately the same maximum concentration. The exception is the Beaufort Sea, where in the CALM simulation the nutricline shallowed from $150\,m$ to $90\,m$, and the maximum nutrient concentration was reduced from $1.2\,mmol\,m^{-3}$ to $0.7\,mmol\,m^{-3}$ from 2002 to 2008. Meanwhile, during the same period, in the CONTROL simulation the nutricline deepened from $150\,m$ to $190\,m$, while the maximum nutrient concentration was reduced from $1.2\,mmol\,m^{-3}$ to $1\,mmol\,m^{-3}$ (panel BG in Figure 4.5). This suggests that the Beaufort Sea is highly sensitive to the atmospheric forcing and it is likely responding to stronger mixing in the CONTROL simulation where we switched from coarse resolution atmospheric data (COREv2) prior to 2002 to the higher resolution CMC-GDPS data after 2002, and to weaker mixing in the CALM simulation where we switched from CORE2 to the filtered fields of CMC-GDPS data after 2002.
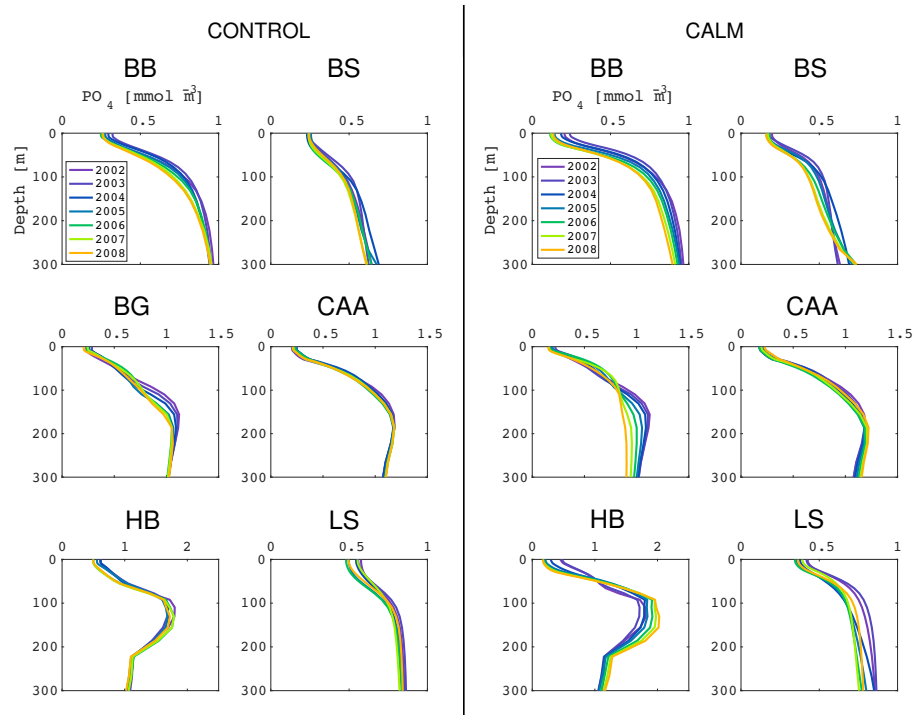


**Figure 4.5.** Nutricline adjustment to switching atmospheric forcing from CORE2 to CGRF (Exp. CONTROL) and to CGRF-filtered (Exp. CALM) in our simulations for each basin. In all basins the nutricline can be found between 30 and $100\,m$ every year. Maximum changes in surface phosphate concentration are $\leq 0.03\,mmol\,P\,m^{-3}$ in Baffin Bay (BB).

### 4.3.3 Analysis of turbulence

Using the simulated temperature ($T$) and salinity ($S$) we calculated the stratification of the water using the buoyancy frequency frequency, $N^2$ (Eq.4.1). In Eq.4.1, $z$ is the vertical coordinate, while $\alpha = 2.0 * 10^{-4}$ and $\beta = 7.7 * 10^{-4}$ are the thermal and saline expansion coefficients, respectively.

$$N^2 = \frac{g}{\partial z}(\alpha \partial_z T - \beta \partial_z S) \tag{4.1}$$

Using the simulated ocean velocity fields we derived the vertical shear of the horizontal velocity ($S^2$, Eq.4.2). $S^2$ measures the capacity of the water column to become turbulent. In Eq.4.2, $\mathbf{U}$ is the vector of the horizontal velocity.

$$S^2 = (\frac{\partial \mathbf{U}}{\partial z})^2 \tag{4.2}$$

The turbulence index, Richardson Number ($Ri$), was then derived by taking the ratio between the square of the buoyancy frequency, $N^2$, and the vertical shear, $S^2$ (Eq. 4.3). We define a state of *turbulent mixing* when the vertical shear is at least fourfold the stratification (e.g. Ri $\leq$ 0.25), a typical threshold used in fluid dynamics to define turbulence.

$$Ri = \frac{N^2}{S^2} \tag{4.3}$$

### 4.3.4 Analysis of obduction

Obduction ($O$) was calculated following the Karleskind et al. (2011) equation for the subduction for biogeo-chemical tracers (Eq. 4.4). This equation is normally multiply by a $-1$ to make subduction positive. Here, however, to preserve obudction positive we do not multiply the equation by the $-1$. Therefore, we chose to adopt the nomenclature of obduction to avoid confusion with previous studies. The equation has four mechanisms controlling the movement of nutrients into (obduction) and out of (subduction) a layer, $h$, which is specified using a density criteria. Obduction (units $mol\,m^{2-}s^{-1}$) is defined as the integral of the mean nutrient concentration within the layer $h$ ($C_h$) integrated in time ($T$).

$$O = \frac{1}{T}\int_0^T \int_h (C_h\frac{\partial h_b}{\partial t} + C_h\nabla \dot{U}_{h_b} + C_h W_{h_b} + A_z^n\frac{\partial C_{h_b}}{\partial z_{h_b}})\,dt\,dh \tag{4.4}$$

We focused on obudction at $50\,m$ depth, and thus our layer-base ($h_b$), is the isopycnal that characterizes $50\,m$ depth in each region. We defined this layer-base isopycnal using an annual climatology to determine the density at $50\,m$.

On the right-hand side of equation 4.4, the first term is the seasonal fluctuation of the isopycnal that defines $h_b$. The second term is the lateral transfer of nutrients across the sloping $h_b$ isopycnal. The third term is the vertical transfer of nutrients across the $h_b$ as a result of the vertical velocity at this interface. Following Williams et al. (2006), the vertical velocity is diagnosed from the wind-driven meridional transport at the interface of $h$

and the vertical velocity at the base of the Ekman layer. The fourth term is the vertical diffusive-flux, which is calculated based on the concentration gradient at the $h_b$ ($\frac{\partial C_{h_b}}{\partial z_{h_b}}$) multiplied by the diffusion coefficient, $A_z^n$. This coefficient varies in space and time as a function of $Ri$. When the water is turbulent ($Ri \leq 0.25$) there is an enhanced diffusion ($A_z^n \approx 10^{-4}\,m^2s^{-1}$) otherwise $A_z^n = 10^{-5}\,m^2s^{-1}$. We chose this definition of $A_z^n$ to make our off-line calculations follow NEMO's turbulent kinetic energy mixing scheme for sub-scale vertical processes (Madec and the NEMO team, 2008).

## 4.4 Evaluation of the CONTROL simulation

We determine the performance of the CONTROL simulation in the six regions by comparing the simulation to satellite, *in situ* data, and a gridded climatological product, WOA13. The CONTROL simulation captured in large part the observed seasonality of sea ice concentration (Figure 4.6), dissolved inorganic nutrient (Figure 4.7) and chlorophyll-a (Figure 4.8) in each region. In the next subsections, we follow with details on the model evaluation on each of the above mentioned fields.

### 4.4.1 Sea ice

To evaluate the simulated sea ice concentration and ice-free period we used Passive Microwave (PMW) sea ice concentration data derived using the Bootstrap Algorithm version 2 (Comiso, 2015). We define the ice-free period as the number of days with $< 25\%$ sea ice concentration. This threshold was chosen because PMW sea ice concentration data has an error of 15% to 20% throughout the Arctic, especially near the ice margin and in seasonally ice-covered regions (Cavalieri et al., 1991; Comiso and Kwok, 1996; Comiso et al., 1997, 2017).

The model captured the seasonality of the sea ice concentration in each region (red shade vs. solid black line in Figure 4.6), with the best agreement in winter and spring (Jan - May) and lowest agreement in late summer and autumn (Aug - Nov). Regionally the lowest accuracy in the winter-spring period was found in Baffin Bay ($-15\%$), and highest accuracy in the Beaufort Sea ($-0.7\%$) and the Canadian Arctic Archipelago ($-0.4\%$). In the summer-autumn period the lowest accuracy was found in the Beaufort Sea ($+31\%$) and the Canadian Arctic Archipelago ($+12\%$).

The ice-free period in Hudson Bay and Baffin Bay was in good agreement with the PMW data with differences $\leq 5\,d$ (red vs. black bars in Figure 4.6c,e). In the ice-free regions, Barents Sea and the Labrador Sea, the model simulated the ice-free period $20\,d$ longer than PMW data (Figure 4.6d,f). These two regions were simulated with sea ice concentration $\leq 25\%$ year-round, and thus the ice-free period was 365 days. Meanwhile the PMW data had winter sea ice concentration of up to 30%, thus having a shorter ice-free season based on our threshold of 25%. These differences, however, are consider to have minor effect on annual productivity because

at these high latitudes light is unavailable during winter regardless of sea ice conditions.
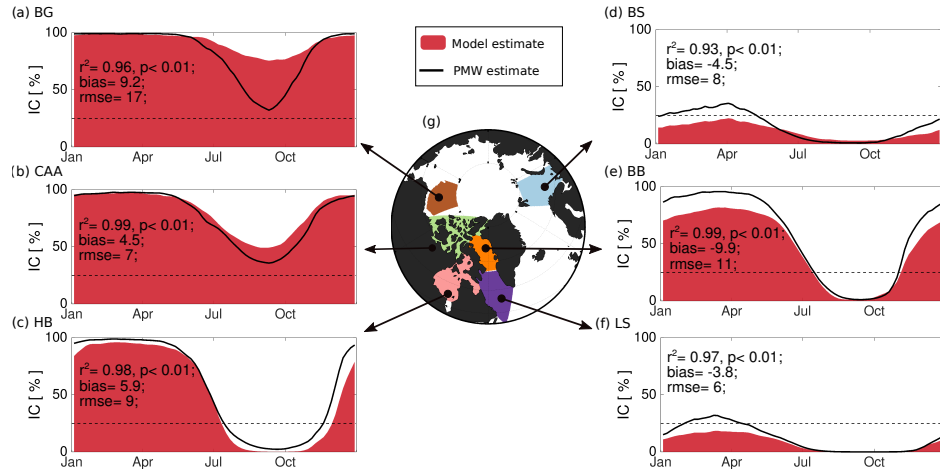


**Figure 4.6.** Simulated sea ice concentration (red area plotted on left-axis) and ice free period (red bar plotted on right-axis) compared with satellite-derived sea ice concentration (solid black line) and ice-free period (black bar). Dashed black line marks the 25% threshold used to define ice-free conditions.

## 4.4.2 Nutrients

We obtained dissolved inorganic nitrate ($NO_3$) and phosphate ($PO_4$) concentrations from gridded WOA13 climatology. Additionally, we used *in situ* dissolved inorganic nitrate and phosphate data within Baffin Bay and the Labrador Sea provided by the Bedford Institute of Oceanography, Department of Fisheries and Oceans Canada (DFO), and within the Beaufort Sea region we downloaded data collected as part of the Beaufort Sea Exploration Program ($http://www.whoi.edu/beaufortgyre$).

Our biogeochemical model, BLINGv0, uses dissolved inorganic phosphate to represent the mean concentrations of the two major macro-nutrients in the ocean: nitrate and phosphate. Therefore, to evaluate BLING's dissolved inorganic phosphate concentration we followed Galbraith et al. (2010) and built an observed nutrient index concentration (Eq. 4.5). The nutrient index is defined as the averaged concentration between dissolved inorganic phosphate and nitrate, but the nitrate concentration is converted to phosphate units using the Redfield ratio of $16 PO_4$ to $1 NO_3$.

$$Nutrient = \frac{1}{2}(PO_4 + \frac{NO_3}{16}),$$

(4.5)

The simulated seasonality of nutrient concentration has a sinusoidal-shape in all basins, except in the Beaufort Sea. There is a maximum in Apr - May and a minimum in Aug - Sept. The model underestimates the monthly nutrient concentration relative to WOA13 in all basins (Figure 4.7). Differences, however, are smaller when the simulation is compared to *in situ* measurements in the Beaufort Sea, Baffin Bay and Labrador Sea.

In the Baffin Bay and the Barents Sea the WOA13 and *in situ* data have a peak in nutrient concentration in Sept that is not present in our simulation (Figure 4.7d,e). This suggests that our simulation is missing a source of nutrient in Aug - Sept. However when looking at chlorophyll-a concentration in satellite data (Figure 4.8) there is no corresponding peak in chlorophyll-a in Sept, which may suggest that these high nutrient concentrations could be a feature of the specific sampling year rather than a climatological signal.

In the Beaufort Sea the model simulates the nutrient concentration within the range of the observations during winter but from Mar - Oct the simulated concentration is half the concentration estimated from WOA13. From Jul - Sept *in situ* data however is in good agreement with the model, suggesting that WOA13 may not be accurate for this basin perhaps due to scarcity of *in situ* observations used to derive the WOA13 estimates (grey-triangles in Figure 4.7). Large values in WOA13 could be attributed to the results of the interpolation process over regions with limited data coverage. In the Beaufort Sea, the closest observations, and thus the ones with highest weight, are in the Pacific Ocean where nutrient concentration are typically higher than in the Arctic Ocean (Torres-Valdés et al., 2013). In Figure 4.7 we show that the percentage of grid-cells per month containing more than 2 data points in the WOA13 is often $< 20\%$ over this region.
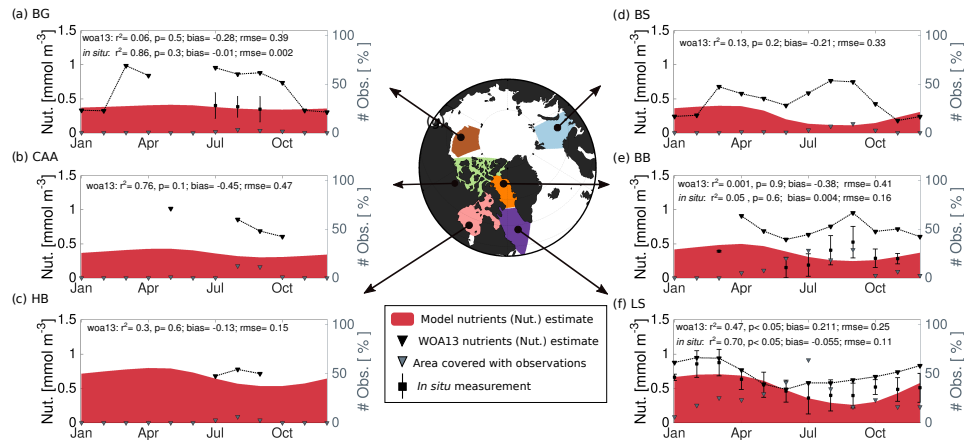


**Figure 4.7.** Simulated nutrient concentration (red area) compared to nutrient concentration data from WOA13 (solid black line with filled triangles) and *in situ* measurements when available (filled black squares $\pm$ one standard deviation). On the right-axis the percentage of WOA13 pixels containing data is presented as gray triangles. Nutrient concentration, from each data sources, has been averaged over the top $50\,m$ of the water column within the regions indicated in panel *g*.

### 4.4.3 Chlorophyll-a

We evaluate the simulated seasonality of the chlorophyll-a concentration using chlorophyll-a data derived from ocean color measurements from the Moderate Resolution Imaging Spectroradiometer sensors on board of the Aqua satellite (MODIS-A) (Group, 2003). We exclude neritic regions (i.e. water depth lower than 100m) because they often contain large loads of coloured dissolved organic matter (CDOM) due to the runoff input

from river and land (Amon et al., 2012; Griffin et al., 2018). The presence of CDOM in surface ocean waters contaminates the satellite chlorophyll-a estimates, generally causing spuriously high values of chlorophyll-a concentration (*Goyens et al.*, 2013; Camara Lins et al., 2017; Griffin et al., 2018) . To avoid including these spurious values, we used the cut-off value of $\geq 20\,g\,m^{-3}$ on the satellite data. Additionally, we used *in situ* chlorophyll-a concentration in the Beaufort Sea from data collected as part of the Beaufort Sea Exploration Program.

The seasonality and the monthly magnitude of chlorophyll-a concentration is captured by the model (Figure 4.8). However, there are some discrepancies with the magnitude of the spring bloom (e.g. maximum of spring chlorophyll-a between Apr - Jun) in the Barents Sea and the Labrador Sea. In these basins the spring bloom magnitude is underestimated by $2\,mg\,m^{-3}$ and $0.5\,mg\,m^{-3}$, respectively.
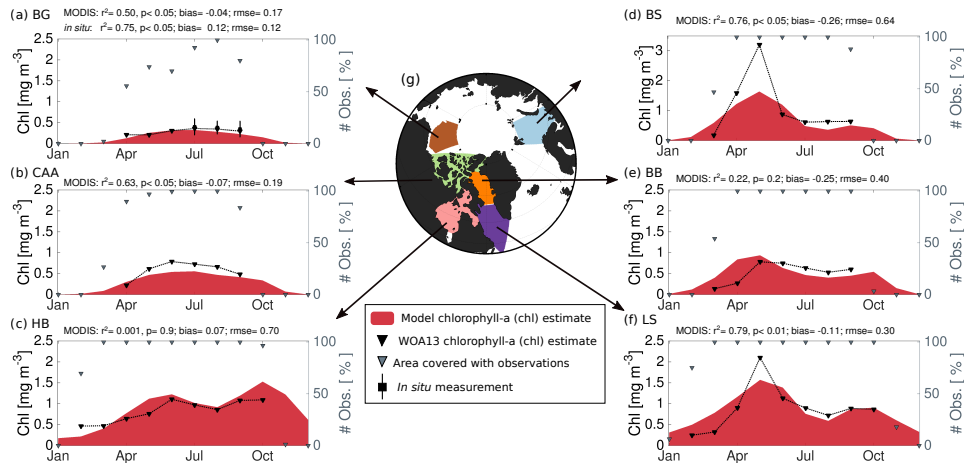


**Figure 4.8.** Simulated chlorophyll-a concentration (red area) evaluated against MODIS-A derived chlorophyll concentration (solid line with black triangles) and *in situ* measurements when available (filled black square $\pm$ one standard deviation). As an accuracy measurement for MODIS-A data we estimated the percentage of pixels with data within each region (gray triangles plotted on right-axis).

The larger MODIS-A peak in Barents Sea may result from the influence of two large rivers, the Northern Dvina and the Pechora, which discharge their waters into the Barents Sea. This input is likely to contain large amounts of CDOM which may be contaminating the chlorophyll-a satellite data, however, rivers also add nutrients to surface water (Holmes et al., 2012) which could be enhancing productivity and thus could explain the higher chlorophyll-a observed in spring. CDOM has also been found within the Labrador Sea (Guéguen et al., 2014) and could also be affecting the MODIS-A signal, however, similar to river runoff, the meltwater from Greenland also contains nutrients (Bhatia et al., 2013; Markussen et al., 2016), which could be enhancing the primary production. In both regions, it is likely that the second reason is more important, given that we show that our simulation had lower nutrient concentration in these two regions (Figure 4.7f,d). This could suggest that lacking the land-nutrient sources in our simulation could be limiting our ability to represent the magnitude

of the spring bloom.

In summer (Jul - Aug) and autumn (Sept - Oct), our simulation is in good agreement with observations, with only slight underestimations in the seasonal and ice-free regions. However in autumn in Hudson Bay, our simulation estimates an autumn bloom that is $0.3\,mg\,m^{-3}$ larger than the observation. This could be associated with the lower Oct ice concentration in our simulation which would results in the phytoplankton having more light to continue to grow through Oct.

## 4.5 Results

### 4.5.1 Sensitivity to stormy wind events

**Total Kinetic Energy (TKE) input**

We calculated the Total Kinetic Energy (TKE) in the surface ocean as a proxy for wind mixing. We quantify the contribution of the high-frequency winds (hereafter stormy winds) to the TKE by subtracting the TKE in the CALM simulation from that of the CONTROL simulation (Figure 4.9a).

To derive the TKE at the surface of the ocean we apply the work-energy-theorem which states that the change in TKE equals the work done by all forces on a particle ($\Delta TKE = F\,\Delta S$). Assuming initial TKE is zero, we can then derive the final TKE from the force acting on the ocean surface (e.g. sea surface stress) over the distance, $\Delta S$ (Eq. 4.6). The sea surface stress, $\tau$, is calculated as combination of the ice-ocean stress ($\tau_{io}$) and the wind-ocean stress ($\tau_{wo}$). We use sea ice concentration ($IC$, range $0-1$) to identify the ice-covered regions.

$$
\begin{aligned}
TKE &= \Delta S\,\tau \\
&= \Delta S\left[\tau_{io}\,IC + \tau_{wo}\,(1-IC)\right]
\end{aligned}
\tag{4.6}
$$

In Figure 4.9a, the shades of red indicate that higher TKE was available in the CONTROL simulation relative to the CALM simulation. The largest differences in $TKE$ ($\geq 20\,J\,m^{-2}$) between the CONTROL and CALM simulations are found within the Subpolar Gyre, which is the main pathway for storms in the North Atlantic (Wang et al., 2017). This helps confirms that the filtering has removed stormy wind events from the CALM simulation.

In the ice-free and the seasonally ice-covered regions, the stormy winds contributed, on average, $20\,J\,m^{-2}$ to the available TKE at the ocean surface. Meanwhile, in ice-cover regions the contribution of stormy winds to the TKE was smaller (maximum of $5\,J\,m^{-2}$). In these regions, it is expected that there is lower energy transfer from the atmosphere into the ocean because the sea-ice acts as a barrier absorbing a portion of the wind energy.
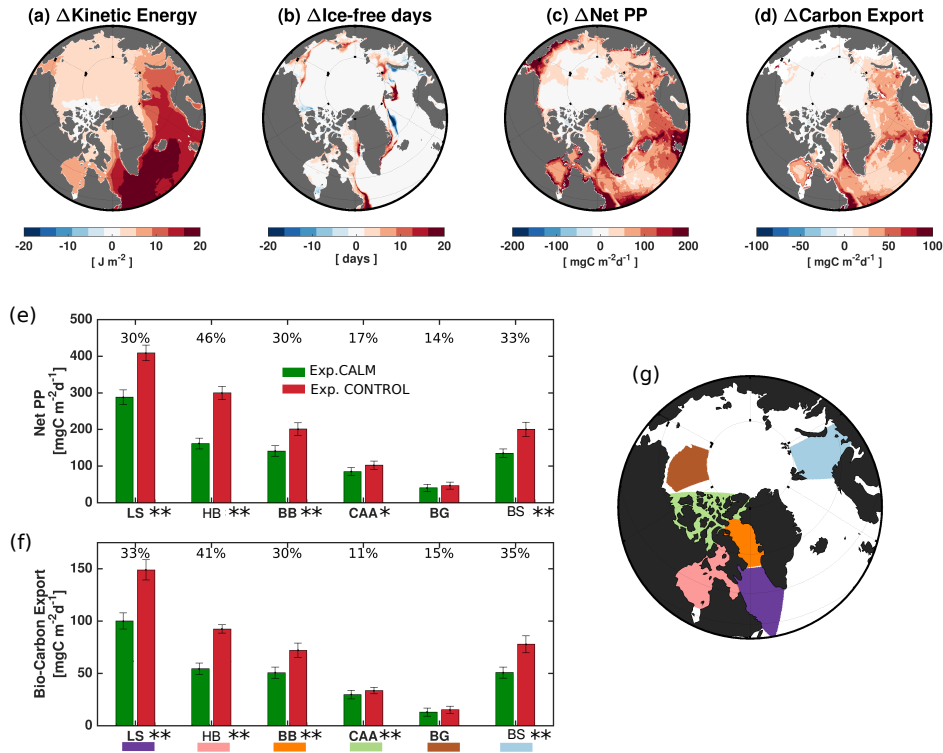
**Figure 4.9.** Impact of stormy wind event on (a) surface ocean energy input, (b) ice-free days, (c) net primary productivity, (d) biogenic carbon export, and its mean impact on the study regions' (e) primary production and (f) carbon export. The map inset in (g) presents the geographical area of the study region. (a-d) Are the differences between CONTROL and CALM simulation, whereby red indicates higher values in the CONTROL simulation. Numbers in panels (e) and (f) indicate the percentage change between CONTROL and CALM simulation, whereby positive number indicates an increase in the CONTROL simulation. One and two stars over the basin abbreviation in (e) and (f) indicate that the differences between CALM (green bar) and CONTROL (red bar) are significant at 95 and 99% confidence, respectively.

The presence of stormy winds had little impact on the length of the ice-free season (Figure 4.9b). The only exception is in the marginal ice-zone where the stormy winds increased the number of ice-free days. Studies have shown that storm-induced waves are responsible for breaking the sea ice up to $100\,km$ from the ice edge and thus contribute to the faster ice melt at the ice-edge (Kohout et al., 2000). This regionally large difference between the two simulations serves to confirm that stormy wind events in the Arctic have been effectively removed from the CALM simulations. The small difference between the two simulation within the icepack is because, here, sea ice melt is primarily controlled by atmospheric temperature (Kauker et al., 2003; Makshtas et al., 2007), and the background temperature field did not differ between filtered and un-filtered CMC-GDPS data (Figure 4.3 and supplementary video).

In general, we note that the absence of stormy winds had a minor impact on the sea ice concentration except in the Labrador Sea (Figure 4.10a). The Labrador Sea is within the marginal ice zone, and thus the absence of stormy winds increased the ice concentration by 31%. However, most of the differences occurred during

winter, such that the light limitation on phytoplankton growth did not differ between simulations. The presence of stormy winds, however, had no significant effect on the length of the ice-free period in either basin (Figure 4.10b). This gives confidence that we have isolated the role of stormy winds without affecting the sea ice environment to which phytoplankton are exposed to in the CONTROL and CALM simulations.
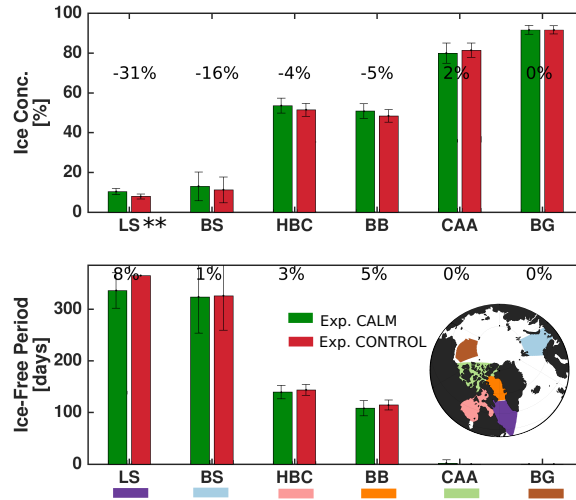


**Figure 4.10.** Climatological mean of (a) sea ice concentration and (b) ice-free period in the CONTROL (red bars) and CALM (green bars) simulation for each basin: Labrador Sea (LS), Barents Sea (BS), Hudson Bay (HB), Baffin Bay (BB), Canadian Arctic Archipelago (CAA) and Beaufort Sea (BG). Numbers in each panel indicate the percentage change of the CONTROL simulation relative to the CALM simulation, whereby positive number indicates that the ice concentration (ice-free period) was higher (longer) in the CONTROL simulation. The two stars over the LS indicate the sea ice concentration in this basin was significantly difference between experiments with 99% confidence.

**Productivity and carbon export**

Stormy winds stimulated the primary production and carbon export throughout the Subarctic, but not within the Arctic interior (Figure 4.9c,d). Based on the difference between the two simulations, stormy winds enhanced primary production by more than $100\,mgCm^{-2}d^{-1}$ and carbon export by more than $50\,mgCm^{-2}d^{-1}$ in areas where stormy winds added $5 - 20\,Jm^{-2}$ to the TKE. These results confirm that stormy winds enhance phytoplankton productivity by increasing the mixing potential (e.g. TKE) as proposed by Ardyna et al. (2014). Such a relation has also been noted in ice-free oceans (Yin et al., 1996). In this previous study the stormy events where suggested to control inter-annual variability of the magnitude of summer primary production.

The effect of stormy winds on seasonally ice-covered regions was similar to that of open water regions, even when open water regions received twice as much energy input from the winds (Figure 4.9e,f; Table 4.1). This suggests that the timing of storm-induced mixing could be an important factor determining the primary production yield. This could be because in the ice-free regions, very strong winds can negatively affect productivity

by deepening the mixed layer depth below the photic zone (Yin et al., 1996; Weise et al., 2002). The Subpolar Gyre is known for the large number and high intensity of storms during fall and winter causing deep mixed layer depths (*Sathiyamoorthy and Moore*, 2002; *Lacour et al.*, 2014; Wang et al., 2017).

Within our ice-free regions and seasonally ice-covered regions, the presence of stormy wind events significantly increased the annual primary production over the upper $50\,m$ of the ocean and the biogenic carbon export at $50\,m$ (Figure 4.9, Table 4.1). In the Hudson Bay, the stormy winds were responsible for 46% of the annual primary production and 41% of the total biogenic carbon export. While in the Labrador Sea, Barents Sea, and Baffin Bay stormy winds accounted for 30% of the primary production and 30% biogenic carbon export. In the perennially ice-covered regions, like the Canadian Arctic Archipelago, the stormy winds enhanced primary production by 17% and biogenic carbon export by 11%. However in the Beaufort Sea region, the stormy winds did not increase productivity or carbon export. This is consistent with observations in 2008 when strong winds did not enhanced primary production at an off-shelf station in the Beaufort Sea because the energy was insufficient to break the strong summer stratification and replenish the surface water with nutrients (Tremblay et al., 2011).

**Phenology and bloom dynamics**

Linking the seasonal response of phytoplankton to atmospheric forcing changes allowed us to uncover how and when stormy winds affected the primary production in each region. In Figure 4.11 we show the five-day climatology of chlorophyll-a concentration (red/green area), in relation to the sea ice concentration (aquamarine blue area), the light regime (grey-white background), the water turbulence (*Ri* solid red/green line) and the nutrient limitation (red/green filled circles) in the six regions.

All regions have a minimum in chlorophyll-a concentration in winter (Dec - Feb) because of low light availability (grey in Figure 4.11). During this period light is limiting because solar radiation is low, and because of a mixed layer depth well below the euphotic zone due to winter convective mixing (solid green/red $Ri \approx 0$) resulting from surface heat loss and brine rejection. However, this strong mixing increases the amount of nutrients in surface water, causing the nutrient limitation to reach its minimum (filled circles). Therefore, with increasing light in spring, phytoplankton is able to bloom (increasing chlorophyll-a concentration) because nutrients are abundant.

In the perennial ice-covered regions (Canadian Arctic Archipelago and Beaufort Sea), where sea ice may still block the spring and summer solar radiation, light levels are lower, and phytoplankton is to some extent, still light limited throughout summer in our simulations. Thus, chlorophyll-a concentration reaches a maximum of only $0.5\,mgm^{-3}$, which is 3 times lower than in seasonal and ice-free regions. In the CONTROL simulation (red), the small, but additional amount of wind energy available to generate more turbulence resulting in lower

**Table 4.1.** Quantifying the role of winds in each region: Labrador Sea (LS), Barents Sea (BS), Hudson Bay (HB), Baffin Bay (BB), Canadian Arctic Archipelago (CAA), Beaufort Sea (BG).

| Productivity $[mgCm^{-2}d^{-1}]$ | LS | BS | HB | BB | CAA | BG |
|---|---|---|---|---|---|---|
| CONTROL (std) | 408.75 (21) | 199.91 (20) | 299.67 (18) | 200.65 (18) | 101.89 (11) | 46.52 (10) |
| CALM (std) | 287.86 (20) | 134.87 (12) | 161.43 (15) | 140.91 (14) | 84.86 (11) | 40.17 (10) |
| Δ[%] | 29.58 | 32.53 | 46.13 | 29.77 | 16.71 | 13.65 |
| p-value | < 0.01 | < 0.01 | < 0.01 | < 0.01 | < 0.01 | 0.097 |
| Export $[mgCm^{-2}d^{-1}]$ | | | | | | |
| CONTROL (std) | 148.85 (10) | 77.72 (8) | 92.36 (4) | 33.40 (7) | 33.40 (3) | 15.02 (4) |
| CALM (std) | 99.94 (8) | 50.67 (5) | 54.27 (5) | 50.50 (5) | 29.67 (4) | 12.82 (4) |
| Δ[%] | 32.86 | 34.80 | 41.24 | 29.80 | 11.18 | 14.65 |
| p-value | < 0.01 | < 0.01 | < 0.01 | < 0.01 | 0.012 | 0.131 |

101
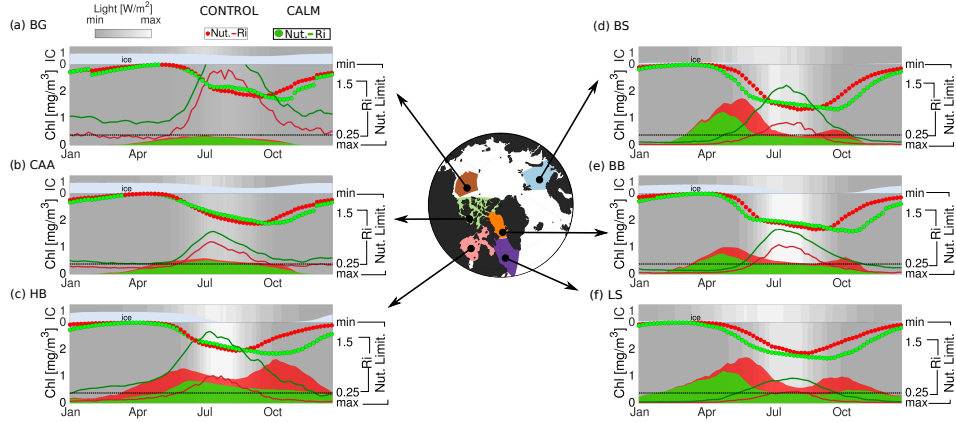
**Figure 4.11.** Phytoplankton phenology in the presence (red) and absence (green) of high-frequency wind events in six Arctic and Subarctic regions. Panels a-f present the model climatology (2002-2015) over each of the areas. Within each panel it is the 5 daily mean the sea ice concentration (gray shade), the solar radiation above the sea ice and the photosynthetically available radiation below the sea ice (grey-white background), the chlorophyll-a (chl-a) concentration (red and green shade), the nutrient limitation (filled circles), and turbulence expressed as the Richardson number ($Ri$; solid line), turbulence threshold, $Ri = 0.25$ (dotted black line). PAR, chl-a, $Ri$, and nutrient limitation are averaged over the top $50\,m$. Note the inverted scale of the nutrient limitation.

nutrient limitation in spring and autumn (red circles generally higher than green circles in Figure 4.11a-b) and lower water stratification (red solid line) relative to the CALM simulation (green).

Most noticeably, in the CONTROL simulation the chlorophyll-a concentration in seasonal and ice-free regions shows that phytoplankton blooms in early spring and in autumn (red in Figure 4.11 c-f). This contrasts with the CALM simulation (green in Figure 4.11 c-f), where phytoplankton only blooms in spring, and with a magnitude that is lower than in CONTROL simulation. These differences are directly related to the larger TKE input in the CONTROL simulation which generated stronger turbulent mixing in winter and autumn in all six regions. In Figure 4.11, the $Ri$ (solid curve) shows that the upper $50\,m$ of the water column is more stable (larger $Ri$) in the CALM simulation (green line) than in the CONTROL simulation (red line). In fact, the turbulent period (number of days with $Ri \leq 0.25$) is longer in the CONTROL simulation than in the CALM simulation, which causes more nutrients to be up-welled to surface waters during winter, and thus results in the larger spring bloom of the CONTROL simulation (e.g. nutrient limitation is lower in the CONTROL simulation).

We find that the spring bloom is thus, a function of the intensity of winter mixing, which pre-conditions surface waters' nutrient concentration. Meanwhile, the autumn bloom is a function of the timing of turbulent mixing (i.e. day of $Ri \leq 0.25$) and the light availability on the day turbulence begins. In Figure 4.12, by comparing the CONTROL (circles) and the CALM (squares) simulations we show that in spring, a deeper mixed layer in the CONTROL simulation corresponded with higher nutrient and higher chlorophyll-a concentration (size of the shape). However, even though nutrient concentration in the two simulations is similar at the beginning of turbulence, the photosynthetically available radiation (PAR) is consistently higher in the CONTROL simulation
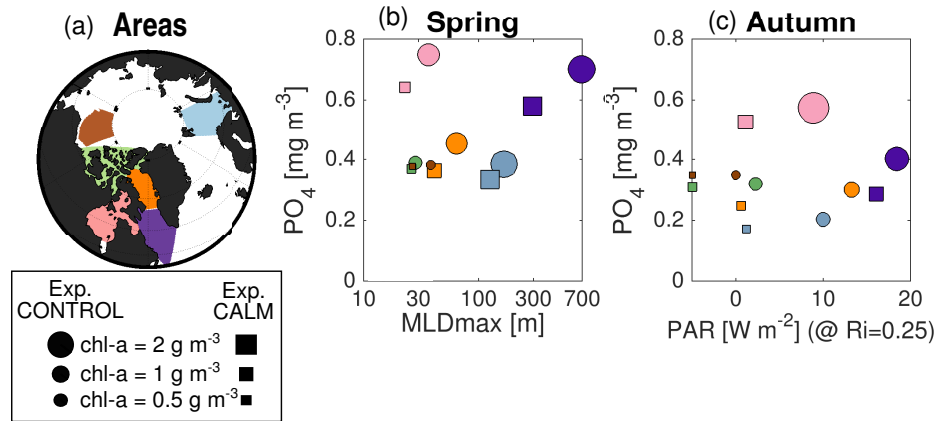
**Figure 4.12.** Controls of the phytoplankton bloom in spring and autumn for the six regions. (a) Map presenting the spatial definition of the region. (b) Drivers of the spring bloom: maximum winter mixed layer (MLDmax) depth defines the nutrient concentration in spring (Mar - May). (c) Drivers of the autumn bloom: light (on the day $Ri < 0.25$) and nutrient concentration in autumn (Oct - Dec) define if phytoplankton can bloom. The different colours in b and c correspond with the regions in (a). In (b) and (c) the circles represent the CONTROL simulation and square the CALM simulation with the size of being the total amount of chlorophyll-a (chl-a) concentration over the specified period.

because the turbulent conditions start in early autumn while in the CALM simulation the turbulent conditions start later in autumn. It is this earlier start of turbulence that allows phytoplankton to grow as nutrient concentrations increase because light is not yet limiting (compare individual basins in the CONTROL and CALM simulations in Figure 4.12c). We estimated a threshold of $PAR \leq 5\,Wm^{-2}$ for autumn light limitation in our simulations, since under this light condition a fall bloom did not develop in Hudson Bay, Baffin Bay or Barents Sea (green area in Figure 4.11c-e). However there is one exception, in the CALM simulation when turbulence begins in the Labrador Sea, $PAR > 5\,Wm^{-2}$, yet there is no increase in chlorophyll-a concentration (green area in Figure 4.11f). This can be explained by the lower nutrient concentration and a rapid decrease in PAR due to deepening of the mixed layer due to large heat losses in autumn. Note that the turbulence starts at the beginning of Oct in the CALM simulation, while in the CONTROL simulation the autumn bloom has already started to decline due to light limitations (red area in Figure 4.11f).

In autumn, the initiation of turbulent mixing is earlier in the CONTROL simulation, this causes an early nutrient replenishment of surface waters which immediately stimulates the autumn bloom in the CONTROL simulation. Our obduction analysis shows how in the CONTROL simulation (red in Figure 4.13c-f), the earlier turbulent mixing (red vertical dashed line) leads to earlier nutrient up-welling (positive red values). The increasing nutrient concentrations in surface waters then causes the reduction of the nutrient limitation to phytoplankton growth (filled circles approaching a minimum in Figure 4.11) and results in higher autumn chlorophyll-a concentration in the CONTROL simulation relative to the CALM simulation (red and green shade in Figure 4.11). In contrast, in the CALM simulation, turbulent mixing starts later in the fall (green vertical line in Figure 4.13)
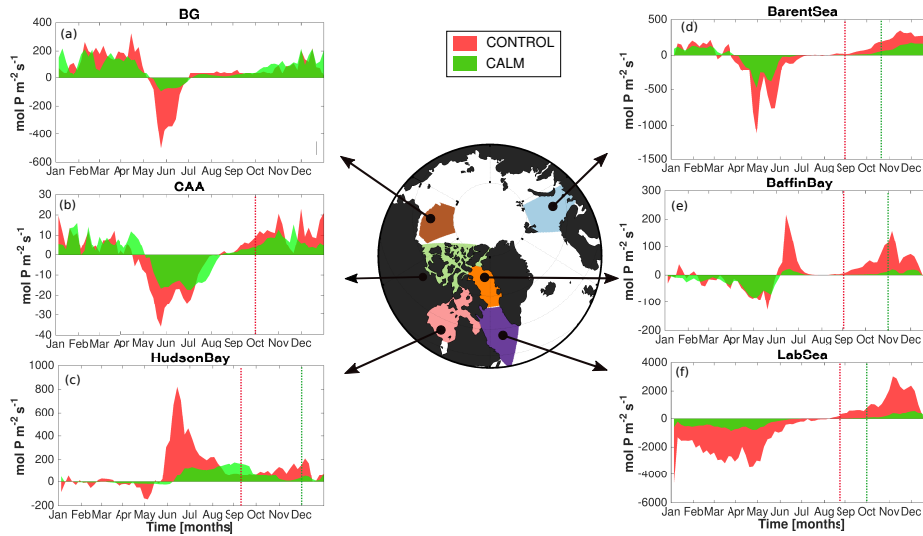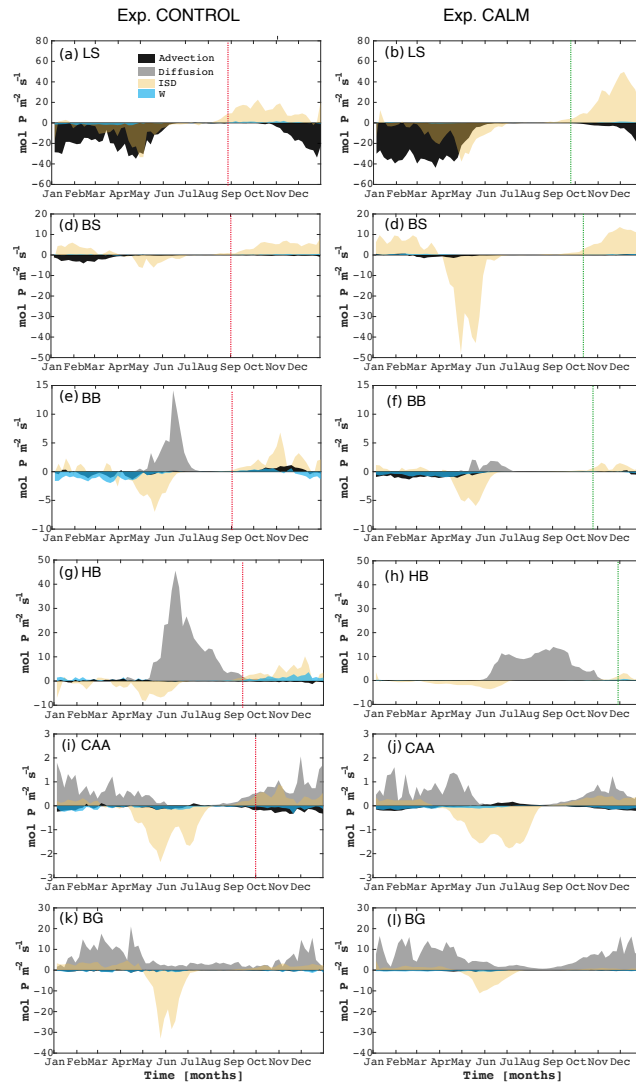
**Figure 4.13.** Five day climatology (2002-2015) of net down-welling (negative) and up-welling (positive) of nutrients across the isopynal that defines the $50\,m$ depth in the CONTROL (red) and CALM (green) simulation in each basin. Doted lines indicate the day the water column becomes turbulent in autumn. Absence of a doted line implies that simulation did not become turbulent in this region. Nutrient refers to dissolved inorganic phosphate which in our model has the role of limiting macronutrient.

and although it also leads to the up-welling of nutrients (positive green shade in Oct in Figure 4.13), light has already become limiting and phytoplankton cannot grow.

The deepening of the isopycnals in the main process driving the obduction of nutrients in autumn (yellow shade in Figure 4.14). Throughout the year, the processes dominating up-welling and down-welling of nutrients varied between regions, but were similar between simulations (Figure 4.14).

In ice-free regions, there was a balance between down-welling by horizontal advection (black shade in Figure 4.14 a-d) at the base the layer and up-welling by isopycnal deepening (yellow shade in Figure 4.14 a-d). In perennial ice-covered regions diffusion (grey shade in Figure 4.14 i-l) was dominating the up-welling year-round, while deepening of the isopycnal down-welled nutrients in summer and up-welled nutrients in winter and autumn. The dominant role of diffusion is likely associated with the strong summer stratification of these regions (Tremblay et al., 2011). Additionally, in our simulation, the melting sea ice diluted the nutrient concentration at the surface ocean, further strengthening the vertical nutrient gradient.

In seasonally ice-cover regions, diffusive flux also had a dominant role up-welling nutrients, however only in summer. In Hudson Bay, the autumn up-welling of nutrients was driven by a deepening of the isopycnal and vertical advection across the base of the isopycnal, while in winter there was little to no exchange of nutrients (Figure 4.14 g-h). In Baffin Bay, the autumn up-welling was primarily driven by the deepening of the isopycnal, meanwhile in winter there was primary a down-welling of nutrients due to vertical and horizontal advection across the base of the layer (Figure 4.14 e-f).

**Figure 4.14.** Monthly climatology (2002-2015) of the different components of equation 4.4 describing the up-welling (positive) and down-welling (negative) of dissolved inorganic phosphate across the isopycnal that defines the $50\,m$ depth in the CONTROL simulation (left) and CALM simulation (right) in each basin. Doted lines indicate the day the water column becomes turbulent in autumn. The absence of doted line implies that the layer did not became turbulent in the region. Note that the range of the y-axis is different in each panel.

Particularly in Hudson Bay there was a relatively high chlorophyll-a concentration in summer compared to other regions. Our obduction analysis suggest that this was maintained by a strong upward diffusive flux. This diffusive flux was present in both the CALM and the CONTROL simulation but it was largest in the CALM simulation which had the strongest stratification. The diffusive flux was likely supported by a high re-mineralization rate below the surface, and may also be a function of the basin depth. For example in Hudson Bay the shallow bathymetry (maximum depth $250\,m$ and mean depth of $100\,m$) helps maintains the high nutrient concentration below the surface, because all organic material that reaches the ocean floor is returned to the water column as inorganic. This acts as a bottom flux of phosphate that helps maintain the phosphate gradient

in Hudson Bay due to its relative proximity to our chosen isopycnal at $50\,m$ depth. In contrast, in Baffin Bay, with maximum depth of $2,500\,m$ and mean depth of $1000\,m$, this bottom flux has very little influence on the diffusive gradient.

## 4.5.2  Sensitivity to ice cover changes

Sensitivity to sea ice loss was addressed in perennial and seasonal ice-covered regions in each simulation. In perennial ice-covered regions we measured the influence of sea ice loss by comparing years with large and small mean annual ice-free area (Figure 4.15a,b). In seasonal ice-covered regions we measured the influence of sea ice loss by comparing years with long versus short ice-free season length (Figure 4.15c,d). Therefore in this study, high ice loss refers to years with large ice-free area or long ice-free seasons, and low sea ice loss refers to years with small ice-free area or short ice-free season.

Years with high and low sea ice loss were selected independently in each simulation and each basin (Figure 4.15). The differences in productivity between years with high and low sea ice losses in the CONTROL simulation help identify which of the regions would benefit from the loss of sea ice in the presence of stormy winds. While the differences between high and low sea ice loss in the CALM simulation helps identify regions that would benefit from the loss of sea ice in the absence of stormy winds.
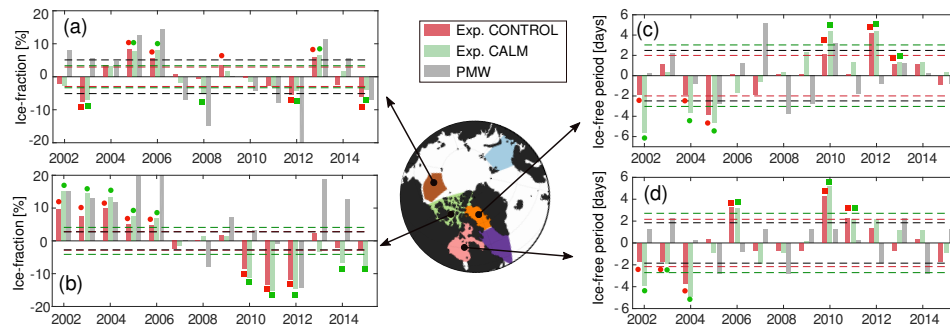


**Figure 4.15.** Selection of high and low sea ice loss years in perennial and seasonal ice-covered regions. Simulated (CONTROL and CALM) and observed (PMW) ice concentration anomalies in (a) Beaufort Sea and (b) Canadian Arctic Archipelago, and ice-free season anomaly in (c) Baffin Bay and (d) Hudson Bay. Symbols mark years selected to build a climatology of high sea ice loss (squares) and low sea ice loss (circles) for the analysis of Figure 4.16 and Table 4.2.

**Productivity and carbon export**

In Baffin Bay and the Beaufort Sea, sea ice loss had no significant effect on the annual primary production or biogenic carbon export in either simulation (Table 4.2). In Hudson Bay, a longer ice-free period significantly increased primary production (11%) in the CONTROL simulation, but primary production was not affected in

the CALM simulation (Table 4.2). Meanwhile in the Canadian Arctic Archipelago years with larger ice-free area significantly increased the annual mean primary production (20%) and biogenic carbon export (16%) with and without the presence of stormy winds.

**Phenology and bloom dynamics**

In the Beaufort Sea, the size of the open water area had no effect on the seasonality of chlorophyll-a or water column stability (Figure 4.16b,f). However, the mean difference in the ice-free area between years with high and low sea ice loss was less than 15% which may not be sufficient to generate significant changes (Table 4.2). In the Canadian Arctic Archipelago, where the difference in open water region between high and low sea ice was on average 20%, the chlorophyll-a concentration was higher in years with high sea ice loss in both the CONTROL and CALM simulation, and especially at the beginning of spring and the end of autumn (Figure 4.16c,g, Table 4.2). This may also suggest that in the Canadian Arctic Archipelago, wind-mixing is not the dominant source of mixing and up-welling. This is supported by a recent study suggesting that the primary source of turbulent mixing within the Canadian Arctic Archipelago is the complex topography (Hughes et al., 2017). Indeed, up-welling of nutrients in the Canadian Arctic Archipelago in the CONTROL and CALM simulation is similar ($\leq 5\,mol\,m^{-2}\,s^{-1}$; Figure 4.13b).

In Hudson Bay, years with a longer ice-free period resulted in an early start of the spring bloom and a later end of the fall bloom in the CONTROL simulation, which resulted in higher primary productivity but this was not the case in the CALM simulation. This suggests that in the future, sea ice loss in Hudson Bay may only enhance productivity if it is accompanied by stormy winds. In Baffin Bay, we found that a longer ice-free period, may actually result in lower productivity and biogenic carbon export (results not significant; Table 4.2).

In seasonally ice-covered regions the loss of sea ice leads to relatively weaker stratification in both the CONTROL and CALM simulations (Figure 4.16d-k). However, in the CALM simulation, the longer ice-free season in Hudson Bay leads to higher stratification during winter-spring period (Jan - Jun) (Figure 4.16k). With a long ice-free season, and in the absence of stormy winds, it is more difficult to break the summer stratification in winter due to large heat accumulation in surface waters. Additionally, because of the shorter ice-cover season, there is also lower sea ice formation and thus less brine rejection, a process that also contributes to the mixing of the surface waters.

**Table 4.2.** Quantifying the role of sea ice loss in: Hudson Bay (HB), Baffin Bay (BB), Canadian Arctic Archipelago (CAA), and Beaufort Sea (BG).

| | CONTROL | | | | CALM | | | |
|---|---|---|---|---|---|---|---|---|
| Productivity $[mgCm^{-2}d^{-1}]$ | HB | BB | BG | CAA | HB | BB | BG | CAA |
| Long/Large (std) | 320.94 (6) | 199.15 (24) | 55.56 (10) | 112.09 (1) | 163.56 (2) | 137.83 (7) | 45.80 (12) | 96.17 (3) |
| Short/Small (std) | 285.17 (15) | 208.10 (28) | 40.24 (8) | 90.76 (7) | 179.02 (25) | 146.21 (23) | 31.24 (5) | 72.95 (4) |
| $\Delta[\%]$ | 11.15 | -2.99 | 27.57 | 19.03 | -9.45 | -6.08 | 31.78 | 24.14 |
| p-value | 0.015 | 0.984 | 0.686 | < 0.01 | 0.776 | 0.796 | 0.865 | < 0.01 |
| Export $[mgCm^{-2}d^{-1}]$ | | | | | | | | |
| Long/Large (std) | 96.45 (1) | 71.14 (10) | 18.21 (4) | 36.32 (1) | 54.01 (3) | 48.91 (2) | 14.96 (5) | 33.98 (1) |
| Short/Small (std) | 90.70 (3) | 73.34 (11) | 12.21 (3) | 30.51 (2) | 61.96 (7) | 52.63 (8) | 9.39 (2) | 25.09 (1.3) |
| $\Delta[\%]$ | 5.96 | -3.09 | 30.15 | 16.00 | -14.07 | -7.61 | 37.22 | 26.16 |
| p-value | 0.071 | 0.922 | 0.362 | < 0.01 | 0.194 | 0.688 | 0.636 | < 0.01 |
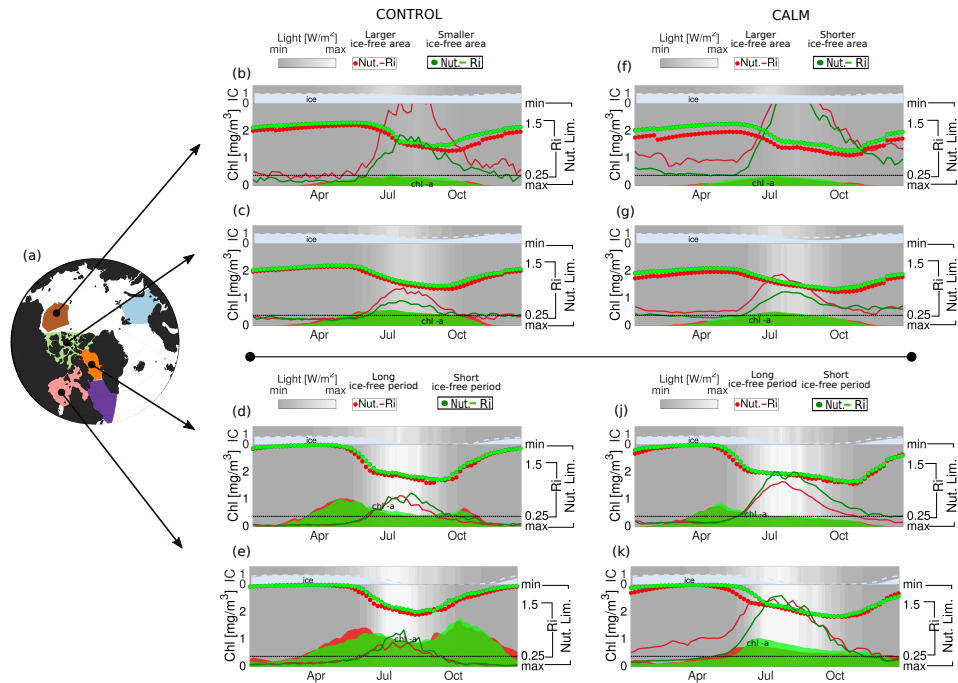
**Figure 4.16.** Impact of sea ice loss on the seasonality of chlorophyll-concentration. A climatology of simulated years with high sea ice loss (red) are compared to a climatology of years with low sea ice loss (green). (a) Map inset with the regions where sea ice loss was assessed. (b-e) Results form the CONTROL simulation. (f-g) Results from the CALM simulation. Each panel shows the 5 daily mean: sea ice concentration (gray shade), solar radiation above the sea ice and the photosynthetically available radiation below the sea ice (grey-white background), chlorophyll-a (chl-a) concentration (red and green shade), nutrient limitation (filled circles), and turbulence expressed as the Richardson number ($Ri$; solid line), turbulence threshold, $Ri = 0.25$ (dotted black line). PAR, chl-a, $Ri$, and nutrient limitation are averaged over the top $50\,m$. Note the inverted scale of the nutrient limitation.

## 4.6 Discussion

Our modelling experiments revealed that stormy wind events add significant amount of energy to surface waters that is then transformed into turbulent mixing. This energy is key in generating surface mixing in early autumn, causing an early deepening of the isopycnals, and contributing to the up-welling of nutrients before light becomes a limiting factor for phytoplankton to grow. Through these mechanisms, stormy wind events become key facilitators for large phytoplankton blooms in autumn.

The CALM simulation with no autumn bloom helps confirm Ardyna et al. (2014)'s hypothesis attributing the more frequent development of the autumn bloom since 2002 to increasing stormy wind events in the Arctic. We are able to geographically expand this hypothesis to subarctic regions like the Hudson Bay and the Labrador Sea, where mixing induced by the high-frequency wind events caused a three fold increase in the chlorophyll-a concentration in our simulations. Arctic regions with a perennial ice-cover had the smallest response to the stormy winds because the sea ice acts as a barrier to the wind-ocean energy exchange.

While the autumn bloom was strongly dependant on the wind-mixing, the spring bloom magnitude was only slightly reduced in the absence of stormy winds. A possible explanation is that in these northern environments, turbulent mixing is also generated by increasing density of the surface water during winter by atmospheric temperature cooling (e.g. high ocean heat losses) and sea ice formation (e.g. brine rejection). Therefore, even without stormy winds a turbulent state can still be reached during winter due to convective mixing. The main difference in our experiments was in the timing, the intensity, and the length of mixing, all of which were favoured in the simulation with stormy winds (e.g. earlier mixing, higher intensity and longer mixing period). Stormy winds led to higher nutrient concentrations at the surface in spring which sustained a larger spring bloom in the CONTROL simulation.

We find that sea ice losses also have the potential to increase primary production in regions with seasonal and perennial ice-covered when stormy winds are present. Perennial ice-covered regions, which are strongly limited by light, may also respond positively to the loss of sea ice, in the absence of stormy winds. However, for a positive effect, ice-losses need to be greater than 20% of the area generally covered.

Combining the response of phytoplankton to stormy wind events and sea ice loss helped us identify regions where phytoplankton productivity is most dependant on the wind-induced mixing, and those which are most dependant on sea ice loss. Hudson Bay and the Labrador Sea were examples of the former. In these two basins stormy winds are responsible for 30% and 46% of the productivity, respectively. These regions are currently located in the path of the North Atlantic storm track, which is predicted to move further north (Wang et al., 2017). This raises questions about future sustainability and productivity in these two regions. On the other hand, our experiments suggest that regions like the Canadian Arctic Archipelago, which is currently strongly limited by light, may become more productive under a larger sea ice loss scenario.

Overall, our results suggest that high-frequency wind events play a crucial role in today's productivity and carbon export throughout the Arctic and Subarctic. In our study, the regions with higher dependence on the high-frequency wind forcing were characterized by low nutrient concentration in summer due to high productivity in spring. In these regions the early wind-induced mixing was able to help break the summer stratification and initiate an early up-welling of nutrients before light conditions became limiting in autumn, allowing phytoplankton to bloom for a second time. Sea ice loss proved to be important in perennial ice-covered regions with or without stormy wind events. Meanwhile, in seasonally ice-covered regions longer ice-free periods can increase primary productivity and biogenic carbon export only in the presence of stormy wind events.

## 4.7 Acknowledgements

# Bibliography

Amon, R., A. Rinehart, S. Duan, P. Louchouarn, A. Prokushkin, G. Guggenberger, D. Bauch, C. Stedmon, P. Raymond, R. Holmes, J. McClelland, B. Peterson, S. Walker, and A. Zhulidov (2012), Dissolved organic matter sources in large Arctic rivers, *Geochimica et Cosmochimica Acta*, *94*, 217 – 237, doi:http://dx.doi.org/10.1016/j.gca.2012.07.015.

Ardyna, M., M. Babin, M. Gosselin, E. Devred, L. Rainville, and J.-E. Tremblay (2014), Recent Arctic Ocean sea ice loss triggers novel fall phytoplankton blooms, *Geophysical Research Letters*, *41*(17), 6207–6212, doi:10.1002/2014GL061047.

Arrigo, K. R., G. van Dijken, and S. Pabi (2008), Impact of a shrinking Arctic ice cover on marine primary production, *Geophysical Research Letters*, *35*(19), doi:10.1029/2008GL035028, 119603.

Bamber, J., M. den Broeke, J. Ettema, J. Lenaerts, and E. Rignot (2012), Recent large increases in freshwater fluxes from Greenland into the North Atlantic, *Geophysical Research Letters*, *39*(19), doi:10.1029/2012GL052552.

Bhatia, M. P., E. B. Kujawinski, S. B. Das, C. F. Breier, P. B. Henderson, and M. A. Charette (2013), Greenland meltwater as a significant and potentially bioavailable source of iron to the ocean, *Nature Geoscience*, *6*, 274, doi:10.1038/ngeo1746.

Camara Lins, R., J.-M. Martinez, D. d. Motta Marques, J. A. Cirilo, and C. R. Fragoso (2017), Assessment of chlorophyll-a remote sensing algorithms in a productive tropical estuarine-lagoon system, *Remote Sensing*, *9*(516), doi:10.3390/rs9060516.

Carranza, M. M., and S. T. Gille (2015), Southern Ocean wind-driven entrainment enhances satellite chlorophyll-a through the summer, *Journal of Geophysical Research: Oceans*, *120*(1), 304–323, doi:10.1002/2014JC010203.

Cavalieri, D. J., J. P. Crawford, M. R. Drinkwater, D. T. Eppler, L. D. Farmer, R. R. Jentz, and C. C. Wackerman

(1991), Aircraft active and passive microwave validation of sea ice concentration from the Defense Meteorological Satellite Program special sensor microwave imager, *Journal of Geophysical Research: Oceans*, *96*(C12), 21,989–22,008, doi:10.1029/91JC02335.

Comiso, J. C. (2000 updated 2015), Bootstrap sea ice concentration from Nimbus-7 SMMR and DMSP SSM/I, Version 2 [1979 - 2016], *NASA DAAC at National Snow and Ice Data Centre, Boulder, CO*.

Comiso, J. C., and R. Kwok (1996), Surface and radiative characteristics of the summer Arctic sea ice cover from multisensor satellite observations, *Journal of Geophysical Research: Oceans*, *101*(C12), 28,397–28,416, doi: 10.1029/96JC02816.

Comiso, J. C., D. J. Cavalieri, C. L. Parkinson, and P. Gloersen (1997), Passive microwave algorithms for sea ice concentration: A comparison of two techniques, *Remote Sensing of Environment*, *60*(3), 357 – 384, doi:http://dx.doi.org/10.1016/S0034-4257(96)00220-9.

Comiso, J. C., C. L. Parkinson, R. Gersten, and L. Stock (2008), Accelerated decline in the Arctic sea ice cover, *Geophysical Research Letters*, *35*(1), L01,703.

Comiso, J. C., W. N. Meier, and R. Gersten (2017), Variability and trends in the Arctic Sea ice cover: Results from different techniques, *Journal of Geophysical Research: Oceans*, *122*(8), 6883–6900, doi: 10.1002/2017JC012768.

Dai, A., T. Qian, T. K. T., and M. J. D. (2009), Changes in continental freshwater discharge from 1948-2004, *Journal of Climate*, *22*, 2773–2791.

Day, J. J., M. M. Holland, and K. I. Hodges (2017), Seasonal differences in the response of Arctic cyclones to climate change in CESM1, *Climate Dynamics*, doi:10.1007/s00382-017-3767-x.

Deser, C., J. E. Walsh, and M. S. Timlin (2000), Arctic sea ice variability in the context of recent atmospheric circulation trends, *Journal of Climate*, *13*(3), 617–633, doi:10.1175/1520-0442(2000)013⟨0617:ASIVIT⟩2.0.CO;2.

Galbraith, E. D., A. Gnanadesikan, J. P. Dunne, and M. R. Hiscock (2010), Regional impacts of iron-light colimitation in a global biogeochemical model, *Biogeosciences*, *7*(3), 1043–1064, doi:10.5194/bg-7-1043-2010.

Galbraith, E. D., J. P. Dunne, A. Gnanadesikan, R. D. Slater, J. L. Sarmiento, C. O. Dufour, G. F. de Souza, D. Bianchi, M. Claret, K. B. Rodgers, and S. S. Marvasti (2015), Complex functionality with minimal computation: Promise and pitfalls of reduced-tracer ocean biogeochemistry models, *Journal of Advances in Modeling Earth Systems*, *7*(4), 2012–2028, doi:10.1002/2015MS000463.

Garcia, H. E., R. A. Locarnini, T. P. Boyer, J. I. Antonov, O. Baranova, M. Zweng, J. Reagan, and D. Johnson (2014), World Ocean Atlas 2013: Dissolved inorganic nutrients (phosphate, nitrate, silicate), *S. Levitus, Ed., A. Mishonov Technical Ed., NOAA Atlas NESDIS*, *4*.

Ginoux, P., M. Chin, I. Tegen, J. M. Prospero, B. Holben, O. Dubovik, and S.-J. Lin (2001), Sources and distributions of dust aerosols simulated with the GOCART model, *Journal of Geophysical Research: Atmospheres*, *106*(D17), 20,255–20,273, doi:10.1029/2000JD000053.

Goyens, C., C. Jamet, and T. Schroeder (2013), Evaluation of four atmospheric correction algorithms for MODIS-Aqua images over contrasted coastal waters, *Remote Sensing of Environment*, *131*, 63 – 75, doi: https://doi.org/10.1016/j.rse.2012.12.006.

Griffin, C., J. McClelland, K. Frey, G. Fiske, and R. Holmes (2018), Quantifying CDOM and DOC in major Arctic rivers during ice-free conditions using Landsat TM and ETM+ data, *Remote Sensing of Environment*, *209*, 395 – 409, doi:https://doi.org/10.1016/j.rse.2018.02.060.

Group, O. B. P. (2003), BMODIS Aqua Level 3 Global Daily Mapped 9 km Chlorophyll a. Ver. 6, *DAAC CA USA. Dataset accessed [2017-02-20]*.

Guéguen, C., C. W. Cuss, C. J. Cassels, and E. C. Carmack (2014), Absorption and fluorescence of dissolved organic matter in the waters of the Canadian Arctic Archipelago, Baffin Bay, and the Labrador Sea, *Journal of Geophysical Research: Oceans*, *119*(3), 2034–2047, doi:10.1002/2013JC009173.

Harrison, W. G., and G. F. Cota (1991), Primary production in polar waters: relation to nutrient availability, *Polar Research*, *10*(1), 87–104, doi:10.3402/polar.v10i1.6730.

Holdsworth, A. M., and P. G. Myers (2015), The influence of high-frequency atmospheric forcing on the circulation and deep convection of the Labrador Sea, *Journal of Climate*, *28*(12), 4980–4996, doi: 10.1175/JCLI-D-14-00564.1.

Holmes, R. M., J. W. McClelland, B. J. Peterson, S. E. Tank, E. Bulygina, T. I. Eglinton, V. V. Gordeev, T. Y. Gurtovaya, P. A. Raymond, D. J. Repeta, R. Staples, R. G. Striegl, A. V. Zhulidov, and S. A. Zimov (2012), Seasonal and annual fluxes of nutrients and organic matter from large rivers to the Arctic Ocean and surrounding seas, *Estuaries and Coasts*, *35*(2), 369–382, doi:10.1007/s12237-011-9386-6.

Huang, C., and F. Qiao (2009), The relationship between sea surface temperature anomaly and wind energy input in the Pacific Ocean, *Progress in Natural Science*, *19*(10), 1409 – 1412, doi:http://dx.doi.org/10.1016/j.pnsc.2009.03.004.

Hughes, K. G., J. M. Klymak, X. Hu, and P. G. Myers (2017), Water mass modification and mixing rates in a 1/12° simulation of the canadian arctic archipelago, *Journal of Geophysical Research: Oceans*, *122*(2), 803–820, doi:10.1002/2016JC012235.

Karleskind, P., M. Lévy, and L. Memery (2011), Subduction of carbon, nitrogen, and oxygen in the northeast Atlantic, *Journal of Geophysical Research: Oceans*, *116*(C2), doi:10.1029/2010JC006446.

Kauker, F., R. Gerdes, M. Karcher, C. Köberle, and J. L. Lieser (2003), Variability of Arctic and North Atlantic sea ice: A combined analysis of model results and observations from 1978 to 2001, *Journal of Geophysical Research: Oceans*, *108*(C6), doi:10.1029/2002JC001573.

Kohout, A. L., M. J. M. Williams, S. M. Dean, and M. H. Meylan (2000), Storm-induced sea-ice breakup and the implications for ice extent, *Nature*, *509*(7502), 604–607, doi:10.1038/nature13262.

Lacour, L., H. Claustre, L. Prieur, and F. D'Ortenzio (2014), Phytoplankton biomass cycles in the North Atlantic subpolar gyre: A similar mechanism for two different blooms in the Labrador Sea, *Geophysical Research Letters*, *42*(13), 5403–5410, doi:10.1002/2015GL064540.

Large, W. G., and S. G. Yeager (2009), The global climatology of an interannually varying air–sea flux data set, *Climate Dynamics*, *33*(2), 341–364, doi:10.1007/s00382-008-0441-3.

Madec, G., and the NEMO team (2008), *NEMO ocean engine*, Note du Pôle de modélisation, Institut Pierre-Simon Laplace (IPSL), France, No 27, ISSN No 1288-1619.

Makshtas, A., D. Atkinson, M. Kulakov, S. Shutilin, R. Krishfield, and A. Proshutinsky (2007), Atmospheric forcing validation for modeling the central Arctic, *Geophysical Research Letters*, *34*(20), doi:10.1029/2007GL031378, l20706.

Markussen, T. N., B. Elberling, C. Winter, and T. J. Andersen (2016), Flocculated meltwater particles control Arctic land-sea fluxes of labile iron, *Scientific Reports*, *6*, 24,033, doi:10.1038/srep24033.

Masina, S., A. Storto, N. Ferry, M. Valdivieso, K. Haines, M. Balmaseda, H. Zuo, M. Drevillon, and L. Parent (2015), An ensemble of eddy-permitting global ocean reanalyses from the MyOcean project, *Climate Dynamics*, pp. 1–29, doi:10.1007/s00382.

Pabi, S., G. L. van Dijken, and K. R. Arrigo (2008), Primary production in the Arctic Ocean, 1998–2006, *Journal of Geophysical Research: Oceans*, *113*(C8), doi:10.1029/2007JC004578.

Pan, S., J. Shi, H. Gao, X. Guo, X. Yao, and X. Gong (2017), Contributions of physical and biogeochemical processes to phytoplankton biomass enhancement in the surface and subsurface layers during the

passage of Typhoon Damrey, *Journal of Geophysical Research: Biogeosciences*, *122*(1), 212–229, doi: 10.1002/2016JG003331.

Rumyantseva, A., N. Lucas, T. Rippeth, A. Martin, S. C. Painter, T. J. Boyd, and S. Henson (2015), Ocean nutrient pathways associated with the passage of a storm, *Global Biogeochemical Cycles*, *29*(8), 1179–1189, doi:10.1002/2015GB005097.

Sathiyamoorthy, S., and G. W. K. Moore (2002), Buoyancy flux at ocean weather station Bravo, *Journal of Physical Oceanography*, *32*(2), 458–474, doi:10.1175/1520-0485(2002)032⟨0458:BFAOWS⟩2.0.CO;2.

Serreze, M. C., M. M. Holland, and J. Stroeve (2007), Perspectives on the Arctic's shrinking sea-ice cover, *Science*, *315*(5818), 1533–1536, doi:10.1126/science.1139426.

Simmonds, I., and I. Rudeva (2012), The great Arctic cyclone of August 2012, *Geophysical Research Letters*, *39*(23), doi:10.1029/2012GL054259, l23709.

Smith, G. C., F. Roy, P. Mann, F. Dupont, B. Brasnett, J.-F. Lemieux, S. Laroche, and S. Bélair (2014), A new atmospheric dataset for forcing ice–ocean models: Evaluation of reforecasts using the Canadian global deterministic prediction system, *Quarterly Journal of the Royal Meteorological Society*, *140*(680), 881–894, doi:10.1002/qj.2194.

Steele, M., R. Morley, and W. Ermold (2001), PHC: A global ocean hydrography with a high-quality Arctic Ocean, *Journal of Climate*, *14*(9), 2079–2087.

Torres-Valdés, S., T. Tsubouchi, S. Bacon, A. C. Naveira-Garabato, R. Sanders, F. A. McLaughlin, B. Petrie, G. Kattner, K. Azetsu-Scott, and T. E. Whitledge (2013), Export of nutrients from the Arctic Ocean, *Journal of Geophysical Research: Oceans*, *118*(4), 1625–1644, doi:10.1002/jgrc.20063.

Tremblay, J.-E., S. Bélanger, D. G. Barber, M. Asplin, J. Martin, G. Darnis, L. Fortier, Y. Gratton, H. Link, P. Archambault, A. Sallon, C. Michel, W. J. Williams, B. Philippe, and M. Gosselin (2011), Climate forcing multiplies biological productivity in the coastal Arctic Ocean, *Geophysical Research Letters*, *38*(18), L18,604, doi:10.1029/2011GL048825.

Vancoppenolle, M., T. Fichefet, H. Goosse, S. Bouillon, G. Madec, and M. A. M. Maqueda (2009), Simulating the mass balance and salinity of Arctic and Antarctic sea ice. 1. Model description and validation, *Ocean Modelling*, *27*(1–2), 33–53, doi:10.1016/j.ocemod.2008.10.005.

Wang, J., H.-M. Kim, and C. E.K.M. (2017), Changes in Northern Hemisphere winter storm tracks under the background of Arctic amplification, *Journal of Climate*, *30*, 3705–3724, doi:10.1175/JCLI-D-16-0650.1.

Weise, A. M., M. Levasseur, F. Saucier, S. Senneville, E. Bonneau, S. Roy, G. Sauvé, S. Michaud, and J. Fauchot (2002), The link between precipitation, river runoff, and blooms of the toxic dinoflagellate Alexandrium tamarense in the St. Lawrence, *Canadian Journal of Fisheries and Aquatic Sciences*, *59*(3), 464–473, doi: 10.1139/f02-024.

Williams, R. G., V. Roussenov, and M. J. Follows (2006), Nutrient streams and their induction into the mixed layer, *Global Biogeochemical Cycles*, *20*(1), doi:10.1029/2005GB002586.

Wu, Y., T. Platt, C. C. L. Tang, and S. Sathyendranath (2007), Short-term changes in chlorophyll distribution in response to a moving storm: a modelling study, *Marine Ecology Progress Series*, *335*, 57–68.

Yin, K., P. J. Harrison, R. H. Goldblatt, and R. J. Beamish (1996), Spring bloom in the central Strait of Georgia: interactions of river discharge, winds and grazing, *Marine Ecology Progress Series*, *138*(1/3), 255–263.

# Chapter 5

# Consequence of melting Greenland Ice Sheet on Baffin Bay heat content

Laura Castro de la Guardia, Xianmin Hu, Paul G. Myers

## 5.1    Abstract

We present results from 8 sensitivity experiments that study the relation between enhanced melt of the Greenland Ice Sheet and the observed warming of shelf waters on the northwest Greenland Shelf. We found a positive relation between melting Greenland Ice Sheet and the heat content along northwest shelf. The heat content increases in response to reduced Arctic water inflow through the Canadian Arctic Archipelago and stronger stratification in Baffin Bay. Increasing the meltwater runoff leads to positive feedbacks resulting in further freshening of surface waters and warming and shallowing of the West Greenland Irminger Water on the northwest Greenland shelf. The warmer waters could now more easily enter the Greenland fjords and provide additional heat to accelerate the melt of marine terminating glaciers. This is a potential positive feedback that requires further study as it can contribute to accelerating the melt of Greenland Ice Sheet.

## 5.2    Introduction

Baffin Bay is a semi-enclosed bay bounded by Greenland on the East, Baffin Island on the west, the Canadian Arctic Archipelago (CAA) to the north and Davis Strait (DS) to the south (Figure 5.1a). Within the basin the

circulation is cyclonic and the waters are a mix of relatively warm and saline Atlantic water, cold and low-salinity Arctic water and meltwater from the Greenland Ice Sheet. The warmer Atlantic-origin waters enter Baffin Bay at depth $(200 - 600\,m)$ in the northward-flowing West Greenland Current through eastern Davis Strait (Tang et al., 2004; Azetsu-Scott et al., 2012; Curry et al., 2014). This forms a warmer layer at subsurface depths that is hereafter referred to as the West Greenland Irminger Water (WGIW). On the surface $(30 - 200\,m)$ of the West Greenland Current and flowing over the West Greenland shelf is a colder low-salinity Arctic water that exited the Arctic Ocean through Fram Strait (Tang et al., 2004; Myers and Ribergaard, 2013). The more significant inflow of Arctic waters into Baffin Bay, however, is through three channels of the CAA: Nares Strait (NS), Jones Sound (JS) and Lancaster Sound (LS) (Tang et al., 2004; Curry et al., 2014). Within Baffin Bay Arctic-origin waters (hereafter polar water) are identified by its cold and low salinity signal and depth between $30 - 200\,m$ (Tang et al., 2004; Myers and Ribergaard, 2013).

The meltwater signal from the Greenland Ice Sheet is found in the upper 30m of the water column in Baffin Bay. It enters Baffin Bay as runoff and/or icebergs that break-off the tongue of marine-terminating glaciers. These glaciers end in fjords which can be more than 800m deep, but have sill depth close to $200\,m$ at the mouth (Johannessen et al., 2011; Myers and Ribergaard, 2013). The sill is the only obstacle to warm-shelf-waters getting into a fjord and contributing to the melting of the glaciers. The circulation within a fjord is driven by basal melting and subglacial discharge whereby low salinity water from melting ice rises and flows out of the fjord as a surface current (Straneo and Heimbach, 2013). This drives a return flow at depth, which in Baffin Bay, is within the depth-range of the WGIW (Holland et al., 2008b; Loyd et al., 2011; Myers and Ribergaard, 2013). In this framework marine-terminating glaciers in northwest Greenland are exposed to rising Atlantic ocean temperatures and Greenland's shelf heat content (Myers and Ribergaard, 2013).

The Greenland Ice Sheet meltwater runoff between 1988 and 2004 was $\sim 373\,km^3\,yr^{-1}$ (Box et al., 2006), and in 2006 it increased to $\sim 450\,km^3\,yr^{-1}$ (Rignot et al., 2011; Bamber et al., 2012; Mernild and Liston, 2012). In western Greenland, the total freshwater discharge into Baffin Bay/Labrador Sea between 1960-2010 was $\sim 190\,km^3$, yielding $\sim 283.8\,km^3\,yr^{-1}$ (Dickson et al., 2007; Mernild and Liston, 2012). In recent decades, and coinciding with warmer subsurface waters entering the fjords, the melting rate of northwest Greenland glaciers has accelerated (Straneo and Heimbach, 2013; Holland et al., 2008b; Myers and Ribergaard, 2013). With predictions of further melt from the Greenland Ice Sheet it is of concern to study how Baffin Bay shelf waters may respond to enhanced meltwater production.

Previous sensitivity studies showed that increased meltwater discharge from Greenland reduces the CAA throughflow and freshens the surface waters in Baffin Bay within 5 years (Rudels, 2011; Brunnabend et al., 2012). The Arctic inflow through the CAA is a large source of cold water and thus it has an important cooling effect on Baffin Bay. The freshening of surface waters stabilizes the near-surface water column, which reduces
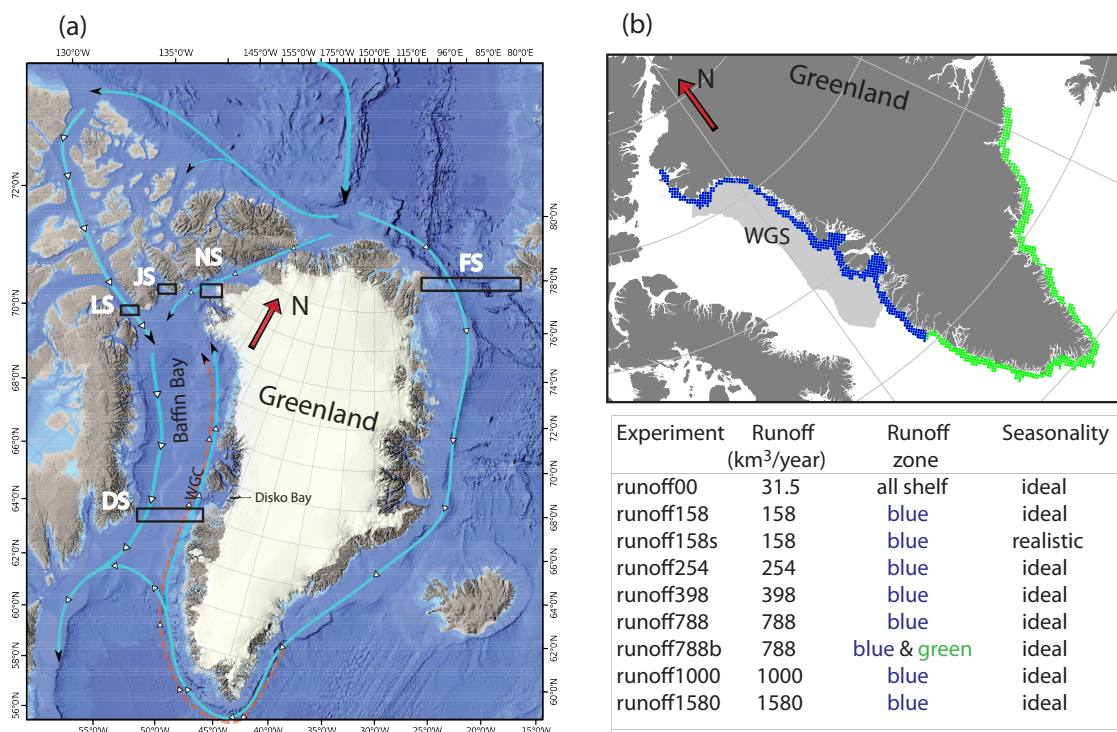
**Figure 5.1.** Study area(a) and experiment set-up (b). (a) A generalized representation of the general circulation within Baffin Bay and water exchanges. Circulation through the Canadian Arctic Archipelago (CAA, group of islands to the east of Baffin Bay) regulates the exchanges between Arctic Ocean and Baffin Bay. Cold Arctic waters enter Baffin Bay through Lancaster Sound (LS), Jones Sound (JS), Nares Strait (NS) (black boxes). Arctic water exiting through Fram Strait (FS) also enter Baffin Bay through Davis Strait (DS) in the upper 200m of the West Greenland Current (WGC). Warm Atlantic water enters Baffin Bay through DS at depth (below 200m) in the WGC (red dash line). (b) Experiments are set-up with runoff added on the northwest Greenland coast (blue shaded area). Experiment *runoff788b* include, in addition to runoff in the northwest, runoff along the southwest and southeast coast (green shaded area). Calculations of temperature and heat content of the West Greenland Shelf (WGS) are done by integrating the temperature and heat changes within the gray shaded region. Bellow is a list of the experiments with details on the experimental set-up.

| Experiment | Runoff (km$^3$/year) | Runoff zone | Seasonality |
|---|---|---|---|
| runoff00 | 31.5 | all shelf | ideal |
| runoff158 | 158 | blue | ideal |
| runoff158s | 158 | blue | realistic |
| runoff254 | 254 | blue | ideal |
| runoff398 | 398 | blue | ideal |
| runoff788 | 788 | blue | ideal |
| runoff788b | 788 | blue & green | ideal |
| runoff1000 | 1000 | blue | ideal |
| runoff1580 | 1580 | blue | ideal |

vertical mixing and the heat loss of the warmer subsurface water (Brunnabend et al., 2012). Based on these findings, we hypothesize that increasing runoff from Greenland could lead to a warming of the WGIW in Baffin Bay.

To test our hypothesis we set-up eight freshwater sensitivity experiments using the sea ice-ocean model NEMO (Madec and the NEMO team, 2008) for a wide range of meltwater discharge (Figure 5.1b). Although icebergs also form part of the Greenland Ice Sheet discharge into Baffin Bay, they more commonly melt south of Davis Strait (Tang et al., 2004). Thus, we assume the impact of icebergs on the freshwater content in Baffin Bay to be small compared to that of the meltwater exiting the fjords.

## 5.3 Method

### 5.3.1 Experiment set-up

We carried out eight Greenland-meltwater-sensitivity experiments. We selected a range of runoff to bracket observed Greenland freshwater discharge (Dickson et al., 2007; Box et al., 2006) and potential future loss. The smaller input experiments, with $158\,km^3\,yr^{-1}$, $294\,km^3\,yr^{-1}$ and $394\,km^3\,yr^{-1}$, are closer to the current estimates of Greenland Ice Sheet freshwater discharge. For example, for the period 1996-2008, van den Broeke et al. (2009) estimated that the total amount of meltwater runoff from Greenland was $\sim 1,500\,km^3$, yielding $\sim 131.7\,km^3\,yr^{-1}$. In western Greenland Mernild and Liston (2012) estimated that the 5 decade average (1960-2010) of freshwater runoff was $14,190\,km^3$, yielding $\sim 283.8\,km^3\,yr^{-1}$. A recent modelling study Bamber et al. (2012) suggest a north-west Greenland freshwater flux of $\sim 350\,km^3\,yr^{-1}$ between 2005-2010. The larger input experiments, with $788\,km^3\,yr^{-1}$, $1000\,km^3\,yr^{-1}$ and $1058\,km^3\,yr^{-1}$, are designed to represent a future where the meltwater runoff from the Greenland Ice Sheet has increased significantly.

In all experiments but one (*runoff788b*) the meltwater was added each year along the north-west Greenland coast uniformly as a constant virtual salt-flux (Figure 5.1b). To simulate a more real Greenland Ice Sheet melting scenario we added the meltwater also along the southwest and southeast coast of Greenland in *runoff788b* (Figure 5.1b). This experiment was designed to test if increasing meltwater runoff in southern Greenland affects Baffin Bay. This was important, since the discharge in the southeast is estimated to be half of the total Greenland mass loss between 2003-2008 (van den Broeke et al., 2009) and results from a Greenland Ice Sheet model show that both southeast and northwest have more rapid increase in freshwater discharge in recent years (2005-2010) (Bamber et al., 2012).

We assume an ideal seasonal cycle and constant melting rate and we evenly distributed runoff between May and October each year. However, to test the effect of seasonality, we ran experiment *runoff158s* with a

more realistic seasonal cycle by adding meltwater runoff with different weight on each month: 3% in May and October, 10% in June and September, 38% in July and August. In addition, a control experiment (*runoff00*) was run to use for comparison with other experiments. The runoff data for our control experiment ($< 31.5 \, km^3 \, yr^{-1}$) was obtained by interpolating to our model domain a 1x1 degree gridded monthly runoff climatology (Dai et al., 2009).

Each of our experiments ran for 10 years. This period was long enough for the initial transient behaviour to level off and show clear impacts of the enhanced Greenland Ice Sheet melt on Baffin Bay (Brunnabend et al., 2012). All our calculations and comparison were done using the last 5 years of the simulations. The heat content was calculated using a reference temperature of $0 °C$.

### 5.3.2 Model details

All simulations were carried out with a coupled ocean-sea ice model, Nucleus for European Modelling of the Ocean (NEMO) (Madec and the NEMO team, 2008), using a regional configuration covering the northern Bering Sea, Arctic Ocean, Canadian Arctic Archipelago (CAA), Nordic Seas and North Atlantic Ocean north of (LAT.45°N) (Hu and Myers, 2013). Our configuration has variable horizontal resolution ranging from $11 \, km$ in the central CAA to $15 \, km$ in the Arctic Ocean, and has 46 vertical levels. The model is initialized with the Polar science center Hydrographic Climatology (PHC 3.0) (Steele et al., 2001) and forced with version 2 forcing of the Coordinate Ocean-ice Reference Experiments data set (CORE II) normal year forcing (Large and Yeager, 2004). There is no surface relaxation for either temperature or salinity, which is important for ensuring that the freshwater signal is not damped (Marsh et al., 2010). Open boundary data are taken from a global 0.25° hindcast using the NEMO model (Barnier et al., 2006). A detail validation of our model configuration including Baffin Bay can be found in a previous study (Hu and Myers, 2013). The validation of the control experiment on year 5 shows a good approximation to recent observations of salinity, temperature, and velocity cross-section as well as volume transports at Davis Strait (Hu and Myers, 2013).

## 5.4 Results and discussion

A comparison between experiments with equal amounts of runoff but different seasonality (i.e. *runoff158* and *runoff158s*) yield similar hydrographic response in Baffin Bay (Figure 5.2b). This suggested that our ideal seasonal cycle was sufficient for examining the mean annual response of Baffin Bay to enhanced runoff. The area of the meltwater discharged, on the other hand, caused comparably larger hydrographic response. Although the physical explanation for the simulated hydrographic changes in Baffin Bay, were similar across experiment. For clarity of the presentation, we follow with a discussion of the results of experiments with enhanced runoff
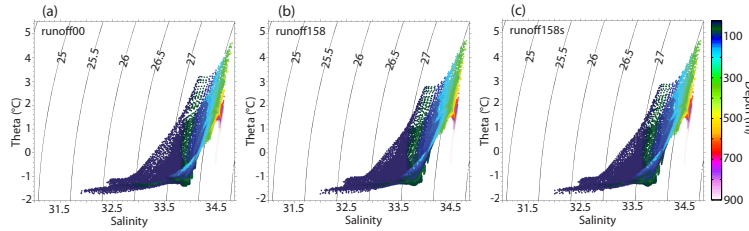
**Figure 5.2.** Potential temperature (theta) and salinity plot for Baffin Bay water in the last year of the simulation: (a) control, (b) *runoff158* with runoff added with an idealized seasonality from May to October, and (c) *runoff158s* with runoff added with a more realistic seasonality (see method). Comparing control experiment with *runoff158* and *runoff158* where runoff has been enhanced by ($158\,km^3\,yr^{-1}$) show that surface waters (dark blue and dark green) within the salinity range of 33.5 to 34.0, and temperature range $1°C$ to $3°C$ become less dense and fresher. Similarities between panels (b) and (c) suggest that a realistic seasonal cycle for the Greenland melt has a small impact on the annual mean response in Baffin Bay.

in northwest Greenland, leaving for later the discussion of the impact of areal extent in experiment *runoff788b*.
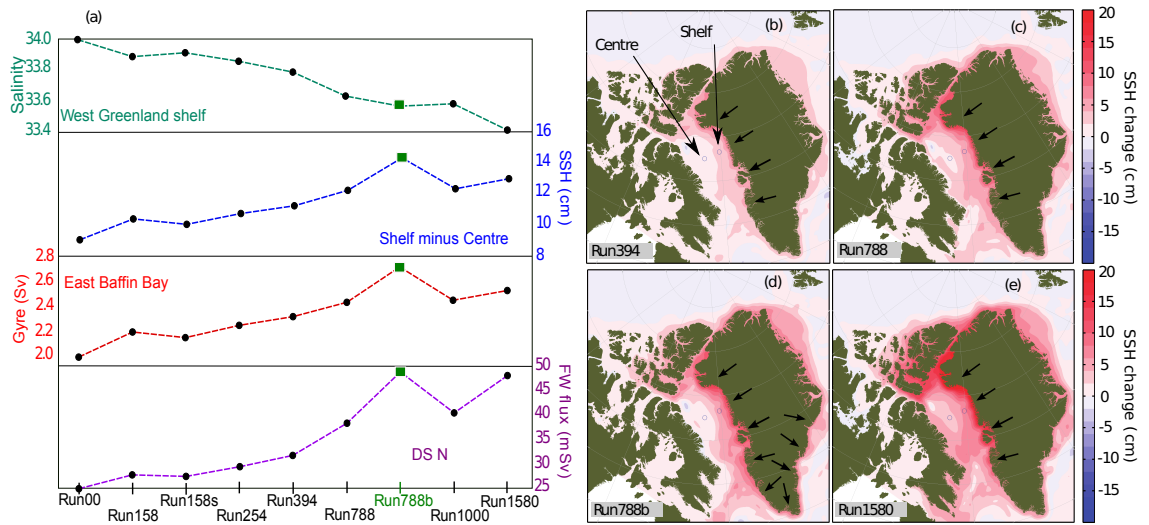
### 5.4.1 Sea surface height

Enhanced meltwater runoff from northwest Greenland Ice sheet leads to a progressive decrease in surface ($0 - 200\,m$) salinity along the northwest coast of Greenland (Figure 5.3a) that is accompanied by large sea surface height changes in Baffin Bay (Figure 5.3b-e). The largest increases in sea surface height (up to $20\,cm$) are along the Greenland's shelf. This increases the sea surface height-gradient between the coast and the centre of the Bay which leads to a strengthening of the east branch of the Baffin Bay gyre: the West Greenland Current (Figure 5.3a). A stronger West Greenland Current positively feedbacks to further reduce salinity in Baffin Bay as more low salinity water is imported through Davis Strait (Figure 5.3a).

The increasing sea surface height within Baffin Bay also affect the transport through the CAA. With raising sea surface height in Baffin Bay being accompanied by a reduction in the transport of cold-Arctic water through the CAA (by $0.2\,Sv$ to $0.9\,Sv$, from experiment *runoff158* to experiment *runoff1580*, respectively) (Figure 5.4a). Previous studies have found similar positive correlation between transport through the CAA and the sea surface height gradient between Baffin Bay and the Arctic Ocean (*Kliem and Greenberg*, 2003; Rudels, 2011). In addition, the freshening of the surface waters contributes to a stronger density stratification (Figure 5.5) that effectively reduce heat exchanges between the surface and subsurface waters (Brunnabend et al., 2012).

### 5.4.2 Temperature and heat content

Resulting from the changes in circulation and stratification, temperature and heat content on Greenland's northwest shelf increased progressively as a function of enhanced runoff (Figure 5.4a). The surface ($0 - 200\,m$) temperature on the shelf increased by $0.2°C$ in experiment *runoff394* and by $0.5°C$ in the strongest runoff ex-

**Figure 5.3.** (a) Mean response of Baffin Bay salinity, sea surface height (SSH) gradient, circulation/gyre strength, and northward David Strait (DS N) freshwater (FW) fluxes to increasing meltwater runoff from Greenland. The mean is calculated over the last four years of the simulation. Salinity changes are calculated over the west Greenland Shelf (WGS) region defined in (Figure 5.1).The SSH gradient between the shelf region and the centre of the Bay is calculated using SSH difference between the two light-blue-open-dots in panels b-e. The gyre strength is the depth integrated flux across the two light-blue-open-dots. The green square marker on the line plots highlights experiment *runoff788b* with freshwater input on all of southern and western Greenland. The panels (b-e) show the SSH anomaly relative to the control run for the last year of the simulation. Red and pink colours represent an increase in SSH relative to the control run. An abbreviated label for the experiments is at the bottom right corner of each panel, with the number in the label indicating the total amount of meltwater added per year in $km^3$.

124
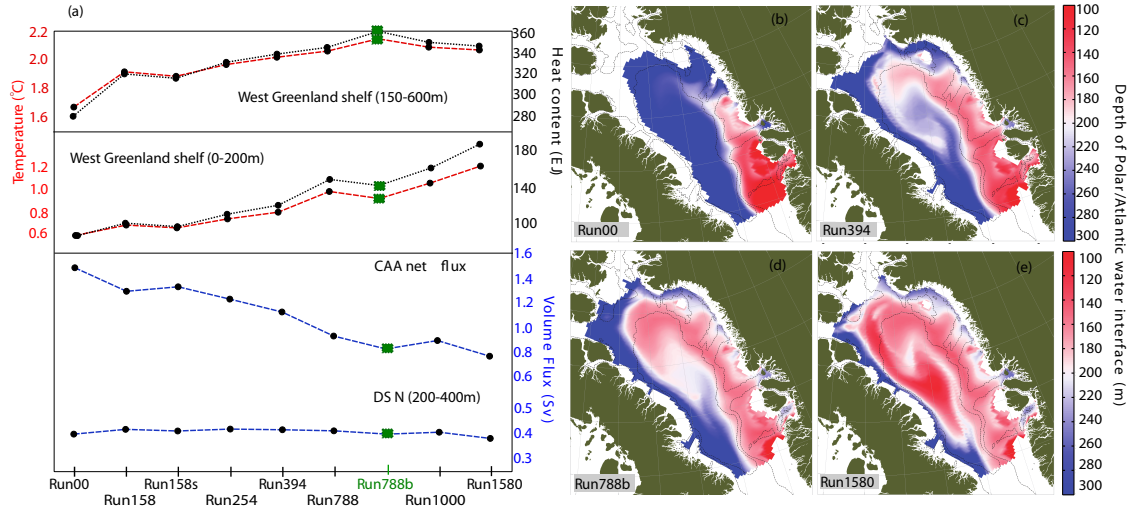
**Figure 5.4.** (a) Mean response of temperature and heat content in the west Greenland shelf (WGS) region (for definition of WGS, see Figure 5.1), and fluxes into Baffin Bay through Canadian Arctic Archipelago (CAA) and David Strait(DS) to increasing amounts of runoff from the Greenland Ice Sheet. The green square marker on the line plots highlights experiment *runoff788b* with runoff on all southern and western Greenland. The panels (b-e) show the depth of the interface between the warm West Greenland Irminger Water (WGIW) and the cold polar water in response to increasing meltwater runoff from Greenland. The transition from blue to red indicates a shallowing of this interface and thus a shallowing of the WGIW. An abbreviated label for the experiments is at the bottom right corner of each panel, with the number in the label indicating the total amount of meltwater added per year in $km^3$.
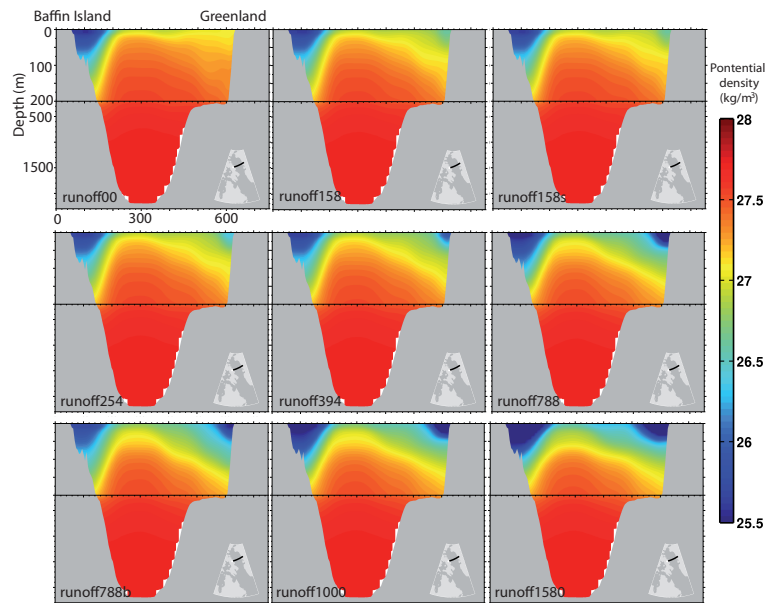


**Figure 5.5.** Potential density across a section located in the centre of Baffin Bay (see inset map). Each panel shows the mean annual density field in the last year of the simulation. Panels are organized from top-left to bottom-right in order of increasing meltwater runoff. The name of the experiment is on the bottom-left of each panel with the number indicating the total amount of runoff added in $km^3 yr^{-1}$. *Runoff00* is the control experiment where a total of ($< 31.5 km^3 yr^{-1}$) was added. The plots show how density decreases at the surface and stratification becomes stronger on the Greenland side of Baffin Bay as a function of increasing runoff.

periment, *runoff1580*, relative to the control run. In the subsurface (150-600m), temperatures warm by $0.3°C$ in *runoff394* and by $0.5°$ in *runoff1580*, also relative to the control run. Similar temperature trends on shelf waters have been detected in Baffin Bay between 1928-2000, although these were associated with an increased inflow of warmer Atlantic water across Davis Strait (Zweng and Münchow, 2006). They suggested that shelf waters have warmed by $0.15 \pm 0.08°C d^{-1}$ and the subsurface waters by $0.23 \pm 0.13°C d^{-1}$. These values compare best to the change described in experiment *runoff394*, which has meltwater discharge most similar to current-day simulated runoff from northwest Greenland (Bamber et al., 2012). This could suggest that warming of Greenland shelf waters is partially associated with the recent melting of the Greenland Ice Sheet. This conclusion is supported by a study that shows that the recent warming of the polar waters is linked to changes in circulation within Baffin Bay (Myers and Ribergaard, 2013).

As a result of increasing water temperature over the shelf, the heat content increases within the subsurface water/WGIW $(150 - 600 m)$ by $55 EJ$ in *runoff394*, and by $65 EJ$ in *runoff1580*. Similar increases in heat content are also simulated within the polar water layer $(0 - 200 m)$ compared to control run (Figure 5.4a). In Disko Bay, located in southern Baffin Bay (Figure 5.1), observations between 1977-1990 and 1996-2008 show increasing heat content (Myers and Ribergaard, 2013) of polar water $(0 - 200 m)$ and the WGIW $(200 - 600 m)$. The authors (Myers and Ribergaard, 2013) suggested the changes in heat content in eastern Baffin Bay were associated with changes in lateral exchanges which are affected by the CAA inflow. In our simulations we explain the increasing heat content in Baffin Bay by the decreasing inflow of cold Arctic waters through the CAA, and the decreasing ocean-surface heat exchanges due to the stronger halocline. Brunnabend et al. (2012) found that a stronger halocline would lead to a decreased heat exchange between the surface and subsurface layers in Baffin Bay. The main heat source in Baffin Bay is the inflow of warmer Atlantic water across Davis Strait, but this remains unchanged across experiments (Figure 5.4a) and time.

### 5.4.3 Circulation

Meanwhile, the strengthening of the cyclonic gyre in Baffin Bay causes stronger Ekman pumping that lifts the isopycnals in the centre of the Bay, and causes the shallowing of the upper interface of the WGIW (Figure 5.4b-e, Figure 5.5 (density), Figure 5.6 (temperature)). The WGIW, which is the warmest water mass in Baffin Bay (defined as $T \geq 1.5°C$ and $S = 34.1$) (Tang et al., 2004; Curry et al., 2014), rises above $200 m$ throughout most of Baffin Bay in response to increasing runoff. On the northwest Greenland shelf, the WGIW shallows to a mean depth of $100 m$ and appears in areas of northern Baffin Bay where it was not previously present. From these shallower depths the warm WGIW can be a substantial heat source to glaciers, as it can more easily overflow the sills and penetrate coastal fjords providing heat to melt the marine terminating glaciers in the region.
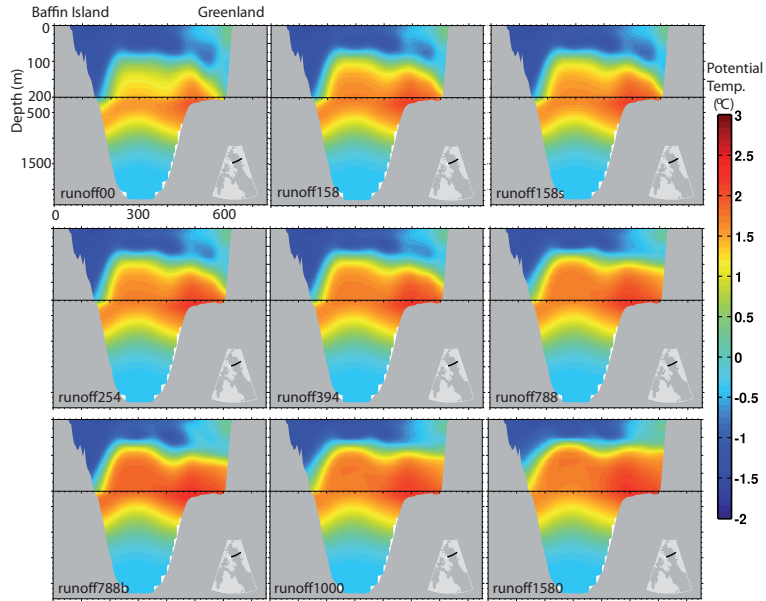
**Figure 5.6.** Potential temperature across a section located in the centre of Baffin Bay (see inset map). Each panel shows the mean annual temperature field in the last year (year 10) of the simulation. Panels are organized from top-left to bottom-right in order of increasing meltwater runoff. The name of the experiment is on the bottom-left of each panel with the number indicating the total amount of runoff added in $km^3 yr^{-1}$. *Runoff00* is the control experiment where a total of ($< 31.5 km^3 yr^{-1}$) was added. The plots show how the subsurface water layer warms, shallows and spills over the Greenland shelf as a function of increasing runoff.

The signal of the simulated circulation changes within Baffin Bay is detected at Davis Strait as a small reduction in the southward transport of Arctic Water ($0-250, m$) by $0.6 Sv$ in experiment *runoff394*, and ranges from $0.2 Sv$ to $1.2 Sv$ from *runoff158* to *runoff1580*, respectively. Mooring data at Davis Strait (Curry et al., 2014) for the periods 2004-10 and 1987-90 show a similar change ($\sim -0.5Sv$) in the southward transport of Arctic Water as in experiment *runoff394*. For the same periods, the mooring data also shows an increase (by $0.6 Sv$) in the inflow of warmer WGIW which is suggested to contribute to the increasing heat content on the northwest Greenland shelf (Holland et al., 2008a). However, in our simulations, the northward volume transport ($200-400m$) at Davis Strait is practically unaffected with a maximum volume flux change of $|0.01Sv|$ (Figure 5.4a) and small increase in heat transport ($\sim 0.5 TW$). Normally changes in the northward transport of WGIW through Davis Strait is dominated by atmospheric variability (e.g. polar cyclones in the Labrador Sea and Irminger Sea) (Curry et al., 2014). By using perpetual year forcing in our simulations we have purposely suppressed atmospheric variability to focus on the impact of enhanced meltwater production. Therefore, we can suggest that the aforementioned changes in heat content on the shelf are induced by changes in the local stratification and reduced Arctic water transport through the CAA.

### 5.4.4   Experiment runoff788b

In experiment *runoff788b*, where meltwater runoff was added from the northwest to the southeast coast of Greenland, we obtained qualitatively similar changes in Baffin Bay as those described previously, but the magnitude of the changes was larger. The main difference in this experiment compared to its twin (*runoff788*) is a larger heat transport through Davis Strait ($+0.2\,TW$, $200-400\,m$) that further increases the heat content ($+20\,EJ$) and temperature ($+0.1^{\circ}C$) of the subsurface waters ($150-600\,m$) on the west Greenland shelf (Figure 5.4a).

As in the other experiments, in *runoff788b*, salinity drops along the Greenland coast and the sea surface height gradient between the coast and the centre of the basin increases. However, because runoff is added over an extended region, both the West and the East Greenland Currents strengthen, leading to a stronger Baffin Bay gyre ($+0.3\,Sv$, relative to *runoff788*) and a larger northward freshwater transport ($0-200\,m$) across Davis Strait ($+10\,mSv$, relative to *runoff788*) (Figure 5.3a). This transport brings the meltwater runoff that was added on the southeast and southwest coast of Greenland into Baffin Bay. Therefore, even when the total freshwater runoff per year added directly into Baffin Bay in *runoff788b* was approximately half of that added in *runoff788* there was still a similar response of: mean Baffin Bay sea surface height, decline in volume transport through the CAA, increase in total northward volume transport through Davis Strait ($200-400\,m$), and increase in shelf heat content ($0-200\,m$) (Figure 5.3 and Figure 5.4). These results highlight the importance of including meltwater from all glaciers in Greenland and not only those draining directly into Baffin Bay.

## 5.5   Conclusion

Large cumulative meltwater discharge ($\sim 14,190\,km^3$) from the west Greenland Ice Sheet entered Baffin Bay/ Labrador Sea over the past 50 years, and rapid increases have been seen in the recent decade. In recent years, a warming of subsurface waters in Disko Bay was detected and associated with Baffin Bay circulation changes. In this paper, we suggest that this warming is linked to the glacier discharge. We tested the hypothesis with eight meltwater-sensitivity experiments set-up on the ocean-sea ice model. Enhanced meltwater-runoff reduced the inflow of Arctic waters and strengthened the boundary current. This increased the heat content on Greenland's northwest shelf ($+80\,EJ$) and also caused a warming ($+0.6^{\circ}C$) and shallowing (up to $50\,m$) of the WGIW. Under this new setting the WGIW can more easily spread into the fjords and enhance basal melting of marine-terminating glaciers. Therefore we suggest that increased meltwater production could positively feedback to accelerate melting of marine-terminating glaciers, although this would need to be further analyzed with a higher resolution/local fjord model.

## 5.6 Acknowledgments

# Bibliography

Azetsu-Scott, K., B. Petrie, P. Yeats, and C. Lee (2012), Composition and fluxes of freshwater through Davis Strait using multiple chemical tracers, *Journal of Geophysical Research*, *117*, C12,011, doi:10.1029/2012JC008172.

Bamber, J., M. den Broeke, J. Ettema, J. Lenaerts, and E. Rignot (2012), Recent large increases in freshwater fluxes from Greenland into the North Atlantic, *Geophysical Research Letters*, *39*(19).

Barnier, B., et al. (2006), Impact of partial steps and momentum advection schemes in a global ocean circulation model at eddy-permitting resolution, *Ocean Dynamics*, *56*(5), 543–567, doi:10.1007/s10236.

Box, J. E., D. H. Bromwich, B. A. Veenhuis, L.-S. Bai, J. C. Stroeve, J. C. Rogers, K. Steffen, T. Haran, and S.-H. Wang (2006), Greenland ice sheet surface mass balance variability (1988-2004) from calibrated Polar MM5 output, *Journal of Climate*, *19*(12), 2783–2800.

Brunnabend, S.-E., J. Schrter, R. Timmermann, R. Rietbroek, and J. Kusche (2012), Modeled steric and mass-driven sea level change caused by Greenland Ice Sheet melting, *Journal of Geodynamics*, *5960*, 219 – 225, doi:10.1016/j.jog.2011.06.001.

Curry, B., C. M. Lee, B. Petrie, R. E. Moritz, and R. Kwok (2014), Multiyear Volume, Liquid Freshwater, and Sea Ice Transports through Davis Strait, 2004–10*, *Journal of Physical Oceanography*, *44*, 1244–1266.

Dai, A., T. Qian, T. K. T., and M. J. D. (2009), Changes in continental freshwater discharge from 1948-2004, *Journal of Climate*, *22*, 2773–2791.

Dickson, R., B. Rudels, S. Dye, M. Karcher, J. Meincke, and I. Yashayaev (2007), Current estimates of freshwater flux through Arctic and subarctic seas, *Progress in Oceanography*, *73*(3-4), 210–230.

Holland, D. M., R. H. Thomas, B. de Young, M. H. Ribergaard, B. Lyberth, M. M. Holland, J. Finnis, A. P. Barrett, and M. C. Serreze (2008a), Acceleration of Jakobshavn Isbrae triggered by warm subsurface ocean waters, *Nature Geoscience*, *1*, 659–664, doi:10.1038/ngeo316.

Holland, D. M., R. H. Thomas, B. De Young, M. H. Ribergaard, and B. Lyberth (2008b), Acceleration of Jakobshavn Isbrae triggered by warm subsurface ocean waters, *Nature Geoscience*, *1*(10), 659–664.

Hu, X., and P. G. Myers (2013), A Lagrangian view of Pacific water inflow pathways in the Arctic Ocean during model spin-up, *Ocean Modelling*, *71*, 66–80, doi:10.1016/j.ocemod.2013.06.007.

Johannessen, O. M., A. Korablev, V. Miles, M. W. Miles, and K. E. Solberg (2011), Interaction between the warm subsurface Atlantic water in the Sermilik fjord and Helheim Glacier in southeast Greenland, *Surveys in Geophysics*, *32*(4), 387–396, doi:10.1007/s10712-011-9130-6.

Kliem, N., and D. A. Greenberg (2003), Diagnostic simulations of the summer circulation in the Canadian Arctic Archipelago, *Atmosphere-Ocean*, *41*(4), 273–289.

Large, W. G., and S. G. Yeager (2004), Diurnal to decadal global forcing for ocean and sea-ice models: the datasets and flux climatologies. NCAR Technical Note TN–460+ STR, *National Center for Atmospheric Research*.

Loyd, J., M. Moros, K. Perner, R. J. Telford, A. Kuijpers, E. Jansen, and D. McCarthy (2011), A 100-year record of ocean temperature control on the stability of Jakobshavn Isbrae, West Greenland., *Geology*, *39*, 131–139.

Madec, G., and the NEMO team (2008), *NEMO ocean engine*, Note du Pôle de modélisation, Institut Pierre-Simon Laplace (IPSL), France, No 27, ISSN No 1288-1619.

Marsh, R., D. Desbruyeres, J. L. Bamber, B. A. De Cuevas, A. C. Coward, and Y. Aksenov (2010), Short-term impacts of enhanced Greenland freshwater fluxes in an eddy-permitting ocean model, *Ocean Science*, *6*(3), 749–760.

Mernild, S. H., and G. E. Liston (2012), Greenland Freshwater Runoff. Part II: Distribution and Trends, 1960-2010, *Journal of Climate*, *25*(17), 6015–6035.

Myers, P. G., and M. H. Ribergaard (2013), Warming of the Polar Water Layer in Disko Bay and Potential Impact on Jakobshavn Isbrae, *American Meteorological Society*, *43*(12), 2629–2640.

Rignot, E., I. Velicogna, M. R. van den Broeke, A. Monaghan, and J. T. M. Lenaerts (2011), Acceleration of the contribution of the Greenland and Antarctic ice sheets to sea level rise, *Geophysical Research Letters*, *38*(5), L05,503, doi:10.1029/2011GL046583.

Rudels, B. (2011), Volume and freshwater transports through the Canadian Arctic Archipelago - Baffin Bay system, *Journal of Geophysical Research: Oceans*, *116*(C8), C00D10, doi:10.1029/2011JC007019.

Steele, M., R. Morley, and W. Ermold (2001), PHC: A global ocean hydrography with a high-quality Arctic Ocean, *Journal of Climate*, *14*(9), 2079–2087.

Straneo, F., and P. Heimbach (2013), North Atlantic warming and the retreat of Greenland's outlet glaciers, *Nature*, *504*(7478), 36–43, doi:10.1038/nature12854.

Tang, C. L., C. K. Ross, T. Yao, B. Petrie, B. M. DeTracey, and E. Dunlap (2004), The circulation, water masses and sea-ice of Baffin Bay, *Progress in Oceanography*, *63*(4), 183–228.

van den Broeke, M., J. Bamber, J. Ettema, E. Rignot, E. Schrama, W. J. van de Berg, E. van Meijgaard, I. Velicogna, and B. Wouters (2009), Partitioning recent Greenland mass loss, *Science*, *326*(5955), 984–986, doi:10.1126/science.1178176.

Zweng, M. M., and A. Münchow (2006), Warming and freshening of Baffin Bay, 1916-2003, *Journal of Geophysical Research: Oceans*, *111*, C07,016.

# Chapter 6

# Conclusions

In response to anthropogenic greenhouse gas emissions our Global Climate is changing. The Northern Hemisphere, and in particular the Arctic and the North Atlantic Oceans, are experiencing multiple stresses such as loss of sea ice, increasing wind energy at the ocean surface and larger freshwater discharge to coastal regions. Some of these translate into higher available solar radiation and stronger water stratification, while others translate into higher surface ocean mixing and weaker stratification. To address how the Arctic and Subarctic marine system may respond to these stresses I designed and analyzed a suite of simulations using a state of the art ocean circulation -sea ice -biogeochemical coupled model. The advantage of using a model is that I can isolate the effect of each stress and quantify its relative role (Saenko et al., 2015).

I focused on three stresses, the role of atmospheric patterns (specifically the NAO index) on ventilation, the relative importance between sea ice loss and increasing wind stress on the ocean surface, and the effect of increasing river runoff on the regional circulation. I find that the ventilation of the deep waters within the Labrador Sea are sensitive to large scale atmospheric forcing, however unlike previously hypothesized, the simulation shows that lateral oxygen fluxes are more important than local air-sea oxygen fluxes. The atmospheric forcing also influences primary production and carbon export throughout the Arctic. In particular, I found that high frequency winds have an important role up-welling nutrients, for which they were responsible for up to 46% of the primary production and 40% of the biogenic carbon export. Finally, in the case study in which I measure the response of Baffin Bay circulation to increasing freshwater discharge from western Greenland Ice Sheet, I found that a positive feedback could develop as a result of increasing SHH and a strengthening of the regional cyclonic circulation, which can ultimately cause an acceleration in the melting of western Greenland Ice Sheet through bringing warm Atlantic Water closer to the marine terminating glaciers.

The work presented in this thesis is an attempt to address some of the uncertainties surrounding how the marine system in the Northern Oceans may respond to climate change. Below I expand on how these research

findings contribute to advance Arctic research and on how the research could be expanded in the future.

## 6.1 Principal findings and future research

### 6.1.1 Ventilation in the Labrador Sea

This study showed that the ventilation of the deep waters within the Labrador Sea is enhanced during NAO+ years and it is reduced during NAO- years. However, the timing of the response to the NAO+ can take up to two years due to a system's stratification memory as suggested by Yashayaev (2007), meanwhile the response to the NAO- is immediate. This response time is associated with a relation between convection and ventilation. A new finding in this study, is however, that the NAO index also affects the laterally advected $O_2$, with less $O_2$ being imported into the Labrador Sea during NAO- years. Unlike previously thought, this lateral $O_2$ flux has the strongest contribution to the ventilation of deep Labrador Sea waters. The lateral fluxes of $O_2$ into the Labrador Sea constitute 75% of $O_2$ that is then advected to the deep layers, whereas air-sea fluxes account only for 25%. These findings highlight the importance of upstream regions (e.g. Baffin Bay, Irminger Sea, Arctic Ocean) as potential sources of $O_2$, and calls for monitoring lines with biogeochemical sensors that can allow researchers to quantify, *in situ*, the dissolved gas exchanged between basins.

This analysis of $O_2$ ventilation suggests that the Labrador Sea acts as a funnel for gases that are transported into the region in surface waters. Although, here I focused on $O_2$, some of the mechanisms could apply to $CO_2$ (e.g. importance of lateral flux) but others not (e.g. the longer time scale for dissolved $CO_2$ to reach atmospheric equilibrium and the opposite relationship with biological productivity and re-mineralization). For this reason I suggest a follow up study using a similar framework but focusing on $CO_2$ fluxes. Such investigation is possible now that BLING has been updated to include inorganic carbon; as an important greenhouse gas, understanding more about the processes that influence the sequestration of $CO_2$ can benefit future climate predictions.

### 6.1.2 Role of high frequency winds

I was able to test the hypothesis of Ardyna et al. (2014), who suggested that increasing stormy winds in the eastern Arctic was responsible for the observed new phytoplankton bloom in autumn. By comparing a control simulation to a sensitivity simulation forced with filtered wind fields, I was able to demonstrate that high frequency wind are responsible for up to 46% and 41% of the phytoplankton productivity and biogenic carbon export, respectively, in the ice-free and seasonal ice regions of the Arctic and Subarctic. However, in perennial ice covered regions the loss of sea ice tended to still dominate the growth of phytoplankton due to a much stronger regional light limitation. The principal mechanism by which high frequency winds helped replenish

the surface ocean with nutrients was the deepening of the isopycnals. In the control simulation the turbulent mixing tended to start earlier and last longer, and thus, this simulation sustained larger nutrient concentration at the surface. In summer, diffusion was the main process of surface water nutrient replenishment, and principally in perennial and seasonal ice cover regions where stratifications was strongest due to the seasonal melt of sea ice.

The continuing loss of sea ice make researchers wonder whether the Arctic Ocean may become a dominant carbon sink that can help mitigate global warming. There are two main processes by which $CO_2$ is exported to the deep ocean, the biogenic carbon pump and the solubility pump. Results from this project, suggest that with the loss of sea ice, and the increasing surface ocean interaction with winds, it is likely that the biogenic carbon pump may become more important in the Arctic. However, to determine the response of the solubility pump one would need to run these simulations with the updated BLING code containing the inorganic carbon. Additionally, I propose that the increasing importance of the Arctic may be counterbalanced by a decreasing importance of Subarctic regions. If the northward displacement of the North Atlantic Storm Track continues (Wang et al., 2017), it will reduce the turbulent mixing in the Labrador Sea and the Subpolar Gyre, in which case, biogenic carbon pump could decline by 40% on these regions.

### 6.1.3 Role of Greenland Ice Sheet melt

Over the past 50 years, the west Greenland Ice Sheet has discharged a cumulative meltwater equivalent of $14,190\,km^3$ into the Baffin Bay-Labrador Sea system (Mernild and Liston, 2012). In this project, I analyzed the impact of such large discharge on Baffin Bay's hydrographic conditions. Using a suite of sensitivity experiments I found that increasing glacier meltwater discharge can positively feedback to accelerate melting by increasing the heat content on Greenland's Northwest shelf ($+80\,EJ$). While previous studies suggested ocean warming is associated with the increasing surface stratification as a result of the meltwater discharge (Nummelin et al., 2015), my results suggest that in Baffin Bay, the warming is not only due to local processes, but also to changes in the regional circulation. Increasing the meltwater discharge strengthens the SSH gradient between coastal and offshore areas, this enhances the regional cyclonic circulation and the imports of warm Atlantic Water while reducing the import of cold Arctic Water into Baffin Bay. Combined, this results in a warming ($+0.6°C$) and shallowing (up to $50m$) of the West Greenland Irminger Water (e.g. modified Atlantic Water).

This analysis was done without including the biogeochemical model. However, runoff from Greenland is rich in nutrients including iron and thus, increasing meltwater discharge is also likely to be accompanied by increases in nutrient exported to the ocean (Bhatia et al., 2013). This may regionally impact the phenology of phytoplankton. A sensitivity analysis testing the response of phytoplankton to increasing nutrient discharged

from Greenland could help determine if this new nutrient flux could enhance productivity in summer where nutrient limitation is most important. Such analysis is especially important for the North Water Polynya (northern Baffin Bay), a region that is among the most productive in the Arctic Ocean (Klein et al., 2002). Recent analysis of phytoplankton productivity in the North Water Polynya between 1998 and 2014 showed that the regional decline in the phytoplankton bloom amplitude was a function of a reduction in the wind entrainment of nutrients (Marchese et al., 2017). The authors concluded that wind entrainment had declined as a result of warmer surface water temperatures. I would add that the declining sea surface salinity due to higher meltwater discharge could also make it potentially harder for wind entrainment. Overall, Marchese et al. (2017) results suggest that the regional relationship may be more complicated than a simple change in the nutrient sources, and that other factors such as stratification, wind energy, and length of the ice free season may also need to be considered to properly assess the net regional impact.

Additionally, our sensitivity experiments of Greenland Ice Sheet melting assumed runoff discharged from Greenland was in the form of meltwater. However, Greenland Ice Sheet also discharges freshwater in the form of glaciers calving, indeed, this solid discharge constitutes 54% of the total freshwater discharged (Bamber et al., 2012). The icebergs transport the freshwater away from coastal areas, which could suggest a different response of the circulation as the SSH gradient changes could be smaller. A more realistic experiment could include half of the freshwater discharged as liquid and half as icebergs calving.



**Figure 6.1.** Photos of a Greenland iceberg carrying sediment and a bird colony as it drifted southward in the East Greenland Current. Photos taken by the author from the Polar Stern during the Arctic Ocean expedition PS87.

Furthermore, icebergs could also transport nutrients to the open ocean. During the PS87 expedition to the

Arctic Ocean we passed by several icebergs containing large loads of sediments, rocks and birds nesting (Figure 6.1). This observation allows me to suggest that icebergs in the Northern Hemisphere may have an important role enriching surface waters with nutrients (e.g. iron, phosphate and nitrogen) and that they may serve to export, not only freshwater, but also nutrients away form the coast.

Although no other such observations have been reported in the literature for the Northern Hemisphere, there is substantial documentation of the importance of icebergs in the Southern Ocean. Icebergs calving off the Antarctic Ice Sheet, are documented to impact primary production positively (e.g. Schwarz and Schodlok, 2009; Klunder et al., 2011; Vernet et al., 2011). Icebergs have been shown to enrich the surface waters with nutrients, directly by releasing nutrients trapped within the ice as they melt, and/or indirectly by inducing up-welling of nutrients from subsurface waters as the submarine melting of the icebergs forms buoyant plumes (Vernet et al., 2011; Gerringa et al., 2012). Thus far, no studies in the North Atlantic have documented the relation between icebergs and phytoplankton blooms. However, one study, did record buoyant plumes of a drifting iceberg (Yankovsky and Yashayaev, 2014). This observation suggests that icebergs in the North Atlantic could also be associated with nutrient up-welling. The authors also pointed out that the melting of this iceberg as it drifted shallowed the mixed layer in a region that was tenfold the iceberg's size. In the North Atlantic shallow stratification can benefit phytoplankton by keeping them close to the sun-lit surface of the ocean, thus it is possible to hypothesize that icebergs could also benefit primary production in the North Atlantic. A modelling experiment where icebergs can provide the ocean with nutrients as they melt and drift could serve as preliminary analysis to test this hypothesis.

## 6.2 Thesis summary

The modelling work performed during this Ph.D. thesis aimed at increasing the understanding of the the environmental response of the Arctic and North Atlantic Oceans to Global Climate Warming. By integrating physical oceanography, biogeochemistry and general ecology, this thesis attempts to give an interdisciplinary perspective on the regional changes. This study approaches the questions using sensitivity experiments to isolate effect - response, and study the underlying processes leading to the marine response. There are three important contributions to Arctic research:

- Ventilation of the deep Labrador Sea is more sensitive to changes in the lateral $O_2$ fluxes than to changes in air-sea $O_2$ fluxes. During an NAO+ year both the lateral and air-sea $O_2$ fluxes increase.

- Windy conditions stimulate primary production and biogenic carbon export in seasonal and ice free regions (maximum regional values of 50% and 49% respectively) but not in perennial ice covered regions.

- Increasing meltwater run-off from Greenland Ice Sheet increases the heat content in Baffin Bay and the likely-hood of warm waters entering the coastal trough system, which can accelerate the basal melt of marine terminating glaciers.

# Bibliography

Ardyna, M., Babin, M., Gosselin, M., Devred, E., Rainville, L., and Tremblay, J.-E. (2014). Recent Arctic Ocean sea ice loss triggers novel fall phytoplankton blooms. *Geophysical Research Letters*, 41(17):6207–6212.

Bamber, J., den Broeke, M., Ettema, J., Lenaerts, J., and Rignot, E. (2012). Recent large increases in freshwater fluxes from Greenland into the North Atlantic. *Geophysical Research Letters*, 39(19).

Bhatia, M. P., Kujawinski, E. B., Das, S. B., Breier, C. F., Henderson, P. B., and Charette, M. A. (2013). Greenland meltwater as a significant and potentially bioavailable source of iron to the ocean. *Nature Geoscience*, 6:274.

Gerringa, L. J., Alderkamp, A.-C., Laan, P., Thurczy, C.-E., Baar, H. J. D., Mills, M. M., van Dijken, G. L., van Haren, H., and Arrigo, K. R. (2012). Iron from melting glaciers fuels the phytoplankton blooms in amundsen sea (southern ocean): Iron biogeochemistry. *Deep Sea Research Part II: Topical Studies in Oceanography*, 71-76:16 – 31.

Klein, B., LeBlanc, B., Mei, Z.-P., Beret, R., Michaud, J., Mundy, C.-J., von Quillfeldt, C. H., ve Garneau, M., Roy, S., Gratton, Y., Cochran, J., Blanger, S., Larouche, P., Pakulski, J., Rivkin, R. B., and Legendre, L. (2002). Phytoplankton biomass, production and potential export in the north water. *Deep Sea Research Part II: Topical Studies in Oceanography*, 49(22):4983 – 5002.

Klunder, M., Laan, P., Middag, R., Baar, H. D., and van Ooijen, J. (2011). Dissolved iron in the southern ocean (atlantic sector). *Deep Sea Research Part II: Topical Studies in Oceanography*, 58(25):2678 – 2694.

Marchese, C., Albouy, C., Tremblay, J.-É., Dumont, D., D'Ortenzio, F., Vissault, S., and Bélanger, S. (2017). Changes in phytoplankton bloom phenology over the North Water (NOW) polynya: a response to changing environmental conditions. *Polar Biology*, 40(9):1721–1737.

Mernild, S. H. and Liston, G. E. (2012). Greenland freshwater runoff. Part II: Distribution and trends, 1960-2010. *Journal of Climate*, 25(17):6015–6035.

Nummelin, A., Li, C., and Smedsrud, L. H. (2015). Response of Arctic Ocean stratification to changing river runoff in a column model. *Journal of Geophysical Research: Oceans*, 120(4):2655–2675.

Saenko, O. A., Yang, D., Gregory, J. M., Spence, P., and Myers, P. G. (2015). Separating the influence of projected changes in air temperature and wind on patterns of sea level change and ocean heat content. *Journal of Geophysical Research: Oceans*, 120(8):5749–5765.

Schwarz, J. and Schodlok, M. (2009). Impact of drifting icebergs on surface phytoplankton biomass in the southern ocean: Ocean colour remote sensing and *in situ* iceberg tracking. *Deep Sea Research Part I: Oceanographic Research Papers*, 56(10):1727 – 1741.

Vernet, M., Sines, K., Chakos, D., Cefarelli, A., and Ekern, L. (2011). Impacts on phytoplankton dynamics by free-drifting icebergs in the nw weddell sea. *Deep Sea Research Part II: Topical Studies in Oceanography*, 58(11):1422 – 1435. Free-Drifting Icebergs in the Southern Ocean.

Wang, J., Kim, H.-M., and E.K.M., C. (2017). Changes in Northern Hemisphere winter storm tracks under the background of Arctic amplification. *Journal of Climate*, 30:3705–3724.

Yankovsky, A. E. and Yashayaev, I. (2014). Surface buoyant plumes from melting icebergs in the Labrador Sea. *Deep Sea Research Part I: Oceanographic Research Papers*, 91:1 – 9.

Yashayaev, I. (2007). Hydrographic changes in the Labrador Sea, 1960-2005. *Progress in Oceanography*, 73:242–276.

# Bibliography

Aksnes, D. L. and Wassmann, P. (1993). Modeling the significance of zooplankton grazing for export production. *Limnology and Oceanography*, 38(5):978–985.

Amante, C. and Eakins, B. W. (2009). ETOPO1 1 Arc-minute global relief model: procedures, data sources and analysis. *NOAA Technical Memorandum NESDIS NGDC-24*, 19.

Amon, R., Rinehart, A., Duan, S., Louchouarn, P., Prokushkin, A., Guggenberger, G., Bauch, D., Stedmon, C., Raymond, P., Holmes, R., McClelland, J., Peterson, B., Walker, S., and Zhulidov, A. (2012). Dissolved organic matter sources in large Arctic rivers. *Geochimica et Cosmochimica Acta*, 94:217 – 237.

Ardyna, M., Babin, M., Gosselin, M., Devred, E., Rainville, L., and Tremblay, J.-E. (2014). Recent Arctic Ocean sea ice loss triggers novel fall phytoplankton blooms. *Geophysical Research Letters*, 41(17):6207–6212.

Arrigo, K. R., van Dijken, G., and Pabi, S. (2008). Impact of a shrinking Arctic ice cover on marine primary production. *Geophysical Research Letters*, 35(19). L19603.

Aumont, O. and Bopp, L. (2006). Globalizing results from ocean in situ iron fertilization studies. *Global Biogeochemical Cycles*, 20(2).

Aumont, O., Ethé, C., Tagliabue, A., Bopp, L., and Gehlen, M. (2015). PISCES-v2: an ocean biogeochemical model for carbon and ecosystem studies. *Geoscientific Model Development*, 8(8):2465–2513.

Azetsu-Scott, K., Petrie, B., Yeats, P., and Lee, C. (2012). Composition and fluxes of freshwater through Davis Strait using multiple chemical tracers. *Journal of Geophysical Research*, 117(C12):C12011.

Bacon, S., Gould, W. J., and Jia, Y. (2003). Open-ocean convection in the Irminger Sea. *Geophysical Research Letters*, 30(5). 1246.

Bamber, J., den Broeke, M., Ettema, J., Lenaerts, J., and Rignot, E. (2012). Recent large increases in freshwater fluxes from Greenland into the North Atlantic. *Geophysical Research Letters*, 39(19).

Barnier, B., Madec, G., Penduff, T., Molines, J., Treguier, A., Le Sommer, J., Beckmann, A., Biastoch, A., Böning, C., Dengg, J., Derval, C., Durand, E., Gulev, S., Remy, E., Talandier, C., Theetten, S., Maltrud, M., McClean, J., and De Cuevas, B. (2006). Impact of partial steps and momentum advection schemes in a global ocean circulation model at eddy-permitting resolution. *Ocean Dynamics*, 56(5):543–567.

Belkin, I. M., Levitus, S., Antonov, J., and Malmberg, S. (1998). "Great Salinity Anomalies" in the North Atlantic. *Progress in Oceanography*, 41(1):1–68.

Bhatia, M. P., Kujawinski, E. B., Das, S. B., Breier, C. F., Henderson, P. B., and Charette, M. A. (2013). Greenland meltwater as a significant and potentially bioavailable source of iron to the ocean. *Nature Geoscience*, 6:274.

Box, J. E., Bromwich, D. H., Veenhuis, B. A., Bai, L.-S., Stroeve, J. C., Rogers, J. C., Steffen, K., Haran, T., and Wang, S.-H. (2006). Greenland Ice Sheet surface mass balance variability (1988-2004) from calibrated Polar MM5 output. *Journal of Climate*, 19(12):2783–2800.

Boyd, P. and Stevens, C. (2002). Modelling particle transformations and the downward organic carbon flux in the NE Atlantic Ocean. *Progress in Oceanography*, 52(1):1–29.

Brunnabend, S.-E., Schröter, J., Timmermann, R., Rietbroek, R., and Kusche, J. (2012). Modeled steric and mass-driven sea level change caused by Greenland Ice Sheet melting. *Journal of Geodynamics*, 59-60:219 – 225.

Camara Lins, R., Martinez, J.-M., Motta Marques, D. d., Cirilo, J. A., and Fragoso, C. R. (2017). Assessment of chlorophyll-a remote sensing algorithms in a productive tropical estuarine-lagoon system. *Remote Sensing*, 9(516).

Carranza, M. M. and Gille, S. T. (2015). Southern Ocean wind-driven entrainment enhances satellite chlorophyll-a through the summer. *Journal of Geophysical Research: Oceans*, 120(1):304–323.

Cavalieri, D. J., Crawford, J. P., Drinkwater, M. R., Eppler, D. T., Farmer, L. D., Jentz, R. R., and Wackerman, C. C. (1991). Aircraft active and passive microwave validation of sea ice concentration from the Defense Meteorological Satellite Program special sensor microwave imager. *Journal of Geophysical Research: Oceans*, 96(C12):21989–22008.

Comiso, J. C. (2000 updated 2015). Bootstrap sea ice concentration from Nimbus-7 SMMR and DMSP SSM/I, Version 2 [1979 - 2016]. *NASA DAAC at National Snow and Ice Data Centre, Boulder, CO*.

Comiso, J. C., Cavalieri, D. J., Parkinson, C. L., and Gloersen, P. (1997). Passive microwave algorithms for sea ice concentration: A comparison of two techniques. *Remote Sensing of Environment*, 60(3):357 – 384.

Comiso, J. C. and Kwok, R. (1996). Surface and radiative characteristics of the summer Arctic sea ice cover from multisensor satellite observations. *Journal of Geophysical Research: Oceans*, 101(C12):28397–28416.

Comiso, J. C., Meier, W. N., and Gersten, R. (2017). Variability and trends in the Arctic Sea ice cover: Results from different techniques. *Journal of Geophysical Research: Oceans*, 122(8):6883–6900.

Comiso, J. C. and Nishio, F. (2008). Trends in the sea ice cover using enhanced and compatible AMSR-E, SSM/I, and SMMR data. *Journal of Geophysical Research*, 113(C2):C02S07.

Comiso, J. C., Parkinson, C. L., Gersten, R., and Stock, L. (2008). Accelerated decline in the Arctic sea ice cover. *Geophysical Research Letters*, 35(1):L01703.

Curry, B., Lee, C. M., Petrie, B., Moritz, R. E., and Kwok, R. (2014). Multiyear volume, liquid freshwater, and sea ice transports through Davis Strait, 2004–10*. *Journal of Physical Oceanography*, 44:1244–1266.

Dai, A., Qian, T., T., T. K., and D., M. J. (2009). Changes in continental freshwater discharge from 1948-2004. *Journal of Climate*, 22:2773–2791.

Day, J. J., Holland, M. M., and Hodges, K. I. (2017). Seasonal differences in the response of Arctic cyclones to climate change in CESM1. *Climate Dynamics*.

de Jong, M. F. and de Steur, L. (2016). Strong winter cooling over the Irminger Sea in winter 2014–2015, exceptional deep convection, and the emergence of anomalously low SST. *Geophysical Research Letters*, 43(13):7106–7113.

de Jong, M. F., van Aken, H. M., Våge, K., and Pickart, R. S. (2012). Convective mixing in the central Irminger Sea: 2002–2010. *Deep Sea Research Part I: Oceanographic Research Papers*, 63:36 – 51.

Deser, C., Walsh, J. E., and Timlin, M. S. (2000). Arctic sea ice variability in the context of recent atmospheric circulation trends. *Journal of Climate*, 13(3):617–633.

Dickson, R., Lazier, J., Meincke, J., Rhines, P., and Swift, J. (1996). Long-term coordinated changes in the convective activity of the North Atlantic. *Progress in Oceanography*, 38(3):241 – 295.

Dickson, R., Rudels, B., Dye, S., Karcher, M., Meincke, J., and Yashayaev, I. (2007). Current estimates of freshwater flux through Arctic and subarctic seas. *Progress in Oceanography*, 73(3-4):210–230.

Dickson, R. R., Meincke, J., Malmberg, S., and Lee, A. J. (1988). The "great salinity anomaly" in the Northern North Atlantic 1968-1982. *Progress in Oceanography*, 20(2):103–151.

Dunne, J. P., Armstrong, R. A., Gnanadesikan, A., and Sarmiento, J. L. (2005). Empirical and mechanistic models for the particle export ratio. *Global Biogeochemical Cycles*, 19(4).

Eldevik, T., Nilsen, J. E. Ø., Iovino, D., Anders Olsson, K., Sandø, A. B., and Drange, H. (2009). Observed sources and variability of Nordic seas overflow. *Nature Geoscience*, 2:406.

Evans, G. T. and Parslow, J. S. (1985). A Model of Annual Plankton Cycles. *Biological Oceanography*, 3(3):327–347.

Fichefet, T. and Maqueda, M. A. M. (1997). Sensitivity of a global sea ice model to the treatment of ice thermodynamics and dynamics. *Journal of Geophysical Research*, 102(C6):12609–12646.

Fofonoff, N.P. Millard, R. (1983). Algorithms for computation of fundamental properties of seawater. In *UNESCO technical papers in marine science*, volume 44, page 53. UNESCO, PARIS.

Fröb, F., Olsen, A., Våge, K., Moore, G. W. K., Yashayaev, I., Jeansson, E., and Rajasakaren, B. (2016). Irminger Sea deep convection injects oxygen and anthropogenic carbon to the ocean interior. *Nature Communications*, 7:13244.

Galbraith, E. D., Dunne, J. P., Gnanadesikan, A., Slater, R. D., Sarmiento, J. L., Dufour, C. O., de Souza, G. F., Bianchi, D., Claret, M., Rodgers, K. B., and Marvasti, S. S. (2015). Complex functionality with minimal computation: Promise and pitfalls of reduced-tracer ocean biogeochemistry models. *Journal of Advances in Modeling Earth Systems*, 7(4):2012–2028.

Galbraith, E. D., Gnanadesikan, A., Dunne, J. P., and Hiscock, M. R. (2010). Regional impacts of iron-light colimitation in a global biogeochemical model. *Biogeosciences*, 7(3):1043–1064.

Garcia, H. E., Locarnini, R. A., Boyer, T. P., Antonov, J. I., Baranova, O., Zweng, M., Reagan, J., and Johnson, D. (2014). World Ocean Atlas 2013: Dissolved inorganic nutrients (phosphate, nitrate, silicate). *S. Levitus, Ed., A. Mishonov Technical Ed., NOAA Atlas NESDIS*, 4:25.

Gerringa, L. J., Alderkamp, A.-C., Laan, P., Thurczy, C.-E., Baar, H. J. D., Mills, M. M., van Dijken, G. L., van Haren, H., and Arrigo, K. R. (2012). Iron from melting glaciers fuels the phytoplankton blooms in amundsen sea (southern ocean): Iron biogeochemistry. *Deep Sea Research Part II: Topical Studies in Oceanography*, 71-76:16 – 31.

Ginoux, P., Chin, M., Tegen, I., Prospero, J. M., Holben, B., Dubovik, O., and Lin, S.-J. (2001). Sources and distributions of dust aerosols simulated with the GOCART model. *Journal of Geophysical Research: Atmospheres*, 106(D17):20255–20273.

Griffin, C., McClelland, J., Frey, K., Fiske, G., and Holmes, R. (2018). Quantifying CDOM and DOC in major Arctic rivers during ice-free conditions using Landsat TM and ETM+ data. *Remote Sensing of Environment*, 209:395 – 409.

Group, O. B. P. (2003). BMODIS Aqua Level 3 Global Daily Mapped 9 km Chlorophyll a. Ver. 6. *DAAC CA USA. Dataset accessed [2017-02-20].*

Gruber, N., Gloor, M., Fan, S.-M., and Sarmiento, J. L. (2001). Air-sea flux of oxygen estimated from bulk data: Implications For the marine and atmospheric oxygen cycles. *Global Biogeochemical Cycles*, 15(4):783–803.

Guéguen, C., Cuss, C. W., Cassels, C. J., and Carmack, E. C. (2014). Absorption and fluorescence of dissolved organic matter in the waters of the Canadian Arctic Archipelago, Baffin Bay, and the Labrador Sea. *Journal of Geophysical Research: Oceans*, 119(3):2034–2047.

Harrison, W. G. and Cota, G. F. (1991). Primary production in polar waters: relation to nutrient availability. *Polar Research*, 10(1):87–104.

Hartmann, D., Klein Tank, A., Rusticucci, M., Alexander, L., Bronnimann, S., Charabi, Y., Dentener, F., Dlugokencky, E., Easterling, D., Kaplan, A., Soden, B., Thorne, P., Wild, M., and Zhai, P. (2013). Observations: Atmosphere and Surface. In Stocker, T., Qin, D., Plattner, G.-K., Tignor, M., Allen, S., Boschung, J., Nauels, A., Xia, Y., Bex, V., and Midgley, P., editors, *Climate Change 2013: The Physical Science Basis. Contribution of Working Group I to the Fifth Assessment Report of the Intergovernmental Panel on Climate Change*, book section 2, pages 159–254. Cambridge University Press, Cambridge, United Kingdom and New York, NY, USA.

Hibler, W. D. (1979). A dynamic thermodynamic sea ice model. *Journal of Physical Oceanography*, 9:815–846.

Holdsworth, A. M. and Myers, P. G. (2015). The influence of high-frequency atmospheric forcing on the circulation and deep convection of the Labrador Sea. *Journal of Climate*, 28(12):4980–4996.

Holland, D. M., Thomas, R. H., De Young, B., Ribergaard, M. H., and Lyberth, B. (2008a). Acceleration of Jakobshavn Isbrae triggered by warm subsurface ocean waters. *Nature Geoscience*, 1(10):659–664.

Holland, D. M., Thomas, R. H., de Young, B., Ribergaard, M. H., Lyberth, B., Holland, M. M., Finnis, J., Barrett, A. P., and Serreze, M. C. (2008b). Acceleration of Jakobshavn Isbrae triggered by warm subsurface ocean waters. *Nature Geoscience*, 1:659–664.

Holmes, R. M., McClelland, J. W., Peterson, B. J., Tank, S. E., Bulygina, E., Eglinton, T. I., Gordeev, V. V., Gurtovaya, T. Y., Raymond, P. A., Repeta, D. J., Staples, R., Striegl, R. G., Zhulidov, A. V., and Zimov, S. A. (2012). Seasonal and annual fluxes of nutrients and organic matter from large rivers to the Arctic Ocean and surrounding seas. *Estuaries and Coasts*, 35(2):369–382.

Howatt, T., Palter, J., Matthews, J. B. R., deYoung, B., Bachmayer, R., and Claus, B. (2018). Ekman and eddy exchange of freshwater and oxygen across the labrador shelf-break. *Journal of Physical Oceanography*, 0(0):in press.

Hu, X. and Myers, P. G. (2013). A lagrangian view of Pacific water inflow pathways in the Arctic Ocean during model spin-up. *Ocean Modelling*, 71:66–80.

Huang, C. and Qiao, F. (2009). The relationship between sea surface temperature anomaly and wind energy input in the Pacific Ocean. *Progress in Natural Science*, 19(10):1409 – 1412.

Hughes, K. G., Klymak, J. M., Hu, X., and Myers, P. G. (2017). Water mass modification and mixing rates in a 1/12° simulation of the canadian arctic archipelago. *Journal of Geophysical Research: Oceans*, 122(2):803–820.

Hunke, E. C. and Dukowicz, J. K. (1997). An elastic-viscous-plastic model for sea ice dynamics. *Journal of Physical Oceanography*, 27(9):1849–1867.

Hurrell, J. W. and Deser, C. (2009). North Atlantic climate variability: the role of the North Atlantic Oscillation. *Journal of Marine Systems*, 78(1):28–41.

Isachsen, P. E., Mauritzen, C., and Svendsen, H. (2007). Dense water formation in the nordic seas diagnosed from sea surface buoyancy fluxes. *Deep Sea Research Part I: Oceanographic Research Papers*, 54(1):22 – 41.

James, I. (1996). Advection schemes for shelf sea models. *Journal of Marine Systems*, 8(3):237 – 254. Joint Numerical Sea Modelling.

Janout, M. A., Hlemann, J., Waite, A. M., Krumpen, T., Appen, W., and Martynov, F. (2016). Sea–ice retreat controls timing of summer plankton blooms in the Eastern Arctic Ocean. *Geophysical Research Letters*, 43(24):12,493–12,501.

Johannessen, O. M., Korablev, A., Miles, V., Miles, M. W., and Solberg, K. E. (2011). Interaction between the warm subsurface Atlantic water in the Sermilik fjord and Helheim Glacier in southeast Greenland. *Surveys in Geophysics*, 32(4):387–396.

Karleskind, P., Lévy, M., and Memery, L. (2011). Subduction of carbon, nitrogen, and oxygen in the northeast Atlantic. *Journal of Geophysical Research: Oceans*, 116(C2).

Kauker, F., Gerdes, R., Karcher, M., Köberle, C., and Lieser, J. L. (2003). Variability of Arctic and North Atlantic sea ice: A combined analysis of model results and observations from 1978 to 2001. *Journal of Geophysical Research: Oceans*, 108(C6).

Keeling, R. F., Stephens, B. B., Najjar, R. G., Doney, S. C., Archer, D., and Heimann, M. (1998). Seasonal variations in the atmospheric $O_2/N_2$ ratio in relation to the kinetics of air-sea gas exchange. *Global Biogeochemical Cycles*, 12(1):141–163.

Kirtman, B., Power, S., Adedoyin, J., Boer, G., Bojariu, R., Camilloni, I., Doblas-Reyes, F., Fiore, A., Kimoto, M., Meehl, G., Prather, M., Sarr, A., Schar, C., Sutton, R., van Oldenborgh, G., Vecchi, G., and Wang, H.

(2013). Near-term Climate Change: Projections and Predictability. In Stocker, T., Qin, D., Plattner, G.-K., Tignor, M., Allen, S., Boschung, J., Nauels, A., Xia, Y., Bex, V., and Midgley, P., editors, *Climate Change 2013: The Physical Science Basis. Contribution of Working Group I to the Fifth Assessment Report of the Intergovernmental Panel on Climate Change*, book section 11, pages 953–1028. Cambridge University Press, Cambridge, United Kingdom and New York, NY, USA.

Klein, B., LeBlanc, B., Mei, Z.-P., Beret, R., Michaud, J., Mundy, C.-J., von Quillfeldt, C. H., ve Garneau, M., Roy, S., Gratton, Y., Cochran, J., Blanger, S., Larouche, P., Pakulski, J., Rivkin, R. B., and Legendre, L. (2002). Phytoplankton biomass, production and potential export in the north water. *Deep Sea Research Part II: Topical Studies in Oceanography*, 49(22):4983 – 5002.

Klunder, M., Laan, P., Middag, R., Baar, H. D., and van Ooijen, J. (2011). Dissolved iron in the southern ocean (atlantic sector). *Deep Sea Research Part II: Topical Studies in Oceanography*, 58(25):2678 – 2694.

Koelling, J., Wallace, D. W. R., Send, U., and Karstensen, J. (2017). Intense oceanic uptake of oxygen during 2014–2015 winter convection in the Labrador Sea. *Geophysical Research Letters*, 44(15):7855–7864. 2017GL073933.

Kohout, A. L., Williams, M. J. M., Dean, S. M., and Meylan, M. H. (2000). Storm-induced sea-ice breakup and the implications for ice extent. *Nature*, 509(7502):604–607.

Kuhlbrodt, T., Griesel, A., Montoya, M., Levermann, A., Hofmann, M., and Rahmstorf, S. (2007). On the driving processes of the Atlantic meridional overturning circulation. *Reviews of Geophysics*, 45(2). RG2001.

Kunkel, K., Robinson, D., Champion, S. Yin, X., Estilow, T., and Frankson, R. M. (2016). Trends and extremes in Northern Hemisphere snow characteristics. *Current Climate Change Reports*, 2(65).

Large, W. G. and Yeager, S. G. (2004). Diurnal to decadal global forcing for ocean and sea-ice models: the datasets and flux climatologies. NCAR Technical Note TN–460+ STR. *National Center for Atmospheric Research*.

Large, W. G. and Yeager, S. G. (2009). The global climatology of an interannually varying air–sea flux data set. *Climate Dynamics*, 33(2):341–364.

Lemieux, J.-F., Tremblay, L. B., Dupont, F., Plante, M., Smith, G. C., and Dumont, D. (2015). A basal stress parameterization for modeling landfast ice. *Journal of Geophysical Research: Oceans*, 120(4):3157–3173.

Lévy, M., Estublier, A., and Madec, G. (2001). Choice of an advection scheme for biogeochemical models. *Geophysical Research Letters*, 28(19):3725–3728.

Li, D., Zhang, R., and Knutson, T. R. (2017). On the discrepancy between observed and CMIP5 multi-model simulated Barents Sea winter sea ice decline. *Nature Communications*, 8:14991.

Light, B., Grenfell, T. C., and Perovich, D. K. (2008). Transmission and absorption of solar radiation by arctic sea ice during the melt season. *Journal of Geophysical Research: Oceans*, 113(C3).

Loyd, J., Moros, M., Perner, K., Telford, R. J., Kuijpers, A., Jansen, E., and McCarthy, D. (2011). A 100-year record of ocean temperature control on the stability of Jakobshavn Isbræ, West Greenland. *Geology*, 39:131–139.

Madec, G., Delecluse, P., Imbard, M., and Lévy, C. (1998). *OPA 8.1 ocean general circulation model reference manual*. Note du Pôle de modélisation, Institut Pierre-Simon Laplace (IPSL), France, No 11, 91pp.

Madec, G. and the NEMO team (2008). *NEMO ocean engine*. Note du Pôle de modélisation, Institut Pierre-Simon Laplace (IPSL), France, No 27, ISSN No 1288-1619.

Makshtas, A., Atkinson, D., Kulakov, M., Shutilin, S., Krishfield, R., and Proshutinsky, A. (2007). Atmospheric forcing validation for modeling the central Arctic. *Geophysical Research Letters*, 34(20). L20706.

Marchese, C., Albouy, C., Tremblay, J.-É., Dumont, D., D'Ortenzio, F., Vissault, S., and Bélanger, S. (2017). Changes in phytoplankton bloom phenology over the North Water (NOW) polynya: a response to changing environmental conditions. *Polar Biology*, 40(9):1721–1737.

Markus, T., Stroeve, J. C., and Miller, J. (2009). Recent changes in Arctic sea ice melt onset, freezeup, and melt season length. *Journal of Geophysical Research*, 114(C12):C12024.

Markussen, T. N., Elberling, B., Winter, C., and Andersen, T. J. (2016). Flocculated meltwater particles control Arctic land-sea fluxes of labile iron. *Scientific Reports*, 6:24033.

Marsh, R., Desbruyeres, D., Bamber, J. L., De Cuevas, B. A., Coward, A. C., and Aksenov, Y. (2010). Short-term impacts of enhanced Greenland freshwater fluxes in an eddy-permitting ocean model. *Ocean Science*, 6(3):749–760.

Marson, J. M., Myers, P. G., Hu, X., Petrie, B., Azetsu-Scott, K., and Lee, C. M. (2017). Cascading off the West Greenland Shelf: A numerical perspective. *Journal of Geophysical Research: Oceans*, 122(7):5316–5328.

Masina, S., Storto, A., Ferry, N., Valdivieso, M., Haines, K., Balmaseda, M., Zuo, H., Drevillon, M., and Parent, L. (2015). An ensemble of eddy-permitting global ocean reanalyses from the MyOcean project. *Climate Dynamics*, pages 1–29.

Mernild, S. H. and Liston, G. E. (2012). Greenland freshwater runoff. Part II: Distribution and trends, 1960-2010. *Journal of Climate*, 25(17):6015–6035.

Motyka, R. J., Truffer, M., Fahnestock, M., Mortensen, J., Rysgaard, S., and Howat, I. (2011). Submarine melting of the 1985 Jakobshavn Isbræfloating tongue and the triggering of the current retreat. *Journal of Geophysical Research: Earth Surface*, 116(F1).

Mowlem, M., Hartman, S., Harrison, S., and Larkin, K. (2008). Intercomparison of biogeochemical sensors at ocean observatories. EurOceans Research & Consultancy Report. 44. pp 45, http://www.whoi.edu/cms/files/EUR-OCEANS˙SensorIntercomparisonReport˙39645.pdf.

Myers, P. G. and Ribergaard, M. H. (2013). Warming of the Polar Water Layer in Disko Bay and Potential Impact on Jakobshavn Isbræ. *American Meteorological Society*, 43(12):2629–2640.

Nummelin, A., Ilicak, M., Li, C., and Smedsrud, L. H. (2016). Consequences of future increased Arctic runoff on Arctic Ocean stratification, circulation, and sea ice cover. *Journal of Geophysical Research: Oceans*, 121(1):617–637.

Nummelin, A., Li, C., and Smedsrud, L. H. (2015). Response of Arctic Ocean stratification to changing river runoff in a column model. *Journal of Geophysical Research: Oceans*, 120(4):2655–2675.

Onarheim, I. H. and Årthun, M. (2017). Toward an ice-free Barents Sea. *Geophysical Research Letters*, 44(16):8387–8395.

Pabi, S., van Dijken, G. L., and Arrigo, K. R. (2008). Primary production in the Arctic Ocean, 1998–2006. *Journal of Geophysical Research: Oceans*, 113(C8).

Pan, S., Shi, J., Gao, H., Guo, X., Yao, X., and Gong, X. (2017). Contributions of physical and biogeochemical processes to phytoplankton biomass enhancement in the surface and subsurface layers during the passage of Typhoon Damrey. *Journal of Geophysical Research: Biogeosciences*, 122(1):212–229.

Perovich, D. K., Elder, B. C., and Richter-Menge, J. A. (1997). Observations of the annual cycle of sea ice temperature and mass balance. *Geophysical Research Letters*, 24(5):555–558.

Peterson, B. J., Holmes, R. M., McClelland, J. W., Vorosmarty, C. J., Lammers, R. B., Shiklomanov, A. I., Shiklomanov, I. A., and Rahmstorf, S. (2002). Increasing river discharge to the Arctic Ocean. *Science*, 298(5601):2171–2173.

Polyakov, I. V., Pnyushkov, A. V., Alkire, M. B., Ashik, I. M., Baumann, T. M., Carmack, E. C., Goszczko, I., Guthrie, J., Ivanov, V. V., Kanzow, T., Krishfield, R., Kwok, R., Sundfjord, A., Morison, J., Rember, R., and Yulin, A. (2017). Greater role for Atlantic inflows on sea–ice loss in the Eurasian Basin of the Arctic Ocean. *Science*, 356(6335):285–291.

Popova, E. E., Yool, A., Coward, A. C., Aksenov, Y. K., Alderson, S. G., de Cuevas, B. A., and Anderson, T. R. (2010). Control of primary production in the arctic by nutrients and light: insights from a high resolution ocean general circulation model. *Biogeosciences*, 7(11):3569–3591.

Ramudu, E., Gelderloos, R., Yang, D., Meneveau, C., and Gnanadesikan, A. (2018). Large Eddy Simulation of Heat Entrainment Under Arctic Sea Ice. *Journal of Geophysical Research: Oceans*, 123(1):287–304.

Årthun, M., Eldevik, T., Smedsrud, L. H., Skagseth, O., and Ingvaldsen, R. B. (2012). Quantifying the influence of Atlantic heat on Barents Sea ice variability and retreat. *Journal of Climate*, 25(13):4736–4743.

Rhein, M., Kieke, D., and Steinfeldt, R. (2015). Advection of North Atlantic Deep Water from the Labrador Sea to the southern hemisphere. *Journal of Geophysical Research: Oceans*, 120(4):2471–2487.

Rhein, M., Steinfeldt, R., Kieke, D., Stendardo, I., and Yashayaev, I. (2017). Ventilation variability of Labrador Sea Water and its impact on oxygen and anthropogenic carbon: a review. *Philosophical Transactions of the Royal Society of London A: Mathematical, Physical and Engineering Sciences*, 375(2102).

Rignot, E., Velicogna, I., van den Broeke, M. R., Monaghan, A., and Lenaerts, J. T. M. (2011). Acceleration of the contribution of the Greenland and Antarctic Ice Sheets to sea level rise. *Geophysical Research Letters*, 38(5):L05503.

Rudels, B. (2011). Volume and freshwater transports through the Canadian Arctic Archipelago - Baffin Bay system. *Journal of Geophysical Research: Oceans*, 116(C8):C00D10.

Rudels, B., Larsson, a.-M., and Sehlstedt, P.-I. (1991). Stratification and water mass formation in the Arctic Ocean: some implications for the nutrient distribution. *Polar Research*, 10(1):19–32.

Rumyantseva, A., Lucas, N., Rippeth, T., Martin, A., Painter, S. C., Boyd, T. J., and Henson, S. (2015). Ocean nutrient pathways associated with the passage of a storm. *Global Biogeochemical Cycles*, 29(8):1179–1189.

Saenko, O. A., Yang, D., Gregory, J. M., Spence, P., and Myers, P. G. (2015). Separating the influence of projected changes in air temperature and wind on patterns of sea level change and ocean heat content. *Journal of Geophysical Research: Oceans*, 120(8):5749–5765.

Sathiyamoorthy, S. and Moore, G. W. K. (2002). Buoyancy flux at ocean weather station Bravo. *Journal of Physical Oceanography*, 32(2):458–474.

Schwarz, J. and Schodlok, M. (2009). Impact of drifting icebergs on surface phytoplankton biomass in the southern ocean: Ocean colour remote sensing and *in situ* iceberg tracking. *Deep Sea Research Part I: Oceanographic Research Papers*, 56(10):1727 – 1741.

Screen, J. A., Deser, C., and Simmonds, I. (2012). Local and remote controls on observed Arctic warming. *Geophysical Research Letters*, 39(10):L10709.

Screen, J. A., Deser, C., Smith, D. M., Zhang, X., Blackport, R., Kushner, P. J., Oudar, T., McCusker, K. E., and Sun, L. (2018). Consistency and discrepancy in the atmospheric response to Arctic sea-ice loss across climate models. *Nature Geoscience*, 11(3):155–163.

Screen, J. A. and Simmonds, I. (2010). The central role of diminishing sea ice in recent arctic temperature amplification. *Nature*, 464(1334).

Serreze, M. C. and Francis, J. A. (2006). The Arctic amplification debate. *Climatic Change*, 76(3-4):241–264.

Serreze, M. C., Holland, M. M., and Stroeve, J. (2007). Perspectives on the Arctic's shrinking sea-ice cover. *Science*, 315(5818):1533–1536.

Shchepetkin, A. F. and McWilliams, J. C. (1998). Quasi-monotone advection schemes based on explicit locally adaptive dissipation. *Monthly Weather Review*, 126(6):1541–1580.

Shine, K. P. and HendersonSellers, A. (1985). The sensitivity of a thermodynamic sea ice model to changes in surface albedo parameterization. *Journal of Geophysical Research: Atmospheres*, 90(D1):2243–2250.

Simmonds, I. and Rudeva, I. (2012). The great Arctic cyclone of August 2012. *Geophysical Research Letters*, 39(23). L23709.

Smedsrud, L. H., Esau, I., Ingvaldsen, R. B., Eldevik, T., Haugan, P. M., Li, C., Lien, V. S., Olsen, A., Omar, A. M., Otterå, O. H., Risebrobakken, B., Sandø, A. B., Semenov, V. A., and Sorokina, S. A. (2013). The role of Barents Sea in the Arctic climate system. *Reviews of Geophysics*, 51(3):415–449.

Smith, G. C., Roy, F., Mann, P., Dupont, F., Brasnett, B., Lemieux, J.-F., Laroche, S., and Bélair, S. (2014). A new atmospheric dataset for forcing ice–ocean models: Evaluation of reforecasts using the Canadian global deterministic prediction system. *Quarterly Journal of the Royal Meteorological Society*, 140(680):881–894.

Steele, M., Morley, R., and Ermold, W. (2001). PHC: A global ocean hydrography with a high-quality Arctic Ocean. *Journal of Climate*, 14(9):2079–2087.

Steffen, K. (1985). Warm water cells in the North Water, Northern Baffin Bay during winter. *Journal of Geophysical Research: Oceans*, 90(C5):9129–9136.

Stramma, L., Johnson, G. C., Firing, E., and Schmidtko, S. (2010). Eastern pacific oxygen minimum zones: Supply paths and multidecadal changes. *Journal of Geophysical Research: Oceans*, 115(C9).

Straneo, F. and Heimbach, P. (2013). North Atlantic warming and the retreat of Greenland's outlet glaciers. *Nature*, 504(7478):36–43.

Stroeve, J. C., Markus, T., Boisvert, L., Miller, J., and Barrett, A. (2014). Changes in arctic melt season and implications for sea ice loss. *Geophysical Research Letters*, 41(4):1216–1225.

Stroeve, J. C., Maslanik, J., Serreze, M. C., Rigor, I., Meier, W., and Fowler, C. (2011). Sea ice response to an extreme negative phase of the Arctic Oscillation during winter 2009/2010. *Geophysical Research Letters*, 38(2):L02502.

Tang, C. L., Ross, C. K., Yao, T., Petrie, B., DeTracey, B. M., and Dunlap, E. (2004). The circulation, water masses and sea-ice of Baffin Bay. *Progress in Oceanography*, 63(4):183–228.

Tivy, A., Howell, S. E. L., Alt, B., McCourt, S., Chagnon, R., Crocker, G., Carrieres, T., and Yackel, J. J. (2011). Trends and variability in summer sea ice cover in the Canadian Arctic based on the Canadian Ice Service Digital Archive, 19602008 and 19682008. *Journal of Geophysical Research: Oceans*, 116(C3). C03007.

Torres-Valdés, S., Tsubouchi, T., Bacon, S., Naveira-Garabato, A. C., Sanders, R., McLaughlin, F. A., Petrie, B., Kattner, G., Azetsu-Scott, K., and Whitledge, T. E. (2013). Export of nutrients from the Arctic Ocean. *Journal of Geophysical Research: Oceans*, 118(4):1625–1644.

Tremblay, J.-E., Bélanger, S., Barber, D. G., Asplin, M., Martin, J., Darnis, G., Fortier, L., Gratton, Y., Link, H., Archambault, P., Sallon, A., Michel, C., Williams, W. J., Philippe, B., and Gosselin, M. (2011). Climate forcing multiplies biological productivity in the coastal Arctic Ocean. *Geophysical Research Letters*, 38(18):L18604.

van Aken, H. M., de Jong, M. F., and Yashayaev, I. (2011). Decadal and multi-decadal variability of Labrador Sea Water in the north-western North Atlantic Ocean derived from tracer distributions: Heat budget, ventilation, and advection. *Deep Sea Research Part I: Oceanographic Research Papers*, 58(5):505 – 523.

van den Broeke, M., Bamber, J., Ettema, J., Rignot, E., Schrama, E., van de Berg, W. J., van Meijgaard, E., Velicogna, I., and Wouters, B. (2009). Partitioning recent Greenland mass loss. *Science*, 326(5955):984–986.

Vancoppenolle, M., Fichefet, T., Goosse, H., Bouillon, S., Madec, G., and Maqueda, M. A. M. (2009). Simulating the mass balance and salinity of Arctic and Antarctic sea ice. 1. Model description and validation. *Ocean Modelling*, 27(1–2):33–53.

Vernet, M., Sines, K., Chakos, D., Cefarelli, A., and Ekern, L. (2011). Impacts on phytoplankton dynamics by free-drifting icebergs in the nw weddell sea. *Deep Sea Research Part II: Topical Studies in Oceanography*, 58(11):1422 – 1435. Free-Drifting Icebergs in the Southern Ocean.

Våge, K., Pickart, R. S., Sarafanov, A., Knutsen, Ø., Mercier, H., Lherminier, P., van Aken, H. M., Meincke, J., Quadfasel, D., and Bacon, S. (2011). The Irminger Gyre: Circulation, convection, and interannual variability. *Deep Sea Research Part I: Oceanographic Research Papers*, 58(5):590 – 614.

Walczowski, W., Piechura, J., Goszczko, I., and Wieczorek, P. (2012). Changes in atlantic water properties: an important factor in the european arctic marine climate. *ICES Journal of Marine Science*, 69(5):864–869.

Wang, J., Kim, H.-M., and E.K.M., C. (2017). Changes in Northern Hemisphere winter storm tracks under the background of Arctic amplification. *Journal of Climate*, 30:3705–3724.

Weise, A. M., Levasseur, M., Saucier, F., Senneville, S., Bonneau, E., Roy, S., Sauvé, G., Michaud, S., and Fauchot, J. (2002). The link between precipitation, river runoff, and blooms of the toxic dinoflagellate Alexandrium tamarense in the St. Lawrence. *Canadian Journal of Fisheries and Aquatic Sciences*, 59(3):464–473.

Williams, R. G., Roussenov, V., and Follows, M. J. (2006). Nutrient streams and their induction into the mixed layer. *Global Biogeochemical Cycles*, 20(1).

Wu, Y., Platt, T., Tang, C. C. L., and Sathyendranath, S. (2007). Short-term changes in chlorophyll distribution in response to a moving storm: a modelling study. *Marine Ecology Progress Series*, 335:57–68.

Xianmin, H. (2012). *Simulation of Freshwater Associated with the Canadian Arcitc Archipelago*. PhD thesis, University of Alberta, Canada.

Yankovsky, A. E. and Yashayaev, I. (2014). Surface buoyant plumes from melting icebergs in the Labrador Sea. *Deep Sea Research Part I: Oceanographic Research Papers*, 91:1 – 9.

Yashayaev, I. (2007). Hydrographic changes in the Labrador Sea, 1960-2005. *Progress in Oceanography*, 73:242–276.

Yashayaev, I. and Loder, J. W. (2017). Further intensification of deep convection in the Labrador Sea in 2016. *Geophysical Research Letters*, 44(3):1429–1438. 2016GL071668.

Yin, K., Harrison, P. J., Goldblatt, R. H., and Beamish, R. J. (1996). Spring bloom in the central Strait of Georgia: interactions of river discharge, winds and grazing. *Marine Ecology Progress Series*, 138(1/3):255–263.

Zweng, M. M. and Münchow, A. (2006). Warming and freshening of Baffin Bay, 1916-2003. *Journal of Geophysical Research: Oceans*, 111:C07016.